

**BONNER METEOROLOGISCHE ABHANDLUNGEN**

Heft 73 (2016) (ISSN 0006-7156)

Herausgeber: Andreas Hense

Christian Bernardus Maria Weijenborg

**CHARACTERISTICS OF POTENTIAL VORTICITY ANOMALIES  
ASSOCIATED WITH MESOSCALE EXTREMES  
IN THE EXTRATROPICAL TROPOSPHERE**



---

**BONNER METEOROLOGISCHE ABHANDLUNGEN**

Heft 73 (2016) (ISSN 0006-7156)

Herausgeber: Andreas Hense

---

---

Christian Bernardus Maria Weijenborg

**CHARACTERISTICS OF POTENTIAL VORTICITY ANOMALIES  
ASSOCIATED WITH MESOSCALE EXTREMES  
IN THE EXTRATROPICAL TROPOSPHERE**

---



# Characteristics of Potential Vorticity anomalies associated with mesoscale extremes in the extratropical troposphere

DISSERTATION  
ZUR  
ERLANGUNG DES DOKTORGRADES (DR. RER. NAT.)  
DER  
MATHEMATISCH-NATURWISSENSCHAFTLICHEN FAKULTÄT  
DER  
RHEINISCHEN FRIEDRICH-WILHELMS-UNIVERSITÄT BONN

vorgelegt von  
**Christian Bernardus Maria Weijenborg**, Master of Science  
aus  
Winterswijk, Niederlande

Bonn, Dezember, 2015

Diese Arbeit ist die ungekürzte Fassung einer der Mathematisch-Naturwissenschaftlichen Fakultät der Rheinischen Friedrich-Wilhelms-Universität Bonn im Jahr 2015 vorgelegten Dissertation von Christian Bernardus Maria Weijenborg aus Winterswijk, Niederlande.

This paper is the unabridged version of a dissertation thesis submitted by Christian Bernardus Maria Weijenborg born in Winterswijk, the Netherlands to the Faculty of Mathematical and Natural Sciences of the Rheinische Friedrich-Wilhelms-Universität Bonn in 2015.

Anschrift des Verfassers:

Address of the author:

Christian Bernardus Maria Weijenborg  
Meteorologisches Institut der  
Universität Bonn  
Auf dem Hügel 20  
D-53121 Bonn

1. Gutachter: PD Dr. Petra Friederichs, Rheinische Friedrich-Wilhelms-Universität Bonn
2. Gutachter: Prof. Dr. Andreas Hense, Rheinische Friedrich-Wilhelms-Universität Bonn

Tag der Promotion: 02. Mai 2016

## ABSTRACT

---

Severe convective weather, which has a huge impact on society, is influenced by a large range of scales. However, extremes, by definition rare events, are especially hard to forecast. This study proposes to use Potential Vorticity (PV) as an analytic tool for diagnosing Deep Moist Convection (DMC) on the convective weather scale ( $\approx 10$  km). On synoptic and planetary scales, PV is a useful conceptual variable. Given a balance condition, and suitable boundary conditions, one can invert a given PV distribution to obtain wind velocity, pressure and (potential) temperature distribution associated with the PV distribution. Ideally, one would like to invert the PV distribution on the convective weather scale, too. Inversion of PV associated with DMC is problematic, because of the unsteady convection and the unknown balance condition. This study hypothesises, however, that PV anomalies might still be seen as “quasi”-balanced. This implies that one would expect consistent PV during DMC, associated with coherent significant flow anomalies. This study tests the coherency of PV anomalies by compositing the PV distribution around convective cells in the nonhydrostatic Numerical Weather Prediction (NWP) model COSMO-DE.

A case study of two severe weather events (5 and 22 June 2011) shows that the COSMO-DE model is capable of reproducing the theoretically described PV dipole around a convective updraft. During the 22 June event, bands of PV are generated. Possible explanations for these bands are advection due to large scale wind shear and the preferential generation of new cells downshear of old cells. Tracks of the evolution of PV dipoles show that for both cases there is a consistent development. In this study 9 severe weather cases are selected, with a large range of synoptic backgrounds. The consistent evolution is confirmed by composites of storm cells during all severe weather cases. Especially intense cells, characterised by e.g. severe precipitation rates or strong PV, have a more monopole morphology. Moreover, strong PV cells last relatively long. This indicates that these intense cells might be regarded as “supercells”: longlasting intense rotating updrafts. This also implies that PV might be an indicator for severe weather. Spectra of potential enstrophy show a consistent correlation with extreme precipitation and the spectral variance on the convective weather scale in COSMO-DE.



# CONTENTS

---

1	INTRODUCTION	1
1.1	Definition extremes	4
1.2	Main objectives and questions	5
2	THEORY AND BACKGROUND	7
2.1	Convection	7
2.1.1	Thermodynamics of dry air	7
2.1.2	Thermodynamics of moist air	8
2.1.3	The complete picture	10
2.2	Influence of the environment on convective characteristics	11
2.2.1	Wind shear	11
2.2.2	Helicity	15
2.2.3	Convective parameters and severe weather predictability	16
2.3	Overview of conserved quantities	18
2.3.1	Circulation and vorticity	18
2.3.2	The introduction of PV	19
2.4	Properties of PV	20
2.4.1	Evolution	22
2.4.2	Moist PV	23
2.4.3	Mesoscale PV dipoles	23
3	MODEL AND DATA	27
3.1	Description of model	27
3.1.1	Model equations and domain	27
3.1.2	Parameterisation	29
3.1.3	COSMO-DE-EPS	30
3.1.4	Reforecast	31
3.1.5	Calculation of post-processed quantities	31
3.2	Data description and case study selection	32
3.2.1	Selection of 9 severe weather cases	32
3.2.2	Synoptic situation	34
3.3	PV budget	37
3.3.1	Variance analysis	38
3.3.2	Linear Regression	41
3.4	Importance full PV	44
4	CASE STUDY: 5 AND 22 JUNE 2011	47
4.1	Aims and Motivations	47
4.2	Background	48
4.3	Data and methodology	51
4.3.1	Model and data	51
4.3.2	Methodology	51
4.4	Mesoscale situation	52
4.5	Storm cell composites	54

	4.5.1	The 22 June case	56
	4.5.2	Different vertical velocity thresholds	60
	4.5.3	Composites at other time steps	61
	4.5.4	The 5 June case	62
	4.6	Summary and discussion	64
5		EVOLUTION OF STORM CELLS	67
	5.1	Aims and Motivations	67
	5.2	Methodology	68
	5.2.1	Choice of tracking on the vertical velocity	68
	5.2.2	Tracking methodology	70
	5.2.3	Compositing	70
	5.3	Variability of environment	74
	5.4	Evolution of convective cells of 22 June 2011	76
	5.4.1	Composites of convective cells	77
	5.4.2	Vorticity budget	81
	5.5	Evolution of convective cells of 5 June 2011	84
	5.5.1	Composites of convective cells	85
	5.5.2	Vorticity budget	88
	5.6	Summary and discussion	90
6		EVOLUTION OF EXTREME CONVECTIVE CELLS	91
	6.1	Aims and motivation	91
	6.2	Rotation of convective cells	91
	6.3	Variability of environmental parameters and storm cell properties	92
	6.3.1	Spatial and temporal dependence of cell characteristics	94
	6.3.2	EOF analysis	98
	6.3.3	Choice of convective variables	102
	6.4	Composites	104
	6.4.1	Diabatic forcing	104
	6.4.2	General evolution	105
	6.4.3	Evolution of extreme cells	106
	6.4.4	Influence environment on storm cell morphology	109
	6.4.5	Properties extreme cells	113
	6.4.6	PV as possible predictor for severe convective cells	114
	6.5	Summary and discussion	115
7		PV AS PREDICTOR FOR SEVERE WEATHER	117
	7.1	Aims and motivations	117
	7.2	Methodology	118
	7.2.1	Spectral severe weather predictors	120
	7.3	Spectra for the severe weather cases	121
	7.3.1	Anisotropy in spectrum	123
	7.4	Relation of spectra to extremes	125
	7.5	Summary and Discussion	128
8		CONCLUSION AND DISCUSSION	131
	8.1	Summary of main results	132
	8.1.1	Main implication of results	134

8.2	Remaining questions and further analysis	134
A	EVOLUTION CONSERVED QUANTITIES	137
A.1	PV evolution equation	137
B	PERFORMANCE OF ROTATION ALGORITHM	139
B.1	Sensitivity of composite on rotation	139
	BIBLIOGRAPHY	143

## LIST OF FIGURES

---

Figure 1.1	Characteristic scales and durations of atmospheric phenomena	2
Figure 1.2	Extremes at 5 June 2011	5
Figure 2.1	Calculation of CAPE and CIN	10
Figure 2.2	Cell development	12
Figure 2.3	Multicell development	13
Figure 2.4	RKW theory	14
Figure 2.5	Synoptic Potential Vorticity (PV) anomalies	21
Figure 2.6	Dipoles created by diabatic heating	23
Figure 2.7	Schematic depiction of generation of PV dipoles	25
Figure 3.1	Domain and grid box of COSMO DE model	29
Figure 3.2	Synoptic overview of 5 and 22 June 2011	35
Figure 3.3	Rain rates for 5 and 22 June 2011	36
Figure 3.4	Volume boxes used in PV budget analysis	37
Figure 3.5	PV budget variances 5 June	39
Figure 3.6	PV budget variances 22 June	40
Figure 3.7	Explained variance budget MLR	41
Figure 3.8	Average regression coefficients PV budget	43
Figure 3.9	Mean PV profiles	44
Figure 3.10	Variance PV profiles	45
Figure 4.1	Schematic overview of PV dipoles generated due to convection	48
Figure 4.2	Schematic overview of PV bands generated due to convection	49
Figure 4.3	PV and precipitation on 5 June 2011	53
Figure 4.4	PV and precipitation on 22 June 2011	54
Figure 4.5	Cross sections of PV on 5 and 22 June 2011	55
Figure 4.6	Composites on 22 June 2011	56
Figure 4.7	Composites on 22 June 2011 for different thresholds	57
Figure 4.8	Dependence between kinetic energy and PV anomalies on 22 June 2011	58
Figure 4.9	Vertical cross sections for different thresholds	59
Figure 4.10	Composites on 22 June 2011 for other time steps	59
Figure 4.11	As in Fig. 4.6, but on 5 June 2011 at 15 UTC.	62
Figure 4.12	As in Fig. 4.7, but on 5 June 2011 at 15 UTC.	63
Figure 4.13	As in Fig. 4.8, but on 5 June 2011 at 15 UTC.	63
Figure 4.14	As in Fig. 4.10, but on 5 June 2011.	64
Figure 5.1	Schematic of tracking algorithm.	69
Figure 5.2	Schematic overview of p-recurrence	73
Figure 5.3	Environment characteristics 5 and 22 June	74
Figure 5.4	Storm cell characteristics 5 and 22 June	75
Figure 5.5	Tracks and storm parameter evolution for 22 June 2011	76

Figure 5.6	22 June 2011 evolution composites	78
Figure 5.7	22 June 2011 intense cells evolution composites	79
Figure 5.8	22 June precipitation composites	80
Figure 5.9	22 June vorticity budget at maximum Gaussian filtered vertical velocity	82
Figure 5.10	22 June vorticity budget evolution.	83
Figure 5.11	As Fig. 5.5, but for 5 June 2011.	84
Figure 5.12	5 June evolution composites	85
Figure 5.13	As in Fig. 5.7, but for 5 June 2011.	86
Figure 5.14	5 June precipitation composites	87
Figure 5.15	5 June vorticity budget	88
Figure 5.16	5 June vorticity budget evolution	89
Figure 6.1	Rotation of wind shear	92
Figure 6.2	Environmental characteristics of storm cells	93
Figure 6.3	Temporal evolution of the environmental characteristics	94
Figure 6.4	Temporal evolution of the cell characteristics	95
Figure 6.5	Spatial variation of the cell characteristics	96
Figure 6.6	Temporal difference $w$ and PV maximum	97
Figure 6.7	EOF of storm cell environmental parameters	100
Figure 6.8	EOF of storm cell properties	103
Figure 6.9	Diabatic heating composites	104
Figure 6.10	General evolution storm cells	107
Figure 6.11	Evolution of storm cells for different thresholds	108
Figure 6.12	Composites of storm cells for different thresholds	110
Figure 6.13	Dependence of evolution storm cells on environment	111
Figure 6.14	Correlation coefficient $r$ for different precipitation and SRH thresholds	113
Figure 6.15	PV as predictor for severe weather	114
Figure 6.16	PV as predictor for supercells	114
Figure 7.1	Schematic depiction of calculation of anisotropic spectral energy	120
Figure 7.2	Kinetic energy spectra for 5 and 22 June 2011	122
Figure 7.3	Potential enstrophy spectra for 5 and 22 June 2011	122
Figure 7.4	Anisotropic PV and Kinetic energy spectra	123
Figure 7.5	Spectra compared with model precipitation and model wind gusts	126
Figure 7.6	Spectra compared with precipitation observations	127
Figure B.1	3 to 7.3 km height integrated mean wind before and after rotation	140
Figure B.2	As in Fig. 6.10, but using only the 5 and 22 June 2011 cases	141

Figure B.3 Composites of storm cells, for different rotation methods 142

## LIST OF TABLES

---

Table 3.1	Selection of the 9 severe weather cases	33
Table 4.1	Storm cell characteristics on 22 June 2011	61
Table 4.2	As Table 4.1, but for 5 June 2011.	64
Table 5.1	Storm cell environment variables	72
Table 5.2	Storm cell characteristics variables	73

## ACRONYMS

---

BRN Bulk Richardson Number

CAPE Convective Available Potential Energy

CAPE<sub>3km</sub> CAPE calculated with an air parcel with thermodynamical properties of the lowest 50 hPa of the atmosphere, up to an ascent of 3 km above the surface

CIN Convective Inhibition

DMC Deep Moist Convection

DSI Dynamical State Index

DWD German Meteorological Service

ECC Ensemble Copula Coupling

EL Equilibrium Level

EOF Empirical Orthogonal Function

EPS Ensemble Prediction System

EPV Equivalent Potential Vorticity

FFT Fast Fourier Transform

GFS Global Forecast System

GSM Global Spectral Model

HDIV	Vertically integrated divergence of specific humidity $q_v$
IFS	Integrated Forecast System
LCL	Lifted Condensation Level
LFC	Level of Free Convection
LHN	Latent Heat Nudging
LI	Lifted Index
MLR	Multiple Linear Regression
NWP	Numerical Weather Prediction
PBL	Planetary Boundary Layer
PES	Potential Enstrophy Spectrum
PV	Potential Vorticity
PVS	Potential Vorticity Substance
PVU	Potential Vorticity Unit
QG	Quasi-Geostrophic
SI	Showalter Index
RH	Relative Humidity
SRH	Storm Relative Helicity
UTC	Coordinated Universal Time
VHT	Vortical Hot Tower
VNM	Vertical Normal Modes



## INTRODUCTION

---

Due to the huge impact on society, knowledge of extreme convective weather events is crucial. Economic costs related to severe weather exceed US\$ 1.4 Trillion for the 1980-2004 period [Mills, 2005]. Most of the insured property losses (about 70%) are related to small scale weather events [Mills, 2005]. One of the major challenges in modern meteorology is the physical understanding and the forecasting of extreme events in general and those associated with Deep Moist Convection (DMC) in particular [Shapiro and Thorpe, 2004]. The fundamental problem in forecasting DMC and its dynamics is the intense interaction of processes acting on a large range of spatial and temporal scales (Fig. 1.1). On one hand, one has microphysical processes which play a role in building clouds, and at the other hand convection can organise itself into systems up to a few hundred kilometres. Another reason for the limited predictability of mesoscale phenomena is that the associated eddy lifetimes are much smaller compared to their synoptic counterparts (Fig. 1.1).

There is no exact definition for the mesoscale. The mesoscale contains roughly scales from 2 up to 2000 km [Orlanski, 1975]. Fujita [1986] defined the mesoscale ranging from 4 to 400 km, a much smaller scale range. The term was first used by Ligda [1951], as an attempt to describe weather phenomena larger than the microscale, but smaller than the synoptic scale. An important dynamical distinction between the mesoscale and the synoptic and microscale is that for the mesoscale the full dynamic equations are relevant. At other scales, some terms in the equations of motion can be neglected, which simplifies the equations. For example on the synoptic scale, vertical accelerations and advection by the ageostrophic wind can be neglected. The consequence is that most of the synoptic scale motions can be approximated by Quasi-Geostrophic (QG) balance. On the mesoscale, however, no general balance condition exists.

The three ingredients necessary for DMC are instability, lift and moisture [Doswell III, 1987]<sup>1</sup>. In forecasting severe weather, often large scale indicators of the atmospheric stability like Convective Available Potential Energy (CAPE) are used. Convective parameters like CAPE combine within a single parameter the information of a thermodynamic profile, but represent only parts of the full dynamics. Conserved quantities like the Ertel Potential Vorticity (PV) [Schubert et al., 2004] may offer new insights in the dynamics of convective weather, which have not yet been investigated thoroughly on the convective weather scale ( $\approx 1-10$  km). One particular reason why this might be worthwhile, is that vorticity dynamics is crucial for severe weather on the storm-scale, e.g. for supercells. PV combines dynamical and thermodynamical information into one variable, and the conservation property of PV might give a relatively simple view on the dynamics without relying on strong assumptions.

---

<sup>1</sup> From here up to section 1.1, parts of introduction of Weijenborg et al. [2015] are reproduced

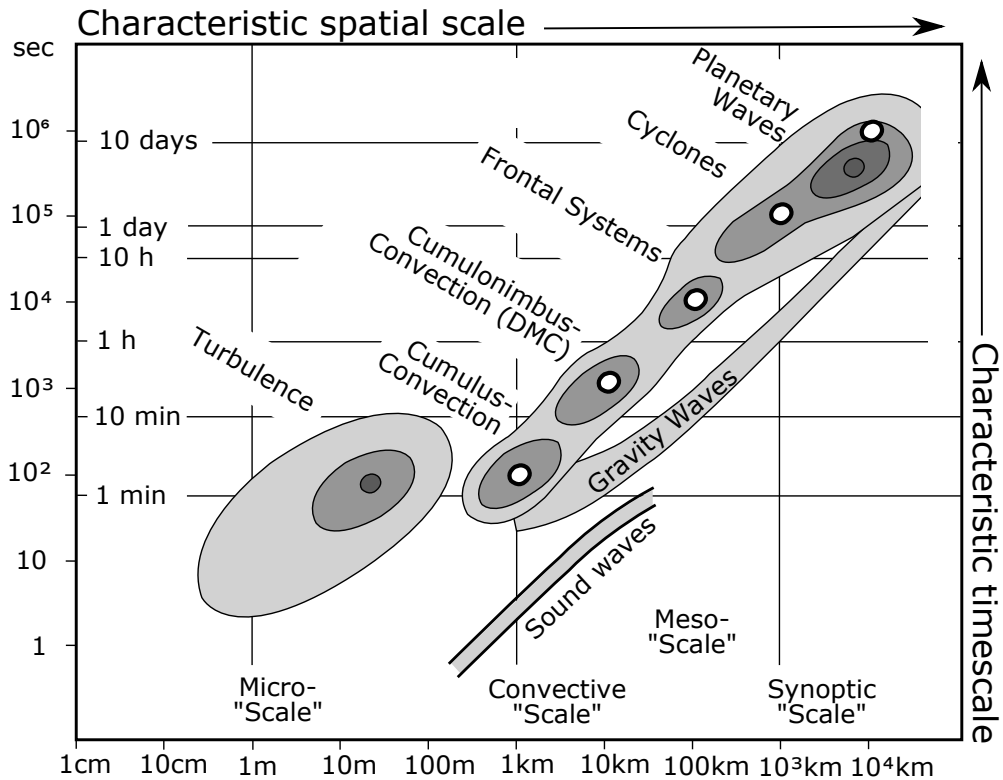


Figure 1.1: Characteristic scales and durations of atmospheric phenomena, reproduced (with permission) and translated after Fortak [1982].

Most of the studies on PV dynamics focus on synoptic to planetary scales, where it is useful in describing e.g. cyclogenesis and Rossby wave propagation [e.g. Hoskins et al., 1985; Hoskins, 1997]. On these scales PV provides insightful conceptual models to describe midlatitude dynamics [e.g. Hoskins et al., 1985; Haynes and McIntyre, 1987]. PV has two useful properties. First, it is materially conserved for frictionless and adiabatic flow, which allows to interpret PV as a dynamical tracer. Furthermore, PV is very useful in indicating the effects of diabatic heating on atmospheric dynamics [Grams et al., 2011; Chagnon et al., 2012]. Secondly, it is tightly related to balanced flow by the invertibility principle. Given suitable boundary and balance conditions, a PV field can be inverted to derive standard meteorological quantities such as wind velocity and pressure [Hoskins et al., 1985]. For synoptic and larger scales the QG balance is generally a good assumption [Holton, 2004]. A positive (negative) QG PV anomaly is associated with cyclonic (anticyclonic) rotation [e.g. Hoskins et al., 1985; Hoskins, 1997]. The static stability inside a positive (negative) QG PV anomaly is generally increased (reduced). Below and above a QG PV anomaly, the static stability perturbation has the opposite sign compared to inside the PV anomaly.

There are some studies of PV dynamics on the mesoscale, mainly focusing on idealised test cases of mesoscale convective vortices [e.g. Raymond and Jiang, 1990; Davis and Weisman, 1994; Cram and Montgomery, 2002; Conzemius and Montgomery, 2009], on mesoscale orographic PV anomalies [e.g. Aebischer and Schär, 1998; Schär et al., 2003], and on PV along fronts [e.g. Malardel et al.,

1993; Appenzeller and Davies, 1996]. On the convective weather scale there is little research on PV. It is an open question what kind of PV anomalies occur during convection and how they compare with synoptic PV anomalies, especially for real cases as represented by forecast data. To the best of our knowledge only Conzemius and Montgomery [2009] and Chagnon and Gray [2009] have analysed PV dynamics on the convective weather scale in the extratropics. They found that horizontal PV anomalies (i.e. anomalies aligned in the horizontal plane) organise as dipoles with a strength of about 10 PVU ( $1 \text{ PVU} \equiv 1 \times 10^{-6} \text{ Km}^2 \text{ s}^{-1} \text{ kg}^{-1}$ ) during convection. This is about  $\mathcal{O}(10)$  larger than typical synoptic PV structures. Although synoptic scale PV anomalies have a stronger influence on flow anomalies (Hoskins et al. [1985], because it is essentially the coarse grained PV that matters), these strong anomalies might still induce significant flow anomalies.

These convective scale PV dipoles are created by the tilting of horizontal vorticity caused by storm-scale updrafts [e.g. Conzemius and Montgomery, 2009], analogously to the creation of a pair of vertical vorticity around an updraft [see Davies-Jones, 1984; Lilly, 1986a]. Chagnon and Gray [2009] found those dipoles in a environment with moderate vertical shear of the horizontal flow to be related to heating on the storm scale originating from heating by moist processes inside clouds. Similar PV dipoles have been found in the vicinity of tropical cyclones. A Vortical Hot Tower (VHT) is a rotating tropical cumulonimbi, which shares characteristics with midlatitude supercells [E.g. Montgomery et al., 2006; Rutherford, 2012]. The main difference with the midlatitude PV dipoles is that for these dipoles the environmental vorticity is provided by a mesoscale convective vortex.

Inversion of mesoscale or convective-scale PV anomalies, like one can do for synoptic scale QG PV anomalies, would be very useful. This would indicate some kind of predictability, since we can obtain flow and thermodynamic variables from “just” the PV distribution (and suitable boundary conditions). A problem is, however, that we also need a balance condition. DMC is very unsteady, therefore it is doubtful if the flow around the mesoscale dipoles is balanced. However, one could argue that the flow is at least quasi-balanced. First, Chagnon and Gray [2009] suggested that the PV dipoles created by convection have a longer lifetime than the original updraft that generated the dipole. They argued that although the PV dipole is created by the horizontal vorticity component due to the vertical wind shear of the horizontal wind, the vorticity is tilted almost immediately into the vertical. This can possibly lead to balanced dipoles which survive after the original diabatic perturbation has vanished. Secondly, Chagnon and Gray [2009] estimated that the time-scale of adjustment to a balanced flow for the convective weather scale is approximately 0.5 h, which is shorter than the lifetime of an individual storm cell. Full balance can never be achieved, since latent heating will continuously perturb the flow away from balance. But the ratio of the estimated adjustment time to the life time of a storm cell is indicative for a balanced flow. A third reason to presume quasi-balance is that severe convective weather associated with rotating storms is often relatively long lasting (e.g. supercells, which can last for several hours). Thus, although PV inversion on the convective weather scale might be impossible, it still would

be very useful to determine the general PV and flow anomalies associated with DMC.

An other open question is if and how these PV dipoles organise into larger structures. Chagnon and Gray [2009] discussed a squall line for which the PV dipoles are aligned in positive and negative PV bands. It is generally known that vertical wind shear influences the organisation of mesoscale convective storms. Weisman and Klemp [1982] found that multicell storms are favoured in moderate shear ( $10\text{-}20\text{ ms}^{-1}$  in the lowest 6 km, referred to as bulk shear). Increasing wind shear and directional shear further favours the generation of super cells. New cells in a squall line are favourably generated at the downshear side of a storm system, since here the lifting by the gust front is enhanced due to background vorticity. Rotunno et al. [1988] and Weisman and Rotunno [2004] hypothesised that squall lines are best maintained when there is an equilibrium between cold pool outflow and wind shear. Although the role of cold pool wind shear in determining an optimal state for long-lived squall lines is still a matter of debate, there is general agreement that the wind shear plays an important role in storm organisation [Stensrud et al., 2005]. The strength of the dipoles is proportional to the wind shear magnitude and the direction is parallel to the direction of the wind shear [Chagnon and Gray, 2009]. Therefore, the wind shear will probably also influence the PV structures on larger scales.

### 1.1 DEFINITION EXTREMES

We have introduced mesoscale weather extremes, but we have not given an exact definition of what we consider as mesoscale weather extremes. There is no generally accepted broad definition for an extreme event [Ghil et al., 2011]. They are per definition rare events, there is an observable which takes an extreme value, and they do not occur regularly. One could define weather extremes using different approaches:

- Threshold definition based on dynamics: e.g. large hail, precipitation rates and/or wind gust above a certain threshold: In the European Severe Weather Database [Kaltenböck et al., 2009], for example hail with a diameter of at least 2 cm and wind gusts stronger than  $25\text{ ms}^{-1}$  are regarded as weather extremes.
- Definition based on societal and/or economic impact [Chagnon et al., 1997].
- Statistical definition: e.g. the 1% most severe precipitation rates or the 1% most severe wind gusts.

Of course, there is a lot of overlap between these definitions. A tornado has huge impact and generates severe wind gusts which are also statistically severe. A typical severe weather event we are interested in is shown in Fig. 1.2. On this day, 5 June 2011, 66 mm of rain fell in Bonn, most of it in just one hour. We will discuss this case in further detail, together with another case (22 June 2011), which had more larger scale forcing. Later on in this thesis we will use the statistical definition, since this is the most objective definition for extremes.

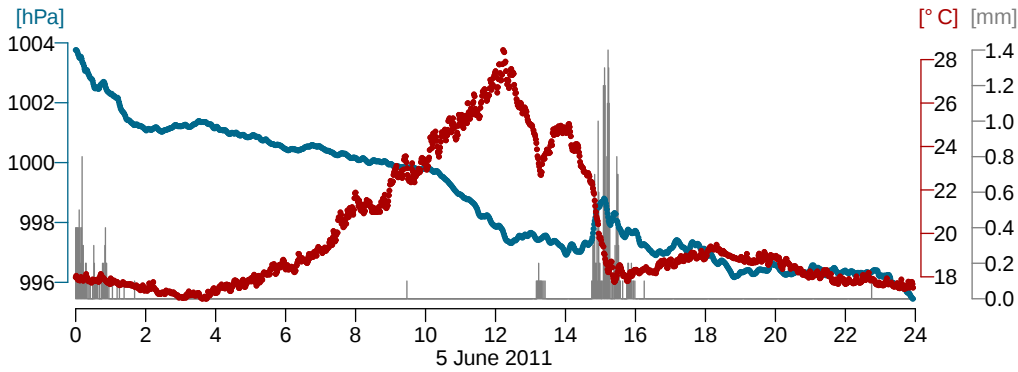


Figure 1.2: Temperature (red line), pressure (blue line) and precipitation (grey bars) at 5 June 2011, measured by the Meteorological Institute, the University of Bonn.

## 1.2 MAIN OBJECTIVES AND QUESTIONS

The main goal of the present study is to describe the consistency of PV anomalies during severe convection in a convection-permitting Numerical Weather Prediction (NWP) using data from operational forecasts. We want to investigate a few of the thoughts of Chagnon and Gray [2009] in deeper detail. Firstly, we investigate the coherency of the horizontal PV dipoles by calculating composites of PV and other fields around storm cells. Secondly, we want to discuss the influence of the synoptic environment on the orientation and other characteristics of the PV dipoles. Furthermore, since we are interested in extremes, we want to investigate if those extremes exhibit significant different characteristics compared to “normal” cells. In this case this might indicate that PV can be used as an indicator of extreme convective storms.

Data from the operational nonhydrostatic NWP model COSMO-DE are used, as well data from its Ensemble Prediction System (EPS) [COSMO-DE-EPS, Baldauf et al., 2011; Peralta et al., 2012]. First, two cases of severe weather over Germany during June 2011 are selected with a different synoptic background. One which consists of local severe convection (5 June 2011) and one of convection along a cold front (22 June 2011). For these two cases composites of PV around convective cells are made. Later composites are calculated of the evolution of PV anomalies around convective cells, for in total nine weather cases. This done by tracking the vertical velocity in COSMO-DE. The tracks of the nine cases serve as a representative climatology, which we use to investigate the difference between “normal” and “severe” convective cells.

Central questions we want to answer are:

- Q1 What are the general characteristics of PV anomalies associated with severe convective weather?
- Q2 Are there (convective scale) PV anomalies that organise themselves on a larger scale than the convective weather scale?
- Q3 How consistent is the evolution of the PV dipole described by Chagnon and Gray [2009] and how does this depend on the environment characteristics?

Q4 Do extreme storm cells have significant different characteristics?

Q5 Could PV be used as predictor for severe convective weather like precipitation and/or wind gust extremes?

The outline of this thesis is as follows. Chapter 2 gives a brief overview of the theory behind convection and behind conserved quantities, with a focus on PV. Chapter 3 describes the COSMO-DE NWP model. A simple budget analysis is carried out to see if PV is conserved and if so, which terms balance each other. In Chapter 4 we look at the two aforementioned weather cases. Main goal of this chapter is to get an overview of typical PV anomalies associated with DMC on the convective weather scale. Chapter 5 introduces the tracking methodology, and we look at composites of the evolution of PV anomalies associated with convective cells for the two cases introduced in Chapter 4. In Chapter 6 we apply this to in total nine severe weather cases. We look at the general composite over all those nine cases, and we discuss if extreme convective cells have significant characteristics. We will briefly discuss if PV might be usable as an indicator or even predictor for severe weather in Chapter 7. Lastly, in Chapter 8, we will discuss the main results.

## THEORY AND BACKGROUND

---

*This chapter consists of two parts. The first part will give background on the theory of Deep Moist Convection (DMC). It discusses under which conditions DMC will take place. It also discusses the most important quantities used in forecasting severe convection, like Convective Available Potential Energy (CAPE) and Storm Relative Helicity (SRH). The second part will discuss an overview of conserved variables related to the rotation and circulation. In this part the conserved quantities Potential Vorticity (PV) and Helicity will be introduced. The fundamental properties of PV and its usefulness in describing large scale and synoptic dynamics will be discussed.*

### 2.1 CONVECTION

In the most general definition, convection refers to a process by which heat is transferred in a fluid, by bulk movement of fluids (i.e. advection) [Serway and Jewett, 2013]. In meteorology, convection is defined as the vertical movement of fluids, as a consequence of unstable stratification [e.g. Markowski and Richardson, 2010]. DMC adds the influence of moisture. Moreover, in contrast to shallow convection, DMC should occur over the whole or a large part of the troposphere. We follow the definition of Markowski and Richardson [2010] of DMC as “air that gets saturated and subsequently acquires positive buoyancy, whereafter it can rise freely to great heights. Necessary ingredients for DMC are instability, lift, and moisture [Doswell III, 1987]. Here, we shortly review the basics of convection, and we discuss the influence of wind shear and helicity on the organisation and structure of convection.

A common way to analyse convection is with the so called “air parcel method”. This method assumes that the air can be divided into parcels, which do not interact with their environment. Although this assumption has its limits, it provides an easy way to describe the characteristics of DMC. One could imagine an air parcel like a rubber balloon, which can change its volume accordingly to adapt to the environmental pressure. It is assumed that the air inside the air parcel does not exchange heat or moisture with its environment.

#### 2.1.1 Thermodynamics of dry air

To determine under which conditions convection will take place, we start at the dry equation of state

$$p = \rho RT, \tag{2.1}$$

with  $p$  the atmospheric pressure,  $\rho$  the density and  $T$  the temperature [e.g. Stevens, 2005]. This implies that for dry air the system can be defined by two variables only, e.g.  $T$  and  $p$ . For a hydrostatic atmosphere, pressure and density are related through  $\frac{\partial p}{\partial z} = -\rho g$  and the spatial and temporal dependence of

the temperature  $T(x, y, z, t)$  plus some boundary conditions of pressure at the surface defines the whole system.

For most meteorological applications, instead of using  $T$  directly, it is more convenient to define a potential temperature  $\theta$ ,

$$\theta \equiv T \left( \frac{p_0}{p} \right)^{R_d/c_{p,d}}, \quad (2.2)$$

with  $p_0$  a reference pressure, often taken as 1000 hPa,  $R_d$  is the dry air constant and  $c_{p,d}$  the specific heat of dry air at constant pressure. The potential temperature  $\theta$  is the temperature an air parcel, with temperature  $T$  and pressure  $p$ , would have if it would be brought adiabatically (i.e. no heat exchange,  $dQ = 0$ ) to a reference pressure  $p_0$ . Since the entropy varies by  $dS = dQ/T$ , this implies that  $\theta$  surfaces are isentropic surfaces (i.e. constant entropy  $S$ ). As a consequence of the definition of the potential temperature, for isentropic displacements the temperature does not depend on the pressure  $p$ .

Convection is defined by buoyancy perturbations related to vertical accelerations. We therefore look at the vertical momentum equation [e.g. Stevens, 2005],

$$\left( \frac{\partial}{\partial t} + \mathbf{u} \cdot \nabla \right) w = -g \frac{\rho'}{\rho} - \frac{\partial p'}{\partial z} + \nu \nabla^2 w, \quad (2.3)$$

where  $\mathbf{u}$  is the 3D velocity vector,  $\nu$  the kinematic viscosity and  $w$  the vertical component of the velocity vector. Primes indicate a deviation from the hydrostatic balance. The first term on the right is relevant for convection, since it measures the buoyancy acceleration  $b$ . By linearisation of the vertical momentum equation, it can be shown that  $b$  is proportional to the ratio of the potential temperature perturbation  $\theta'$  and hydrostatic potential temperature  $\theta_0$  [e.g. Stevens, 2005]:

$$b = -g \frac{\rho'}{\rho} \approx -g \frac{\rho'}{\rho_0} \approx g \frac{\theta'}{\theta_0}. \quad (2.4)$$

Here the variables denotes with a 0 indicate a hydrostatic reference state. Therefore, the buoyancy is proportional to variations in  $\theta$ . If there is a positive perturbation  $\theta'$ , the buoyancy force is positive. It is easy to show, using a Taylor expansion of a vertical displaced air parcel from height  $z$  to  $z + \delta z$ , that this implies that a negative gradient of  $\theta$  with height is unstable. If such a negative gradient exists, the atmosphere will react by rearranging the fluid particles in such way that the atmosphere is stable again ( $\partial_z \theta = 0$ ).

### 2.1.2 Thermodynamics of moist air

To include the effect of moisture, a measure for the moisture content has to be defined. This is not trivial, since moisture constituents like water vapour,  $q_v$ , and liquid and ice water contents,  $q_l$  and  $q_i$  are strongly dependent on the temperature [Stevens, 2005]. A good choice might be the total water specific humidity  $q_t$ . One can then get the mass fraction of dry air  $q_d$  from  $q_d = 1 - q_t$ . An advantage of using  $q_t$  is that it does not change under reversible fluid displacements.

Starting again with the ideal gas law, but now with inclusion of moisture,

$$p = \rho_d R_d T + \rho_v R_v T = \rho_d R_d \left(1 + \frac{q_v}{\epsilon}\right), \quad (2.5)$$

with  $\rho_d$  and  $\rho_v$  the density of dry air and water vapour respectively,  $R_d$  and  $R_v$  are the corresponding gas constants,  $q_v$  is the specific humidity and  $\epsilon \equiv \frac{R_d}{R_v} = 0.6220$  is the ratio of the gas constants of dry air and water vapour. Here it is assumed that dry air and water vapour have the same temperature. The moist air constant  $R$  depends on the composition of air, but the water vapour concentration is highly spatial and temporal variable. Therefore, it is convenient to define the moist air constant  $R$  in terms of  $R_d$ ,

$$R = R_d \frac{1 + r_v/\epsilon}{1 + r_v}, \quad (2.6)$$

with  $r_v \equiv \rho_v/\rho_d$ , the water vapour mixing ratio. This allows us to write the ideal gas law as  $p = \rho R_d T_v$ , with  $T_v$  the virtual potential temperature  $T_v$ ,

$$T_v = T \frac{1 + r_v/\epsilon}{1 + r_v} \quad (2.7)$$

The virtual temperature is the temperature a dry air parcel must have, to have the same density as the moist air parcel. Equivalently, virtual potential temperature can be defined ( $\theta_v \equiv T_v (\frac{p_0}{p})^{R_d/c_{pd}}$ ). It appears, see e.g. Stevens [2005], that virtual potential temperature variations are proportional to density variations for the moist system:

$$\frac{\rho'}{\rho_0} \approx \frac{-\theta'_v}{\theta_{v0}}. \quad (2.8)$$

The potential temperature  $\theta$  is materially conserved (i.e. following air motion) for unsaturated air, in case of adiabatic displacements. Similar as for dry air, one would like to define a moist potential temperature, which is independent of reversible displacements of fluid parcels. For saturated adiabatic motion of air, a distinction has to be made, between reversible adiabatic motion, for which the total water content is conserved and irreversible moist adiabatic process for which the condensate is assumed to be removed as soon as it forms [E.g. Markowski and Richardson, 2010]. The latter is also called a pseudoadiabatic process. The corresponding potential temperatures are the equivalent potential temperature  $\theta_e$  and the pseudoequivalent potential temperature  $\theta_{ep}$  [e.g. Bolton, 1980], respectively,

$$\theta_e \equiv T \frac{p_0}{p_d} \times \exp\left[\frac{l_v r_v}{(c_{pd} + r_t c_l) T}\right] \quad (2.9)$$

$$\theta_{ep} \equiv T \left(\frac{p_0}{p}\right)^{0.2854(1-0.28r_v)} \exp\left[r_v(1 + 0.81r_v)\left(\frac{3376}{T^*} - 2.54\right)\right]. \quad (2.10)$$

Here  $l_v$  is the specific latent heat of vaporisation,  $r_t = r_v + r_h$  is the total water mixing ratio,  $c_l$  is the specific heat of liquid water at constant pressure, and  $T^*$  is the temperature at which air becomes saturated. The physical interpretation of the equivalent potential temperature  $\theta_e$  is that it is the potential temperature

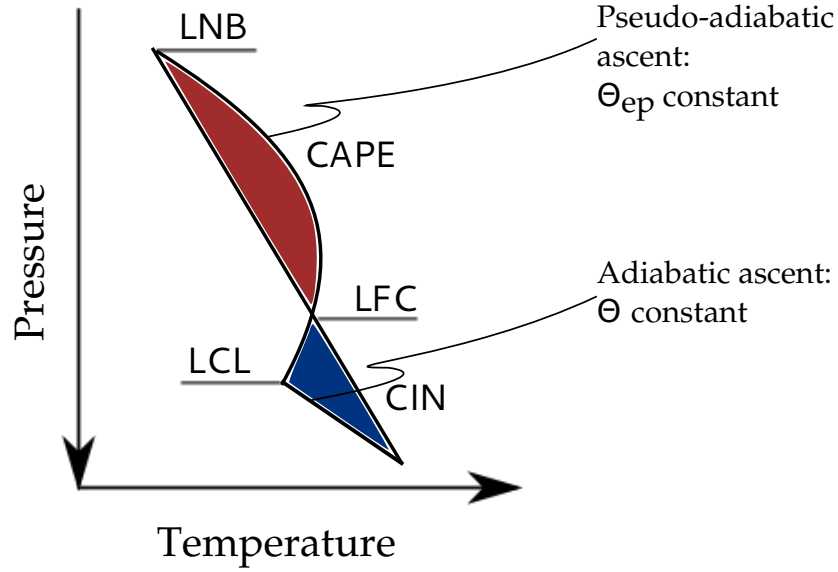


Figure 2.1: Schematic depiction of CAPE (red area) and CIN (blue area) associated with an atmospheric profile, for more details see text. Translated and adapted from Hense [2012].

an air parcel would obtain if all water vapour would condensate adiabatically. The pseudoequivalent potential temperature is the temperature achieved by an air parcel that is lifted pseudoadiabatically to zero pressure and after that compressed dry adiabatically towards the reference pressure of 1000 hPa.  $\theta_e$  and  $\theta_{ep}$  are often interchanged and differences are small for most purposes [Markowski and Richardson, 2010]. In this thesis we will assume that  $\theta_e$  is materially conserved for moist adiabatic processes.

### 2.1.3 The complete picture

From the above discussion it is clear that an air parcel which is positively buoyant will be accelerated vertically. The level at which the buoyancy is zero, is called the Level of Free Convection (LFC). Above this level an air parcel can rise freely until the buoyancy becomes neutral again, at the Equilibrium Level (EL). One commonly used way to measure the total (positive) buoyancy in the atmosphere is CAPE, which is defined as the height integrated buoyancy  $B$  between the LFC and EL (Fig. 2.1),

$$\text{CAPE} \equiv \int_{\text{LFC}}^{\text{EL}} B dz \approx \int_{\text{LFC}}^{\text{EL}} \frac{\theta'_v}{\theta_{v0}} dz. \quad (2.11)$$

CAPE is proportional to the maximum vertical kinetic energy  $\frac{\Delta w_{\text{max}}^2}{2}$  an air parcel can gain during the ascent,

$$\frac{\Delta w_{\text{max}}^2}{2} = \text{CAPE}. \quad (2.12)$$

Therefore, CAPE is often used as a predictor for severe DMC [McCaul Jr and Weisman, 2001], or with severe weather associated with DMC, such as hail and lightning [Groenemeijer and van Delden, 2007].

Presence of CAPE can be seen as a necessary, but not a sufficient condition for atmospheric instability. It is not a sufficient condition, since it is not guaranteed that the energy stored in the vertical profile is accessed. Below the LFC, there is often a stable layer which has to be overcome before convection can be initiated. The work needed to overcome this stable layer is measured by Convective Inhibition (CIN),

$$\text{CIN} \equiv - \int_0^{\text{LFC}} B dz \approx - \int_0^{\text{LFC}} \frac{\theta'_v}{\theta_{v0}} dz. \quad (2.13)$$

CIN is a measure of the negative buoyancy below the LFC. Note that because of the minus sign in Eq. 2.13, CIN is defined as a positive value. Since the atmosphere itself is almost never absolute unstable, lifting processes on the meso- or synoptic scale are necessary to overcome the CIN [Schultz and Schumacher, 1999; Markowski and Richardson, 2010]. Most commonly, convection is initiated along some kind of air mass boundary, e.g. along fronts, drylines and sea breezes [e.g. Wilson and Roberts, 2006; Weckwerth and Parsons, 2006; Markowski and Richardson, 2010]. Large-scale ascent can induce convection by reducing CIN, thereby making it more easy for an air parcel to reach the LFC. Convection can also be induced by orographic lift, which plays a huge role e.g. in the Alps. At smaller scales, convection might be induced by the cold pool outflow of mature storm cells. The gust front of a storm cell, which is created by evaporational cooling processes, has been hypothesised to favourably induce convection down-shear of old cells [Rotunno et al., 1988].

## 2.2 INFLUENCE OF THE ENVIRONMENT ON CONVECTIVE CHARACTERISTICS

There have been a lot of idealised modelling studies [e.g. Weisman and Klemp, 1982; Davies-Jones, 1984; Droegemeier et al., 1993], and observational studies on how the convective (cell) characteristics depend on the environment in which the cells are generated. Here we briefly review the main results of these studies.

### 2.2.1 *Wind shear*

Maybe most important is the dependence on the vertical wind shear (of the horizontal wind). Wind shear is often divided in the speed wind shear, defined as the increase of wind speed with height, and directional wind shear, defined as the change of direction of the wind velocity with height. As an estimate of the speed wind shear, bulk wind shear is often used, which is defined as the magnitude of the vector wind difference between 0 and 6 km height. In this thesis we will use the terms bulk wind shear and wind shear interchangeably.

Weisman and Klemp [1982] found that storms tend to organise if the bulk wind shear is larger. For values lower than  $10 \text{ ms}^{-1}$  storms tend to form as isolated cells, and convection tends to be relatively short lived. The life cycle of such a singular cell consists out of three phases [Byers and Braham, 1949]. The

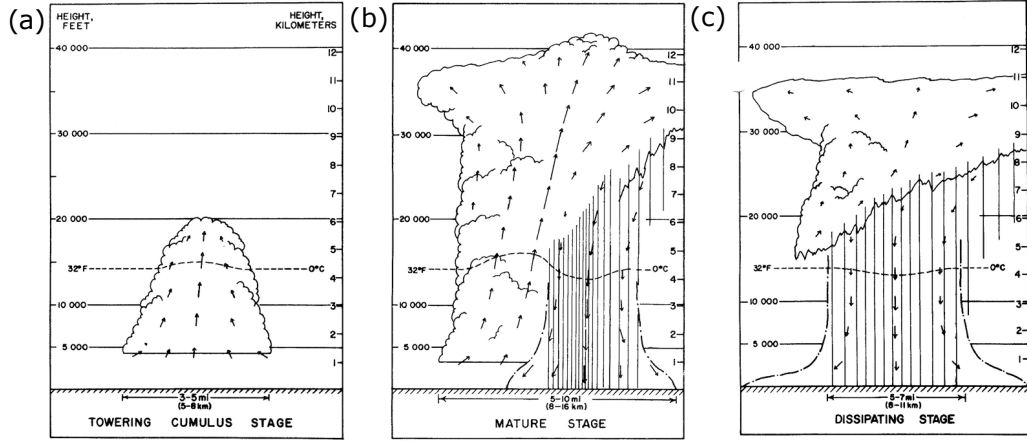


Figure 2.2: Schematic overview of the three stages associated with the evolution of a singular cell, (a) Tower cumulus stage, (b) Mature stage, and (c) Dissipating stage, for details see text. Figure reproduced from Doswell III [1985], after [Byers and Braham, Jr, 1948; Byers and Braham, 1949] (original Figure © American Meteorological Society, used with permission).

first stage is the cumulus stage, during this stage only an updraft exists (Fig. 2.2). In the mature stage precipitation forms, and an anvil cloud is generated. Evaporation of precipitation generates a downdraft, which spreads out at the surface to create the cold pool. In the dissipating stage the downdraft dominates the updraft. The updraft is cut off, and cannot be longer maintained. The lifetime  $\tau$  of a singular, ordinary cell can be estimated from the time it takes for an updraft to reach the height  $H$  of the EL plus the time it takes for precipitation to fall,

$$\tau \approx \frac{H}{w_0} + \frac{H}{v_t}. \quad (2.14)$$

Substituting typical numbers for the height  $H \approx 10$  km, updraft speed  $w_0 \approx 5$ -10  $\text{ms}^{-1}$ , and  $v_t \approx 5$ -10  $\text{ms}^{-1}$  the fall speed of precipitation gives a typical lifetime of a convective cell of about 30 to 60 minutes [Markowski and Richardson, 2010].

Increasing wind shear up to values to 10-20  $\text{ms}^{-1}$  favourably initiates multicell storms. CAPE values can range from small to large. While singular cells rarely generate severe weather, multicell storms can last for a few hours and can create strong wind gusts and hail balls up to the size of golf balls [Markowski and Richardson, 2010]. Multicell storms are often organised as a cluster on the meso- $\beta$  scale or as a convective line, e.g. a squall line or a bow echo. A typical evolution of a multicell storm cluster is shown in Fig. 2.3. In this figure a multicell storm is plotted at three different time steps. Each of the individual cells is in a different stage of evolution. In the top picture, cell 1 is in the dissipating stage, and therefore it is dominated by the downdraft. In this panel, cell 2 is in the mature stage and cell 3 is dominated by the updraft (i.e. the Tower cumulus stage in Fig. 2.2). Cell 4 just begins to form, but it has not reached the EL. After 10 minutes (middle panel in Fig. 2.3), cell 4 almost reached the EL. The precipitation associated with cell 2 has reached the ground, and this cell starts to weaken now. In the bottom picture, which shows the situation after 20 minutes after the top panel, cell 3 starts to weaken and cells 1 and 2 are almost dissipated. Cell 4 is

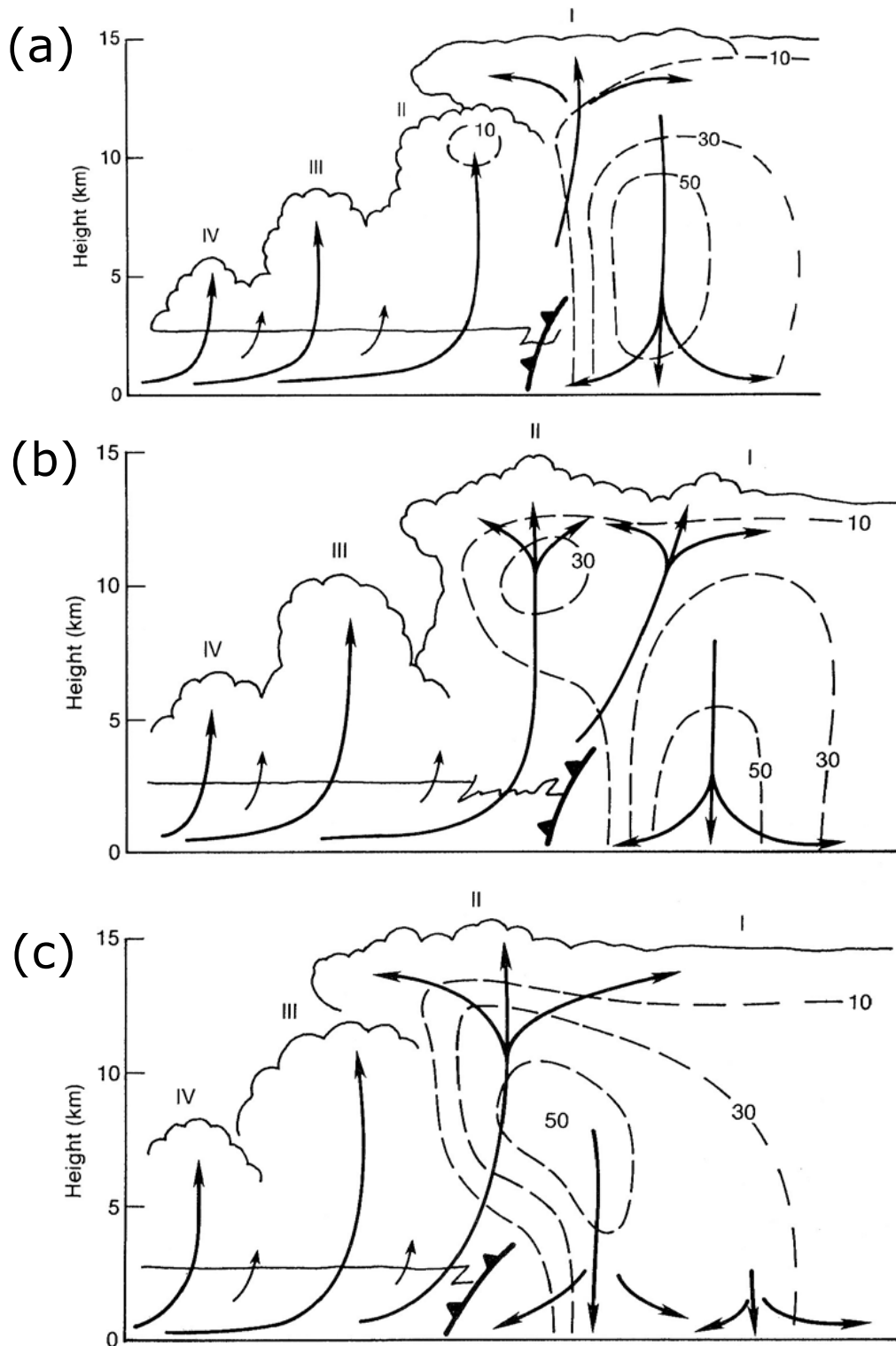


Figure 2.3: (a) Schematic overview of the evolution of a multicell cluster, showing four cells in different stages. Up- and and downdrafts are indicated by arrows and the dashed contour lines indicate radar reflectivity (10, 30, 50 dBZ). (b) As (a), but 10 minutes later. (c) As (a), but 20 minutes later. For details, see text. Figure reproduced from Doswell III [1985].

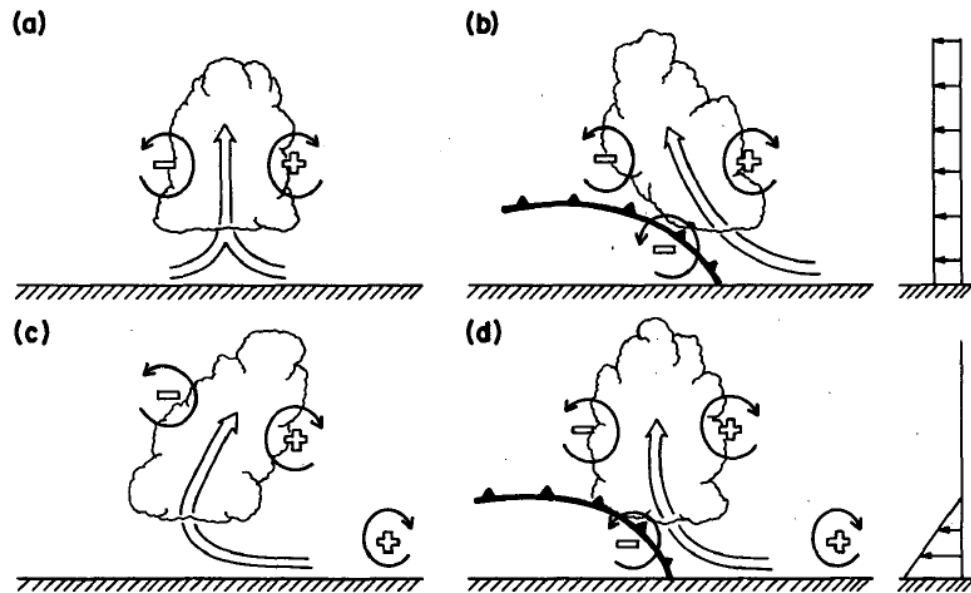


Figure 2.4: Schematic overview of the RKW theory, after Rotunno et al. [1988] and Weisman and Rotunno [2004]. Figure shows the orientation of the updraft in case of (a) no ambient shear and no cold pool, (b) only a cold pool (indicated by the leading edge or gust front, the black line with triangles), (c) only ambient wind shear and (d) both a cold pool and ambient shear. In these panels are positive (negative) horizontal vorticity anomalies indicated by + (-) symbols. © American Meteorological Society, used with permission.

almost in its mature stage. There is a continuous cycle, in which the new cells replace the old cells. One has to note that although the individual cells tend to move with the height averaged mean wind, the movement of the multicell storm can be slower or faster and also in a different direction [Markowski and Richardson, 2010].

The reason why the vertical wind shear influences the storm organisation, persistence, and severity is twofold. First, deep level shear tends to reduce the interference of the storm outflow and precipitation with the updraft. Generally, the distance at which the precipitation falls from the updraft tends to increase with increasing bulk wind shear. Secondly, the low level shear influences where new cells along the gust front of old cells are initiated. Rotunno et al. [1988] argued that new cells are favourably generated at the downshear side of a squall line. They argued that the negative vorticity created by the cold pool can interact positively with the positive vorticity associated with the ambient shear. This hypothesis is commonly called RKW theory, a schematic depiction of it is shown in Fig. 2.4. Deepest lifting occurs when the circulation due to the ambient shear and the cold pool are in balance [Weisman and Rotunno, 2004]. Although the role of cold pool and wind shear in determining an optimal state for long-lived squall lines is still a matter of debate, there is general agreement that the wind shear plays an important role in storm organisation [Stensrud et al., 2005; Coniglio et al., 2012].

Figure 2.4 also shows the role of speed wind shear on the orientation of updraft. If no ambient shear is present and no cold pool is present (Fig. 2.4a), the updraft will be upright, and the vorticity pair associated with the updraft will be symmetric. If a cold pool is generated (Fig. 2.4b), the updraft will be vertically tilted over the cold pool. This is because of the negative vorticity associated with the cold pool. In case of strong ambient wind shear (Fig. 2.4c), the updraft will be tilted downshear. If both a cold pool and ambient shear exists (Fig. 2.4d) a straight updraft will be generated, since both processes counteract each other [Rotunno et al., 1988; Weisman and Rotunno, 2004].

Increasing the wind shear even further, favours the generation of supercell storms. Supercell is a term first used by Browning [1964] and usually refers to a convective storm with a deep and persisting mesocyclone [Doswell III and Burgess, 1993]. Not only does the tilting of horizontal vorticity lead to storm rotation, but the dynamic vertical pressure gradients that accompany large-shear environments, especially if the shear is distributed over a significant fraction of the cloud depth, can also enhance updrafts at altitudes high above the gust front.

### 2.2.2 Helicity

In addition to speed wind shear directional wind shear also influences how convection is organised. Directional wind shear is most often measured in terms of the helicity  $H$ , which is defined as the inner product of the relative vorticity  $\zeta$  and the velocity  $\mathbf{u}$

$$H \equiv \zeta \cdot \mathbf{u}. \quad (2.15)$$

Helicity can be seen as a measure of spiralling motion and is large in storms and their environment [Lilly, 1986b]. Supercell storm flow can be well described by a purely Beltrami flow (i.e. vorticity and velocity are parallel and there is no cross-wise vorticity present).

The effect of helicity on turbulence has been known since Betchov [1961]. They pointed out that helicity can suppress the inertial cascade to smaller scales. Lilly [1986b] diagnosed this idea further and they found that for a purely helical flow, advection of helicity exactly balances vortex stretching and tilting. Stretching and tilting are crucial in forming the inertial ranges of turbulence. Therefore, this suppression of turbulence dissipation in a helical flow, might explain the relative persistence of supercells and other mesoscale convective systems.

To measure the effect of helicity on a storm, the helicity in the storm-relative flow is important. The helicity in the storm-relative reference frame is relevant, because it is the moving updraft which tilts vorticity into the vertical. Therefore, it is customary in studies of convective storms to integrate the helicity over the storm's inflow depth  $d$ :

$$H = \int_0^d \bar{\mathbf{u}} \cdot \bar{\zeta} dz. \quad (2.16)$$

For the depth of inflow layer  $d$ , mostly estimates of 1 or 3 km are used. In Eq. 2.16 the bars represent a characteristic environmental value. Moreover, it

is often assumed that the relative vorticity can be estimated by the horizontal component  $\zeta_h$  related to the vertical wind shear of the horizontal wind  $\bar{\mathbf{u}}_h$  only, i.e.  $\zeta \approx \zeta_h \approx \mathbf{k} \times \mathbf{S}$ . Here  $\mathbf{k}$  is a unit vector into the vertical, and  $\mathbf{S} \equiv \frac{\partial \bar{\mathbf{u}}_h}{\partial z}$ . Substituting the storm relative flow  $\bar{\mathbf{u}} - \mathbf{c}$ , with  $\mathbf{c}$  the storm movement into the above equation gives the SRH,

$$\text{SRH} \equiv \int_0^d (\bar{\mathbf{u}} - \mathbf{c}) \cdot \zeta_h dz = - \int_0^d \mathbf{k} \cdot (\bar{\mathbf{u}} - \mathbf{c}) \times \bar{\mathbf{S}} dz, \quad (2.17)$$

The SRH is used to forecast supercell storms. In the neighbourhood supercell storms and tornadoes, sometimes SRH (integrated from 0 to 3 km) of  $400 \text{ m}^2\text{s}^{-2}$  or larger are observed [Markowski and Richardson, 2010]. Moreover, Thompson et al. [2003, 2007] found SRH to be effective in distinguishing nontornadic and tornadic supercell storms.

### 2.2.3 Convective parameters and severe weather predictability

Besides the SRH, various authors have stated the Bulk Richardson Number (BRN), which is a combination of CAPE and a measure of the wind shear, as a parameter to discriminate between non-supercell and supercell storms [Weisman and Klemp, 1982, 1984]. BRN is defined as

$$\text{BRN} \equiv \frac{\text{CAPE}}{1/2(\Delta u^2 + \Delta v^2)}, \quad (2.18)$$

with  $\Delta u^2$  and  $\Delta v^2$  the difference between the density weighted wind velocity over the lowest 6 km and surface layer wind velocity over 500 metre. Physically, BRN represents a measure for the kinetic energy in the inflow layer of the storm. Values between 10 and 45 are thought to be favourable for supercell storms, while values above 45 are favourable for single cell or multicell storms [Weisman and Klemp, 1984]. Most authors look at wind shear only, since the storm type depends more on the wind shear than on CAPE. For some storms, the product instead of the quotient might be a better predictor for the storm type [Markowski and Richardson, 2010].

McCaul Jr and Weisman [2001] found that the shape of the shear and buoyancy profiles can influence the morphology of thunderstorms, especially for weak CAPE case. They simulated storms using soundings where the buoyancy and wind shear peaked at different heights, leaving the total CAPE and shear constant. They found that in the small CAPE regime, the updraft and vertical vorticity are often correlated. This is consistent with other studies that supercells can even form in an environment with only  $600 \text{ J/kg}$  CAPE.

As an estimate for atmospheric instability, stability indices like the Lifted Index (LI) and the Showalter Index (SI) are used. The LI measures the differences in temperature of an air parcel  $T_p$  lifted adiabatically towards 500 hPa and the temperature of the environment  $T_e$  at the same pressure level [Galway, 1956],

$$\text{LI} \equiv T_e - T_p. \quad (2.19)$$

A negative LI implies that a lifted air parcel has a higher temperature compared to the environment. This indicates that the boundary layer is unstable compared

to the air higher up in the troposphere at 500 hPa. A LI of 0 till -4 indicates marginal instability, while below -4 values indicate large instabilities. The SI is defined in a similar way, with the subtle difference that the parcel temperature measured at 500 hPa is measured from an air parcel lifted from the 850 hPa surface [Showalter, 1953]. This stability index has especially advantages in mountainous areas [Huntrieser and Schiesser, 1997].

Most of the idealised studies focused on severe weather in the United States. There have been, however, several observational studies on severe weather in western Europe. Using 32 different convective predictors and rawinsonde observations, Haklander and van Delden [2003] found that the lowest 100 hPa LI is the best predictor for forecasting thunderstorms in the Netherlands, with other versions of the LI performing almost equally good. For severe weather in the Netherlands, Groenemeijer and van Delden [2007] found that CAPE, the bulk wind shear and LI all have significant skill in forecasting hail associated with thunderstorms. They also found that for weak tornadoes low level CAPE has the best skill, and for stronger tornadoes low level wind shear is the most important parameter. Kaltenböck et al. [2009] found that CAPE and other instability indicators have considerable skill in predicting the occurrence of convective storms. Moreover, both the 0-1 km and the 0-3 km SRH can be useful in predicting tornadoes and severe wind gusts.

### 2.3 OVERVIEW OF CONSERVED QUANTITIES

#### 2.3.1 Circulation and vorticity

The meteorological relevance of conserved quantities related to the rotation of the fluid has been known since the introduction of the circulation theorem by Lord Kelvin in 1867. The circulation  $C_\Gamma$  is defined as the integration of the wind velocity vector  $\mathbf{u}$  around a closed loop of particles  $\Gamma$ ,

$$C_\Gamma \equiv \oint_\Gamma \mathbf{u} \cdot d\mathbf{l}. \quad (2.20)$$

The circulation  $C_\Gamma$  is a macroscopic measure of the rotation of the fluid. By Stokes theorem it can be related to the microscopic measure of the rotation, the relative vorticity  $\boldsymbol{\zeta} = \nabla \times \mathbf{u}$ ,

$$C_\Gamma = \iint_\Gamma \boldsymbol{\zeta} \cdot \mathbf{n} dA, \quad (2.21)$$

with  $\mathbf{n}$  the vector normal to an arbitrary surface  $\mathbf{A}$  containing the loop.

In the reference frame which takes the rotating earth into account, the vorticity contains an extra term associated with the planetary rotation rate the planetary rotation rate  $\Omega$ . The corresponding vorticity  $\zeta_a = \zeta + 2\Omega$  is called the absolute vorticity. The general absolute vorticity equation can be written as (see e.g. Salmon [1998]),

$$\frac{D\zeta_a}{Dt} = (\zeta_a \cdot \nabla)\mathbf{u} + \frac{\nabla\rho \times \nabla p}{\rho^2} + \nabla \times \mathbf{F}. \quad (2.22)$$

Here incompressible flow has been assumed. In Eq. 2.22,  $\mathbf{F}$  represents a general body force on the fluid, e.g. due to friction. The first term on the right describes the effect of vorticity stretching and tilting, the second term is the baroclinic term (also called the solenoid or pressure torque term) which is zero when the flow is barotropic. The last term represents effects due to viscosity. Rossby [1939] was one of the first to note that the vertical component of the absolute vorticity is conserved for planetary scale motion, which can be seen as a special case of PV conservation.

The circulation defined in Eq. 2.21 is the integrated version of the relative vorticity, normal to the surface  $\mathbf{A}$ . We could also define the circulation theorem in the inertial reference frame with  $C_{\Gamma_a} = C_\Gamma + 2\Omega A$ , with  $A$  the area bounded by a projection normal to  $\Omega$ ,

$$C_{\Gamma_a} = \iint \zeta_a \cdot \mathbf{n} dA. \quad (2.23)$$

This equation can be rewritten using the momentum equation, see e.g. [Salmon, 1998], for frictionless motion giving

$$\frac{dC_{\Gamma_a}}{dt} = \oint_\Gamma \frac{1}{\rho} dp. \quad (2.24)$$

This implies that the circulation is conserved for a barotropic fluid (i.e.  $p = p(\rho)$ ), known as the Kelvin circulation theorem. A further consequence is that only the pressure-torque contributes to changes in the circulation. The effects of vorticity tilting and stretching are built into the definition of the circulation (i.e. they do not change the circulation, see Salmon [1998]). If the material loop of fluid particles lies completely on an isentropic surface, then even the pressure-torque term does not destroy the conservation of the circulation.

### 2.3.2 The introduction of PV

One of the aims of Rossby [1940] was to introduce a new quantity related to the vertical component of the vorticity in the same way as the potential temperature is related to the temperature [McIntyre, 2015]. Here “vertical” should be interpreted as normal to isentropic surfaces. Rossby [1940] found that for a barotropic fluid the absolute vorticity  $\zeta_a$  divided by the fluid depth  $D$  is conserved following the fluid column,

$$\frac{d}{dt} \frac{\zeta_a}{D} = 0. \quad (2.25)$$

The dominant vorticity budget on larger scales, vorticity stretching and advection of absolute vorticity, is summarised in a simple and elegant way. Ertel [1942] elaborated this idea further for baroclinic fluids. He showed that for any state variable  $s$ , which depends on pressure  $p$  and density  $\rho$  only, a PV can be derived of the form

$$\Pi = \frac{\zeta_a \cdot \nabla s}{\rho}, \quad (2.26)$$

which is conserved for isentropic and frictionless flow. If the potential temperature  $\theta$  is used as state variable, the corresponding PV is referred to as Ertel’s PV.

Equivalent to the idea of a new vorticity quantity related to the potential temperature, is that this quantity should be proportional to the circulation  $C$ , with the closed material contour  $\Gamma$  lying completely on an isentropic surface. Therefore, an elegant and maybe the most fundamental way to define PV is via the Kelvin circulation theorem:  $\Pi \propto C_\Gamma$  [McIntyre, 2015]. We choose the potential temperature  $\theta$  as state variable  $s$ . With this choice for  $s$ , Eq. 2.26 is consistent with  $\Pi \propto C_\Gamma$ . To show this, we rewrite Eq. 2.26 first following [McIntyre, 2015],

$$\Pi = \sigma^{-1} \zeta_a \cdot \mathbf{n}. \quad (2.27)$$

Here  $\sigma \equiv \frac{\rho}{|\nabla\theta|}$  is the mass density related to the stratification, and  $\mathbf{n} \equiv \frac{\nabla\theta}{|\nabla\theta|}$  a unit vector directed upwards with respect to the isentropic surfaces. Given the small-slope approximation (i.e.  $\nabla\theta$  is nearly vertical),  $\sigma$  can be interpreted as the mass density in isentropic coordinates. Then,  $\sigma d\theta$  is exactly the mass per unit area between two isentropic surfaces differing  $d\theta$ .

As described in Section 2.3.1, the circulation  $C_\Gamma$  can be defined as (in the inertial frame),

$$C_\Gamma = \iint_{s(\Gamma)} \zeta_a \cdot \mathbf{n} dA. \quad (2.28)$$

Here  $\mathcal{S}(\Gamma)$  is again a closed loop of fluid particles, now lying on the isentropic surface  $\mathcal{S}$ . Using Eq. 2.27 we get,

$$C_\Gamma = \iint_{\mathcal{S}(\Gamma)} \Pi \sigma dA. \quad (2.29)$$

We also know that mass is conserved, and that  $\sigma d\theta$  is the mass per unit area between two isentropic surfaces with potential temperatures  $\theta$  and  $\theta + d\theta$ . Therefore,  $\sigma dA d\theta$  is a mass element of integration between those two isentropic surfaces. Moreover, one knows that the potential temperature  $\theta$  is materially conserved, hence [McIntyre, 2015],

$$\iint_{\mathcal{S}(\Gamma)} \sigma dA = \text{constant}. \quad (2.30)$$

In the limit of small  $\Gamma$ , i.e. take the greatest diameter of  $\Gamma$  to be arbitrary small compared to all lengthscales of the flow, the PV is Eq. 2.29 divided by Eq. 2.30 [McIntyre, 2015]. This proves that we can define Ertel PV using  $\Pi \propto C_\Gamma$ . An alternative derivation of PV, using directly the momentum equations is given in Section A.1.

#### 2.4 PROPERTIES OF PV

Two important properties of PV make it an essential variable in studying atmospheric dynamics:

- It is materially conserved for frictionless and adiabatic flow.
- PV can be inverted, given suitable balance and boundary conditions, to give more intuitive meteorological variables like the pressure, wind fields and potential temperature.

Because of its material conservation, PV can be used as a dynamical tracer. It has been used to describe cyclogenesis, large scale atmospheric dynamics and in defining a dynamical blocking index [Hoskins et al., 1985; Hoskins, 1997; Pelly and Hoskins, 2003].

The invertibility principle of PV is similar to that of vorticity in the barotropic case. It is so powerful because one single variable can be used to obtain both dynamic and thermodynamic information. This is not trivial, since PV is the product of absolute vorticity and static stability. Therefore one has to specify, besides the global distribution of the PV,

1. Some balance condition, e.g. the (quasi-)geostrophic balance, or a more accurate balance condition like the nonlinear balance
2. A reference state, which expresses the spatial distribution of  $\theta$

Furthermore, the PV inversion has to be solved globally.

For synoptic scales, Quasi-Geostrophic (QG) is a good balance assumption. The typical flow and static stability anomalies associated with a QG PV anomaly

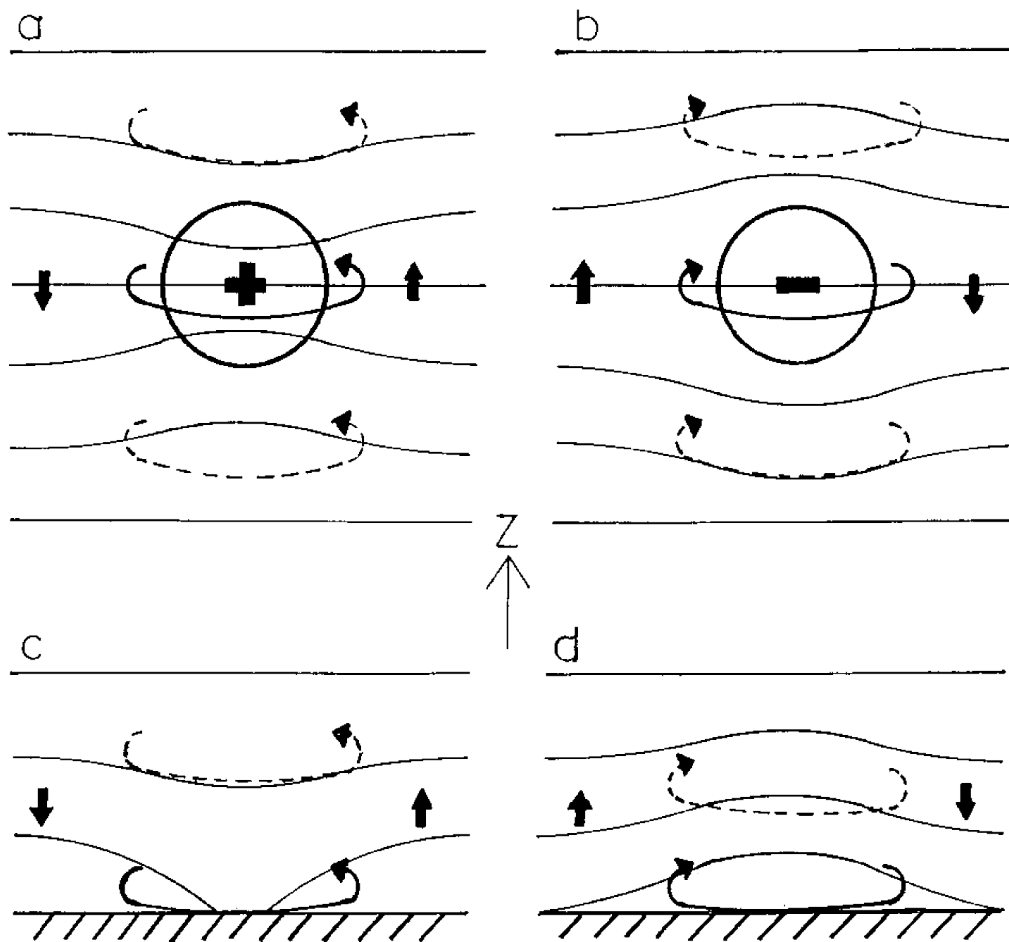


Figure 2.5: Isentropes (solid lines) and induced circulation (arrows) for (a) a positive PV anomaly, (b) a negative PV anomaly, (c) a positive  $\theta$  anomaly at the surface and (d) a negative  $\theta'$  anomaly at the surface. Reproduced (with permission) from Hoskins [1997], © 1997 Royal Meteorological Society.

are shown in Fig. 2.5. From Fig. 2.5 one can see that a positive PV anomaly, a region in which stronger PV than the surrounding air, is associated with a positive vorticity and a positive static stability ( $\propto \frac{\partial \theta}{\partial z}$ ) anomaly [Hoskins, 1997]. A synoptic scaled PV acts on distance, i.e. it influences surrounding air. Just outside a positive PV anomaly the isentropic surfaces are closer together than they would be if no anomaly was present. Furthermore, the absolute vorticity is larger than the ambient planetary vorticity  $f$  [Hoskins, 1997]. This leads to cyclonic circulation around the positive PV anomaly. One can also show that there is ascent (descent) on the eastern (western) side of the anomaly [Hoskins, 1997]. For a negative PV anomaly flow and static stability anomalies are exactly reversed, i.e. there is anticyclonic rotation around a negative PV anomaly and a low static stability inside the PV anomaly.

From Fig. 2.5 we can also deduce the circulation associated with positive or negative surface  $\theta$  anomalies. From Fig. 2.5(c) one can see that the isentropic surfaces are relatively drawn towards the surface. At the surface there is relatively high  $\theta$  air. This warm anomaly at the surface is associated with cyclonic

circulation [Hoskins, 1997]. Just as for a positive PV anomaly in the interior, a surface positive  $\theta$  anomaly influences surrounding air. Similarly, one can see from Fig. 2.5(d) that a negative surface  $\theta$  anomaly is associated with anticyclonic flow.

#### 2.4.1 Evolution

Locally, PV is only conserved for adiabatic and frictionless flow. PV conservation can be generalised to include diabatic and frictional effects. To accomplish this, a PV substance flux  $\mathbf{J}$  is defined as

$$\frac{\partial \rho \Pi}{\partial t} + \nabla \cdot \mathbf{J} = 0, \quad (2.31)$$

$$\mathbf{J} = \mathbf{u} \Pi \rho - \zeta_{\alpha} \dot{\theta} - \mathbf{F} \times \nabla \theta, \quad (2.32)$$

with  $\dot{\theta}$  is the diabatic heating rate,  $\mathbf{F}$  a general body force applied to the fluid (e.g. friction). A complete derivation of this equation can be found in Section A.1. The PV times the density of air  $\rho$  is called the Potential Vorticity Substance (PVS) and this can be seen as a sort of PV charge [Haynes and McIntyre, 1987, 1990]. There can be no PVS flux across isentropic surfaces. Although isentropic surfaces can be permeable for mass and chemical substances, they always behave like they are completely impermeable to PVS fluxes. This is even valid when there are diabatic or frictional effects present. In the free atmosphere PV can only be redistributed, and PV can only be created and destroyed at the surface of the earth, where isentropic surfaces intersect with the ground.

Schär [1993] showed, that for a statistical steady flow the PV flux  $\mathbf{J}$  reduces to,

$$\mathbf{J} = \nabla \theta \times \nabla B \quad (2.33)$$

with  $B$  the Bernoulli stream function. This can be regarded as a generalisation of the classical Bernoulli theorem.

Equation 2.33 directly implies that there no PV flux is possible across surfaces of equal  $\theta$  and  $B$ . A general stationary solution of the PV evolution can be derived from this [see N evir, 2004],

$$\mathbf{u}_{st} = \frac{1}{\rho \Pi} (\nabla \theta \times \nabla B). \quad (2.34)$$

This is the most general stationary solution of the primitive equations one can derive, all other balance conditions, like the geostrophic winds are a generalisation of this. N evir [2004] further defined the Dynamical State Index (DSI), an index which characterises how far away the state of the atmosphere is from this generalised balanced flow  $\mathbf{u}_{st}$ :

$$DSI = \frac{1}{\rho} \nabla \Pi \cdot \nabla \theta \times \nabla B. \quad (2.35)$$

The DSI can be used as a predictor for severe weather, e.g. Clau snitzer and N evir [2009] showed that there is a correlation between the area mean DSI and the area mean precipitation over Germany.

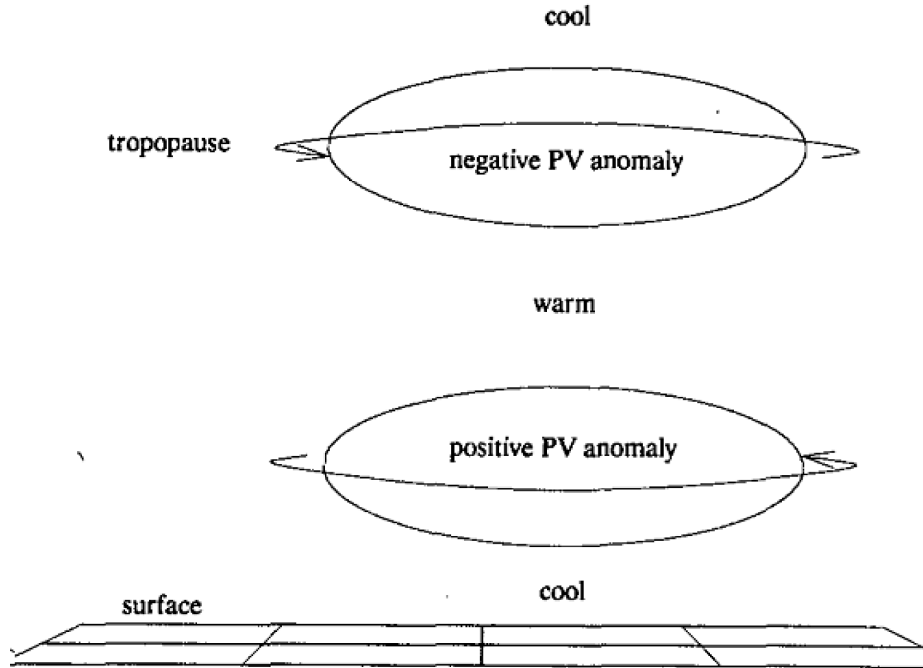


Figure 2.6: Schematic overview of vertical orientated dipoles, associated with a mesoscale convective vortex, from [Raymond and Jiang, 1990]. © American Meteorological Society, used with permission.

#### 2.4.2 Moist PV

The definition of Ertel PV, and its conservational properties, are not generally valid for a moist and precipitating atmosphere. There have been several attempts to generalise PV to a moist equivalent (e.g. Schubert et al. [2001] and Marquet [2014]). We shall follow McCann [1995] to use the equivalent potential temperature as the basis for a moist PV,

$$\Pi_e \equiv \zeta_a \cdot \nabla \theta_e \quad (2.36)$$

with  $\Pi_e$  the Equivalent Potential Vorticity (EPV). It is useful to e.g. quantify the conditional symmetric instability [McCann, 1995].

#### 2.4.3 Mesoscale PV dipoles

For the mesoscale it is important to revise the general ideas of PV thinking. First, diabatic effects will play a huge role during deep moist convection and therefore on the distribution of PV. Although diabatic and frictional effects only redistribute the PV in the free atmosphere, these effects can create and destroy PV at the earth's surface. It is also questionable if the inversion principle can still be applied to mesoscale or even smaller scales.

Raymond and Jiang [1990] explained the existence of a vertical dipole pair of PV with a mass flux related to diabatic heating caused by convection. The

physical interpretation of this is understood quite easily. One of the main consequences of DMC is mass transport across isentropic surfaces. According to Haynes and McIntyre [1987], there can be no PVS flux across isentropic surfaces. Therefore, in terms of PVS, a mass sink (source) will cause an increase (decrease) of PV. Although there is much variation in the vertical mass flux profiles, generally there is mass removed from the lower troposphere to the upper troposphere (i.e. an upward mass flux). This leads to a vertical dipole of PV in the troposphere, i.e. a positive PV anomaly in the middle troposphere and a negative PV anomaly in the upper troposphere (Fig. 2.6). The positive PV anomaly can be interpreted as a mesoscale convective vortex. Raymond and Jiang [1990] hypothesised that this positive PV can self-maintain itself by inducing convection by isentropic upgliding downshear of the positive PV anomaly.

Conzemius and Montgomery [2009] and Chagnon and Gray [2009] found PV dipoles generated by convection on a much smaller scale. These horizontal PV dipoles are generated by tilting of vorticity of the background vertical wind shear of the horizontal wind. Chagnon and Gray [2009] used the linearised Boussinesq equations to theoretically explain the PV dipoles. They assumed a Boussinesq gas on a  $f$ -plane with constant static stability  $N$  and constant density  $\rho_0$ . The background wind  $\bar{v} = \bar{v}(z)$  is unidirectional in the  $y$ -direction, and is vertically sheared. The linearised set of equations of Chagnon and Gray [2009] are given as

$$\frac{\partial u'}{\partial t} = fv' - \frac{\partial}{\partial x} \left( \frac{p'}{\rho_0} \right) \quad (2.37)$$

$$\frac{\partial v'}{\partial t} = -fu' - \Delta w' \quad (2.38)$$

$$\frac{\partial w'}{\partial t} = -\frac{\partial}{\partial x} \left( \frac{p'}{\rho_0} \right) + b \quad (2.39)$$

$$\frac{\partial b}{\partial t} = -N^2 w' + B \quad (2.40)$$

$$\frac{\partial u'}{\partial x} + \frac{\partial w'}{\partial z} = 0, \quad (2.41)$$

with  $u'$ ,  $v'$  and  $w'$  the three components of the perturbation velocity,  $p'$  is the perturbation pressure,  $b$  is the buoyancy,  $B$  is the rate of heating expressed as a buoyancy, and  $\Delta = \frac{\partial \bar{v}}{\partial z}$  is the vertical shear of the background wind. From this set of equations, Chagnon and Gray [2009] derived a linearised PV

$$\Pi' = \zeta_v + f \frac{\partial}{\partial z} \left( \frac{b}{N^2} \right) - \Delta \frac{\partial}{\partial x} \left( \frac{b}{N^2} \right), \quad (2.42)$$

with  $\Pi'$  the linearised PV and  $\zeta_v$  the vertical component of the relative vorticity. The corresponding conservation equation of this linearised PV is given by

$$\frac{\partial \Pi'}{\partial t} = \left( f \frac{\partial}{\partial z} - \Delta \frac{\partial}{\partial x} \right) \left( \frac{B}{N^2} \right). \quad (2.43)$$

Equation 2.43 essentially states that the generation of PV can be either due to a vertical gradient of heating against the planetary vorticity  $f$ , or a horizontal gradient of heating against the shear  $\Delta$ . The former produces a vertical dipole pair, see Raymond and Jiang [1990], while the latter produces horizontal dipoles

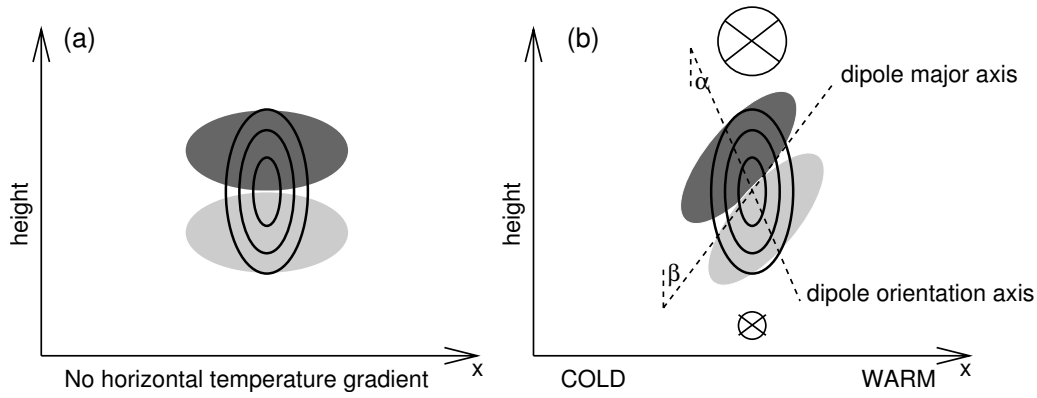


Figure 2.7: Schematic depiction of generation of PV dipoles which arises from diabatic heating. In (a) the background is barotropic, and only a background vertical vorticity (i.e. planetary vorticity) is present. (b) represents the baroclinic case, in which the background wind is vertically sheared (directed into the page). In this pictures the positive (negative) PV anomaly is indicated by light (dark) shading. Reproduced (with permission) from Chagnon and Gray [2009], © 2009 Royal Meteorological Society.

of PV (see also Fig. 2.7). Chagnon and Gray [2009] use a simple Gaussian heating profile to derive that the angle  $\alpha_{\text{theory}}$  of the line joining the two PV maxima can be approximated by:

$$\alpha_{\text{theory}} = \arctan(\Delta/f). \quad (2.44)$$

Thus the dipole becomes more horizontally orientated when the background shear  $\Delta$  is relatively strong compared with the planetary vorticity  $f$ . These theoretical findings were confirmed by idealised modelling simulations.



## MODEL AND DATA

---

*In this chapter we will introduce the non-hydrostatic Numerical Weather Prediction (NWP) model COSMO-DE and its ensemble prediction system (COSMO-DE EPS) will be described. The COSMO-DE model data used in this study is described, and we will describe the calculation of post-processed variables like Potential Vorticity (PV). Nine severe weather cases are selected. For each of these cases a reforecast is made, which is needed in analysing the PV anomalies associated with severe convection. The two cases used in the case study (5 and 22 June 2011, see Chapter 4), will be described in more detail. A short synoptic description of these severe weather cases will be given. Lastly, the conservational properties of PV in the COSMO-DE model will be investigated.*

### 3.1 DESCRIPTION OF MODEL

We use data from the limited-area non-hydrostatic weather prediction model COSMO-DE model [Baldauf et al., 2011] of the German Meteorological Service (DWD). The COSMO model is especially designed to operate on the meso- $\beta$  and meso- $\gamma$  scale [Schättler et al., 2014]. On these scales, Deep Moist Convection (DMC) is modelled explicitly by COSMO-DE. Therefore, the DWD expects that severe convection phenomena, like supercells and intense mesoscale convective systems, can be simulated directly.

#### 3.1.1 Model equations and domain

The COSMO-DE model uses the primitive compressible thermo-hydrodynamical moist equations for compressible flow, after subtracting a basic state. The basic state is horizontally homogeneous, and it is assumed to be dry, stationary and hydrostatically balanced. See the COSMO-user guide [Schättler et al., 2014] for the exact details. The prognostic variables used in the model are the three components of the wind velocity vector  $\mathbf{u}$ , the pressure  $p$ , the temperature  $T$ , the specific humidity  $q^v$ , the cloud liquid water content  $q^c$ , the specific ice cloud content  $q^i$ , and the specific water content for rain  $q^r$ , snow  $q^s$  and hail  $q^g$ :

$$\rho \frac{d\mathbf{u}}{dt} = -\nabla p + \rho \mathbf{g} - 2\Omega \times (\rho \mathbf{u}) - \nabla \mathbf{t} \quad (3.1)$$

$$\frac{dp}{dt} = (-c_p/c_v)p \nabla \cdot \mathbf{u} + (c_p/c_v - 1)Q_h + (c_p/c_v)Q_m \quad (3.2)$$

$$\rho c_p \frac{dT}{dt} = \frac{dp}{dt} + Q_h \quad (3.3)$$

$$\rho \frac{dq^x}{dt} = -\nabla \cdot \mathbf{J}^x + I^x \quad (3.4)$$

$$\rho = p \{ R_d (1 + (R_v/R_d - 1)q^v - q^c - q^i - q^r - q^s - q^g) T \}^{-1} \quad (3.5)$$

Here  $g$  is the standard acceleration due to gravity,  $\Omega$  is the constant angular velocity due to the earth rotation,  $\underline{t}$  is the stress tensor due to viscosity.  $c_p$  and  $c_v$  are the specific heat constants for constant pressure and volume, respectively.  $Q_h$  is the diabatic heating rate per unit volume of air,  $Q_m$  is a moisture source term. In Eq. 3.3  $x$  represents a specific constituent of the total air mixture, e.g.  $d$  for dry air and  $v$  for water vapour.  $I^x$  represents sources/sinks for constituent  $x$  and  $J^x$  is the diffusion flux for constituent  $x$ .  $R_d$  is the gas constant of dry air, and  $R_v$  the heat constant of moist air.

The above set of equations represents a closed set of equations for the prognostic variables. Mass is not explicitly conserved, since  $\rho$  is a diagnostic variable determined from the equation of state (Eq. 3.5). Petrik et al. [2011] found that there are relatively large errors in the conservation of total mass and energy, but total water is conserved by the COSMO model. Likewise, for conserved variables like PV and helicity, since they are not prognostically forecasted, conservation of these variables is not ensured. The conservation of PV is later on tested briefly in Section 3.3.

The model domain is centred over Germany and surrounding countries (see Fig. 3.1). It contains  $421 \times 461$  grid points in the horizontal with a grid spacing of  $0.025^\circ$  (approximately 2.8 km). The horizontal grid is rotated in order to make sure the equator of the model domain lies over Germany, so that grid spacing is approximately equal over the whole domain. In the vertical, a modified hybrid coordinate is used, which follows the orography at the bottom levels and gradually flattens at higher levels. In total there are 50 vertical levels, with the first level at 10 m height and the top level at 21.5 km<sup>2</sup>.

The model equations are defined on an Arakawa C-grid, which implies that the wind vector variables are displaced a half grid point from the centre of the grid box (Fig. 3.1b). All other (scalar) variables, like the pressure  $p$ , temperature  $T$ , and the PV, are defined in the centre of the grid box.

Since the model is nonhydrostatic, sound waves and other fast waves as gravity waves are part of the solution of the primitive equations. They influence the stability of the model and therefore the maximum time step which the model can use [Schättler et al., 2014]. Since they are meteorologically not very relevant for most situations, they have to be treated in a practical way. In the COSMO model this is done by introducing two time steps, of which one treats fast waves like sound waves and another solves the slower dynamics.

At the boundaries the model is driven by the larger scale non-hydrostatic weather model COSMO-EU, which is driven by the global hydrostatic weather model GME. Since the boundaries of the domain are heavily influenced by the dynamics of the large scale, we use in all analyses in this thesis a subdomain, as indicated by the dashed black lines of Fig. 3.1. Here 50 grid points are removed at each boundary.

---

<sup>2</sup> Parts of Weijenborg et al. [2015] from here up to section Section 3.1.2 have been reproduced

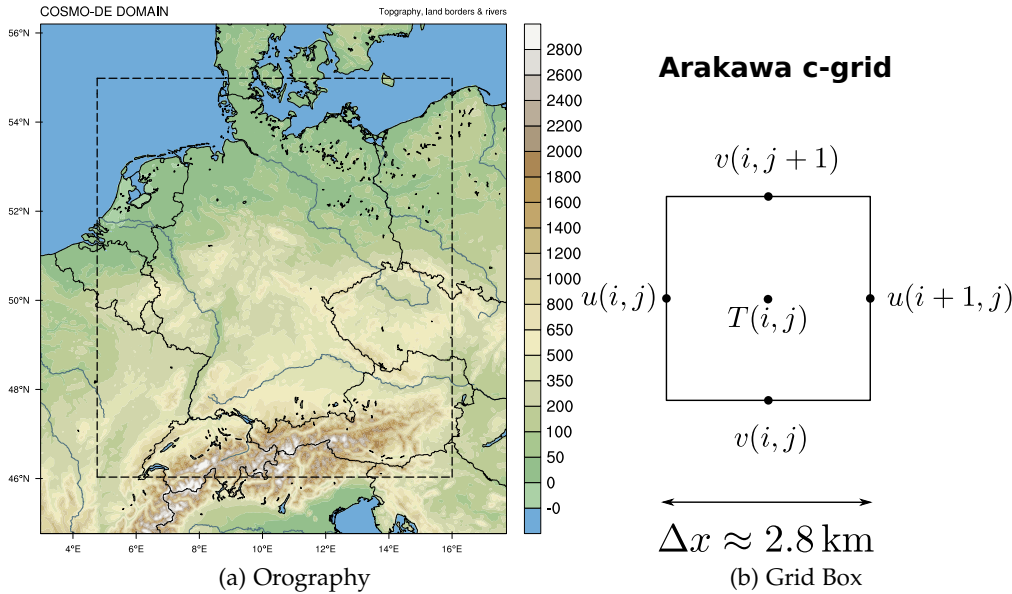


Figure 3.1: (a) Domain and orography (in metres above sea level) of the COSMO-DE nonhydrostatic weather model. The dashed box indicates the inner domain of  $321 \times 361$  grid points used in the most calculations. (b) Schematic depiction of Arakawa C-grid used in COSMO-DE, scalar variables are calculated in the centre of the box, the wind velocities are displaced half a grid length.

### 3.1.2 Parameterisation

Since a weather model uses a grid box of a finite size, all subgrid processes can not be modelled explicitly. These subgrid processes have to be parameterised.

Note: The effective resolution of a numerical weather model, is about 5-6 times lower than the grid distance used [e.g. Bierdel et al., 2012]. This implies that probably even grid-scale processes have to be parameterised.

This section gives a brief overview of the parameterisations included in the COSMO-DE model, with a focus on those relevant for this study. By no means we intend to give a complete overview, for that see e.g. Baldauf et al. [2011] or Doms et al. [2014].

No parameterisation for deep moist convection is included in the model. It is assumed that at the spatial resolution of 2.8 km it is resolved by the model. Shallow convection is parameterised by a Tiedtke mass flux scheme [Tiedtke, 1989]. This scheme is adapted in such a way that it only treats shallow convection. Moreover, no precipitation is generated by the scheme.

Stratiform precipitation and cloud microphysics are parameterised by a one moment bulk water-continuity model. The different moisture constituents used are water vapour, cloud water, cloud ice, rain water, snow and hail. In such kind of bulk model the total mass fraction of a specific cloud constituent is directly predicted. This scheme also takes the conversion from moisture constituents by physical processes (e.g. evaporation, sublimation) into account.

To initialise convection during the first model hours, Latent Heat Nudging (LHN) is used. LHN introduces an extra heat source in the thermodynamic

equation at location where the modelled rain deviates from the observed rain rates [Stephan et al., 2008]. These observed rain rates are derived from radar reflectivity. The idea behind LHN is that a positive temperature perturbation will induce upward motion (convection) and will therefore locally increase the rain rate. LHN improves the prediction of rain rates during the first model hours and also the climatology is improved using LHN [Stephan et al., 2008].

Other parameterisations in the COSMO model include a turbulence scheme similar to the level 2.5 Mellor-Yamada scheme [Mellor and Yamada, 1982], a radiation scheme along Ritter and Geleyn [1992] and a multilayer soil model.

### 3.1.3 COSMO-DE-EPS

Deep moist convection is highly nonlinear. Small errors in the initial conditions can therefore have significant impacts on the forecast of precipitation in later forecast hours. A probabilistic approach in handling the errors of the initial conditions is therefore necessary. The standard approach is using an ensemble prediction system [Lewis, 2005]. COSMO-DE-EPS aims at improving the prediction of severe weather and quantifying the uncertainty of the forecast. Moreover, we can assess the origin of the uncertainty, either from the boundary data or from a parameterised process.

The COSMO-DE ensemble prediction system (COSMO-DE-EPS) consists of 20 ensemble members. These 20 members are driven by 4 different global models: The global model (GME) of DWD, the Global Forecast System (GFS) of the National Centers for Environmental Prediction, the Integrated Forecast System (IFS) of the European Centre for Medium-range Forecasts and the Global Spectral Model (GSM) of the Meteorological Agency of Japan [Peralta et al., 2012]. Moreover, 5 parameters in parameterisations are altered [Gebhardt et al., 2008].

The deterministic COSMO-DE analysis assimilates radar data by LHN [Stephan et al., 2008]. It is therefore useful to preserve at least part of the unperturbed COSMO-DE data. This is achieved by adding the difference between the boundary conditions of the runs driven by the 4 different global models and a reference COSMO-EU run to the unperturbed COSMO-DE run [Peralta et al., 2012]. The 4 different boundary conditions out of the 4 global models are first passed to the larger scale model COSMO-EU with a grid spacing of 7 km. The COSMO-DE model is nested into the COSMO-EU domain. This forms the boundary conditions of the Ensemble Prediction System (EPS). By modifying parameters in different parameterisations, the physics of the model is perturbed. The turbulence length, entrainment rate of shallow convection, scaling factor of laminar sublayers (an increase and decrease) and the cloud saturation rate are modified [Peralta et al., 2012]. The ensemble members with a modified turbulence length also have a reduced LHN coefficient. This leads to smaller precipitation rates during the nudgecast period (first few hours of a model run) and higher precipitation rates afterwards. See Peralta et al. [2012] for further details.

### 3.1.4 Reforecast

Since convective cells have a lifetime of about an hour, it is useful to have data with a smaller temporal resolution than the standard hourly output of COSMO-DE and COSMO-DE-EPS. To achieve this, reforecasts of severe weather cases are made. We start each of these reforecast from the deterministic COSMO-DE analysis. An analysis provides the best estimate for the state of the atmosphere. No further observation data is assimilated during the model run, i.e. LHN is not used. All reforecasts are run for 24 hours, and the output of the wind velocity components ( $u$ ,  $v$ ,  $w$ ), the relative vorticity vector  $\zeta$ , and the scalar variables  $p$ ,  $T$ ,  $PV$  and  $q_v$  are saved for all model levels. For these variables we choose a temporal output of 2.5 minutes, except for two cases used in a PV budget analysis (see the discussion below). Beside the high temporal resolution data, the standard output of COSMO-DE, e.g. convective parameters like Convective Available Potential Energy (CAPE) and Convective Inhibition (CIN), is saved every 15 minutes.

### 3.1.5 Calculation of post-processed quantities

The COSMO-DE model can calculate PV, but the standard output of the COSMO-DE-EPS forecast does not include conserved quantifying like PV, helicity and potential temperature  $\theta$ . Therefore, we have to post-process these quantities using the standard output like the wind velocities, pressure and temperature. This is done by using centred differences for the spatial and temporal gradients. At boundaries, e.g. the first and upper model levels, forward and backward differences are used. No further assumptions are made, i.e. we use the full three dimensional absolute vorticity vector in the calculation of PV. On synoptic scales, often the hydrostatic balance is applied and/or only the vertical component of the absolute vorticity vector is used. The influence of this assumption is discussed later on in Section 3.4.

Likewise, for the Dynamical State Index (DSI) all components are calculated, contrary to e.g. Clausnitzer and Névir [2009] who neglected the vertical derivatives of PV and B in the DSI calculation. Moreover, they neglected the vertical velocity in the calculation of PV, which is particularly important for convection.

Moist variables like the Equivalent Potential Vorticity (EPV)  $\Pi_e$  are calculated using the specific humidity  $q_v$ :

$$\Pi_e \equiv \zeta_a \cdot \nabla \theta_e \quad (3.6)$$

$$\theta_e = T(p_0/p)^{(R_d/c_{pd} + r_t c_l)} \exp\left(\frac{l_v r_t}{(c_{pd} + r_t c_l) T}\right) \quad (3.7)$$

$$r_t = q_v / (1 - q_v) \quad (3.8)$$

Here  $r_t$ , the water mixing ratio, is calculated with the specific humidity  $q_v$  only, neglecting the other moisture constituents. We intend to make composites, and since the other moisture constituent have only a small and local influence, differences will be negligible.

We calculate all post-processed variables (PV,  $\theta$ , EPV,  $\theta_e$ , DSI, the helicity  $H$  and the relative vorticity vector  $\zeta$ ) on model level 24 ( $\approx 5.5$  km, the height where

maximum PV anomalies are expected for deep moist convection). We do this for the 0 and 12 UTC forecasts of COSMO-DE-EPS for the summer months (June, July and August) of 2011, 2012 and 2013. This data will be used in Chapter 7 to briefly discuss the ability of PV to predict severe weather.

As an estimate of precipitation in Chapter 7, the direct hourly precipitation rates from the COSMO-DE model is used. The COSMO-DE model also estimates the wind gust, by using

$$v_{\text{gust}} \equiv |v_{30\text{m}}| + 3.0 \cdot 2.4 \cdot u_*, \quad (3.9)$$

where  $|v_{30\text{m}}|$  is the absolute value of the wind speed interpolated to 30 metres height and  $u_*$  is the friction velocity. The multiplication factors are determined empirically and their motivation is in Prandtl-layer theory [Born et al., 2012].

### 3.2 DATA DESCRIPTION AND CASE STUDY SELECTION

In this section the different data are shortly described. We use a combination of COSMO-DE-EPS forecast data, single run reforecasts from the COSMO-DE NWP model made for 9 selected severe weather cases, and precipitation observations:

- Reforecasts of 9 severe weather cases are made. For a description how the reforecast are generated, see Section 3.1.4. For a discussion how the cases are selected, see Section 3.2.1. Two of the 9 cases, namely the 5 and 22 June 2011 cases, are used in the PV budget study (see Section 3.3). For these two cases the data is saved at a temporal resolution of 25 seconds. Reforecast data for the other 7 cases is saved every 2.5 minutes. These reforecasts serve as a basis for the composites in Chapter 5 and Chapter 6.
- From the COSMO-DE-EPS, both the forecast data saved by the DWD and post-processed data are used. The complete COSMO-DE-EPS forecast of the 0 and 12 UTC runs is available for the 5 and 22 June 2011 weather cases analysed in Chapter 4. Furthermore, we use data at model level 24 to test if PV can be used as a predictor for severe weather in Chapter 7. At this model level, the kinetic energy, PV, and EPV are calculated for the summer months (June, July and August) of the years 2011 till 2013. Details about how these post-processed quantities are calculated can be found in Section 3.1.5.
- Hourly precipitation observations are available for 1060 stations over Germany for the summer months of 2011, 2012 and 2013. These data are provided by the DWD<sup>3</sup> and are used to test if PV can be used as a predictor for severe precipitation in Chapter 7.

#### 3.2.1 Selection of 9 severe weather cases

The goal of this study is to characterise PV anomalies typically associated with (severe) DMC. The weather cases for the case study and other analyses have to

<sup>3</sup> [http://www.dwd.de/EN/climate\\_environment/cdc/cdc\\_node.html](http://www.dwd.de/EN/climate_environment/cdc/cdc_node.html)

Case	Run	Extremes
5 June 2011	0 UTC	68 mm in Bonn (Germany) in 2 h
6 June 2011	0 UTC	73 mm in Kirchdorf/Poel (Germany) in 24 h
22 June 2011	0 UTC	Wind gusts over 120 km/h in Baden-Württemberg
28 June 2011	12 UTC	100 mm precipitation in Herwijnen (The Netherlands) in 24 h
30 June 2012	12 UTC	Wind gust over 100 km/h in South Germany
28 July 2012	12 UTC	78 mm in Bahno (Czech Republic) in 6 h
20 June 2013	12 UTC	101 mm precipitation in Deuselbach in 24 h, wind gusts of 156 km/h in Andermatt-Gütsch (Switzerland)
28 July 2013	12 UTC	60 mm in Feldberg/Schwarzwald in 24 h
6 Augustus 2013	12 UTC	Winds gusts of 140 km/h at Wasserkuppe

Table 3.1: Description of the extremes associated with the 9 severe weather cases which are used in this study. The 5 and 22 June 2011 weather cases are used in the case study (Chapter 4). For each of the cases a single run reforecast is made, starting at the time step indicating in the Run column.

be chosen with care. They have to be representative for severe weather over the model domain. Selection criteria for these weather cases are:

- There should be severe weather observed over Germany. We select cases for which severe rain, severe wind gusts or significant hail was observed. Although we do not expect that the COSMO-DE model captures accurately all those extremes, we still want to know what kind of model weather is associated with those observed extremes.
- As a further constraint, there should be a considerable amount of DMC generated in the COSMO-DE model. It is possible that only locally (severe) DMC is generated. However, since we are planning to make composites of fields around convective cells, we need a reasonable large sample of modelled convective cells.
- The quality of the COSMO-DE NWP model forecasts should be reasonable compared with observations. A perfect forecast does not exist, and forecasting the location perfectly might not be relevant for our study. It is important, however, that the forecast represents at least the precipitation structure of the observed case reasonably well.
- There should be a variation in synoptic and mesoscale situations associated with the severe weather events. For example, we want to select frontal cases (which are characterised by larger wind shear and larger large scale frontal forcing) and local convective events. Furthermore, we want to select cases in which there is directional wind shear with height and cases in which the environment wind is more unidirectional.

Based on these criteria, we select 9 severe weather cases for which a reforecast is made (Table 3.1). Of these weather cases 4 are from June 2011, 2 cases are from 2012 and 3 cases are from 2013. Typical extremes observed during these cases can be found in Table 3.1. The choice of starting at 0 or 12 UTC is based on when the

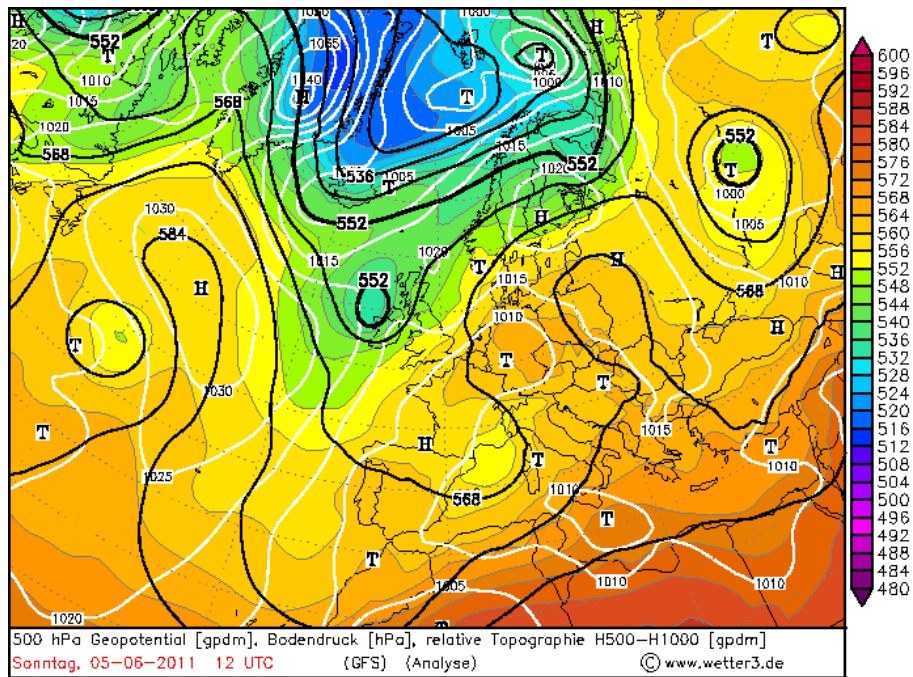
convection is dominant. For the cases on 5, 6 and 22 June 2011, convection took place mainly in the afternoon, while for the other cases in the (early) evening. These 9 cases have a good variability in background characteristics like wind shear, CAPE and Storm Relative Helicity (SRH). These differences in convective characteristics will be further discussed in Chapter 6.

### 3.2.2 *Synoptic situation*

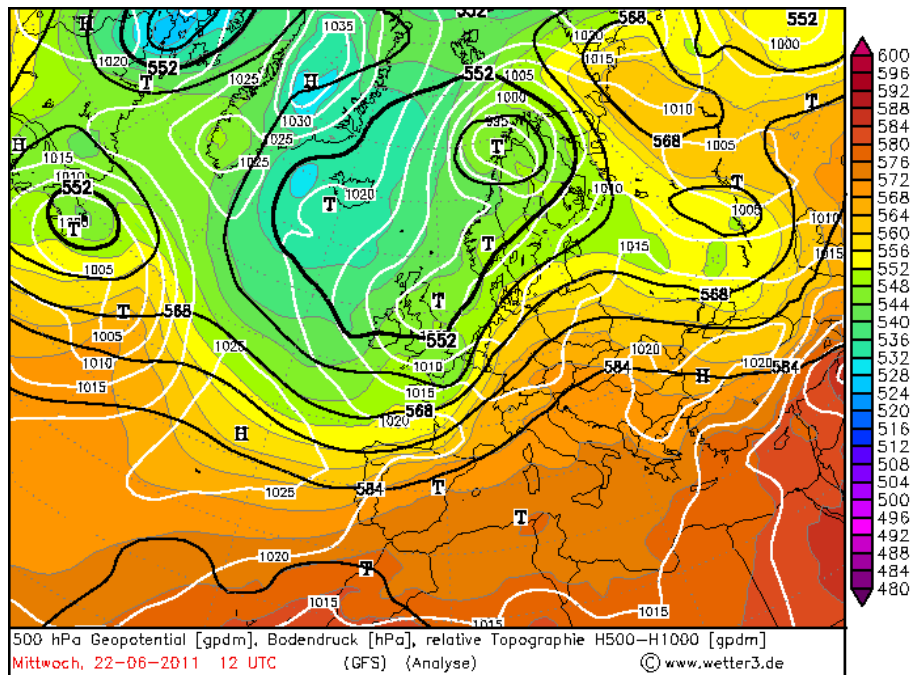
In this section the synoptic situation for the two cases which are thoroughly analysed (05-06-2011 and 22-06-2011) will be described, see for further details Weijenborg et al. [2015]. Also the quality of the reforecasts will be shortly discussed.

Figure 3.2a presents the synoptic analysis of the GFS analysis for 5 June. The days preceding 5 June 2011 were characterised by sunny and relatively warm weather associated with a high pressure system. East of the high pressure system intensifying south-easterly to southerly winds advected warm and humid air northwards. Dew points of up to 20° C were measured. This humid air together with the confluent flow of a low pressure system provided the main ingredients for the heavy thunderstorms occurring during 4 June 2011 and the following days. On 4 June, most heavy thunderstorms were located in northern France and southern Germany. The most heavy precipitation in Germany occurred on 5 June, with 87 mm in 24 hours at the weather station Lennestadt-Theten and more than 60 mm within a few hours in the vicinity of Bonn. Convection was scattered over Germany, although there were some large scale precipitation areas (Fig. 3.3a, which shows the radar precipitation rates derived from RADOLAN data [Bartels et al., 2004]).

In Fig. 3.2b the synoptic analysis for 22 June 2011 is shown. Responsible for the severe weather on 22 June 2011 was a cold front associated with a low pressure system, which formed around 16/17 June 2011 over the North-West Atlantic. It moved eastward to the British Isles on 21 June. The cold front associated with the low pressure system crossed Middle Europe during the night of 21 to 22 June with the southern part of the cold front lying westward of the northern part. Along the southern part of the cold front, a secondary low formed. The cold front and the secondary low moved over Germany during 22 June and caused precipitation and large wind gusts over large parts of Germany. Wind speeds of up to 130 km/h were measured in Southern Germany, and precipitation was less strong compared to 5 June with 20 mm rain in 24 hours but over a much larger area (Fig. 3.3b). Besides the heavy wind gusts, large hail stones were observed. The main difference to the 5 June case is that the convection was much more organised. Thus, banded structures of PV as discussed in Chapter 1 are more likely to form on 22 June.



(a)



(b)

Figure 3.2: (a) Synoptic overview of 5 June 2011 at 12 UTC, from the GFS forecast. 500 hPa geopotential height (black contour lines, in gpdam), surface pressure (white contour lines, in hPa) and relative topography (i.e. the thickness between 500 hPa and 1000 hPa, filled contours). (b) As (a), but for 22 June 2011 at 12 UTC. Source: R. Behrendt/H. Mahlke, [www.wetter3.de](http://www.wetter3.de).

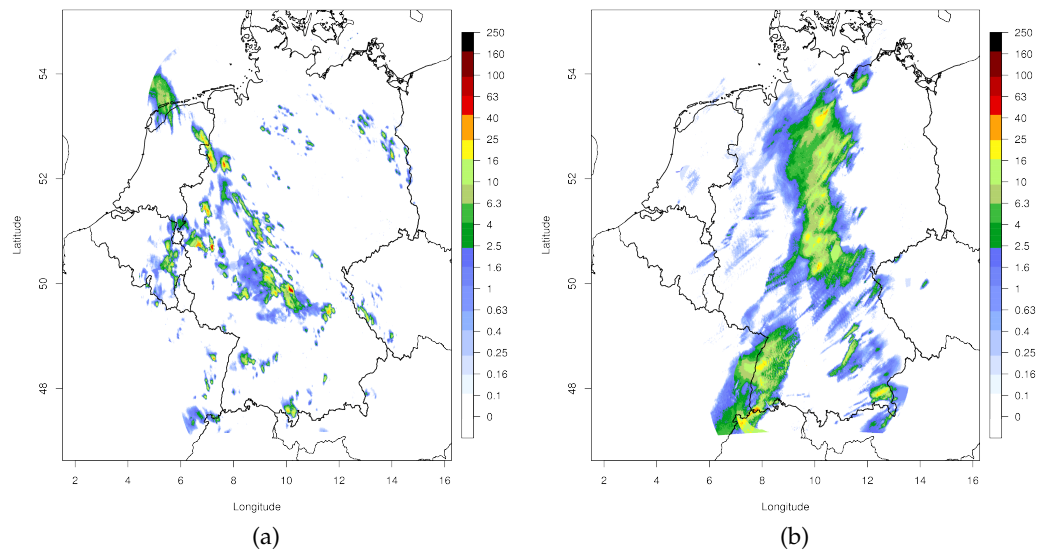


Figure 3.3: Rain rates in mm/hour, using RADOLAN RW data [Bartels et al., 2004] for (a) 5 June and (b) 22 June 2011 at 14:50 UTC, respectively.

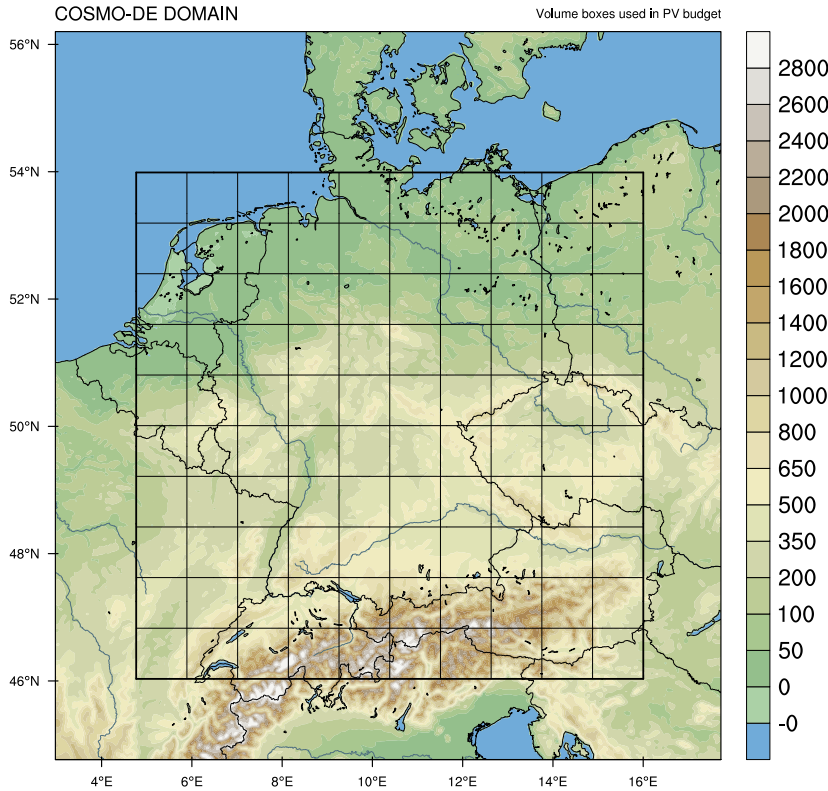


Figure 3.4: Volume boxes used in PV budget analysis, every volume box consists of  $32 \times 32$  grid points in the horizontal and 5 vertical levels.

### 3.3 PV BUDGET

In this section the PV budget analysis is described. The main goal is to test if the COSMO model is able to accurately represent PV dynamics. PV is not a prognostic variable in the model, therefore we do not expect that PV is perfectly conserved. Therefore, PV conservation is tested by using the PV evolution equation of Haynes and McIntyre [1987] (see Eq. 2.31). For convenience, we repeat this equation here,

$$\frac{\partial \rho \Pi}{\partial t} + \nabla \cdot (\mathbf{u} \Pi \rho - \zeta_a \dot{\theta} - \mathbf{F} \times \nabla \theta) = 0, \quad (3.10)$$

Remind that the terms at the left hand side represent local change of PV, generation of PV due to diabatic heating, and frictional effects. The two reforecasts of 5 June and 22 June 2011 are used. For the budget analysis, we will use the model output from 6h to 21h for these two cases (25 seconds time step, in total 2160 time steps).

The model domain is divided into  $10 \times 10$  grid boxes of 32 grid points in the horizontal and 5 levels in the vertical direction (Fig. 3.4). The size of a box is about 90 km in the horizontal, and it has variable height in the vertical, since at the lower levels the model levels are much closer together.

### 3.3.1 Variance analysis

For each of the 2160 time steps, the spatial variance of the sum of all terms at the left hand side of Eq. 3.10 is compared to the sum of the variances of the individual terms:

$$\text{Fr} \equiv \frac{\langle \frac{\partial \rho \Pi}{\partial t} + \nabla \cdot (\rho \Pi \mathbf{u} - \dot{\theta} \zeta_a) \rangle}{\langle \frac{\partial \rho \Pi}{\partial t} \rangle + \langle \nabla \cdot (\rho \Pi \mathbf{u}) \rangle + \langle -\nabla \cdot (\theta \zeta_a) \rangle}, \quad (3.11)$$

where  $\langle .. \rangle$  denote spatial variances (i.e. variance over the 100 volume boxes in Fig. 3.4 ). Here we neglected the effect of friction, which probably plays only an important role in the boundary layer. The part between the brackets in the nominator can be seen as the residuals of Eq. 3.10, which are zero if PV is perfectly conserved. If there is no perfect PV conservation, the variance of the residuals should be at least negligible. The question is to which extent the variance is negligible. We thus normalise the variance with the sum of the variances of the individual terms. If the terms in Eq. 2.31 do not balance, then there are no correlations between the terms. In this case, the nominator is equal to the denominator and the fraction is equal to 1. In case that (some of) the terms are uncorrelated, the fraction will be smaller than 1.

We find that, neglecting  $\mathbf{F}$ , Fr in Eq. 3.11 amounts to about 4-5% in the troposphere for both cases (Fig. 3.5 and Fig. 3.6). This is remarkably good, since effects due to moisture are not included in the dry Ertel PV. The solenoid term in the vorticity equation ( $\nabla \rho \times \nabla p$ ) does not appear in Eq. 3.10, since we assumed that the potential temperature  $\theta$  only depends on  $\rho$  and  $p$ , which is only valid for dry flow. Moisture do not seem to influence the middle troposphere that much, at least not on the scale used in the budget analysis. In the stratosphere (i.e. upper 10 model levels), Fr is equal to about 1, which indicates that PV is not conserved here. This could be due to the Rayleigh damping applied in the upper model levels. Also, the variance is relatively small in the stratosphere, one has to be careful in interpreting the fraction.

There is no correlation between the local change of PV and the diabatic term, but in the upper troposphere the local change and advection are highly anti-correlated (3rd panel from the bottom of Fig. 3.5 and Fig. 3.6). The mean correlation in the upper troposphere is about -0.77 for both days. These negative correlations indicating that the PV is approximately materially conserved, i.e.  $\frac{d\Pi}{dt} = 0$ . There is a large cancellation in the lower troposphere between the diabatic and the advection term in Equation 3.10, with negative correlations of -0.9 in the lowest 10 levels (Fig. 3.5 and Fig. 3.6). These negative correlations are especially strong during the afternoon, when DMC takes place. During DMC, the negative correlations extend up to level 20, at about 6 km height. This might not be physically interesting, Tory et al. [2011]) argued that the cancellation between the diabatic forcing term and PV advection term in deep convective systems is due to an adiabatic response due to local buoyancy gradients that largely cancels any change due to the diabatic forcing. In conclusion, the results confirm that overall the COSMO-DE model accurately describes PV dynamics during convection.

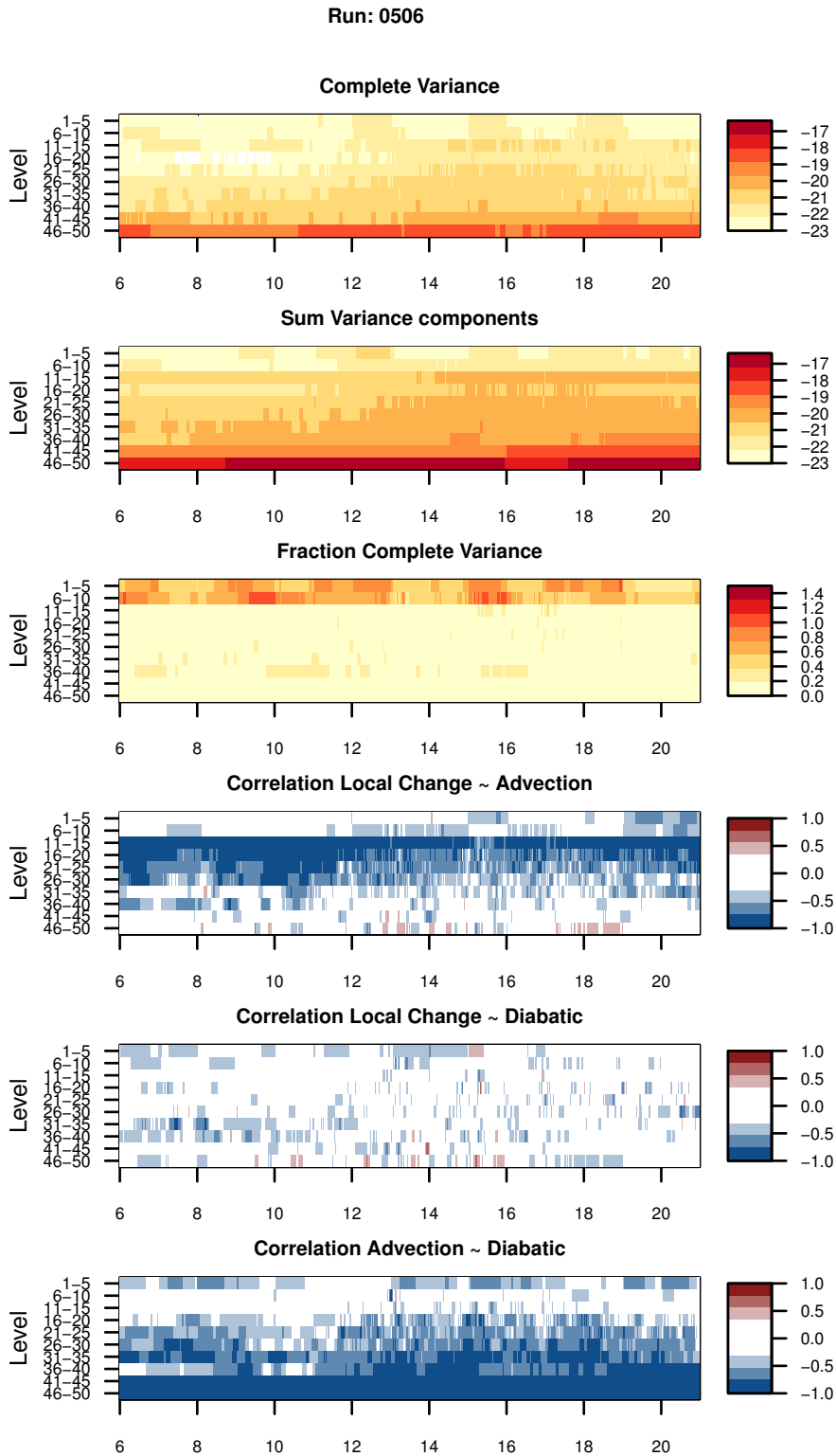


Figure 3.5: Variance analysis of PV budget, as function of time (in UTC), for 5 June 2011. From top to bottom the complete variance (numerator of Eq. 3.11), the sum of the variance of the individual terms (denominator of Eq. 3.11), the fraction of the two ( $Fr$  in Eq. 3.11)), and the correlations between the individual terms of the PV evolution equation (Eq. 2.31) are indicated.

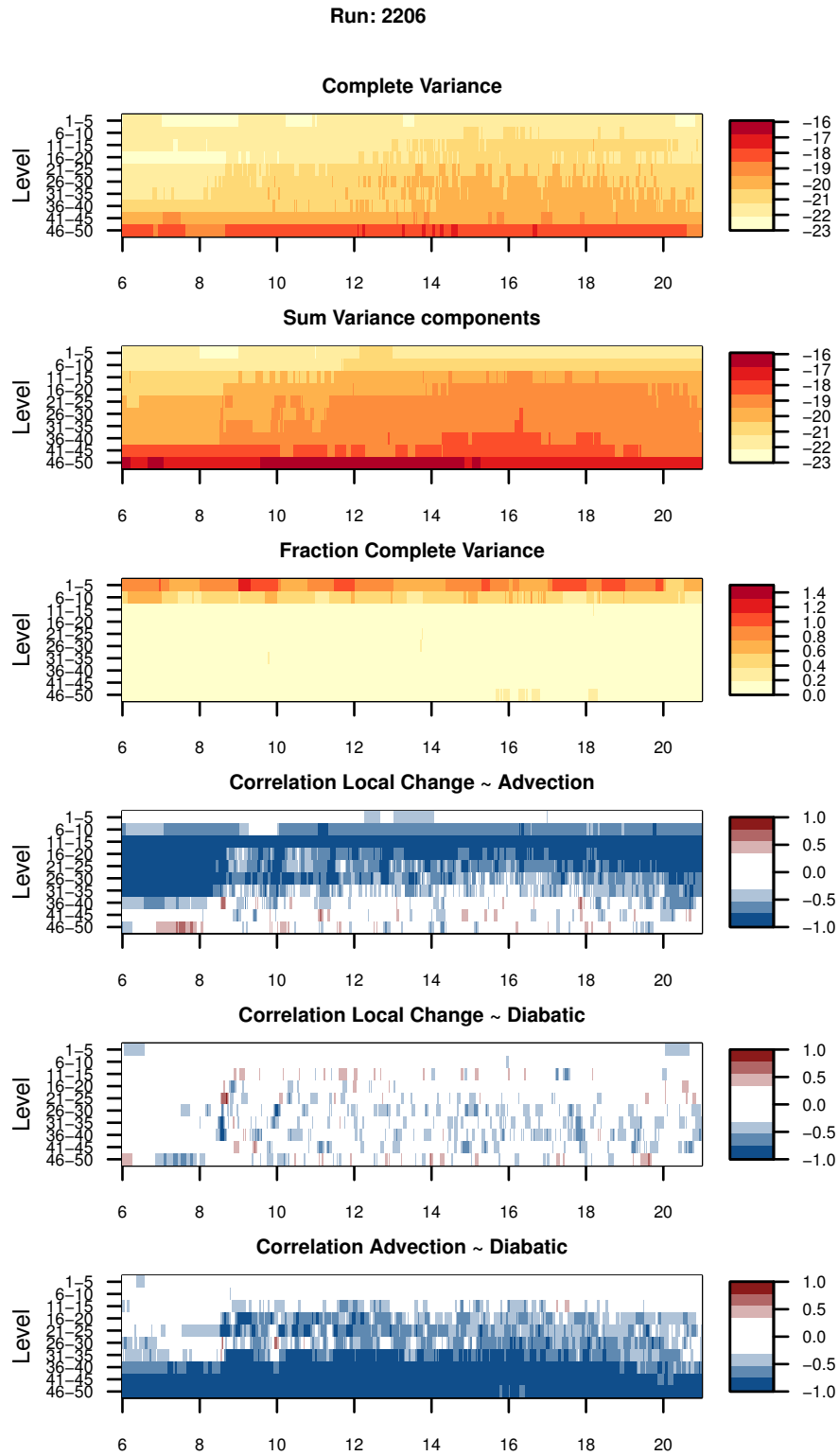


Figure 3.6: Variance analysis of PV budget, as function of time (in UTC), for 22 June 2011. From top to bottom the complete variance (numerator of Eq. 3.11), the sum of the variance of the individual terms (denominator of Eq. 3.11), the fraction of the two ( $F_r$  in Eq. 3.11)), and the correlations between the individual terms of the PV evolution equation (Eq. 3.10) are indicated.

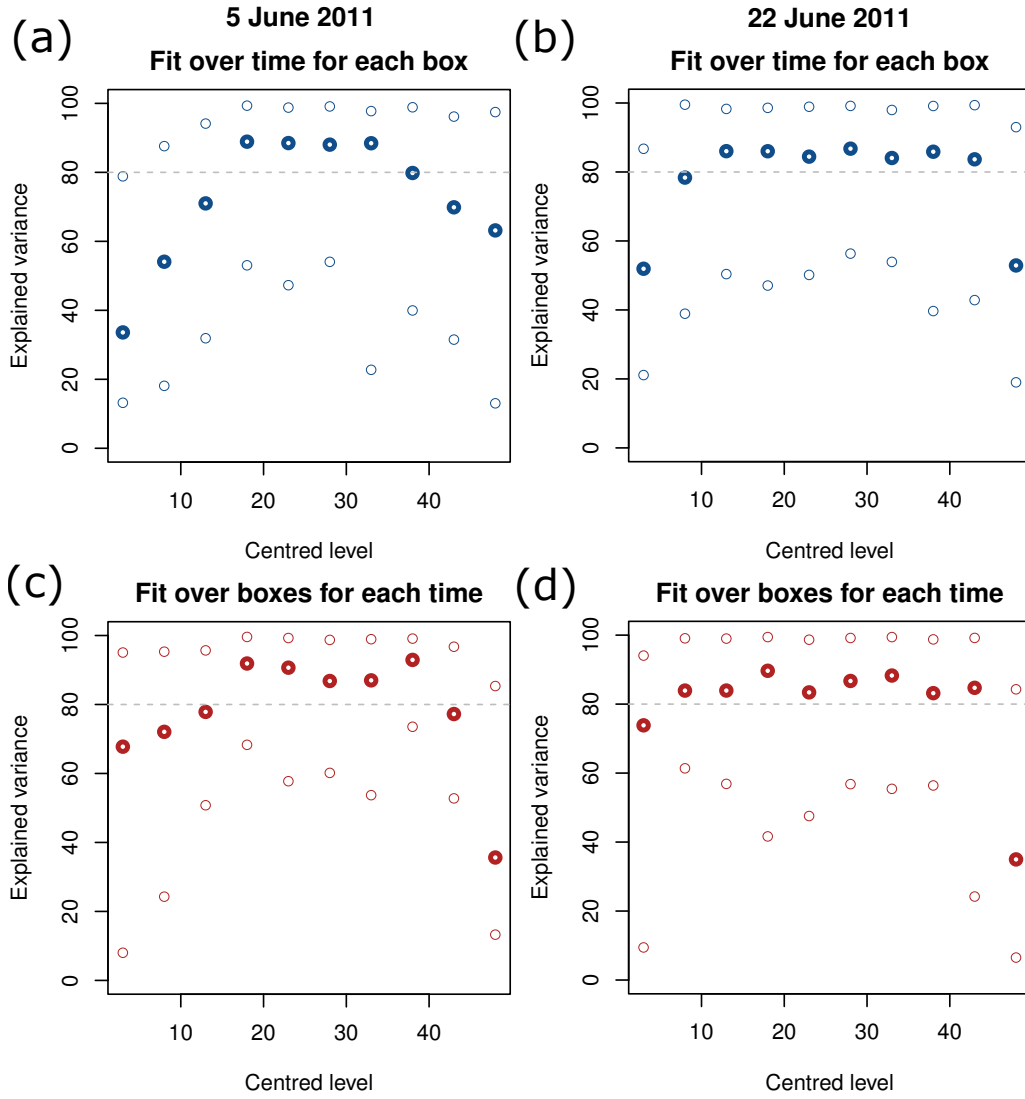


Figure 3.7: Explained variance of the budget MLR. (a) Regression performed over all times for a specific box for 5 June 2011. Bold dots indicate median explained variance over all boxes and the dots indicate 5% and 95% quantiles for each vertical level. (b) as (a), but for 22 June 2011. (c) Regression performed over all boxes for a specific time step, for 5 June 2011. Bold dots indicate median explained variance over all times and the dots indicate 5% and 95% quantiles for each vertical level. (d) as (c), but for 22 June 2011.

### 3.3.2 Linear Regression

A more thorough budget analysis is performed using a MLR [e.g. Wilks, 2011]. We take the residual of Eq. 3.10 as predictand, and the other terms in the PV evolution equation as predictors:

$$y_i = \alpha_1 x_{1i} + \alpha_2 x_{2i} + \alpha_3 x_{3i}, \quad (3.12)$$

$$x_{1i} = \left(\frac{\partial \rho \Pi}{\partial t}\right)_i \quad (3.13)$$

$$x_{2i} = (\mathbf{u} \Pi \rho)_i \quad (3.14)$$

$$x_{3i} = (-\zeta_a \dot{\theta})_i \quad (3.15)$$

with  $i = 1, 2, \dots, n$ , and  $n$  is number of volume boxes used in the regression. Here,  $x_{1i}$  is the volume integrated PV tendency of box  $i$ ,  $x_{2i}$  is the advection term of box  $i$  and  $x_{3i}$  is the diabatic term for box  $i$ . All “predictands”  $y_i$  are set to zero, since Eq. 3.12 represents the residual of Eq. 3.10, which is zero if PV is conserved. A further restriction is that the sum of the regression coefficients  $\alpha_j$  ( $j = 1, 2, 3$ ) is set to be equal to 3. This is done to ensure that the resulting  $\alpha_j$  are close to one. If Eq. 3.10 describes the dynamics of the COSMO-DE NWP perfectly, the three regression coefficients  $\alpha_j$  should be exactly equal to 1. In this case, Eq. 3.12 is exactly equal to Eq. 3.10. Moreover, the explained variance of the MLR should be equal to 100%. The regression is performed first over all the different boxes in the model domain (for all 2160 times), and after that another MLR is calculated over all times for each box (for all 100 boxes).

Explained variance for the 5 and 22 June 2011 cases are plotted in Fig. 3.7. Fig. 3.7 shows that for most boxes in the middle troposphere the explained variance of the MLR is around 90%. Especially for the regression over time for each box (Fig. 3.7a and b), the explained variance is much less for the 10 upper and lower model levels of the COSMO-domain. At lower model levels we saw that the diabatic and advection terms are highly correlated. This might indicate that moisture effects, which are not included in Eq. 3.10, play a huge role especially in the lower troposphere. At the upper levels Rayleigh damping might prohibit PV conservation. The explained variance of the MLR is smaller for the 5 June case (Fig. 3.7a), compared to the 22 June case (Fig. 3.7b). The 5 June case is characterised by more local convection, what could explain these differences. Although the MLR shows that the fit is in general good, there are a lot of boxes for which the explained variance is much lower. The spatial MLR over all boxes at a specific time gives similar results (Fig. 3.7c and d).

The average regression coefficients in Fig. 3.8 show that in general the regression coefficients for the local change is much higher (lower) than 1 at the upper (lower) model levels. This is particularly visible around 14 till 16 UTC, when DMC took place. As noted in the previous section, one has to take care of interpreting these results, because the variance of the residuals of Eq. 3.10 is small. For the regression coefficients for the other two predictors (diabatic heating and advection) the opposite is true. At lower levels, especially at levels 46-50 the PV is solely determined by the diabatic term and the advection term in Eq. 3.10. This is consistent with the discussion in Section 2.4.1, in that diabatic effects only redistribute PV. In conclusion, this indicates again that especially at these lower and upper model levels, Eq. 3.10 does not describe the full dynamics for the COSMO-DE model, e.g. because of baroclinic effects. In the middle troposphere most of the time the values for  $\alpha$  are around 1, indicate that here the PV budget is approximately closed.

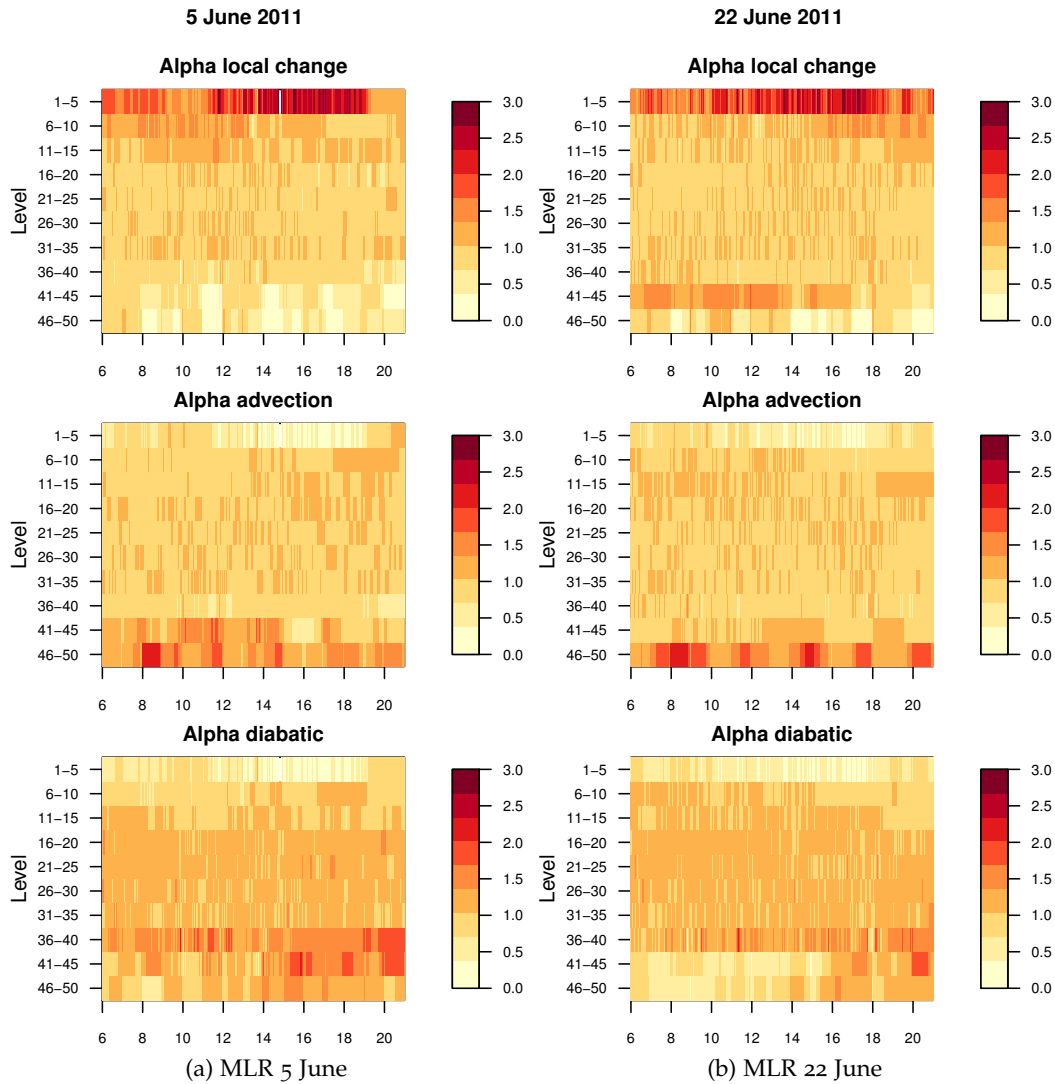


Figure 3.8: Regression coefficients  $\alpha$ , as function of time (in UTC), for the PV budget for (a) 5 June 2011 and (b) 22 June 2011. The regression is performed over all boxes at a specific time step, and the average  $\alpha$  over all boxes is plotted.

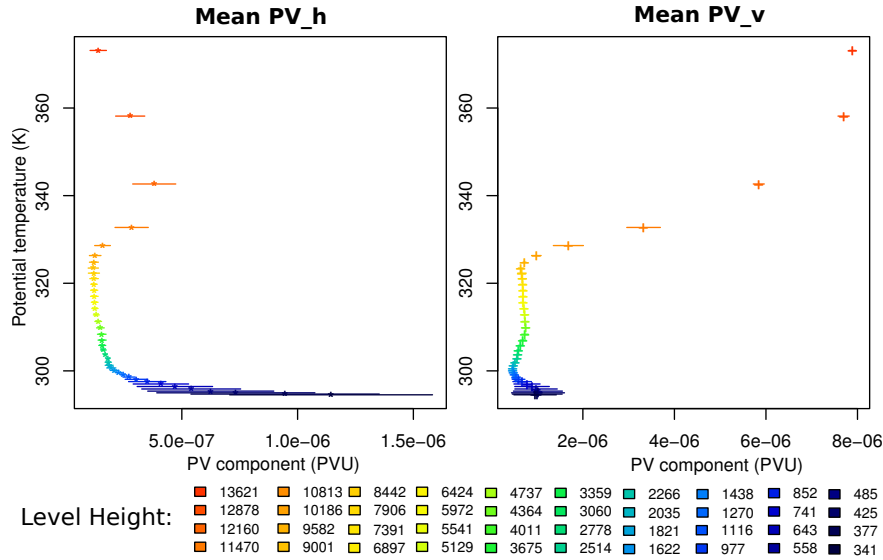


Figure 3.9: Mean profiles for vertical and horizontal PV for 5 June 2011. Means are calculated over the model domain, for each forecast hour, at a specific level (height indicated by the colours). The horizontal stripes indicate the temporal variance over the 21 different hourly timesteps. For the potential temperature  $\theta$  on the y-axis the model domain mean on a particular level is taken.

### 3.4 IMPORTANCE FULL PV

In most synoptic studies which use PV, PV is approximated by the vertical component of the vorticity times the vertical gradient of potential temperature [e.g. Clausnitzer and Névir, 2009]. For the mesoscale, this might be a bad approximation, since the horizontal components of the vorticity vector  $\zeta_a$  are generally one to two orders of magnitude stronger than the vertical component [Markowski and Richardson, 2010]. To check the accuracy of this approximation the full PV is divided in a “horizontal” and a “vertical” component:  $\Pi \equiv \Pi_h + \Pi_v = \omega_h \nabla_h \theta + \zeta \frac{\partial \theta}{\partial z}$ .

Mean vertical profiles of both components of PV displayed in Fig. 3.9 for the 5 June 2011 weather case. One can see that over a large part of the atmosphere the vertical component is much larger than the horizontal component. In the middle troposphere the vertical component is  $\mathcal{O}(1)$  Potential Vorticity Unit (PVU). The tropopause is clearly visible as an increase of PV at about 330 K. In the Planetary Boundary Layer (PBL) and the lower troposphere, the horizontal component and vertical components have an equal size, of about 0.5 PVU. Moreover, there is a lot of (temporal) variation in the mean horizontal component of PV, for a few time steps mean horizontal PV of 1.5 PVU is observed. Therefore, in the PBL the approximation of taking only the vertical component of PV is a bad one. The reason why the vertical component of PV is dominant in the middle troposphere, is that the vertical vorticity associated with it originates from horizontal vorticity due to the wind shear. The horizontal vorticity component is normally much larger than the vertical component for the mesoscale. The gradient of potential temperature, however, is normally directed into the vertical direction. When the

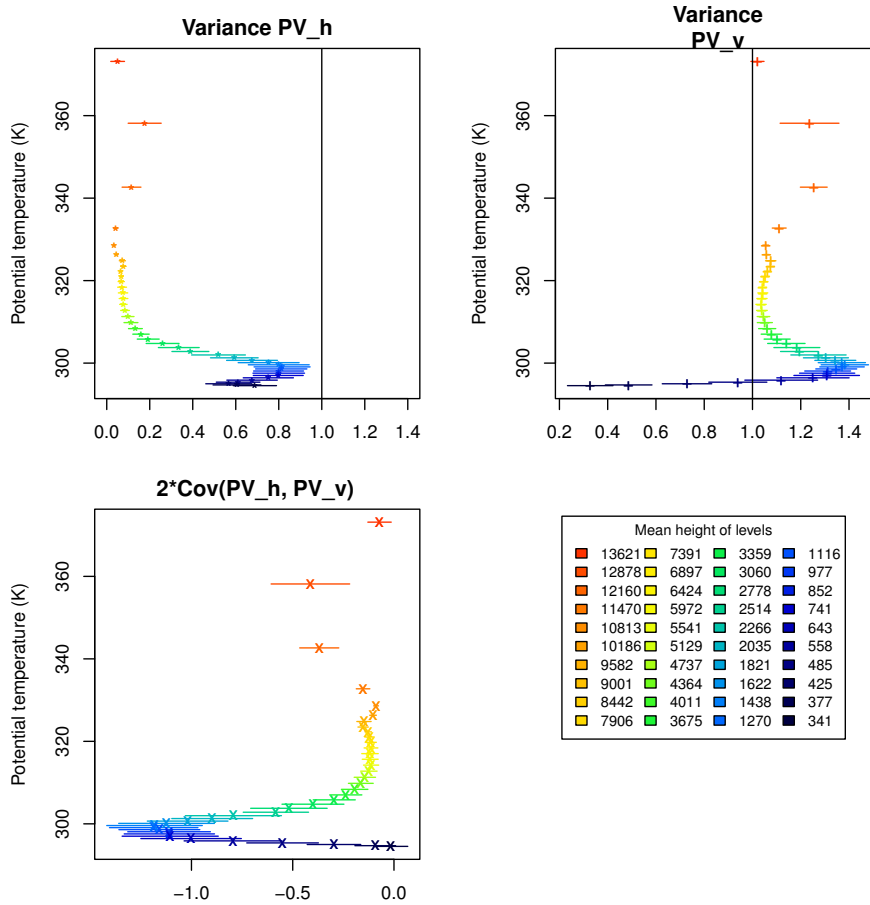


Figure 3.10: Variance profiles for vertical and horizontal PV for 5 June 2011. Variances are calculated over the model domain, for each forecast hour, and each variance component is normalised by the variance of the total PV (details see text). The horizontal stripes indicate the temporal variance over the 21 different hourly timesteps. For the potential temperature  $\theta$  on the y-axis the model domain mean on a particular level is taken.

relative large horizontal vorticity is tilted into the vertical, as is the case around convective cells, large PV anomalies will be generated (see Section 2.4.3).

This relative importance of horizontal and vertical PV can also be seen analysed by using the (spatial) variance of the different components in Fig. 3.10. Generally,

$$\text{VAR}(\Pi) \equiv \text{VAR}(\Pi_h) + \text{VAR}(\Pi_v) + 2\text{COV}(\Pi_h, \Pi_v) \quad (3.16)$$

Here  $\text{VAR}(x)$  indicates a spatial variance of  $x$ , and  $\text{COV}(x, y)$  indicates the covariance of  $x$  and  $y$ , with  $x$  and  $y$  data vectors containing all grid points of the COSMO-DE model domain at a given time. All of the components at the right of Fig. 3.10 are normalised by the variance of the total PV ( $\text{VAR}(\Pi)$ ). Therefore their sum should be equal to one. At lower model levels the variance of the horizontal component is comparable with the variance of the vertical component (Fig. 3.10). The negative covariance at about 1 km height indicates that there is a strong negative correlation between the vertical and horizontal PV components at lower levels. The large variance of both of the components at this height indicate that

tilting (of horizontal vorticity) might be the important at around 1 km height. As for the mean PV, the vertical component dominates the variance of PV in the middle troposphere.

In conclusion, particularly in the boundary layer the horizontal PV component is relatively stronger compared to the vertical component. This study will subsequently use the complete PV. Although on average the horizontal PV might not be very important in the middle troposphere, locally it might be important.

*The focus in this chapter will be on characterising typical Potential Vorticity (PV) anomalies associated with typical severe weather events. Two weather cases with a different synoptic background are analysed, on 5 June 2011 and 22 June 2011. Composites of PV and other quantities like wind velocity around storm updrafts are calculated to test consistency of PV anomalies associated with storm updrafts. For the 22 June case the PV dipoles are much more consistent than in the 5 June case in direction, and bands of positive and negative PV are formed approximately in the direction of the wind shear. A possible explanation of these elongated PV bands is the preferential generation of new cells downshear of old cells in an atmosphere with moderate to high vertical wind shear. Differences between the ensemble members suggest that the orientation of the bands is mainly dependent on large scale flow and initial conditions. For both cases the wind anomalies around the convective PV anomalies are consistent with the flow around synoptic PV anomalies. The results of this chapter have been previously published in Weijenborg et al. [2015]<sup>4</sup>.*

#### 4.1 AIMS AND MOTIVATIONS

The main goal of this chapter is to describe the consistency of PV anomalies during severe convection in a convection-permitting Numerical Weather Prediction (NWP) using data from operational forecasts. Data from the operational Ensemble Prediction System (EPS) of the nonhydrostatic NWP model COSMO-DE are used [COSMO-DE-EPS, Baldauf et al., 2011; Peralta et al., 2012]. Two cases of severe weather over Germany during June 2011 are selected with a different synoptic background. One case which consists of local severe convection (5 June 2011), and another case characterised by convection along a cold front (22 June 2011). We want to investigate a few of the thoughts of Chagnon and Gray [2009] in deeper detail. Firstly, we investigate the coherency of the horizontal PV dipoles by calculating composites of PV and other fields around storm cells. With the use of COSMO-DE-EPS we have a relatively large sample of convective cells, to calculate robust composites. Secondly, we want to discuss the influence of the synoptic environment on the orientation and other characteristics of the PV dipoles.

The central questions we want to answer in this study are:

1. How consistent are the forecasted PV dipoles in strength and direction for non-idealised real weather events investigated in a state-of-the-art convection permitting NWP model?
2. Is there any coherent flow around these PV dipoles, i.e. are the wind velocity and  $\theta$  anomalies around a PV anomaly comparable to Quasi-

---

<sup>4</sup> DOI: <http://dx.doi.org/10.3402/tellusa.v67.25705>

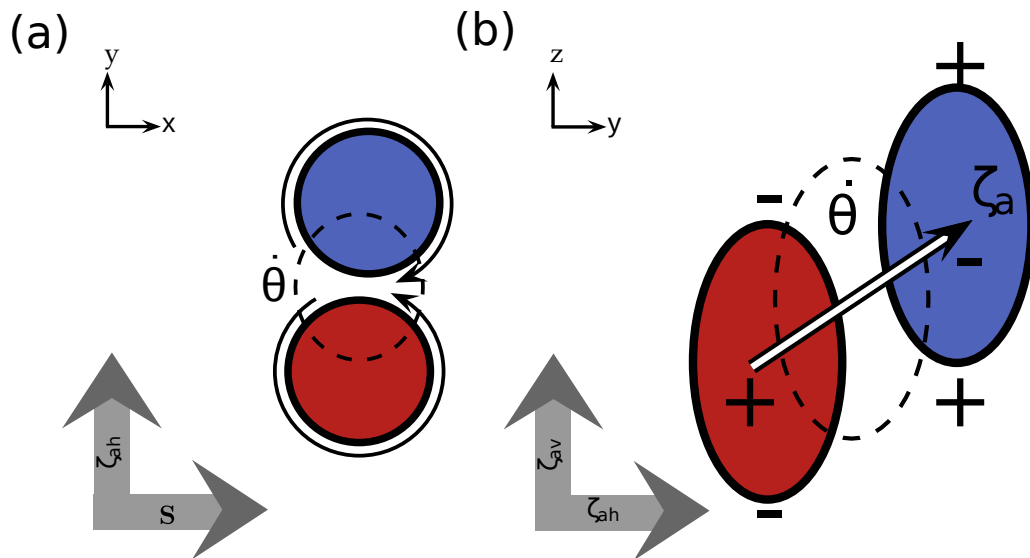


Figure 4.1: Schematic overview of PV dipoles generated due to convection, diabatic perturbation indicated by dashed black circle and positive (negative) PV pole indicated by red (blue) circle. The +/- signs indicate regions of high and low static stability and  $\zeta_{ah}$  the direction of the (dominant) horizontal vorticity vector. (a) Horizontal cross section, PV dipoles created in the direction of absolute vorticity  $\mathbf{k} \times \mathbf{S}$ , with  $\mathbf{S}$  the vertical wind shear. Storm relative wind velocities associated with the PV anomalies are indicated by black arrows. (b) Vertical cross section along the direction of  $\mathbf{k} \times \mathbf{S}$ .

Geostrophic (QG) PV anomalies as discussed in Hoskins et al. [1985] and Hoskins [1997]?

### 3. Is there any organisation of PV structures on larger scales?

The chapter is organised as follows. In Section 4.2 we shortly review how the PV anomalies are created, and we hypothesise how they will differ in the different synoptic backgrounds of the two cases. Section 4.3 gives an overview of the model data and the methodology used. In Section 4.4 we present mesoscale case description of the two weather cases under investigation. Section 4.5 discusses composites of fields around storm updrafts. Section 4.6 summarises results and discusses implications and further analyses.

## 4.2 BACKGROUND

The purpose of this section is to shortly review the characteristics of the PV dipoles theoretically described in Chagnon and Gray [2009]. We will discuss how the general orientation of the dipoles depends on the characteristics of the synoptic environment like wind shear and storm relative helicity.

A schematic depiction of the creation of the dipoles is shown in Fig. 4.1, which shows a horizontal and vertical cross section of the dipoles created around a convective cell (depicted in Fig. 4.1 as a diabatic heating anomaly). Neglecting

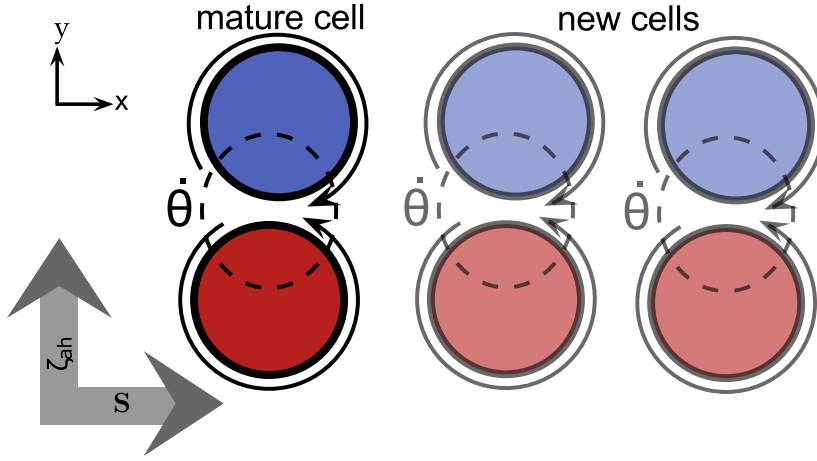


Figure 4.2: As in Fig. 4.1, a diabatic perturbation is indicated by a dashed black circle and a positive (negative) PV pole by a red (blue) circle. New cells (transparent) are preferentially generated downshear, which could in combination with advection lead to bands of positive and negative PV.

friction, the PV evolution equation can be written as [e.g. Haynes and McIntyre, 1987],

$$\frac{d\Pi}{dt} = \frac{\zeta_a \cdot \nabla \dot{\theta}}{\rho}, \quad (4.1)$$

with  $\Pi$  the PV, defined by  $\Pi = \rho^{-1} \nabla \theta \cdot \zeta_a$ ,  $\rho$  is the density,  $\zeta_a$  the 3-dimensional absolute vorticity,  $\theta$  is the potential temperature,  $\dot{\theta}$  it's deviation with time (i.e. diabatic heating), and  $\nabla$  denotes the 3-dimensional gradient operator. Generally, deep moist convection creates a local heating anomaly with a maximum in the middle troposphere due to condensational heating [Houze Jr, 2004; Xie et al., 2014]. This diabatic heating anomaly  $\dot{\theta}$  will create PV dipoles in the direction of the absolute vorticity vector  $\zeta_a$ . We assume that the horizontal vorticity due to the vertical wind shear of the horizontal wind ( $\zeta_{ah} = \mathbf{k} \times \mathbf{S}$ , with  $\mathbf{k}$  as the unit vector in the vertical direction and  $\mathbf{S} \equiv \frac{\partial \mathbf{u}_h}{\partial z}$ ) will dominate the absolute vorticity on the convective weather scale. Therefore, the dipoles are normally created in the horizontal plane (see Fig. 4.1a). The exact angle with respect to the horizontal plane of the dipole depends on the ratio of vorticity due to wind shear and the planetary vorticity [see Chagnon and Gray, 2009]. The vertical component of the background planetary vorticity is positive in the northern hemisphere because there is always a part related to planetary rotation. Therefore, it is expected that the dipole will be slightly tilted in the vertical (Fig. 4.1b).

In Fig. 4.1a and b it is assumed that the directional wind shear (i.e. changes of the angle of the wind velocity vector with height) is zero. Chagnon and Gray [2009] described the dipoles in unidirectional wind shear (i.e. zero helicity, which is generally not the case). Helicity  $H \equiv \zeta \cdot \mathbf{u}$  is defined as the inner product between the three dimensional wind velocity and relative vorticity vectors. The integrated form is conserved for 3 dimensional barotropic fluids. In this study we consistently use the term helicity for the local form, which is sometimes referred to as the helicity density [Lilly, 1986b]. The helicity plays a role in the relative persistence of supercells and tornadoes. Droegemeier et al. [1993]

found that storms forming in a helical environment are relatively longer lived than storms in an environment without helicity. The reason for this is that the helicity conservation restricts the downward cascade of energy to smaller scales [Betchev, 1961; Lilly, 1986b]. Although the energy cascade might be restricted for 2D turbulence, there are indications that there is a joint energy-helicity cascade for 3D turbulence [Chen et al., 2003]. It is important to take helicity into account, since we are interested in the consistency of the PV dipoles in different synoptic backgrounds. Storm Relative Helicity (SRH), which is defined in terms of storm-relative wind (i.e. the difference between storm motion and total wind velocity), is high for supercells and tornadoes. In case of positive (negative) SRH, the PV dipole will be advected towards the updraft [see e.g. Davies-Jones, 1984; Lilly, 1986b], which would change Fig. 4.1a in the sense that the positive (negative) PV anomaly is located at the position of the diabatic heating.

Chagnon and Gray [2009] investigated briefly how the PV dipoles can organise themselves into bigger structures. There is a tendency of PV to form bands, either related to orography [e.g. Aebischer and Schär, 1998; Schär et al., 2003], or along fronts [e.g. Appenzeller and Davies, 1996]. As already discussed in the introduction, in moderate to high shear flows new cells are most likely to form downshear of old cells due to the lifting by the gust front [Rotunno et al., 1988]. These new updrafts downshear of old cells will themselves induce a PV dipole. Moreover, the dipole induced flow might advect the dipoles downshear [Chagnon and Gray, 2009]. The combination of these two effects may lead to bands of positive and negative PV along the direction of the wind shear (see Fig. 4.2). We will be able to investigate these effects, since for the 22 June case the wind shear is much stronger than that for the 5 June case (see next section).

As discussed in the introduction, full balance cannot be expected for the PV dipoles, since there is always unsteady convection. We might still be able to estimate how balanced the flow is around the dipoles by investigating the stationarity of the flow. If composites from different stages of instationary dipoles give on average a significant anomaly pattern, then we have a quasi stationary picture. Because the flow has a coherent structure we can argue that there is a statistically derived balance. We do know, however, that for steady flow Schär [1993] found that the wind speed can be given in terms of the PV and the gradient of the potential temperature as

$$\mathbf{u}_{st} = \frac{1}{\rho\Pi} \nabla\theta \times \nabla B, \quad (4.2)$$

with  $\mathbf{u}_{st}$  the stationary flow and B the Bernoulli stream function. A stationary flow will therefore be oriented along the surfaces of constant  $\theta$  and B. The Dynamical State Index (DSI) is an index based on this stationary flow [see N vir, 2004], and is given by

$$DSI = \frac{1}{\rho} \nabla\Pi \cdot \nabla\theta \times \nabla B. \quad (4.3)$$

Since the DSI is zero for a stationary flow, we can use the DSI to check if the PV dipoles are (quasi-)stationary. The flow cannot be completely stationary, because there is a diabatic perturbation  $\dot{\theta}$  in between the two PV poles. But if the dipoles

are at least quasi-stationary, there should be in general no DSI perturbation except at the updraft in between the dipoles.

To summarise, we expect that:

- PV dipoles are created around the updraft, orientated in the direction of the horizontal vorticity vector  $\zeta_{ah} = \mathbf{k} \times \mathbf{S}$ . The strength of the PV anomalies, and therefore the corresponding flow anomalies, depends on the diabatic heating anomaly and the background wind shear.
- Directional wind shear (i.e. non-zero helicity) advects the dipole pair towards/away from the updraft: in case of a positive (negative) helical environment, the positive (negative) PV is colocated with the updraft.
- Elongated PV bands form in strong shear environments.
- If the dipoles are quasi-balanced, we only expect DSI anomalies associated with the diabatic heating perturbation (i.e. the convective updraft). Moreover, the kinetic energy anomalies should consistently increase for stronger PV anomalies.

### 4.3 DATA AND METHODOLOGY

#### 4.3.1 *Model and data*

Data is used of the limited-area nonhydrostatic NWP model COSMO-DE [Baldauf et al., 2011] operated by the German Meteorological Service (DWD). See Chapter 3 for a model description.

All data presented in this chapter are from the 5 and 22 June 2011 forecasts initialised at 00 UTC. The overview plots in Section 4.4 are from the reforecasts, all the other plots are based on the COSMO-DE-EPS forecasts. Since the dynamics near the lateral boundaries are largely determined by the boundary forcing, we remove 50 grid points at each lateral boundary (see Fig. 3.1a). PV, helicity and DSI are calculated on model levels using all three wind components with centred differences for the gradients. The calculation of SRH requires the use of storm-relative wind. An estimation is made of the SRH with help of the perturbation velocities, which estimates the storm velocity with the mean environment wind.

#### 4.3.2 *Methodology*

The central aim of this study is to characterise the consistency of PV anomalies associated with deep moist convection. In order to investigate the coherency of the convective PV anomalies and associated flow anomalies, we calculate composites of the PV anomalies associated with storm updrafts. The composites offer an easy and dynamically unbiased way to check whether the PV anomalies and accompanied flow around the dipoles are coherent or not.

For the composites we define storm cells by local maxima in the vertical mean vertical velocity that exceed a certain threshold. To ensure that we select only

deep convective storm cells, we use a threshold of  $5 \text{ ms}^{-1}$  of the vertical mean vertical velocity between model level 31 ( $\approx 3 \text{ km}$ ) and 20 ( $\approx 7.3 \text{ km}$ ). Since the maximum diabatic heating is expected at around 5 km height during deep convection [Houze Jr, 2004; Xie et al., 2014], it is roughly the vertical height at which we expect the largest anomalies of PV. To prevent that we select vertical maxima too close to each other, the maxima have to be separated by at least 3 gridpoints ( $\approx 8 \text{ km}$ ).

All relevant fields are extracted in a  $50 \times 50 \text{ km}$  ( $19 \times 19$  gridpoints) domain around the updraft. Composites are calculated over all updrafts that are detected in all ensemble members during a specific hour, and provide typical structures of PV, wind velocity, DSI, helicity and static stability. Since we are interested in coherent anomalies, we subtract a typical height profile of the respective variable. The height profile is the average over the  $19 \times 19$  gridpoints around each updraft. Composites of wind shear are estimated from the 0 to 6 km wind difference of the horizontal wind velocity (also known as the bulk wind shear). The use of all convective cells that occur in any of the 20 COSMO-DE-EPS members creates a relatively large sample of independent convective cells and should give a good indication of the environment profile associated with the convective cells.

Since we are interested in coherent composite anomalies, it is important to test if they are significant. A standard Student's t-test is used to test if the composite anomalies are significantly different from zero [von Storch and Zwiers, 2001]. Since a quantile-quantile plot indicates that the data are not normally distributed in the tails, a Wilcoxon signed rank test is performed, too [Wilks, 2011]. Both give similar results, as the Student's t-test is quite robust against deviations from the normal distribution for large sample sizes [von Storch and Zwiers, 2001]. Therefore, only the PV, wind velocity, DSI, helicity anomalies for which the Student's t-test can be rejected at the 0.01 significance level are presented in the plots.

#### 4.4 MESOSCALE SITUATION

PV on model level 30 ( $\approx 3 \text{ km}$ ) in the COSMO-DE model is used to get an indication which PV anomalies are associated with convection. On 5 June PV dipoles of large magnitude (i.e. around 10 Potential Vorticity Unit (PVU) on average) are found scattered over the domain (Fig. 4.3a). As expected, they coincide with regions of diabatic perturbations and precipitation (Fig. 4.3b). Most convection forms in the middle of the domain, where Convective Available Potential Energy (CAPE) is highest with local values of about 1000-1500 J/kg (not shown). There is also a weak convergence zone in the middle of the domain which could provide some of the necessary lifting. There are a few larger precipitation areas, but generally convection is scattered over the domain, which is consistent with the measurements during that day (Fig. 3.3a). The PV dipoles are not very consistent in orientation, but there seems to be a slight preference of dipoles along the direction of the large scale flow. The bulk wind shear (from 0 to 6 km) over Germany is quite low, about  $8 \text{ ms}^{-1}$ , which could explain the inconsistent direction of the dipoles. Moreover, the wind direction is not consistent with large

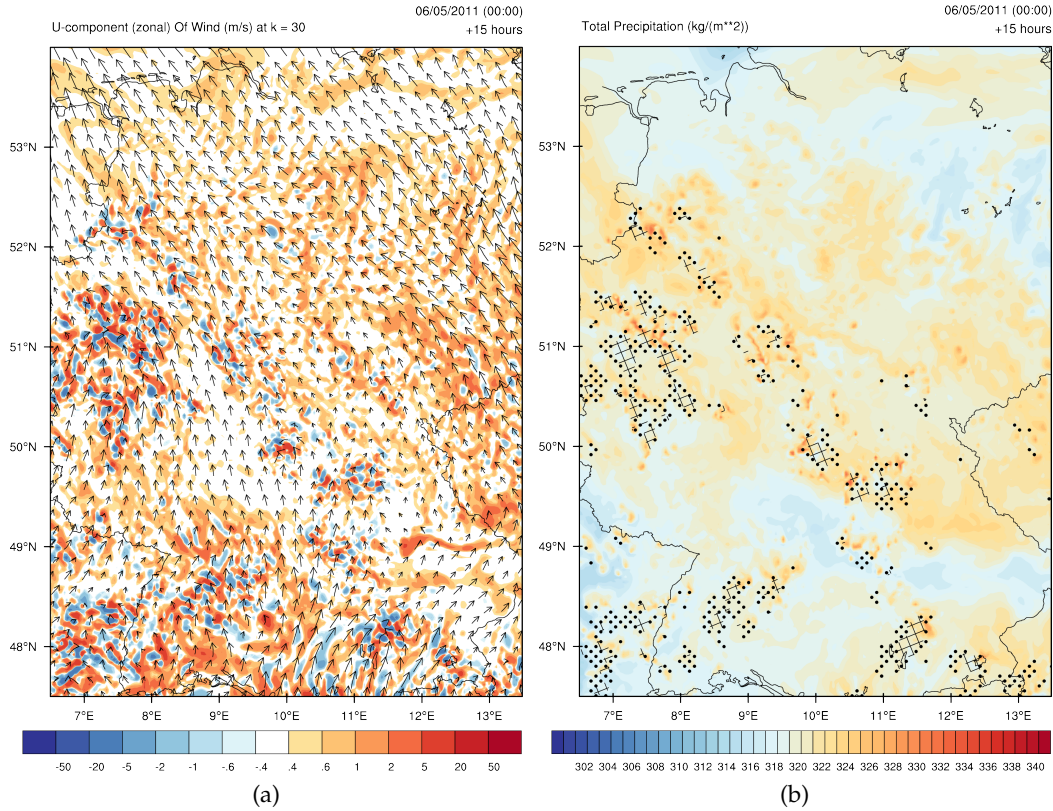


Figure 4.3: (a) PV (contours) and wind flow (arrows). (b) Equivalent potential temperature and precipitation (dots indicate hourly precipitation rates above 0.5 mm, dashed patterns above 5.0 mm in the previous hour). Both plots on 5 June 2011 at 15 UTC at model level 30 (about 3 km).

scale winds from the south-west in Southern Germany and from south-east over the rest of the domain. Besides the dipoles, there are also bands of positive PV in the north-east of Germany, which are weak compared to the strength of the dipoles. These bands are not associated with any precipitation. The PV dipoles extend over a large part of the troposphere (Fig. 4.5a). The PV dipoles maximise in the mid-troposphere at a height of about 5 to 6 km.

For 22 June CAPE is weaker compared to 5 June with values of about 500 J/kg, but the large scale forcing due to the cold front is much larger. On average we observe bulk wind shear of about  $20 \text{ ms}^{-1}$  with local values of up to  $30\text{--}35 \text{ ms}^{-1}$ . The large scale wind shear is orientated in the north-east direction. Along the direction of the large scale wind, bands of positive and negative PV are visible (Fig. 4.4a) mainly along the cold front. Higher up in the troposphere at 7 km height, these PV bands cover a larger region and they seem to be advected in the downshear direction (not shown). The cold front is clearly visible as a potential temperature gradient. Precipitation is generated over a much larger area than on 5 June. There are no PV anomalies west of the frontal system. An explanation could be that the precipitation is caused by shallow convection here. No PV anomalies are expected in the middle troposphere, where the diabatic perturbation is zero for shallow convection. The direction of the PV bands are

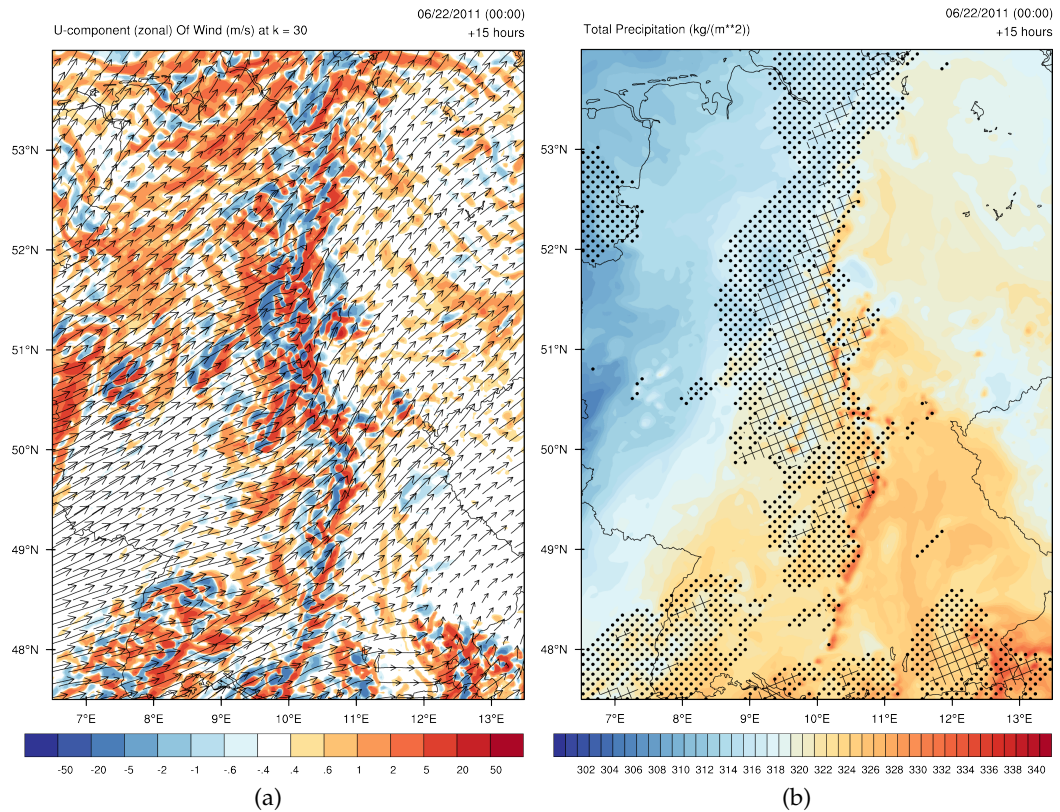


Figure 4.4: (a) PV (contours) and wind flow (arrows). (b) Equivalent potential temperature and precipitation (dots indicate precipitation above 0.5 mm, dashed patterns above 5.0 mm in the previous hour). Both plots on 22 June 2011 at 15 UTC at model level 30 (about 3 km).

mainly orientated along the large scale wind direction (i.e. the gradient of PV is perpendicular to the wind direction). As for the 5 June case, the PV dipoles can be seen over the whole troposphere, up to 12 km height (Fig. 4.5b). Although the storm scale PV anomalies are much larger, one synoptic PV feature is clearly visible: a strong tropopause fold associated with the cold front system is present for the 22 June case (Fig. 4.5b). These folds occur especially in regions with strong wind shear and (surface) temperature gradients [Holton, 2004].

#### 4.5 STORM CELL COMPOSITES

Consistency of flow patterns and anomalies of conserved quantities as PV and H associated with deep convective perturbations is investigated with composites of these fields around storm updrafts. For both days the single time step 15 UTC is chosen when there was deep moist convection over a large part of the domain. The composites at this time step are characteristic for the two weather cases discussed; differences with composites at other time steps at the same days are small. These differences are shortly discussed in Section 4.5.3.

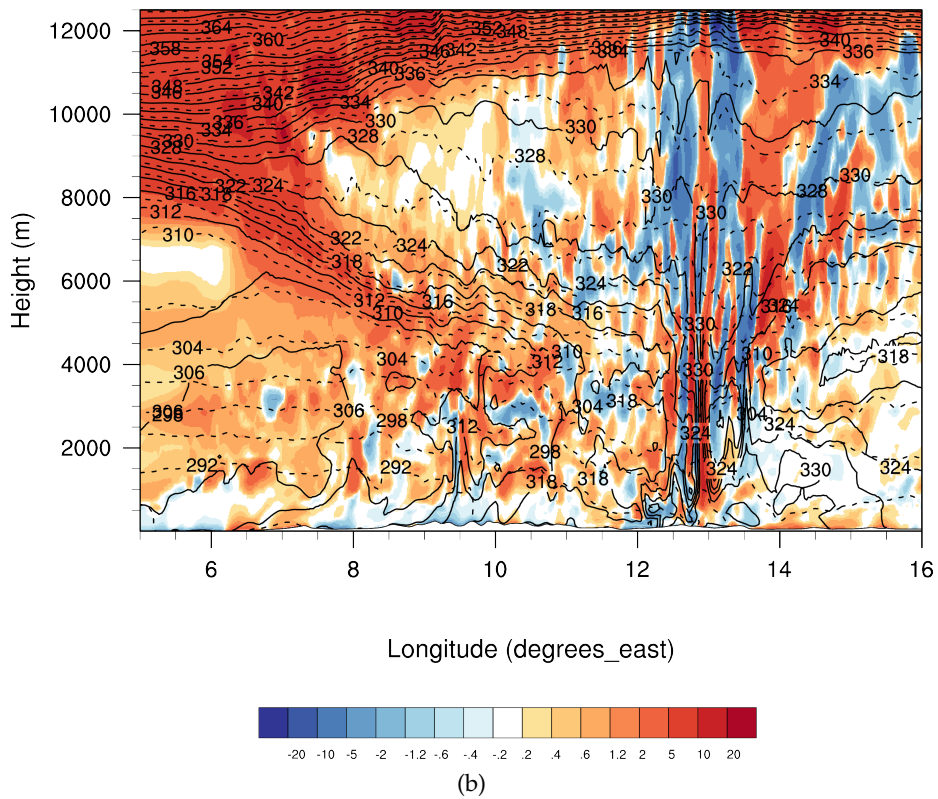
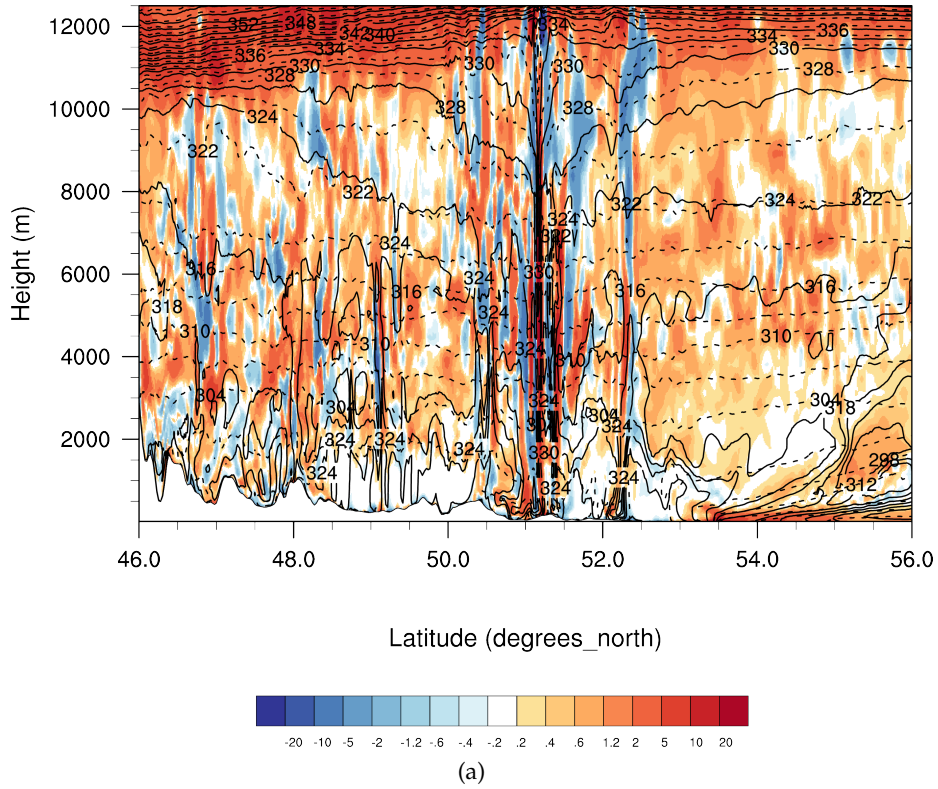


Figure 4.5: Figures (a) and (b) show the PV (contours), the equivalent potential temperature  $\theta_e$  (dashed contour lines) and potential temperature  $\theta$  (solid contour lines) for a longitudinal cross section at  $7^\circ$  E at 5 June 2011 at 15 UTC and a latitudinal cross section at  $52^\circ$  N for 22 June 2011 at 18 UTC.

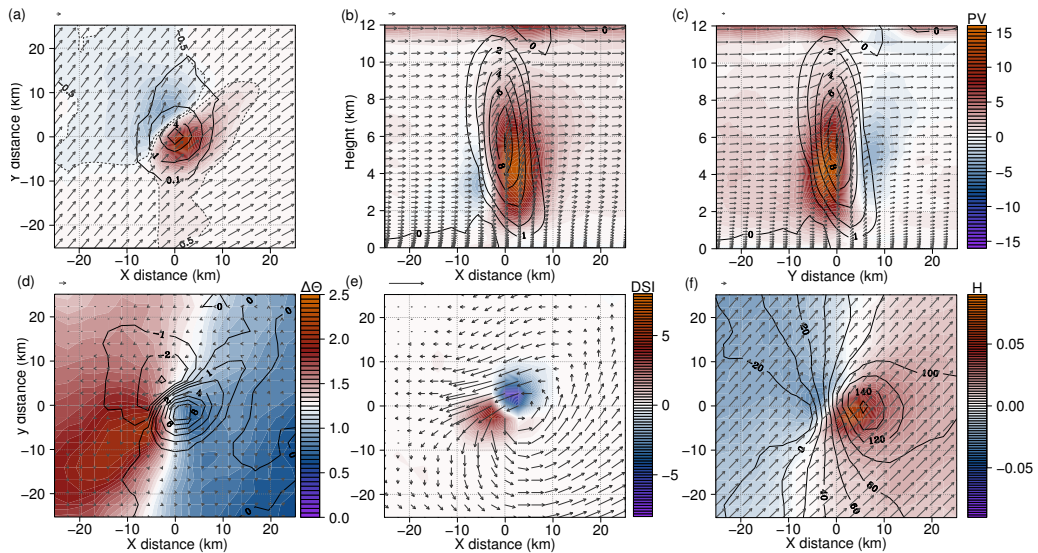


Figure 4.6: Composites for 22 June 2011 at 15 UTC. (a) 3 till 7.3 km height integrated composites of PV (contours, in PVU), vertical velocity (contour lines, in  $\text{ms}^{-1}$ ) and 0-6 km wind difference (arrows). Dashed lines indicate PV contours of -0.5 PVU and 0.5 PVU. (b) Longitudinal cross section at 0 km of (a), with PV (contours, in PVU), vertical wind (black contours, in  $\text{ms}^{-1}$ ) and wind velocity (arrows). (c) as (b), but latitudinal cross sections at 0 km. (d)  $\theta$  difference in the lowest 500 metres (contours, in  $\delta\text{K}$ ), 3-7.3 km height integrated PV (black contours, in PVU) and wind velocity (arrows). (e) 3 till 7.3 km height integrated composites of DSI (contours, in  $\text{PVU}^2 \text{ s}^{-1}$ ) and perturbation wind (arrows). (f) 3 till 7.3 km height integrated composites of helicity  $H$  (contours, in  $\text{ms}^{-2}$ ), 0-3 km SRH (black contour lines) and full wind velocity (arrows). Reference arrow at top of each plot of  $5 \text{ ms}^{-1}$ .

#### 4.5.1 The 22 June case

We discuss the 22 June weather case first because for this situation the composites are clearer. The composite is based on 596 storm cells. First of all, a remarkable dipole pattern in PV is visible and its direction is well in the direction of the wind shear (Fig. 4.6a). The anomalies are significant at the 0.01 significance level. The strength of the PV anomalies is more than 10 times larger than the mean environment values of about 0.5 PVU. The positive anomaly (10.9 PVU) is stronger than the negative anomaly (-4.3 PVU) and the positive anomaly seems to be displaced towards the vertical velocity maximum. The dipoles are elongated along the direction of the wind shear (Fig. 4.6a). The elongated bands mainly appear at the downshear side of the anomalies. At the upshear side the PV anomalies are much smaller. This suggests that advection plays a role here.

Longitudinal and latitudinal cross sections of the composites show that the PV dipoles are visible over a large part of the troposphere with maxima in the middle troposphere just above 5 km (Fig. 4.6b and Fig. 4.6c). The updraft is tilted upshear with height. Rotunno et al. [1988] and Weisman and Rotunno [2004] suggested that this can occur in an environment with a relative strong circulation associated with the cold pool compared to the circulation due to low level wind shear. Also clearly visible is a lowered tropopause defined by the 2

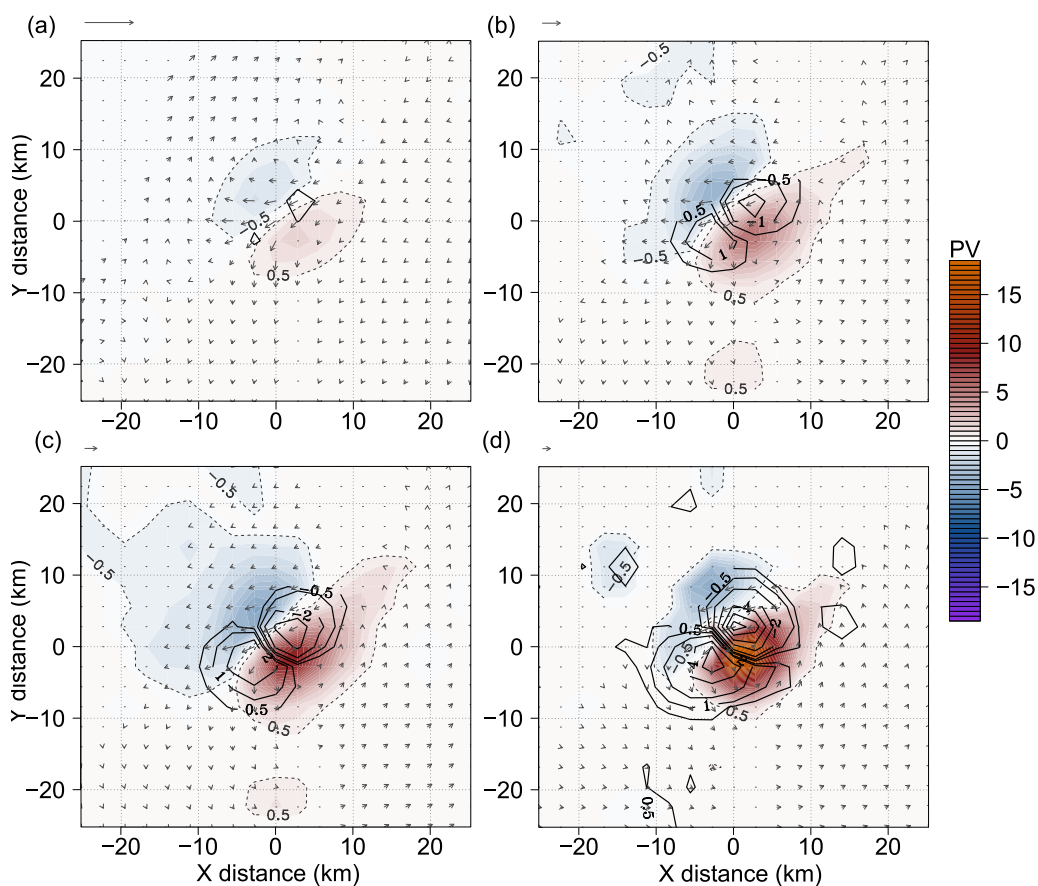


Figure 4.7: 3 Till 7.3 km height integrated composites for 22 June 2011 at 15 UTC of PV (contours, in PVU), DSI (black contour lines, in  $\text{PVU}^2\text{s}^{-1}$ ) and perturbation wind for height averaged vertical velocity threshold of (a) 1 till  $3 \text{ ms}^{-1}$ , (b) 3 till  $5 \text{ ms}^{-1}$ , (c) 5 till  $10 \text{ ms}^{-1}$  and (d) above  $10 \text{ ms}^{-1}$ . Reference arrow at top of each plot of  $5 \text{ ms}^{-1}$ .

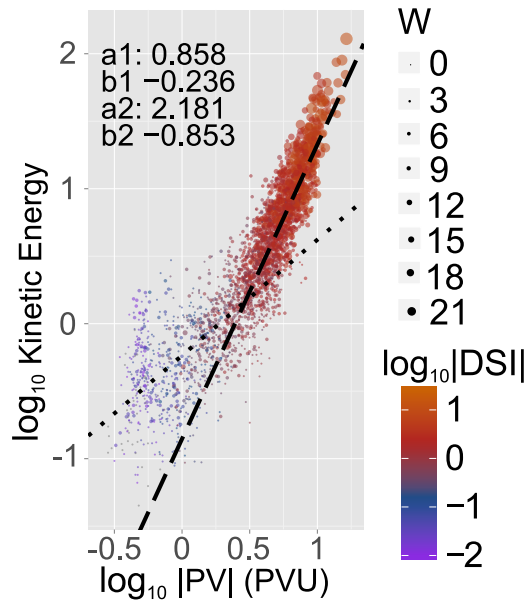


Figure 4.8: 3-7.3 km height averaged  $\log_{10}(|PV|)$  against height averaged  $\log_{10}(U_{kin})$  (in a  $7 \times 7$  grid point domain around updraft) for 22 June 2011 at 15 UTC. Height averaged  $\log_{10}(|DSI|)$  and vertical velocity ( $\text{ms}^{-1}$ ) indicated by dot colour and dot size respectively. Fit of  $\log_{10}(U_{kin}) = a \log_{10}(|PV|) + b$  indicated in plot, for cells with  $\log_{10}(|PV|) < 0.5$  ( $a_1, b_1$ , dotted line) and cells for which  $\log_{10}(|PV|) > 0.5$  ( $a_2, b_2$ , dashed line).

PVU surface above the positive anomaly. The 2 PVU surface is approximately 2 km lower above the positive than above the negative PV anomaly.

Chagnon and Gray [2009] found that the PV dipoles are mainly generated as a dipole in the vertical component of the vorticity vector. This is consistent with Hoskins et al. [1985] who stated that balanced flow around a tall QG PV anomaly tends to appear mainly as an absolute vorticity anomaly and not as a static stability anomaly. Our composites seem to confirm this, since there is a very high relation between the 3 till 7.5 km height integrated PV and the vertical component of the vorticity (not shown). This might indicate that the static stability anomalies are small. To check this, the  $\theta$  difference over the lowest 500 metres is used as an estimate for the static stability below the PV anomalies. PV-thinking predicts a decreased (increased) static stability below a positive (negative) PV anomaly. Indeed, the static stability is lower below the positive anomaly and slightly higher below the negative anomaly (Fig. 4.6d).

The scale effect associated with QG PV inversion states that a small PV anomaly of a given strength has less influence on the flow than a large PV anomaly with the same strength [Hoskins et al., 1985]. So, although the PV anomalies are relatively strong compared to the environmental values, the flow anomalies are expected to be quite small compared to the background flow. The largest anomalies of the perturbed flow are of about  $5 \text{ ms}^{-1}$  (see Fig. 4.6e). These large values appear between the dipoles, where the anticyclonic flow around the negative and cyclonic flow around the positive flow are superimposed (see Fig. 4.1). The cyclonic flow around the positive anomaly is dominant, which is consistent with the much larger magnitude of this PV anomaly.

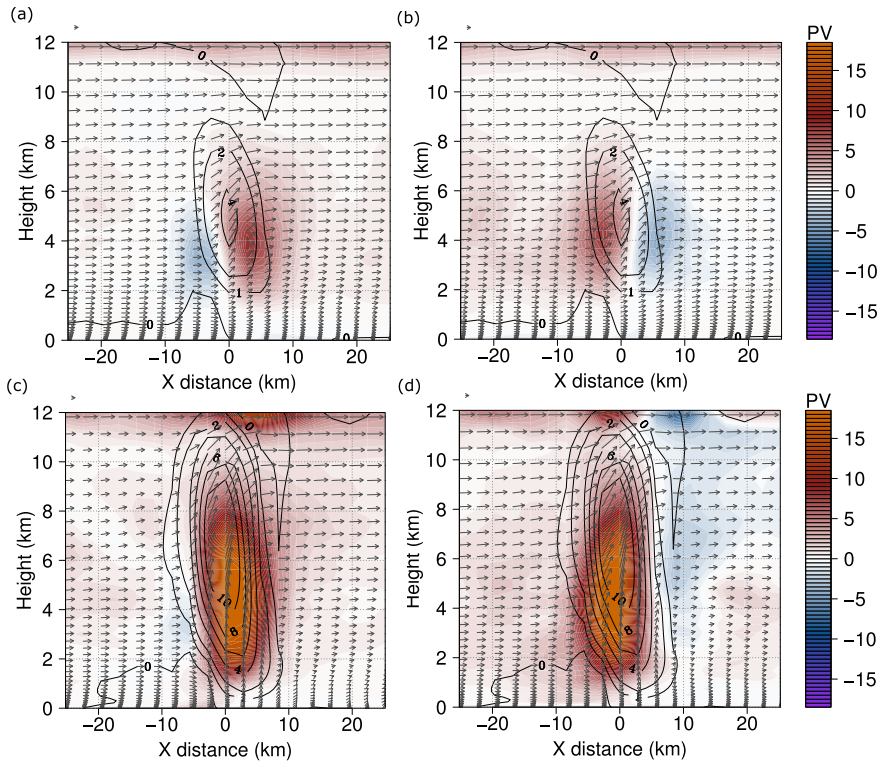


Figure 4.9: (a) Longitudinal cross section for composites using a height average vertical velocity threshold of 3 till 5 ms<sup>-1</sup> for 22 June 2011 at 15 UTC (at 0 km of Fig. 4.7b). PV indicated by contours (in PVU), vertical wind by black contours (in ms<sup>-1</sup>) and wind velocity by arrows. (b) as (a), but latitudinal cross sections at 0 km. (c-d) as (a-b) but for composites with a vertical velocity threshold above 10 ms<sup>-1</sup>.

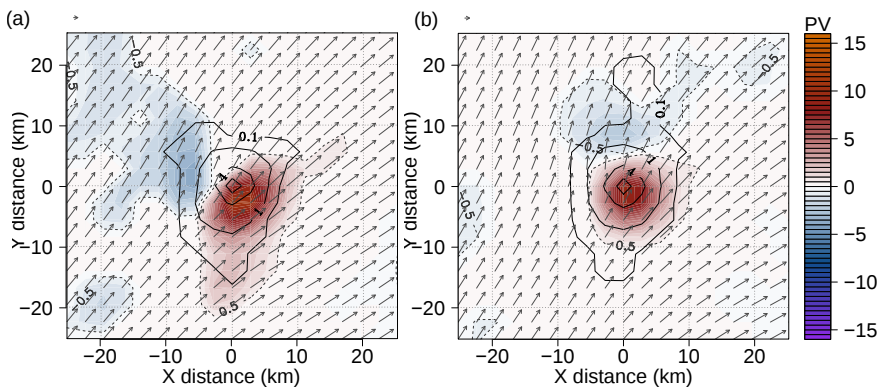


Figure 4.10: (a) 3 till 7.3 km height integrated composites of PV (contours, in PVU), vertical velocity (contour lines, in ms<sup>-1</sup>) and 0-6 km wind difference (arrows) for 22 June 2011 at 11 UTC. (b) Same as (a) but for 22 June 2011 at 18 UTC. Reference arrow at top of each plot indicates a wind speed of 5 ms<sup>-1</sup>.

Other variables show similarly consistent anomalies. For DSI (Fig. 4.6e) there is a dipole pattern with a magnitude of about  $5 \text{ PVU}^2 \text{ s}^{-1}$ , but the dipole is  $90^\circ$  turned with respect to the PV dipoles. The DSI anomalies are proportional to the advection of  $\Pi^2$  [Claußnitzer and Névir, 2009], where positive (negative) DSI indicates negative (positive)  $\Pi^2$  advection. The DSI patterns suggest that there is advection of  $\Pi^2$  downshear of a few  $\text{PVU}^2 \text{ s}^{-1}$ . The DSI anomalies are centred around the updraft and confirm that mainly the updraft region is instationary.

Helicity anomalies also exhibit a dipole pattern with positive helicity located at the positive PV anomaly and negative helicity at the negative PV anomaly (Fig. 4.6f). One source term in the helicity evolution equation is given by  $(\mathbf{k} \times \mathbf{u}) \cdot \nabla b$ , with  $b$  the buoyancy [Lilly, 1986b]. The buoyancy  $b$  is proportional to the diabatic heating  $\dot{\theta}$  and for the 22 June case the large scale wind is in the direction of the large scale wind shear  $\mathbf{S}$ . This explains that the helicity anomalies are co-located with the PV anomalies, since the same term appears in the PV evolution equation. The positive anomaly in Fig. 4.6a seems to be displaced towards the vertical velocity maximum. Davies-Jones [1984] argued that if the environment has positive SRH, the updraft is advected towards the anticyclonic vorticity pole. For the environment SRH we estimate the storm motion by subtracting the 0 to 6 km mean wind velocity, assuming that the updraft moves with the height integrated velocity. The positive SRH anomaly (Fig. 4.6f) is consistent with the hypothesis of Davies-Jones [1984] that the positive pole is advected towards the updraft in case of positive environment SRH.

#### 4.5.2 Different vertical velocity thresholds

In the previous section, the composites were made by selecting updrafts with a vertical velocity of at least  $5 \text{ ms}^{-1}$ . The strength of the PV anomalies is not only related to the strength of the wind shear, but also depends on the strength of the diabatic anomaly and therefore on the vertical wind velocity. Figure 4.7 shows the composites for 4 different thresholds of the vertical wind velocity for 22 June 2011. The PV, DSI, and wind flow anomalies all consistently intensify with increasing thresholds (Fig. 4.7a-d). When we change the threshold from  $1\text{-}3 \text{ ms}^{-1}$  (Fig. 4.7a) to  $5\text{-}10 \text{ ms}^{-1}$  (Fig. 4.7c) the PV and DSI anomalies increase by a factor of 5. The PV composites with a threshold of  $10 \text{ ms}^{-1}$  have a PV maximum of more than 18 PVU and a wind perturbation maximum of about  $8 \text{ ms}^{-1}$  (Fig. 4.7d). There are small qualitative differences between the composites using different thresholds. The dipole asymmetry (i.e. stronger positive pole) is more pronounced for increased thresholds.

For both cases there is a correlation between the height averaged absolute value of PV and kinetic energy anomalies (Fig. 4.8). A linear regression is calculated over all the storm cells of the form  $\log_{10}(U_{\text{kin}}) = a \log_{10}(|\Pi|) + b$ , with  $U_{\text{kin}}$  the kinetic energy and  $|\Pi|$  the PV, both spatially and height averaged (see line in Fig. 4.8). Since  $a$  is approximately equal to 2, the increase of kinetic energy associated with PV anomalies is approximately quadratic. The explained variance for the fits in Fig. 4.8 is approximately 85%. This confirms the consistency of the flow anomalies around the PV dipoles. An exception are low

Time step	Number of cells	Max PV (5%/mean/95%)	Min PV (5%/mean/95%)	Correlation W and PV
11	132	3.77/15.53/34.50	-28.11/-13.11/-3.43	0.43
12	253	5.98/16.48/30.64	-26.93/-13.20/-4.11	0.36
13	399	6.53/16.43/29.58	-23.30/-13.12/-4.49	0.45
14	549	7.48/16.63/32.34	-24.48/-13.76/-5.20	0.45
15	596	6.95/17.48/35.37	-22.87/-13.08/-5.42	0.49
16	613	6.68/17.10/32.84	-25.38/-12.82/-4.58	0.50
17	552	6.08/16.82/35.04	-22.54/-11.97/-4.04	0.52
18	454	5.66/15.61/31.21	-22.23/-10.95/-4.28	0.57
19	390	5.68/15.78/30.57	-21.83/-11.22/-4.25	0.54

Table 4.1: Storm cell characteristics on 22 June 2011, calculated over all storm updrafts for all ensemble members. Maximum and minimum PV (in PVU) are searched in a 3x3 grid point surroundings of the vertical velocity maximum. The correlation coefficient between W and PV is calculated with Eq. 4.4, following Davies-Jones [1984].

magnitude PV storm cells on 22 June, which have a much broader variation in kinetic energy. These have quite low vertical velocity and are therefore probably not always related to storm cells. There is also a consistent increase of |DSI| and vertical velocity with the perturbation PV (Fig. 4.8).

The longitudinal and latitudinal cross sections also show a higher correlation between vertical velocity and the PV, as shown in Fig. 4.9 for the 22 June case. For the 1-3 ms<sup>-1</sup> composites, the positive PV anomaly is slightly stronger than the negative PV anomaly, and the updraft is almost centred in the middle. For the strong updraft composites, however, the positive PV anomaly is much stronger and the negative PV anomaly almost nonexistent (Fig. 4.9c-d).

#### 4.5.3 Composites at other time steps

The composites in the previous sections were made at one specific forecast hour, 15 UTC. The composites of the investigated fields are very similar for other time steps, as seen in Fig. 4.10 for 11 UTC and 18 UTC. There are no large changes in strength of the PV anomalies or other quantities. As mentioned in Section 4.2, the updraft can be collocated with either the positive or negative PV anomaly. We measure this with a correlation coefficient  $r$ .  $r$  in Table 4.1 between PV and the vertical velocity is calculated in a similar way as in Davies-Jones [1984]

$$r = \frac{\langle \Pi w \rangle}{(\langle \Pi^2 \rangle \langle w^2 \rangle)^{1/2}}, \quad (4.4)$$

where angular brackets denote a height integral (from 3 to 7.5 km, in a 3x3 grid point surrounding of the updraft). There are some qualitative differences, since at 18 UTC the PV dipole is orientated along the longitudinal axes (Fig. 4.10c). The bands of PV become less clear and change their orientation slightly clockwise when compared to the direction of the wind shear. The change of orientation could be due to a change of the wind direction at the back side of the front (Fig. 4.4a). However, the wind shear does not change in direction with time

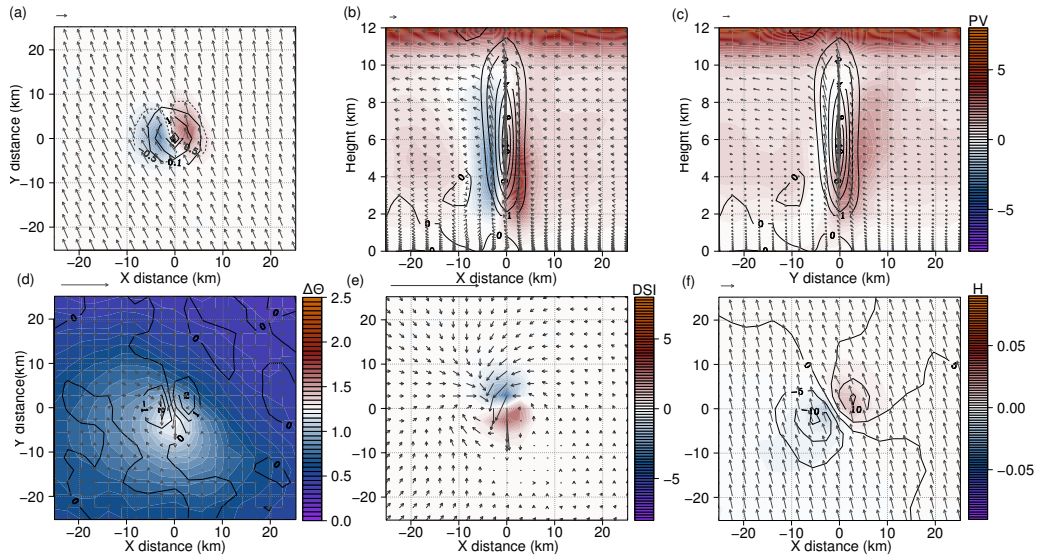


Figure 4.11: As in Fig. 4.6, but on 5 June 2011 at 15 UTC.

(compare Fig. 4.10a and b). This suggests that other factors play a role in the change of the orientation of the PV dipole. The correlation between the vertical velocity maximum and the positive PV anomaly slightly increases in the afternoon (Fig. 4.10b and Table 4.1).

#### 4.5.4 The 5 June case

The orientation of the dipole in the composites on 5 June 2011 is again consistent with the general wind shear direction (Fig. 4.11a). For this case, the composites are taken over 1421 convective cells. As expected by the lower wind shear ( $8 \text{ ms}^{-1}$  wind difference between 0 and 6 km compared to  $20 \text{ ms}^{-1}$  for 22 June), the magnitude of the PV anomalies is weaker (about 4 PVU for both poles). The direction of the dipole is consistent with the northwestward direction of the wind shear (Fig. 4.3a). There is no asymmetry; the PV dipole is centred around the updraft and the magnitude of the positive and negative anomalies are equal. Another difference is that the anomalies on 5 June are much more localised around the updraft; no elongated bands of PV are visible. Compared to the 22 June composite, the updraft is more upright (Fig. 4.11b and c). There is, however, a slight tilt of the PV dipole with height; the negative anomaly is slightly higher than the positive PV anomaly. This is consistent with the schematic picture in Fig. 4.1b. Static stability anomalies are smaller than for the 22 June case (Fig. 4.11d), but still consistent with the anomalies depicted in Fig. 4.1b. The largest flow anomalies are of a few  $\text{ms}^{-1}$  on 5 June (Fig. 4.11e). The DSI dipole is again shifted  $90^\circ$  counterclockwise. Helicity anomalies are much smaller compared to 22 June (Fig. 4.11f), which is consistent with the more unidirectional background wind shear for this case. This is also confirmed by the much lower values for the 0 to 3 km SRH.

On 5 June there is a similar increase of PV and DSI anomalies with increasing threshold (Fig. 4.12a-d), though the qualitative differences between the com-

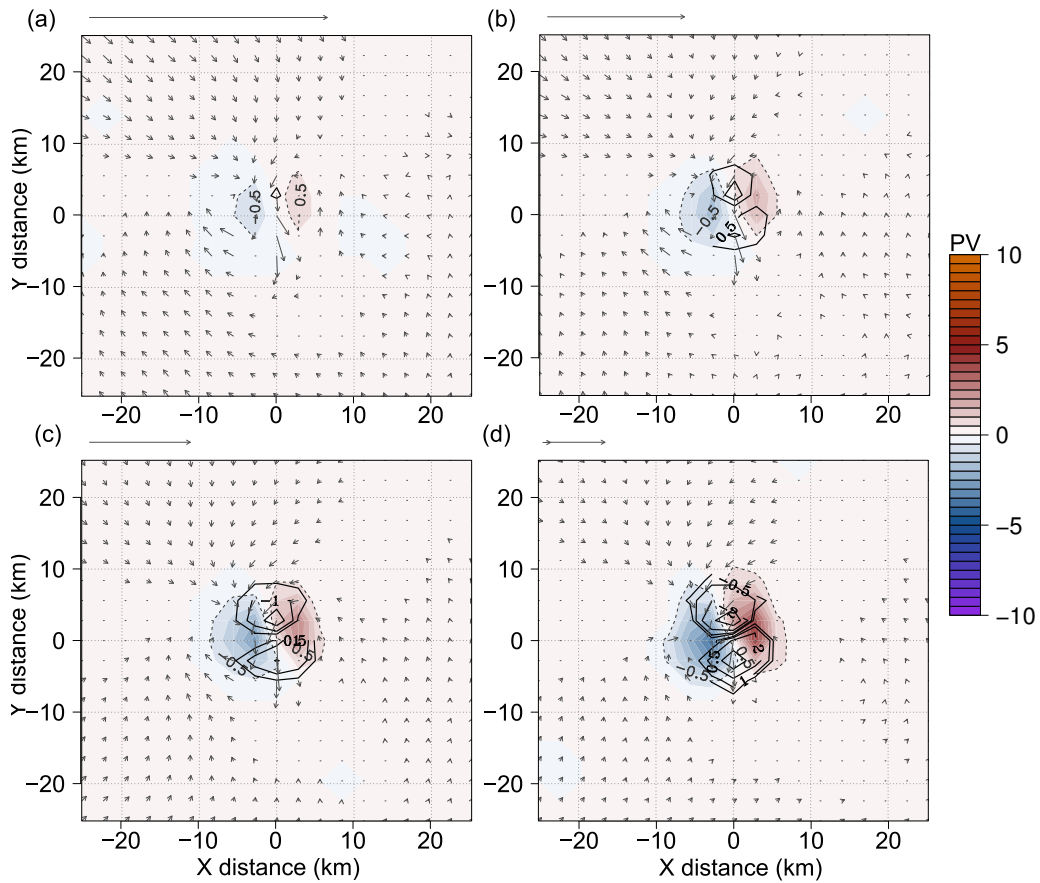


Figure 4.12: As in Fig. 4.7, but on 5 June 2011 at 15 UTC.

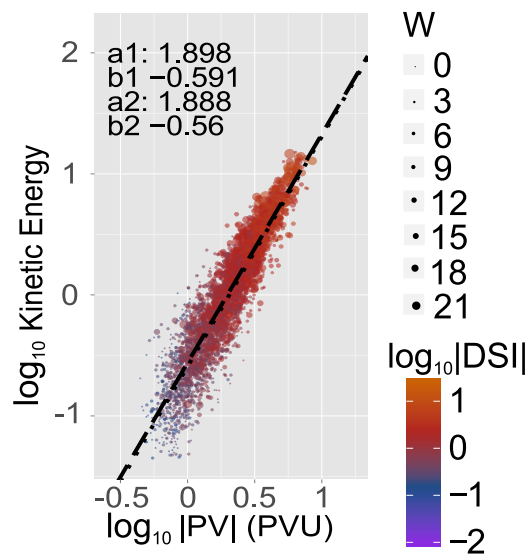


Figure 4.13: As in Fig. 4.8, but on 5 June 2011 at 15 UTC.

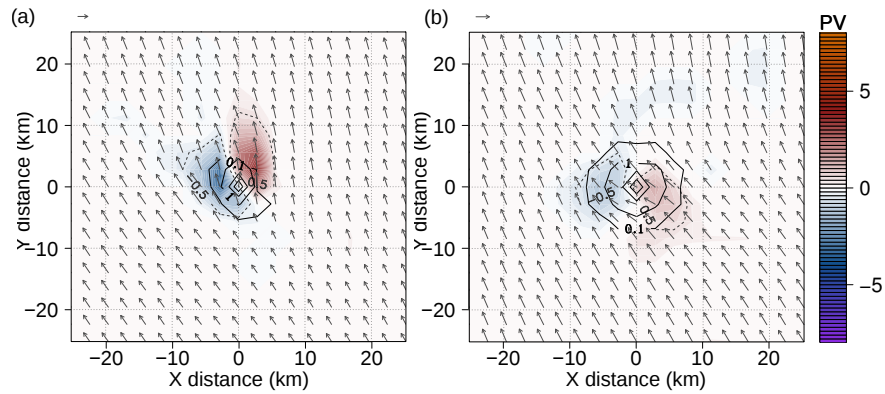


Figure 4.14: As in Fig. 4.10, but on 5 June 2011.

Time step	Number of cells	Max PV (5%/mean/95%)	Min PV (5%/mean/95%)	Correlation W and PV
11	389	1.53/5.69/12.33	-12.58/-5.72/-1.53	0.02
12	807	1.36/5.59/12.25	-12.53/-5.91/-1.52	0.04
13	1225	1.74/6.75/14.16	-14.69/-6.97/-1.81	0.06
14	1479	1.94/7.29/15.72	-14.64/-7.23/-2.00	0.07
15	1421	1.97/7.87/17.29	-16.00/-7.76/-2.11	0.08
16	1245	1.85/8.40/19.02	-17.00/-7.81/-1.92	0.12
17	966	1.74/8.31/18.31	-16.37/-7.61/-1.88	0.13
18	653	1.80/8.24/18.56	-16.35/-7.65/-1.95	0.12
19	528	2.01/8.11/18.20	-16.62/-7.25/-2.09	0.13

Table 4.2: As Table 4.1, but for 5 June 2011.

posites using different thresholds are not that high. For this case the dipole stays centred around the updraft for higher updraft strength, and the strength of the negative and positive anomaly is approximately equal. Again, there is a quadratic increase of kinetic energy with increasing strength of the PV dipoles (Fig. 4.13). The main difference between the longitudinal and latitudinal cross section composites for the different thresholds is that the magnitude of the anomalies of all variables increases (not shown).

At other time steps the composites look similar (Fig. 4.14 and Table 4.2). The composite at 11 UTC (Fig. 4.14a) seems to be advected downshear. As indicated by the correlation coefficient  $r$  in Table 4.2 the updraft stays centred between the dipoles at all times. At later time steps, from 18 UTC onwards, the composites for the 5 June case get less consistent (Fig. 4.14b). For these forecast hours the large scale wind shear is less consistent, too, which explains the more variable direction of the PV dipoles.

#### 4.6 SUMMARY AND DISCUSSION

The main goal of the chapter was to describe the consistency of PV dipoles, theoretically described by Chagnon and Gray [2009], associated with convective cells in a convection permitting weather model. Therefore, PV anomalies on

the convective weather scale in a convection permitting model COSMO-DE have been analysed. We posed that PV anomalies can organise themselves in elongated bands of positive and negative PV, with a direction dependent on large scale wind shear.

In this chapter, all fields, independent how far the storm cell was in his evolution, are averaged in a single composite. In the next chapter, we will investigate the balanced structure of PV dipoles further by tracking individual cells for the two cases. Clustering on storm environment like wind shear, CAPE, helicity and/or storm characteristics could tell more about differences in storm characteristics in different environments. It is especially interesting to look at the most intense convective cells as the composites for the two cases discussed in this chapter suggests that the morphology of the PV dipoles can change with cell intensity.



## EVOLUTION OF STORM CELLS

---

*Central aim of this chapter is to determine the coherent evolution associated with storm cells for the 5 and 22 June weather cases. The coherent structure is determined by tracking storm cells for different days which showed (severe) convection. The tracking algorithm used is described and the choices made in the design of the algorithm are explained. This chapter discusses differences between the evolution of convective cells for the two weather cases, as well as the differences between normal and intense cells. Furthermore, precipitation composites associated will be analysed. Lastly, a vorticity budget will be used to investigate the difference between normal and intense cells.*

### 5.1 AIMS AND MOTIVATIONS

Composites using the Ensemble Prediction System (EPS) forecast data of the COSMO-DE Numerical Weather Prediction (NWP) for 5 and 22 June 2011 have shown that there is a consistent Potential Vorticity (PV) dipole associated with a convective updraft (Chapter 4). For the 22 June weather case, there is a clear correlation between the convective updraft and the positive pole of the PV dipole. It has been proposed that this is due to high Storm Relative Helicity (SRH), and that these storms are particularly intense and persistent. Disadvantage of the composites using the hourly EPS data is that the evolution of the storm cells is not taken into account. They include storm cells in all life stages. Composites of the storm cell evolution might indicate how and why we see this evolution particularly for the more intense storms.

As stated in Chapter 2, there is a lot of research on storm dynamics, but this research focuses mainly on idealised case studies. These studies investigate often only a few “ideal” convective cells. Moreover, such studies tend to be positively biased towards more intense storm cells, since they focus on severe convection like supercells. Furthermore, the focus is often on the United States, where the synoptic and mesoscale environment is different compared to West-Europe. Most studies focus on vorticity dynamics and not on PV dynamics.

The main goal of this chapter is to characterise the evolution of storm cells using PV for the two 5 and 22 June 2011 weather cases discussed in Chapter 4. Convective cells in the COSMO-DE model are tracked for these two cases. The tracking algorithm will be introduced and its performance will be shortly discussed. The evolution of storm cells for 5 and 22 June will be described. In Chapter 6, we will generate a composite over all 9 severe weather cases, and we will focus on the differences between intense and “normal” convective cells.

Research questions to be answered are:

- Q1 Does a coherent evolution of storm cells exist for the 5 and 22 June severe weather cases?

Q2 What are the main differences in storm cell evolution between these two severe weather cases?

Q3 Do the extreme cells during 5 and 22 June 2011 have significant different characteristics?

## 5.2 METHODOLOGY

To determine the coherent evolution of the storm cells, we make composites of the evolution of a typical storm cell. To accomplish this, we track storm cells for the severe weather cases discussed in Chapter 4. Similar approaches have been used to characterise the typical evolution of cyclones in global NWP models [e.g. Murray and Simmonds, 1991; Zhang et al., 2004; Pinto et al., 2005; Rudeva and Gulev, 2007; Dacre and Gray, 2009], to track jet stream features [Limbach et al., 2012], to track mesoscale convective systems [Arnaud et al., 1992], and to track convective cells using radar data [e.g. Dixon and Wiener, 1993; Johnson et al., 1998; Han et al., 2009; Kyznarová and Novák, 2009; Moseley et al., 2013; Stein et al., 2015]. On the convective weather scale using model data, tracking is a less used technique, although it recently got more attentions [Plant, 2008; Caine et al., 2013; Clark and Bullock, 2014; Moseley and Hohenegger, 2015; Stein et al., 2015].

### 5.2.1 *Choice of tracking on the vertical velocity*

Most of the convection-tracking based studies focus on tracking precipitation areas, and/or simulated radar reflectivity rates. Since we are interested in PV anomalies associated with storm updrafts, we have to track a variable which is related to the updraft more directly. We choose to track the vertical velocity  $w$  in the mid troposphere. It is justifiable to use  $w$  instead of PV, since all PV dipoles will have a diabatic origin and will therefore be associated with a vertical velocity anomaly. Although PV might seem the most logical and worthwhile variable to track, since it is the variable directly tied to the balanced structure of the storm, there are several advantages on tracking the vertical velocity instead of PV:

- Tracking using the vertical velocity is cleaner in the sense that less splitting and merging occurs for  $w$  anomalies compared to PV anomalies.
- PV is a consequence of the diabatic anomalies associated with convection. Therefore, the vertical velocity anomaly will intensify first, before the PV anomalies will arise. Hence, it is easier to follow the intensification process of the PV dipole.
- It is easier to identify a PV dipole associated with a storm cell using tracks of  $w$ : During the intensification period of  $w$  the PV dipole will be centred across the updraft and therefore better identifiable. Often PV dipoles are close to each other and it is therefore difficult to assign a PV anomaly to a certain vertical velocity perturbation. Moreover, often either the positive or the negative PV anomaly is dominating.

Disadvantage is that one cannot follow the PV dipoles anymore after the updraft has vanished. Since they are tilted in the vertical, they might survive for a significant time after the original updraft has died out [Chagnon and Gray, 2009]. It is therefore still useful to track PV, at least for cases for which this is possible (e.g. the cases which do not show any splitting/merging).

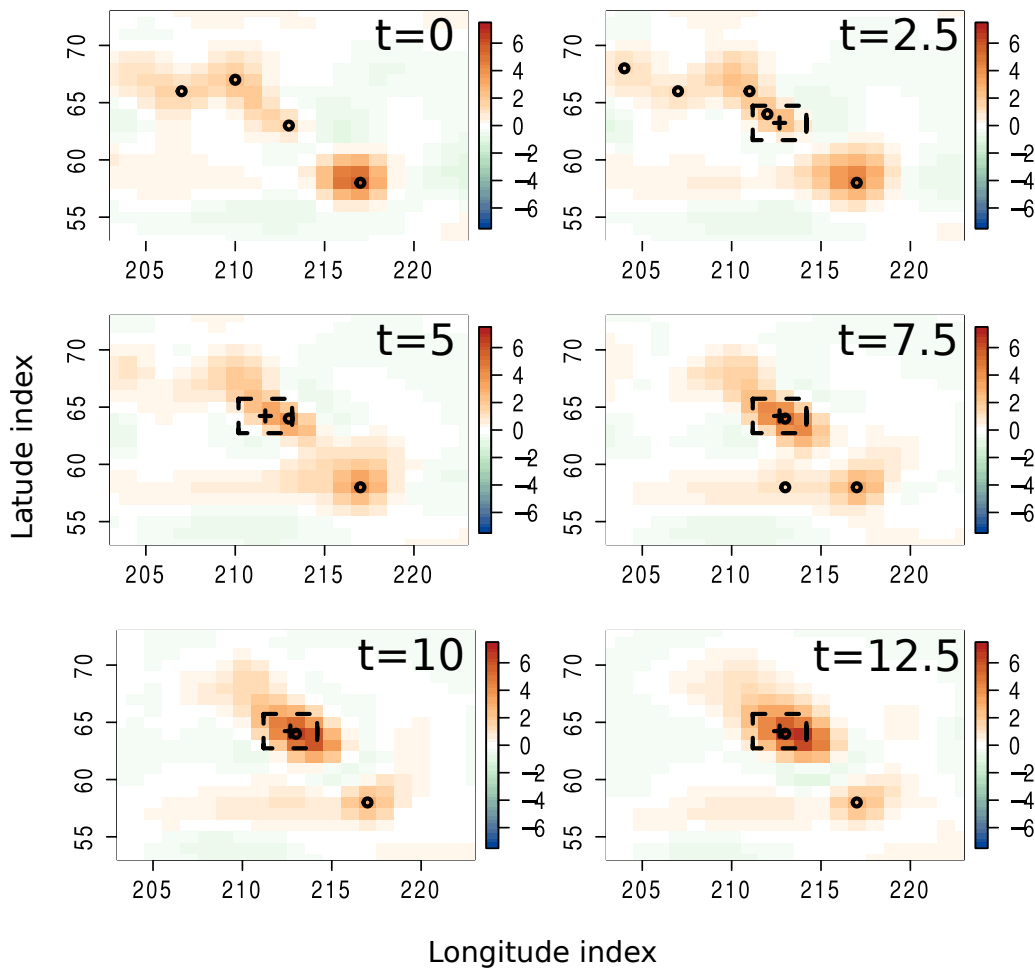


Figure 5.1: Schematic of tracking algorithm. For each time step (indicated in the upper right of each panel), the Gaussian filtered vertical velocity is plotted (coloured contours, in  $\text{ms}^{-1}$ ). For every 2.5 minutes, the maxima of the vertical Gaussian filtered velocity are determined (o in plots). For each maximum, the next location is predicted (+, only shown for one maximum here, details see text). If there is a new maximum at the next time step within a box of  $\pm 2$  grid points (-) from the predicted location (+), the respective maxima are connected in a track.

### 5.2.2 Tracking methodology

To reduce noise in the vertical velocity field, the vertical velocity  $w$  at level 23 ( $\approx 5.8$  km) is Gaussian filtered, i.e. we convolve the vertical velocity  $w$  with the Gaussian  $g(x, y)$ ,

$$g(x, y) = \frac{1}{2\sigma^2} e^{-\frac{x^2+y^2}{2\sigma^2}}, \quad (5.1)$$

where  $x, y$  denote the distance of the origin (i.e. the point at which the Gaussian filter is applied). We choose a standard deviation  $\sigma$  of 1 grid point, and we calculate the Gaussian convolution only in a 5x5 grid point environment. In this environment,  $g(x, y)$  is normalised, so that the sum of  $g(x, y)$  is equal to one.

The reason we select one level in the upper troposphere is that we only want to select the deep convective cells. As shown in Chapter 4, 5.5 to 6 km is about the height where we expect maximum PV anomalies. We determine maxima of  $w$  every 2.5 minutes, i.e. we calculate local maxima of the Gaussian filtered  $w$  above  $1 \text{ ms}^{-1}$  for every time step (see Fig. 5.1). For each of these maxima, its next location is predicted using an environment wind. It is assumed that the storm moves with this environment wind, which is calculated in a 19x19 grid point environment of the updraft. If there is a maximum in the neighbourhood of the predicted maximum (i.e. within  $\pm 2$  grid points of the predicted maximum, see Fig. 5.1), the two maxima are connected. If there are multiple maxima in the vicinity of the updraft, the track is tagged as problematic and results are not used. During the tracking, the variables (PV,  $u$  etc.) are saved in a 31x31 grid point environment of the maximum Gaussian filtered velocity. Only tracks which last at least 30 minutes are saved.

The time step we use in tracking, 2.5 minutes, is about the minimum temporal resolution that shows changes between time steps (6 times temporal resolution in model). The tracking method is relatively simple, an advantage is that determining composites will be easier compared with more advanced object bases tracking algorithms. The temporal resolution should be small enough to capture all changes. Assuming a horizontal speed of the updraft of  $30 \text{ ms}^{-1}$ , the maximum movement expected of an updraft in 2.5 minutes is 4.5 km (1.5 grid points)<sup>5</sup>. Fig. 5.1 shows that 2.5 minutes is a reasonable choice. There is quite a lot variation between the 0 and 10 minutes time step. There are 4 maxima in the 0 minute time step, but only 2 at the 10 minute time step. It would be difficult to connect the maxima with each other between these two time steps. One could argue that 5 minutes might be enough, but we choose 2.5 minutes to be sure that there are no missings.

### 5.2.3 Compositing

We want to derive a composite which characterises a typical storm cell. However, the duration of the different storm cells differs considerably. Therefore, we centre the composites around the maximum vertical Gaussian filtered velocity. This will be defined at the “0” time step. Secondly, we exclude storm cells which have

<sup>5</sup> The maximum storm speed (averaged over storm lifetime) over all 9 cases is  $32 \text{ ms}^{-1}$

more than one maximum in their evolution. Although this is a considerable fraction of the cells (about  $1/3$ ), we want to make sure that before the “o” time step the cell intensifies and that the decay phase starts after the “o” time step. As in Chapter 4 we calculate the 3 till 7.3 km height integrated composites.

For every storm cell, environmental characteristics like CAPE, Convective Inhibition (CIN), Lifted Index (LI), Showalter Index (SI), SRH and bulk shear are calculated (Table 5.1). For SRH, we use for every convective cell its average storm speed  $c$  during its lifetime. The goal is to calculate the environmental characteristics for each storm cell, but especially the buoyancy and instability indices are largely influenced by the storm cell itself. For example, convection stabilises the atmosphere, therefore CAPE will be reduced during convection. To avoid this influence of the storm cell, we calculate the storm environmental properties in a  $31 \times 31$  grid point environment 30 to 15 minutes before the tracking starts. The exact time step varies per convective cell, because the data of environmental parameters like CAPE is only available at a 15 minute temporal resolution (see Section 3.1.4).

Besides the storm environment properties, we calculate characteristics of storm cell like maximum and minimum PV, and their starting location of tracking (see Table 5.2). Moreover, we want to investigate how the PV anomalies differ for “extreme” cells. Therefore the model precipitation rates and wind gust (as measured by  $V_{\text{gust}}$ ) are determined around the maximum Gaussian filtered vertical velocity. These model precipitation rates are determined in a 15 minute time frame at the Gaussian filtered vertical velocity. Likewise, the wind gust is determined at the time step closest to the maximum Gaussian filtered vertical velocity.

As for the composites in Chapter 4, only the results which are significant against the zero hypothesis that the anomalies are zero are plotted. Both a Student’s t-test and a recurrence analysis after von Storch and Zwiers [1988] are used. Only the PV and wind velocity anomalies for which the Student’s t-test can be rejected at the 0.01 significance level are presented in the plots. For the recurrence analysis, the maximum p-recurrence at which the null hypothesis can be rejected at the 0.05 significance level is calculated. A Student’s t-test measures only significant differences in the mean, but this test does not tell how large this difference is. The p-recurrence is a measure of how large the difference in means is, 69% (84%) p-recurrent implies that the experiment ensemble and a control ensemble are separated by 1.0 (2.0) standard deviations (see Fig. 5.2, or for more details [von Storch and Zwiers, 1988]). In our case we test how much the PV anomalies are separated from a hypothetical control ensemble, centred around 0, with the same variance as the PV distribution. The Student’s t-test as well the p-recurrence are calculated at every grid point of a composite, with as sample all the storm cells contributing to the composite at that location and time.

Variable	Definition	Remarks
INSTABILITY PARAMETERS		
CAPE	Convective Available Potential Energy, see Eq. 2.11.	Convective Available Potential Energy (CAPE) and the other instability parameters are calculated with an air parcel with thermodynamic properties of the lowest 50 hPa of the Planetary Boundary Layer (PBL).
CAPE <sub>3km</sub>	CAPE calculated with an air parcel with thermodynamical properties of the lowest 50 hPa of the atmosphere, up to an ascent of 3 km above the surface	Measure of CAPE in the lower troposphere.
CIN	Convective Inhibition, see Eq. 2.13.	
SI	Showalter Index, see Eq. 2.19	
LI	Lifted Index, see Eq. 2.19	
LFC	Level of Free Convection	
LCL	Lifted Condensation Level	
SHEAR PARAMETERS		
SRH <sub>0-1km</sub>	Storm Relative Helicity, integrated from 0 to 1 km height, see Eq. 2.17.	The storm motion $c$ is estimated from the average storm motion over the whole lifetime.
SRH <sub>0-3km</sub>	Storm Relative Helicity, integrated from 0 to 3 km height, see Eq. 2.17.	The storm motion $c$ is estimated from the average storm motion over the whole lifetime.
Bulk wind shear	The magnitude of the wind velocity difference between 6 km and 0 km height.	Wind velocities at model level 23 ( $\approx 5.8$ km) and at 2 metres are used.
Low wind shear	The magnitude of the wind velocity difference in the lowest 10 model levels (approximately lowest 700 metres).	Wind velocities at model level 41 ( $\approx 0.7$ km) and at 2 metres are used.
MOISTURE PARAMETERS		
RH	Relative Humidity, the quotient of the water vapour mixing ratio $r$ and saturation water vapour mixing $r_{vs}$ .	
HDIV	Vertically integrated divergence of specific humidity $q_v$ .	

Table 5.1: Storm cell environment variables. All variables are calculated from the mean value in a  $31 \times 31$  grid point environmental around the storm updraft, 15 to 0 minutes before the maximum Gaussian filtered vertical velocity.

Variable	Definition
Max. Intensity	Maximum Gaussian filtered vertical velocity (in $\text{ms}^{-1}$ ), during lifetime of storm cell.
w maximum	Maximum vertical velocity (in $\text{ms}^{-1}$ ), during lifetime of storm cell.
PV maximum	Maximum PV anomaly (in Potential Vorticity Unit (PVU)) in a $5 \times 5$ grid point environment of the updraft, during its whole lifetime.
PV minimum	Minimum PV anomaly (in PVU) in a $5 \times 5$ grid point environment of the updraft, during its whole lifetime.
Duration	Duration (in minutes) of updraft.
Speed	Average horizontal movement of cell (in $\text{ms}^{-1}$ ).
Correlation r	Correlation coefficient r, see Eq. 4.4, measures how much the maximum PV anomaly and the updraft are collocated.
Location	Longitude and latitude of grid point at maximum Gaussian filtered vertical velocity.
Precipitation rate	Precipitation rates (in mm/hour), averaged over a $11 \times 11$ grid point environment of the updraft.
Wind gust	Wind gusts (in $\text{ms}^{-1}$ ), using $V_{\text{gust}}$ , averaged over a $11 \times 11$ grid point environment of the updraft.

Table 5.2: Storm cell property variables.

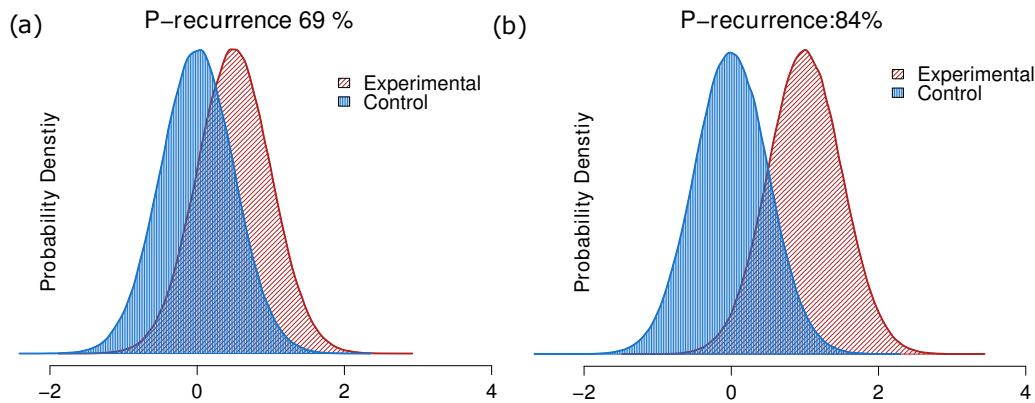


Figure 5.2: Schematic overview of p-recurrence, after von Storch and Zwiers [1988], (a) an experimental distribution which is 69% p-recurrent (1  $\sigma$  separation in the means), and (b), an experimental distribution which is 84% p-recurrent (2  $\sigma$  separation in the means). Here, the control and experimental ensemble are assumed to be Gaussian, with same variance. See for further details, von Storch and Zwiers [1988].

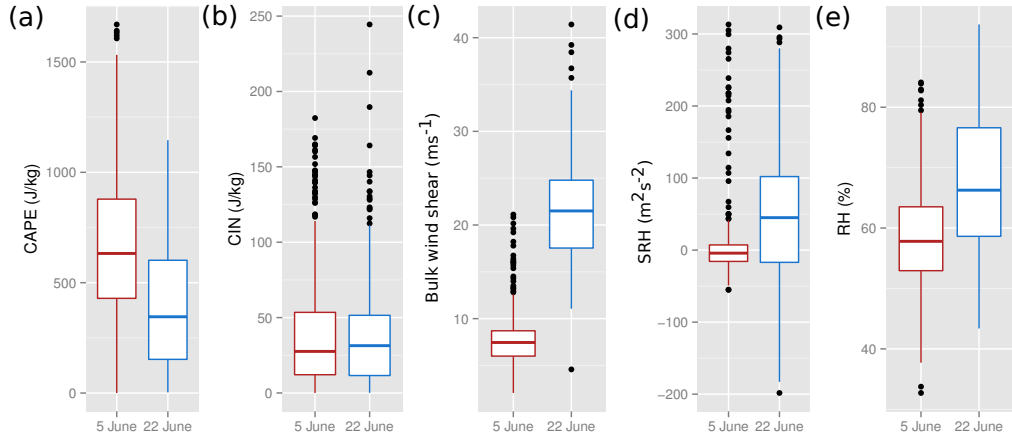


Figure 5.3: Environment characteristics for storm cells for 5 and 22 June 2011. (a) CAPE (J/kg), (b) CIN (J/kg), (c) Bulk wind shear ( $\text{ms}^{-1}$ ), (d) 0 to 3 km integrated SRH ( $\text{m}^2\text{s}^{-2}$ ) and (e) RH (%). All environment characteristics are calculated before the start of tracking, in a  $31 \times 31$  grid point environment of the maximum Gaussian filtered vertical velocity. The box plot indicates the variation over all convective cells for the specific weather case.

### 5.3 VARIABILITY OF ENVIRONMENT

To quantify which differences to expect in the evolution of storm cells, we first look at differences in synoptic and mesoscale environment. As described in the previous sections, for each storm cell parameters like CAPE, bulk wind shear and SRH are calculated. For the 5 and 22 June weather cases, these parameters are shown in Fig. 5.3.

There is a considerable amount of variation in the environment in which storm cells are initiated. CAPE values (Fig. 5.3a) range from almost zero to more than 1000 J/kg for both cases. The main difference between the two weather cases is that for 5 June the CAPE is considerably higher (median values of about 400 J/kg for 22 June, compared to about 600 J/kg for the 5 June case). For both cases there is neglectable CIN (Fig. 5.3b), about 75% of the convective cells have CIN less than 50 J/kg. Large differences are found in the shear parameters, with a median bulk shear (Fig. 5.3c) of more than  $20 \text{ ms}^{-1}$  for 22 June and less than  $10 \text{ ms}^{-1}$  for 5 June. For some convective cells on 22 June, the bulk wind shear is higher than  $35 \text{ ms}^{-1}$ , while only a few storm cells have a bulk wind shear of less than  $10 \text{ ms}^{-1}$ . The median SRH (Fig. 5.3d) is almost zero for 5 June and about  $50 \text{ m}^2\text{s}^{-2}$  for 22 June. There are, however, about 20 convective cells for 5 June with a SRH larger than  $50 \text{ m}^2\text{s}^{-2}$ . The RH (Fig. 5.3e), is slightly larger for 22 June (median approximately 67%) compared to 5 June (median less than 60%).

Differences in storm properties between the two cases are smaller, as shown in Fig. 5.4. For the Gaussian filtered vertical velocity (Fig. 5.4a) the median is about  $4 \text{ ms}^{-1}$  for both cases. The median of PV maxima (Fig. 5.4b) is slightly larger for the 22 June case, but this difference is very small. The median duration (Fig. 5.4c) of the convective cells is about 37.5 minutes for both cases. This is roughly equal to the convective time scale. There is, however, a lot of variation in the duration

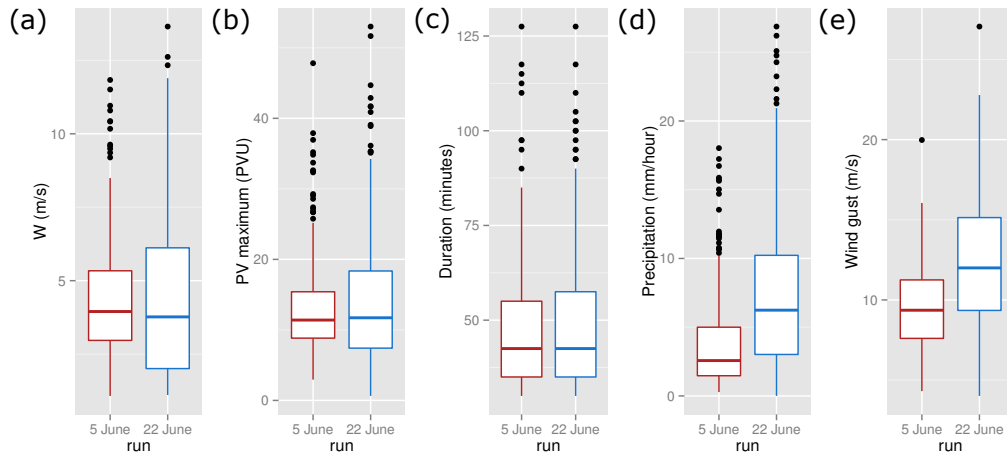


Figure 5.4: Storm cell characteristics for the 5 and 22 June 2011 cases. (a) Maximum (Gaussian filtered) vertical velocity, (b) Maximum PV during tracking, (c) Duration, (d) and (e) Wind gust associated with convective cell (in  $\text{ms}^{-1}$ ). The box plot indicates the variation over all convective cells for the specific weather case.

of the convective cells, with mainly outliers towards longer durations. Although 75% of the convective cells last 60 minutes or shorter, there are some convective cells which last for over two hours. Note that we only selected the convective cells which last at least 30 minutes, so there are no cells with a duration shorter than half an hour. Larger differences between the two weather cases are found in the precipitation and wind gusts associated with the storm cells. Median precipitation rates (Fig. 5.4d) are twice as high for the 22 June case, compared to the 5 June case (7 mm/h and 3.5 mm/h respectively). Modelled wind gusts (Fig. 5.4e) are also significantly stronger for the 22 June case, with median values of  $12 \text{ ms}^{-1}$  against  $9 \text{ ms}^{-1}$  for the 5 June case.

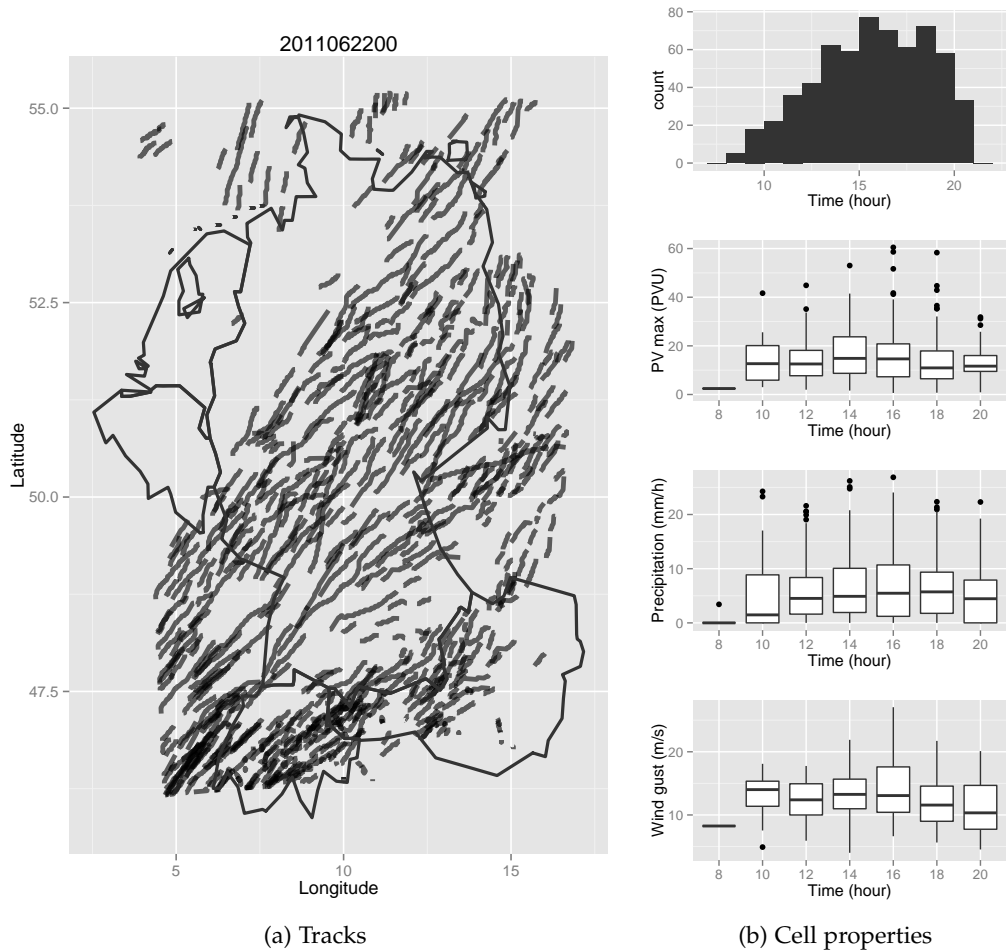


Figure 5.5: (a) Tracks for the 22 June 2011 case. For each storm cell the location of the cell is plotted along its lifetime. (b) Evolution of storm cell properties for the 22 June 2011 case. The cells are divided in bins of two hours. From top to bottom, the number of storm cells, the PV maximum associated with a convective cell, the precipitation rates associated with a convective cell and the wind gusts associated with a convective cell are plotted, as function of time of the day (in UTC). The time of a storm cell is the moment of maximum Gaussian filtered vertical velocity.

#### 5.4 EVOLUTION OF CONVECTIVE CELLS OF 22 JUNE 2011

The tracks for the 22 June case show a preferred movement to the North-East, with some exceptions mainly over the North Sea where storm cells move almost northwards (Fig. 5.5a). Most of the tracks are predominantly straight, and almost all of the cells move towards the North-East. Comparison with the bulk wind shear (not shown) shows that there is a slight preference to move to the right with respect to the wind shear (i.e. the bulk wind shear is more northwards). The majority of the storm cells are found in a band from the North-East of France to the North-East of Germany. There seems to be a split in the density of tracks over South-Germany, consistent with the split of the front observed during that day (Fig. 3.3b).

To show the typical PV anomalies, precipitation rates, and wind gusts associated with a convective cells, the daily variation of these parameters is plotted in Fig. 5.5b. Most storm cells occurred during the late afternoon and early evening, from about 15h to 18h UTC (Note that the forecast and therefore the tracking ends at 21h UTC). In total 615 storm cells are found of which 385 are used for the composites (i.e. convective cells with only one  $w$  maximum, which are not too close to the boundary of the tracking domain). The PV maxima, precipitation rates and wind gust anomalies associated with convective cells show high variability (Fig. 5.5b). There is, however, not a clear daily variation for the median of these variables. Median PV maxima are 15 PVU during the day, but a few convective cells have maxima up to 40 or even 60 PVU. Precipitation rates rise up to about 6 mm/h in the afternoon, and about 25% of the convective cells are associated with precipitation rates larger than 10 mm/hour. Largest precipitation rates are about 25 mm/hour at 16 UTC. A typical wind gust associated with a convective cell is  $12.5 \text{ ms}^{-1}$ , there is low variability in the median, maximum wind gusts of about  $25 \text{ ms}^{-1}$  are observed.

#### 5.4.1 Composites of convective cells

The evolution of the composite of the storm cells at 22 June (Fig. 5.6) shows that 30 minutes before the maximum Gaussian filtered vertical velocity, both of the poles of the PV dipole are of similar strength. At the -30 minutes time step (Fig. 5.6a), the positive PV anomaly is only slightly larger (5.15 PVU) compared to the negative PV anomaly (-4.86 PVU). 30 minutes later at the time of maximum Gaussian vertical velocity (Fig. 5.6b), the positive PV has intensified (5.45 PVU), and it is now clearly stronger than the negative PV pole. Although there is a clear cyclonic circulation around the positive PV anomaly, there are only small hints of anticyclonic flow around the negative PV anomaly visible. As for the composites using the COSMO-DE-EPS data in Chapter 4, the PV dipole appears as elongated bands in the composite.

From the 385 convective cells which are used in the composite, about a third (130) survives until 30 minutes after the maximum intensity (Fig. 5.6c), and almost 12.5% (48 cases) survives for 45 minutes (Fig. 5.6d). After 30 minutes and especially after 45 minutes, the positive PV pole is clearly collocated with the updraft. Flow anomalies show a similar pattern with a dominant cyclonic flow in Fig. 5.6c and Fig. 5.6d. This cyclonic flow is associated with the positive PV pole. The reason why the collocation especially occurs in the decay phase of the updraft, is probably that during the intensification phase of the updraft there is continuous tilting of background shear into the vertical. This implies that there is continuous intensification of the PV dipole. Once all or most of the background vorticity is tilted, advection processes take over and the positive PV pole is advected towards the updraft.

Most of the PV anomalies and corresponding flow anomalies in Fig. 5.6 are significant using a Student's  $t$ -test. As indicated in Section 5.2.3, also a recurrence analysis after von Storch and Zwiers [1988] is determined. The PV maximum is about 60% recurrent, with a maximum  $p$ -recurrence for the 0 time step (63.5%).

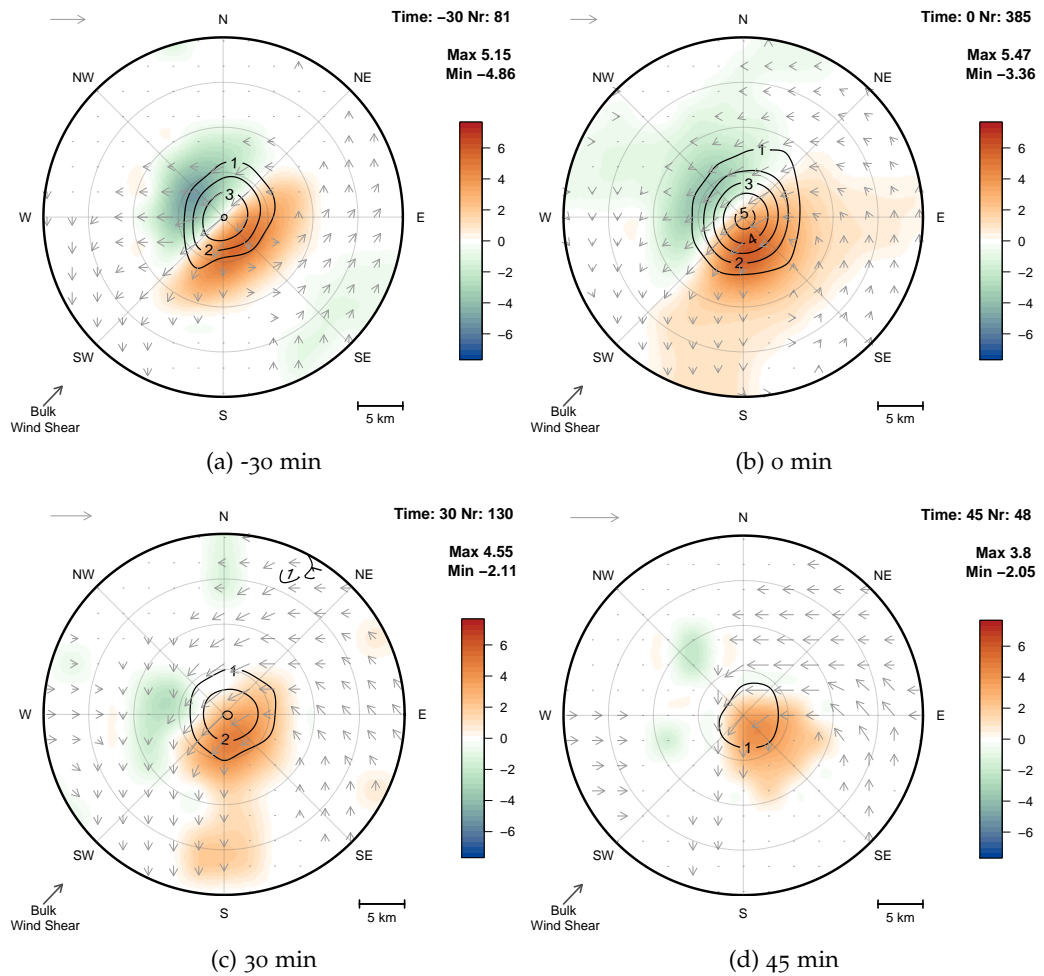


Figure 5.6: Composite of evolution of storm cells for 22 June 2011, for (a) -30 min, (b) 0 min, (c) 30 min, and (d) 45 min. Here the 0 time step indicates the time step with maximum (Gaussian filtered) vertical velocity. Filled contours denote PV anomalies (in PVU), contour lines indicate vertical velocity (non-filtered) anomalies (in m/s) and arrows denote horizontal wind velocity, a reference vector of 5 m/s is added at the top-left. Indicated at the top-right: the time (in minutes after the maximum Gaussian filtered vertical velocity), the number of cells in the composite, and the spatial maximum and minimum PV of the composite.

This indicates that the variance of the PV maxima is large, which we already have shown in Fig. 5.4. A 63.5% p-recurrence corresponds roughly to a separation of 0.75 standard deviations between the ensemble of PV maxima and a hypothetical control ensemble, centred around 0 with the same standard deviation [von Storch and Zwiers, 1988]. In conclusion, even though the PV dipole is very consistent in the mean (indicated by the Student's t-test), it might have limited predictability. Since we applied the p-recurrence at every grid point individually, this variance might also be caused by difference in orientation of the PV dipole.

We have seen in Chapter 4 that especially intense cells (as measured by the vertical velocity) show the asymmetry described above. We further test this by clustering on the intense cells. In the composites of (Fig. 5.7a-b) only the con-

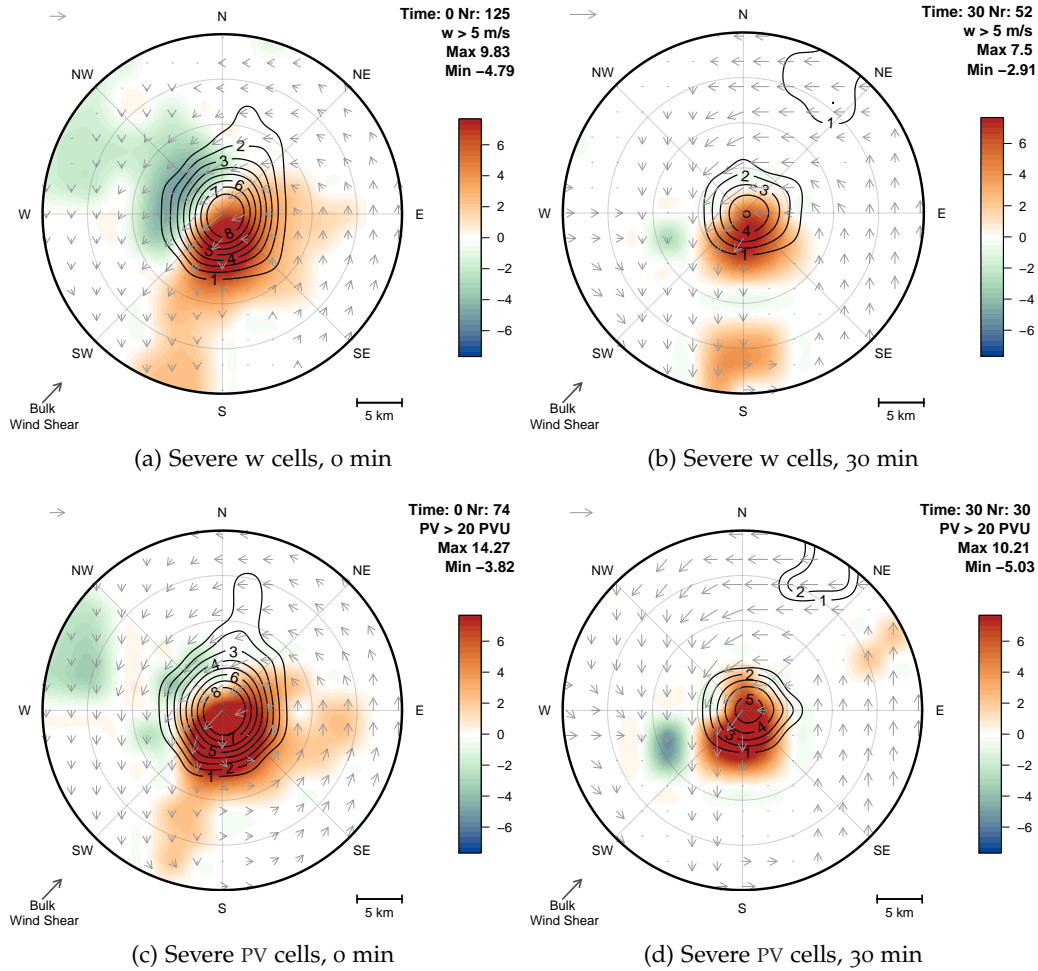


Figure 5.7: As in Fig. 5.6, but for the convective cells with a Gaussian filtered vertical velocity of at least  $5 \text{ ms}^{-1}$  at (a) 0 min and (b) 30 min, and for the convective cells with PV anomalies of at least 20 PVU at (c) 0 min and (d) 30 min.

ective cells with a maximum (Gaussian filtered) vertical velocity of  $5 \text{ ms}^{-1}$  and above are used. This corresponds to about the 25% strongest cells (see Fig. 5.4). At the 0 time step (Fig. 5.7a), the updraft is already almost colocated with the positive PV pole. Compared to the composite using all cells at the same time step (Fig. 5.6b), the PV anomalies are almost twice as strong. After 30 minutes (Fig. 5.7b), the negative PV anomaly is almost non-existent. At this time, there are significant vertical velocity anomalies downshear of the updraft, indicating that a new updraft is generated.

The intensity can also be measured by using a PV threshold. Fig. 5.7c and d show the composite using the convective cells with PV anomalies of at least 20 PVU. Of the 74 storm cells included in these strong PV composites, 59 (approximately 80%) are also included in the strong (Gaussian filtered) vertical velocity composites. At both time steps the “supercell” structure is even clearer than for the composite using the cells with strong vertical velocity. The positive PV pole is more than 14 PVU at the time of maximum Gaussian vertical velocity (Fig. 5.7c), and it is still more than 10 PVU at the 30 minutes time step (Fig. 5.7d). For both

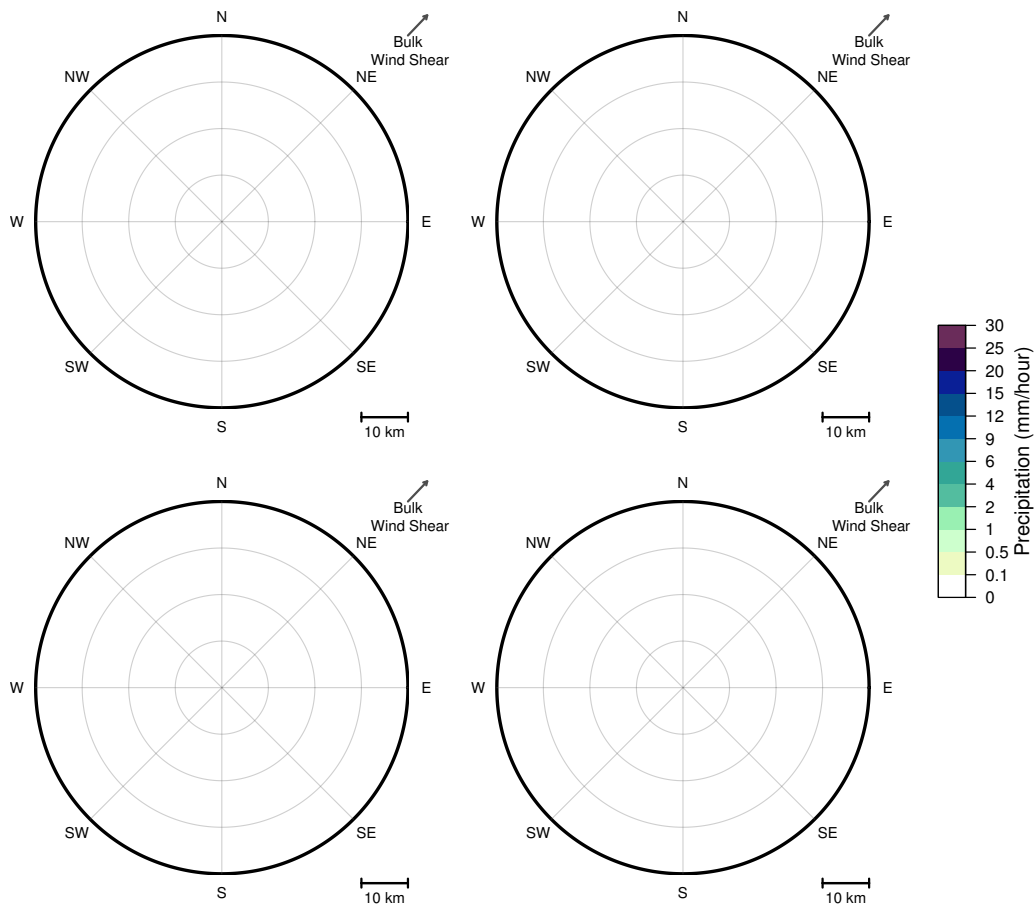


Figure 5.8: Precipitation composite (coloured contours in mm/hour) on 22 June 2011, for (a) all cells at the 0 h time step, (b) all cells at the 30 min time step, (c) for the storm cells with a PV maximum between 15 and 20 PVU, 30 minutes after maximum Gaussian filtered vertical velocity and (d) for convective cells with a PV maximum larger than 20 PVU, 30 minutes after maximum Gaussian filtered vertical velocity. The reference vector at the top right in each panel indicates the average direction of the bulk wind shear over all cells.

time steps, flow anomalies of over  $5 \text{ ms}^{-1}$  are found. As for the strong vertical velocity composite, after 30 minutes significant vertical velocity anomalies are present downshear of the updraft, but here these are even larger than  $2 \text{ ms}^{-1}$ . This supports our hypothesis that the PV bands seen for the 22 June weather case can be (partially) explained due to the preferential generation of new cells downshear of old updrafts.

Up to now, composites were made of PV anomalies associated with all storm cells and with intense cells. The PV dipoles have a diabatic origin, and precipitation and condensational processes are associated with latent heating. Therefore, it is also useful to look at the precipitation composite of a typical convective cell, and at precipitation composites of strong PV cells. Fig. 5.8a shows the composite (hourly) precipitation rates around the time of maximum Gaussian vertical velocity. There are clear precipitation anomalies over a relatively large domain, and they are largest at the upshear side of the updraft, but turned slightly clockwise. This is consistent with the average cell movement of the cells for the 22 June case

which was slightly more westerly compared to the orientation of the bulk wind shear (see Fig. 5.5a). Average precipitation anomalies range between 6 and 10 mm/h, and they tend to be a bit larger for the 30 minutes time step (Fig. 5.8b).

If we cluster only on the severe PV cells (Fig. 5.8c and d), we see that the precipitation rates get much larger, with average maxima of approximately 16 mm/h for the most intense PV cells. Moreover, the precipitation maxima are more localised compared to the composite over all cells. The precipitation anomalies are almost zero at the downshear side of Fig. 5.8d.

#### 5.4.2 Vorticity budget

Since the PV contains information about all three components of the vorticity at the same time in one scalar quantity, it is difficult to see which processes contribute to the intensification of the PV anomalies. It is thus useful to look into the vorticity, too. Since this is a vector quantity, we can see processes like tilting and stretching more directly. We calculate a simple vorticity budget for the vertical component of the vorticity, since the PV dipoles are dominated by the vertical vorticity. Cram and Montgomery [2002] found that for a convective line, the solenoid term is at least one order of magnitude smaller. We assume that we can neglect the solenoid term, and concentrate on the stretching and tilting terms only, then the vorticity budget is given by,

$$\frac{\partial \zeta_z}{\partial t} = \zeta \frac{\partial w}{\partial z} - \left( \frac{\partial w}{\partial x} \frac{\partial v}{\partial z} - \frac{\partial w}{\partial y} \frac{\partial u}{\partial z} \right), \quad (5.2)$$

where  $\zeta_z$  refers to the vertical component of the vorticity vector  $\zeta$ . The first term represents the stretching of vertical vorticity, and the second term represents the tilting of horizontal vorticity (e.g. vorticity associated with the wind shear) into the vertical.

The tilting term (Fig. 5.9a) shows a dipole structure, at the same location at which the PV dipole is located at the 0 time step. The asymmetry as seen for the PV composite in Fig. 5.6b, is also visible in this tilting term. The stretching term (Fig. 5.9b) is clearly weaker than the tilting term for the composite taken over all cells. As expected, since vertical velocity is needed (first term on the left in Eq. 5.2), the stretching term is largest directly at the updraft. The tilting term (Fig. 5.9c) and stretching term (Fig. 5.9d) are of comparable magnitude for the severe precipitation cells. As expected, strongest tilting terms are found for severe PV cells (Fig. 5.9e). The tilting term is about 1.5 to 2 times as large compared to the composite over all cells. Moreover, in contrast to the composite of all cells, the stretching term is of similar magnitude compared to the tilting term (Fig. 5.9f).

The evolution of the maximum tilting and stretching in the neighbourhood of the updraft (Fig. 5.10a), indicates that especially up to the maximum Gaussian filtered velocity the tilting term dominates over the stretching term. There is a sudden increase right before the 0 time for the stretching term. This is expected, since at the stretching term in Eq. 5.2 is proportional to the vertical derivation of  $w$ . After the maximum Gaussian filtered vertical velocity, both terms are of similar strength, and they gradually weaken over time. Intense precipitation cells

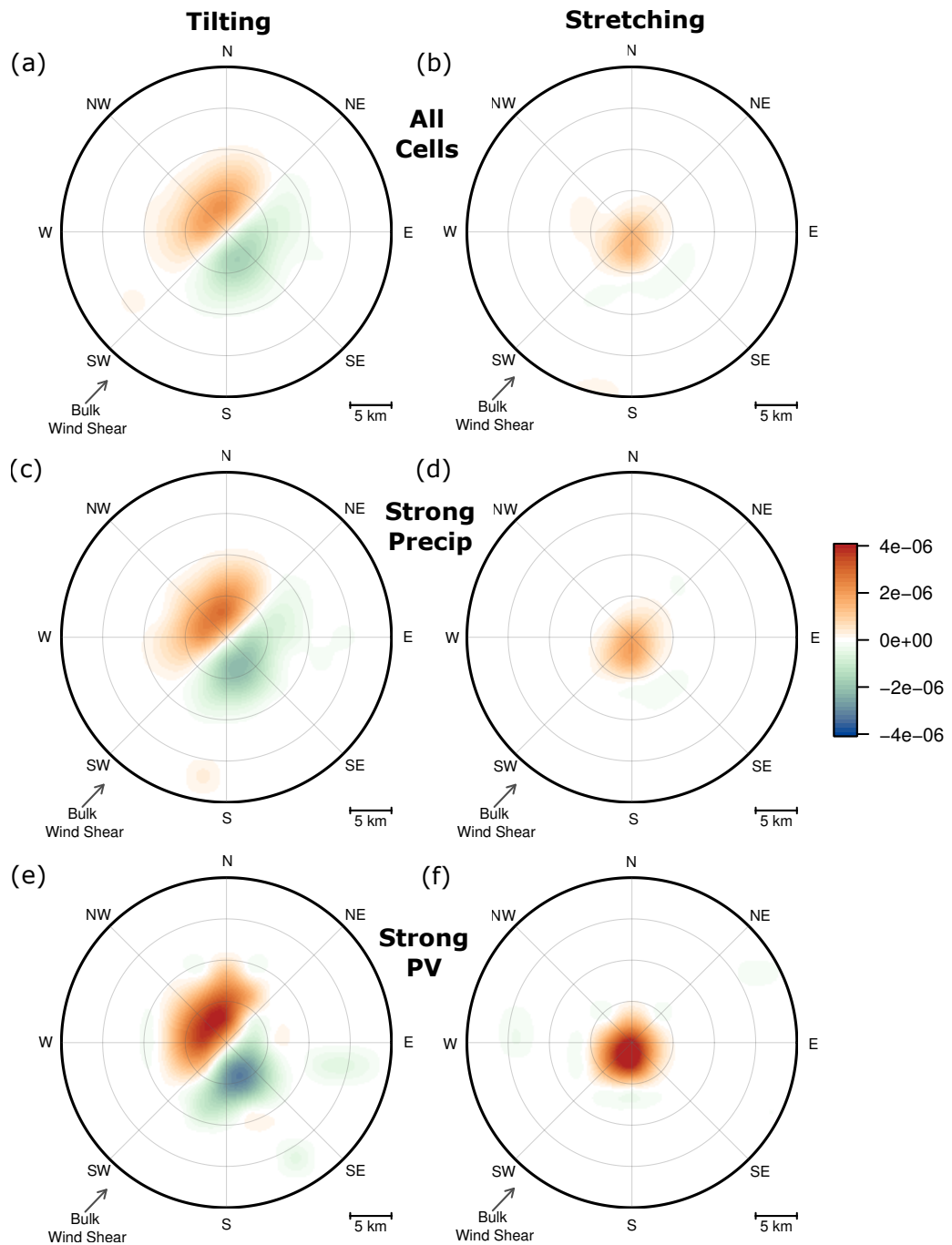


Figure 5.9: Vorticity Budget of storm cells of 22 June 2011. (a) Shows the composite of the tilting and (b) stretching terms of Eq. 5.2 (indicated by the coloured contours in  $s^{-1}$ ), for all cells at the maximum Gaussian filtered vertical velocity. (c-d) As (a-b), but for strong precipitation cells (i.e. the cells with precipitation rates larger than 6 mm/hour). (e-f) As (a-b), but for the convective cells with a maximum PV of at least 20 PVU. The reference vector at the lower left corner indicates the average direction of the bulk wind shear over all cells.

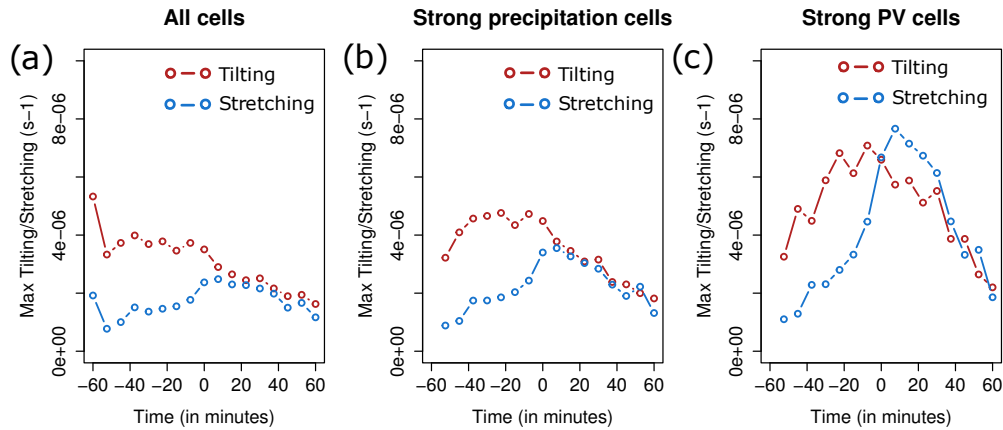


Figure 5.10: Evolution of vorticity Budget of storm cells of 22 June 2011. (a) Shows the temporal evolution of the maximum tilting and stretching terms of Eq. 5.2 (in a  $7 \times 7$  grid point environment around the updraft). The composite is taken over all storm cells. (b) as in (a), but for strong precipitation cells (i.e. the cells with precipitation rates larger than 6 mm/hour). (c), as in (a) but for the convective cells with a PV maximum of at least 20 PVU.

(Fig. 5.10c) show a similar temporal variation. For intense PV cells (Fig. 5.10c) the stretching terms tends to dominate over the tilting term at about 10 to 20 minutes after the Gaussian filtered vertical velocity. Moreover, both terms are in general much stronger compared to the composites over all cells in Fig. 5.10a. The results are again consistent with the results of Cram and Montgomery [2002] for an idealised convective line. Similar findings about the relative importance of vorticity stretching have been found by Montgomery et al. [2006] for Vortical Hot Towers (VHTs), and by Klemp [1987] for tornadic thunderstorms.

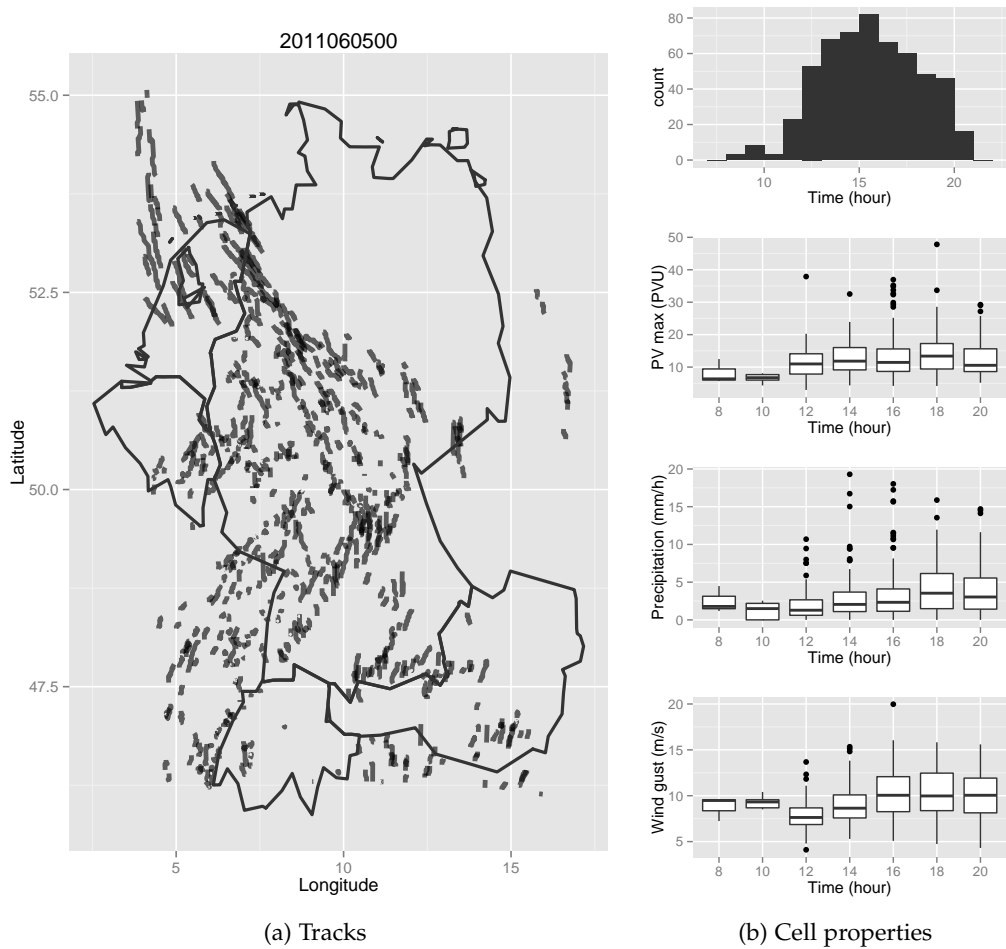


Figure 5.11: As Fig. 5.5, but for 5 June 2011.

## 5.5 EVOLUTION OF CONVECTIVE CELLS OF 5 JUNE 2011

Tracks of the storm cells of the 5 June case are generally much shorter compared to the 22 June case (Fig. 5.11a). This is mainly due to the weaker background wind speed, the average duration is about the same (see Fig. 5.4). The tracks are also more scattered over the COSMO-DE domain, consistent with the observations. The storm cell movement is more towards the North-East in South-Germany and towards the North-West in the northern part of the domain. As for the 22 June case, the movement of the cells is slightly to the right compared to the large scale wind shear.

In total 548 convective cells have been tracked for this case, of which 376 contribute to the composites (Fig. 5.11b). Most convection is generated around 16 UTC, there is however considerable convection during 12 till 20 Coordinated Universal Time (UTC). Median precipitation rates and median PV anomalies maximise at the early evening (at 18 UTC). Differences during the day are again small. Compared to 22 June, precipitation rates ( $\approx 2.5$  to 3 mm/h) in the model are smaller. This is not consistent with observations during this day, which showed that the precipitation extremes of 5 June were larger. The COSMO-DE

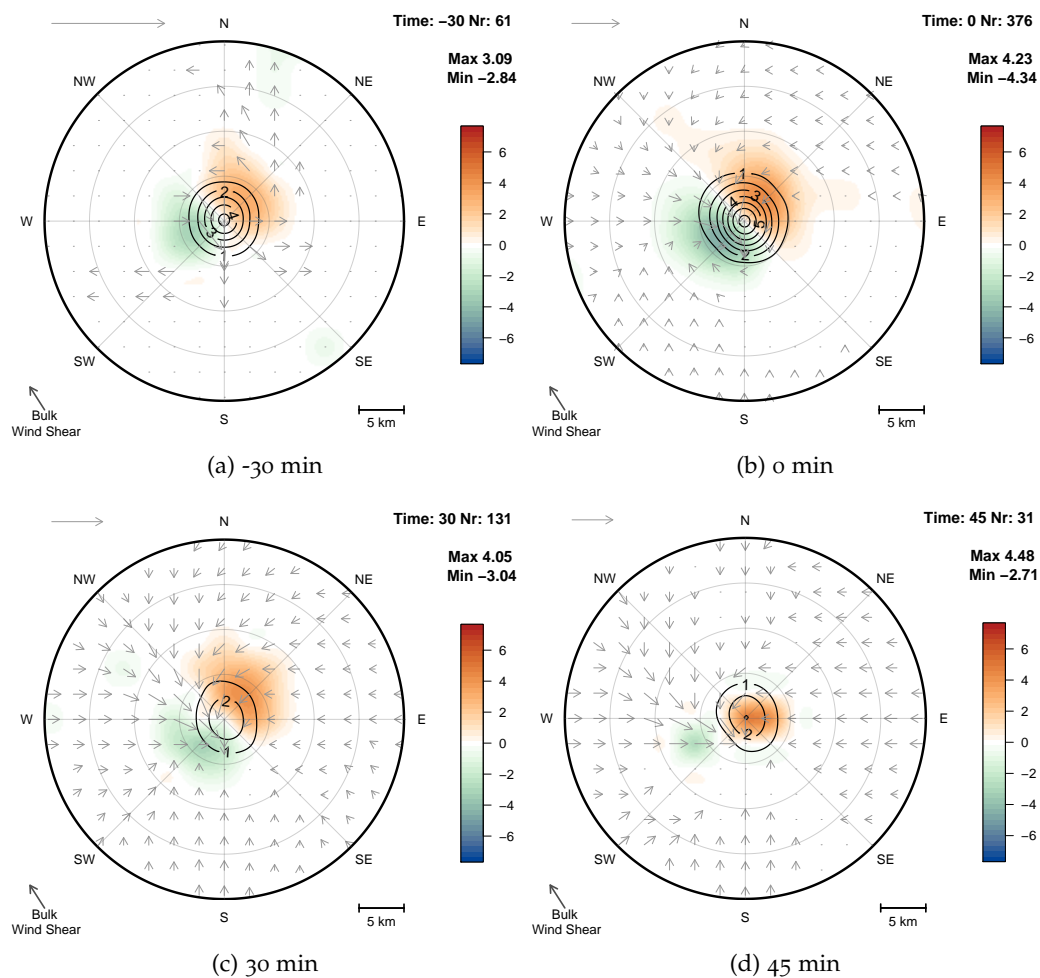


Figure 5.12: As in Fig. 5.6, but for 5 June 2011.

model is probably not able to capture those extremes associated with local severe convection. Wind gusts are also weaker compared to the 22 June case, which is consistent with observations.

### 5.5.1 Composites of convective cells

The composites in Fig. 5.12 show that almost over the whole evolution of the storm cell, except at the 45 minutes time step, both PV anomalies of the dipole are of similar amplitude. The negative anomaly is even stronger (4.34 PVU) compared to the positive anomaly (4.23 PVU) at the -30 minutes (Fig. 5.12a) and the 0 time step (Fig. 5.12b). Again about a 1/3 of the cells survives until 30 minutes after the maximum Gaussian filtered velocity (Fig. 5.12c), but less than 10% survives for 45 minutes (Fig. 5.12d). Wind velocity anomalies are again not always significant, especially in the upshear region, but for the 0 time step a cyclonic flow around the positive and anticyclonic flow around the negative anomaly is visible. Only the long lasting (45 minutes after the maximum Gaussian filtered vertical velocity) updrafts have a more monopole

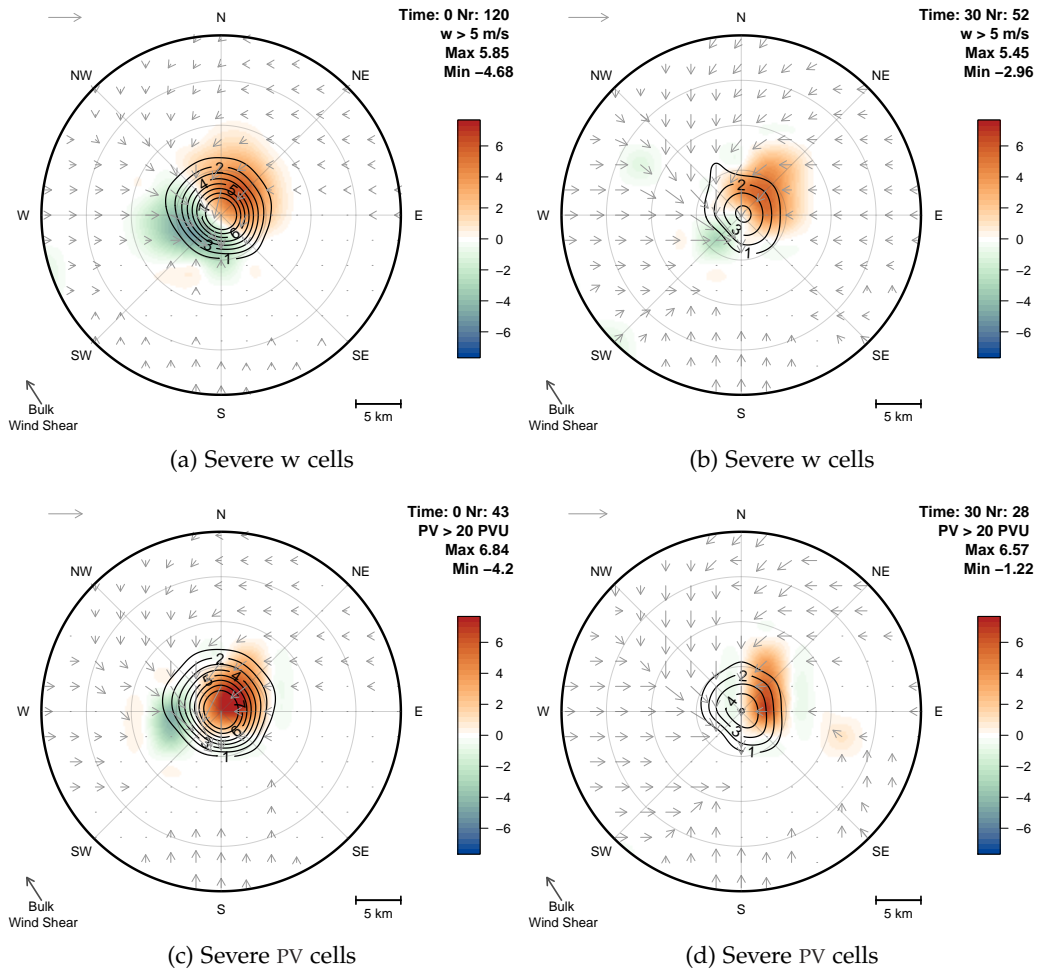


Figure 5.13: As in Fig. 5.7, but for 5 June 2011.

structure, with a weak negative PV anomaly. For this time step the positive PV anomaly is relatively strong (4.48 PVU), indicating that especially the strong PV cells have a long duration.

We again cluster on the intense  $w$  and intense PV cells, using the same thresholds as for the 22 June case (i.e.  $5 \text{ ms}^{-1}$  for the Gaussian filtered vertical velocity and 20 PVU for the intense PV cells). For the intense cells on 5 June (Fig. 5.13a-b), the monopole supercellular structure is less prominent than compared to the 22 June case. Although the positive PV pole is clearly dominant after 30 minutes (Fig. 5.13b), the updraft is located in the centre of the two poles. One explanation for this could be is the lower SRH for the convective cells for the 5 June case (see Fig. 5.3). According to Davies-Jones [1984], significant positive SRH is needed to advect the positive PV pole towards the updraft, generating a persistent rotating updraft. For 5 June, environmental values of SRH were close to zero, while for 22 June, there was on average positive SRH (Fig. 5.3), which might explain the differences between the two cases. The composites with only the intense PV cells confirm this (Fig. 5.13c-d), again the positive PV dominates, but the updraft stays almost centred. Approximately 90% (39 of 43 storm cells) of the convective cells

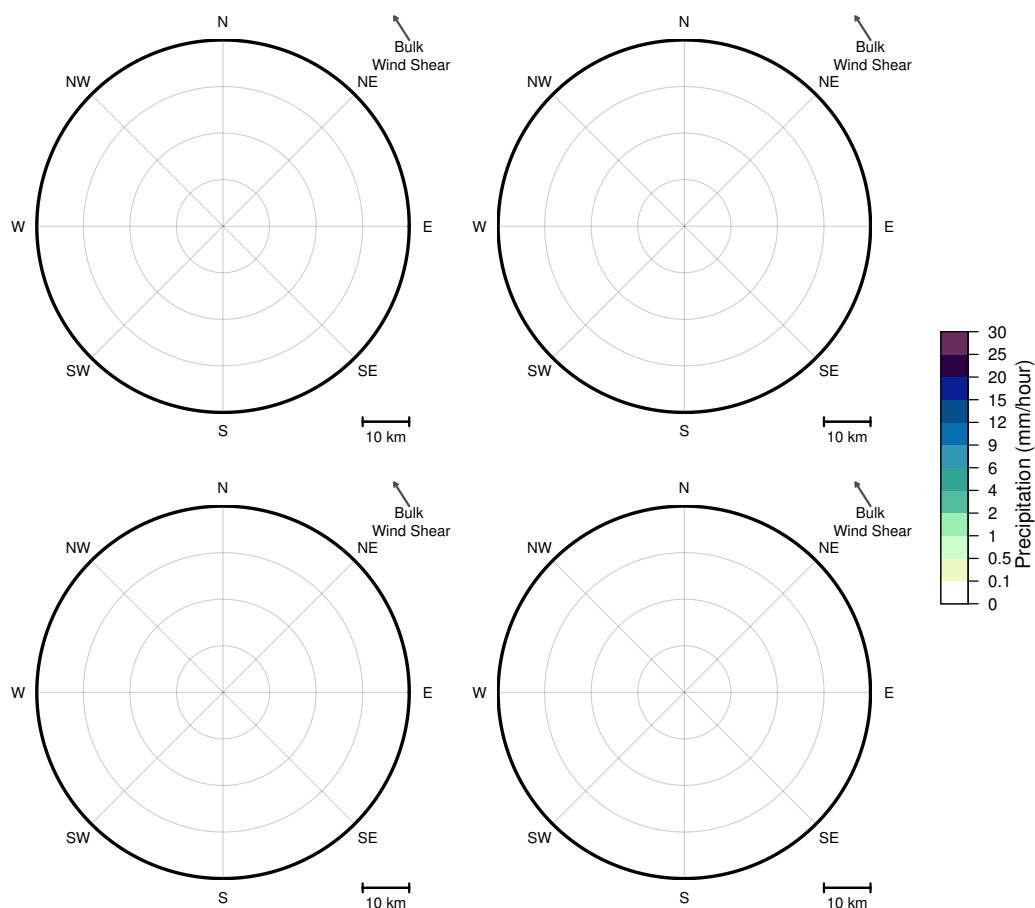


Figure 5.14: As in Fig. 5.8, but for 5 June 2011.

in the strong PV composites are also included in the strong (Gaussian filtered) vertical velocity composites.

The precipitation composites (Fig. 5.14) for the 5 June case are much more local than for the 22 June case. Moreover, the hourly precipitation rates are also smaller, around 4 mm/hour at the 0 time step (Fig. 5.14a) and about 6 mm/hour 30 minutes later (Fig. 5.14b). Again, the strong PV cells show significant larger precipitation rates (Fig. 5.14c-d). For the 5 June case, the average horizontal movement of the convective cells was much less (see Fig. 5.11a), which explains the more local precipitation composite. A possible explanation for the differences in precipitation rates between the 5 and 22 June case could be that for the latter case some stratiform rain could be included in the composite, since this weather case is associated with a cold front. Moreover, for the 22 June case the updrafts are located quite close to each other. Neighbouring cells might influence the precipitation rates in the composite, for example for the intense cells during 22 June there is a updraft visible downshear of the old cell after 30 minutes (see Fig. 5.7b and d). Beside the qualitative differences, the qualitative picture is the same as for the 22 June case. The precipitation anomalies are mainly generated in the direction of cell movement, and strong PV cells are associated with strong precipitation anomalies.

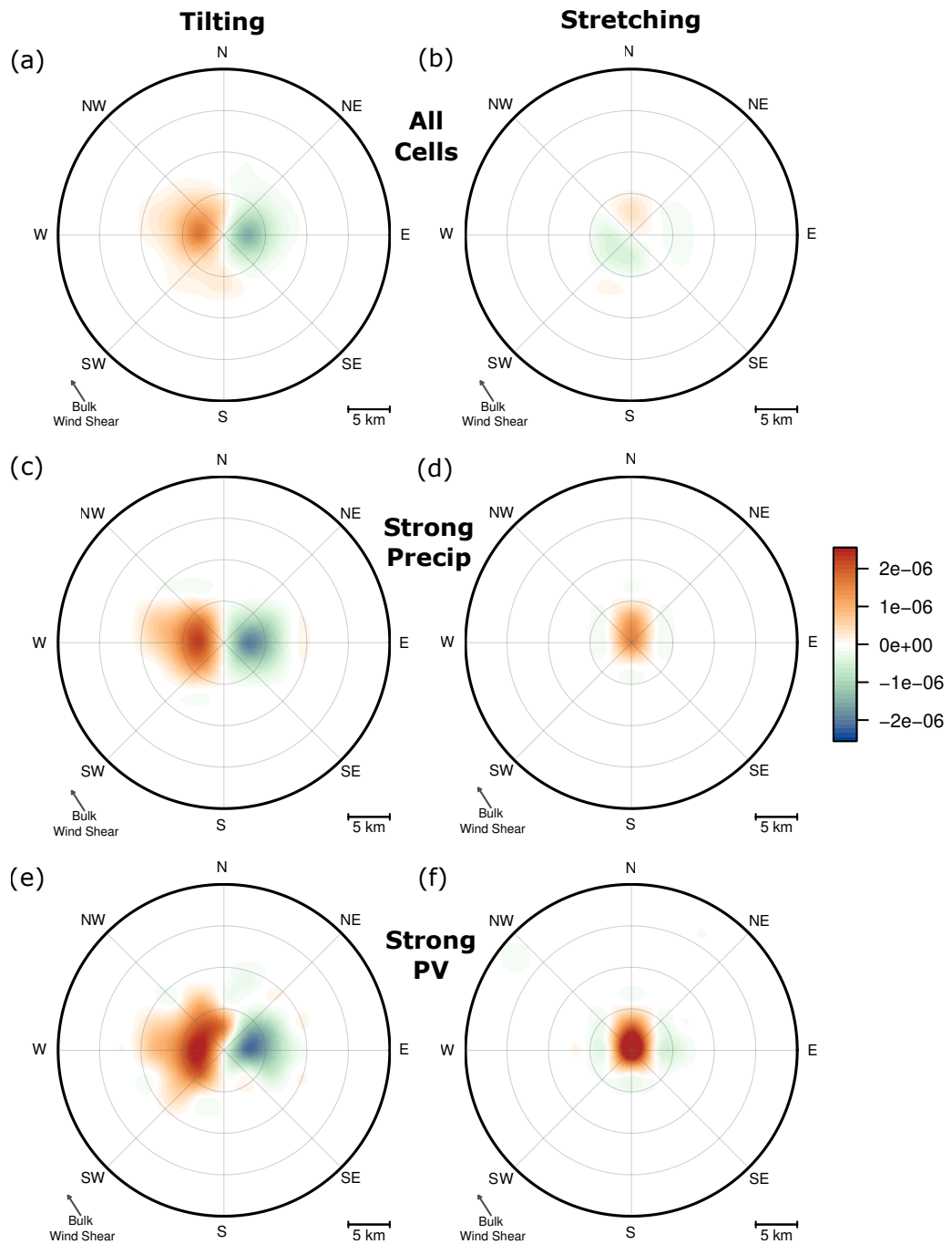


Figure 5.15: As in Fig. 5.9, but for 5 June 2011.

### 5.5.2 Vorticity budget

As for the 22 June case, we calculated a vorticity budget for the vertical component of the vorticity vector, thereby concentrating on the stretching and tilting terms. This vorticity budget shows that for the 5 June case, the tilting term is relatively more important compared to the stretching term, at the 0 time step (Fig. 5.15a). Moreover, the tilting term is much weaker and more localised compared to 22 June, which is consistent with the much weaker bulk wind shear for

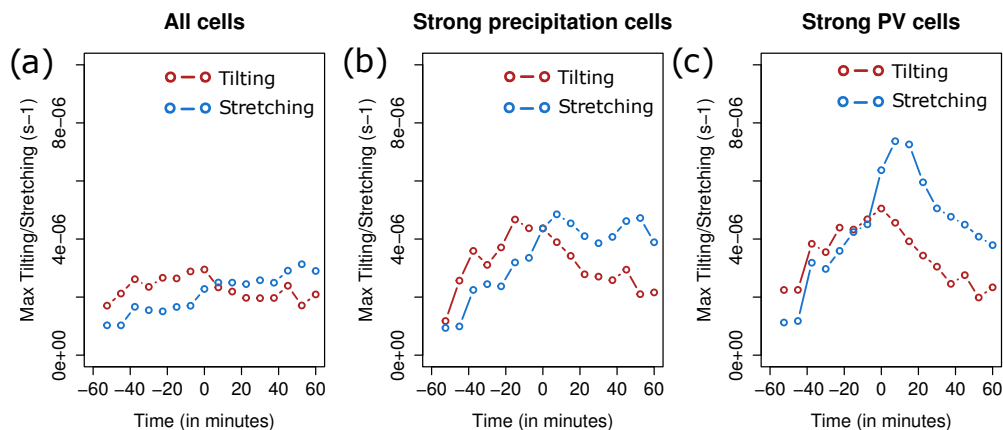


Figure 5.16: As in Fig. 5.10, but for 5 June 2011.

this case. Remember that tilting of environmental wind shear generates the PV dipole. Remarkably, the orientation of the tilting term differs from the orientation of the PV dipole (see Fig. 5.12). The composites in Fig. 5.16 are calculated over the same height as for the PV composites (i.e. height integrated from 3 till 7.3 km). At lower model levels (e.g. on model level 30, at 3.1 km height) the orientation of the tilting term is consistent with the orientation of the PV dipole. For the composite over all cells, the stretching term is almost not visible (Fig. 5.15b). There are significant stretching anomalies for strong precipitation cells (Fig. 5.15d), but these are very local. Only for the intense PV storm cells, the stretching term is of equal magnitude compared to the tilting term (Fig. 5.15c-d).

The evolution of the maximum tilting terms (Fig. 5.16), is comparable to 22 June. Up to the time of maximum Gaussian vertical velocity, the tilting term dominates over the stretching term. After the 0 time step, both of the terms are of about equal magnitude (Fig. 5.16a), and the stretching term gets dominant for severe precipitation and severe PV cells (Fig. 5.16b-c). A difference between the 5 and 22 June weather cases is that for 5 June the stretching term for intense precipitation cells clearly dominates after the Gaussian filtered vertical velocity. For 22 June both of the terms were approximately equal. In the strong precipitation composites of 22 June almost 50% of the convective cells at that day are included, while only approximately 20% of the cells are included in the 5 June composite. For larger thresholds, e.g. for cells with precipitation rates larger than 14 mm/hour, the composites of 22 June do show a slightly dominant stretching term after the maximum Gaussian filtered vertical velocity.

## 5.6 SUMMARY AND DISCUSSION

For 5 and 22 June 2011, there is a consistent evolution of PV anomalies associated with convective cells, with a lifetime similar or longer as the convective time scale. The synoptic background for the two cases is different, which is visible in more elongated and stronger PV anomalies for the 22 June case. There are, however, also a lot of similarities between the two cases. For both cases there is a clear PV dipole structure, up to the time step of maximum (Gaussian filtered) vertical velocity. Particularly for the 22 June 2011 case, the most intense cells, show a “supercell” structure: a long lasting rotating updraft. For 5 June this supercell structure is not visible, although the positive PV is more dominant after the maximum Gaussian filtered vertical velocity. This is consistent with the lower environmental SRH for this weather case.

A vorticity budget showed that especially for intense cells stretching plays a dominant role in intensifying the positive PV pole. Stretching dominates after the intensification of the PV dipole due to tilting of horizontal vorticity. Average precipitation rates with convective cells show a correlation with PV, there are stronger precipitation rates in the composites of the intense PV cells.

In the next chapter we will further analyse if these results can be extended towards more cases.

## EVOLUTION OF EXTREME CONVECTIVE CELLS

---

*In this chapter the composites analysis as made for the 5 June and 22 June 2011 weather cases will be extended to seven more cases. The composites over nine severe weather cases give a good indication if coherent and statistically significant Potential Vorticity (PV) anomalies associated with convective storm cells exist. Diabatic heating profiles will be determined, afterwards a general composite over all 9 weather cases will be discussed. This chapter also determines composites for intense cells (i.e. cells with strong updrafts, strong PV anomalies or large precipitation rates). Lastly, the influence of environmental parameters as bulk wind shear and Storm Relative Helicity (SRH) on storm cell structure is discussed.*

### 6.1 AIMS AND MOTIVATION

Chapter 5 introduced the tracking algorithm and the compositing method to estimate the characteristic evolution of a convective cell. The focus on the weather cases used in the case study of Chapter 4, i.e. composites of 5 and 22 June 2011. To get a better view of the general evolution of a convective cell, one needs to take the composites over more cases, so that we have enough convective cells to create a representative climatology of storm cells. This chapter discusses composites over nine weather events with a different synoptic background (see Section 3.2.1). Main objective is to characterise how the evolution of the convective cells depends on storm environment and storm cell characteristics.

Questions we want to answer in this chapter are:

- Q1 Can the evolution of convective cells discussed in Chapter 5 be generalised to other cases?
- Q2 Is the (coherent) evolution of storm cells for intense cells different as for weak cells?
- Q3 How does the (coherent) evolution of convective cells depend on the synoptic and/or mesoscale environment?

### 6.2 ROTATION OF CONVECTIVE CELLS

Since the dipole of PV will be orientated along the large scale wind shear, the height integrated PV dipoles will be orientated in different directions for the different cases. Therefore, the fields of the individual storm cells have to be rotated to ensure that the orientation of the PV dipole is consistent. Every storm is rotated in such way that the bulk wind shear is in the eastern direction. The large scale wind shear is calculated as the horizontal wind velocity difference between 0 and 6 km in a 19x19 grid point environment of the Gaussian filtered velocity maximum. The variation in orientation of bulk wind shear (see Fig. 6.1)

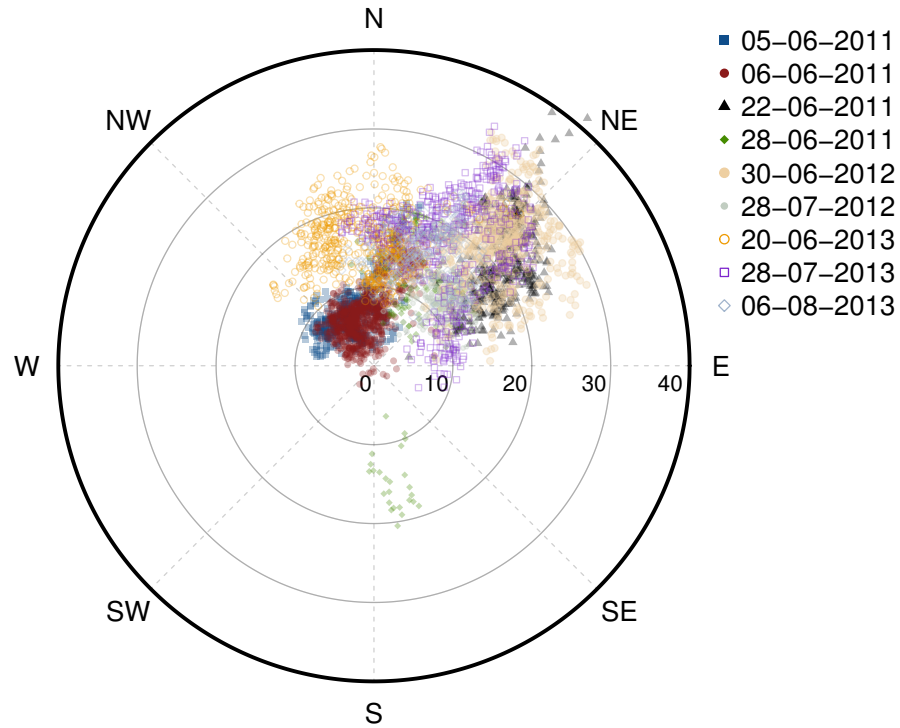


Figure 6.1: Average bulk wind shear, in a 19x19 grid point environment around the Gaussian filtered vertical velocity, Each point indicates the direction of the bulk wind shear (0-6 km wind velocity difference), the nine different weather cases are indicated by different colours. The values on the x-axis indicate the bulk wind shear in  $\text{ms}^{-1}$ , a circle for every 10  $\text{ms}^{-1}$  is drawn.

shows that rotation is necessary. Before rotation, most of the convective cells have southwesterly wind shear. Exceptions are the 5 June 2011, 6 June 2011 and 30 June 2012 weather cases. For these cases the wind shear is more south to southeasterly (see dark blue, dark red and orange symbols in Fig. 6.1). Moreover, for 28 June 2011, for a few convective cells the bulk wind shear was from the north. A more detailed discussion about (the performance) of the rotation algorithm can be found in Appendix B.

### 6.3 VARIABILITY OF ENVIRONMENTAL PARAMETERS AND STORM CELL PROPERTIES

The variation of the different environmental characteristics of the storm cells for the nine weather cases is shown in Fig. 6.2. Median values of CAPE per weather case (Fig. 6.2a) vary from a few hundred J/kg to about 650 J/kg for the 5 June 2011 weather case. These values might seem low, e.g. typical CAPE values associated with severe convective weather typical ranges from 1000 till 2000 J/kg [Thompson et al., 2003]. Remember, however, that the convective parameters are calculated over a large environment, 31x31 gridpoints around the maximum Gaussian vertical velocity. Moreover, there is often already convection generated in this environment, which consumes CAPE. Furthermore, Groenemeijer and van Delden [2007] found that median CAPE values of about 300 J/kg during

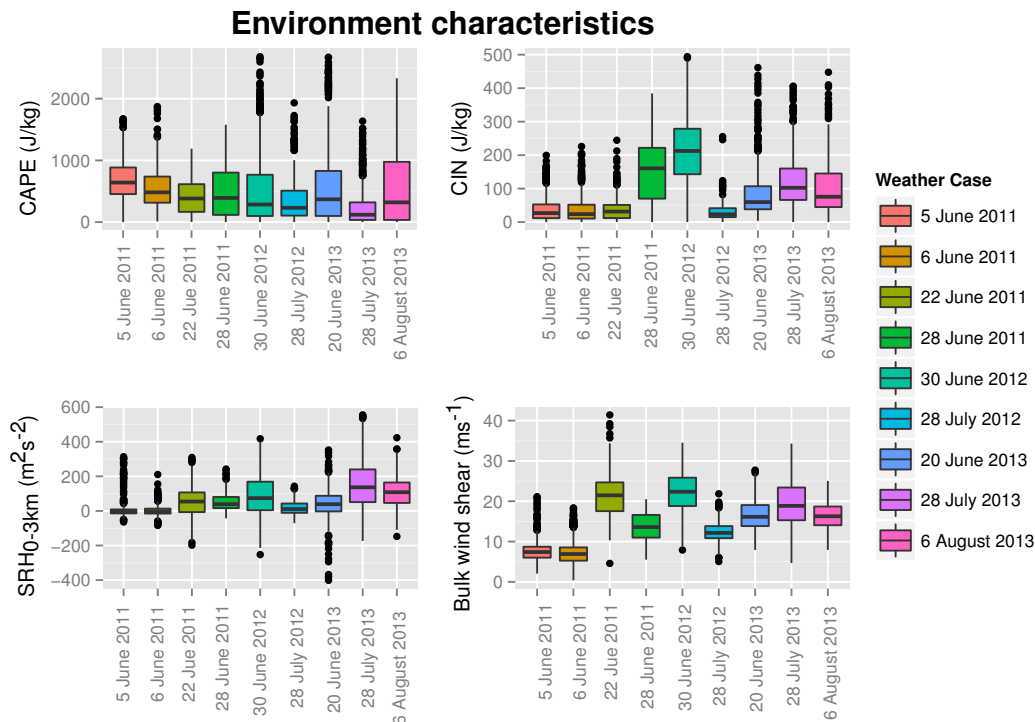


Figure 6.2: Environmental characteristics for the convective storms in the nine different weather cases. (a) CAPE, in J/kg, (b) CIN, in J/kg, (c) SRH, integrated over 0 to 3 km height in  $\text{m}^2\text{s}^{-2}$ , and (d) bulk wind shear in  $\text{ms}^{-1}$ . The colours indicate the different weather cases, and the box plot indicates the variation of the respective variable for that weather case.

thunderstorms in the Netherlands. Therefore, these values might be realistic for Western Europe. The spread of CAPE is quite large, some convective cells have almost no CAPE, while other storm cells have more than 2000 J/kg CAPE. CIN values (Fig. 6.2b) are generally low, median CIN is lower than 100 J/kg for most weather cases. Exceptions are the 28 June 2011 and the 30 June 2012 weather cases, where median CIN values of 150 J/kg and 200 J/kg are observed. For the latter case (30 June 2012), 25% of storm cells have CIN values of more than 300 J/kg.

The shear related variables show a similar variation between the cases. The median of SRH (Fig. 6.2c) varies between almost zero for the 5 and 6 June 2011 case, up to  $100 \text{ m}^2\text{s}^{-2}$  for two of the three weather cases in 2013. Thompson et al. [2003] found that for supercells the mean 0-3 km height integrated SRH is about  $180 \text{ m}^2\text{s}^{-2}$  for nontornadic supercells and about 250 for tornadic supercells. Especially for the 30 June 2012 and 28 July 2013 cases such high values (higher than  $200 \text{ m}^2\text{s}^{-2}$ ) are found. The bulk wind shear (Fig. 6.2d) also shows a considerable amount of spread. For a few cases (5 and 6 June 2011), the wind shear is weak with median values of about  $8 \text{ ms}^{-1}$ . There are about 5 cases with moderate vertical wind shear ( $10\text{-}20 \text{ ms}^{-1}$ ). Strong shear cases are 22 June 2011 and 30 June 2012, for these cases the median bulk wind shear is larger than  $20 \text{ ms}^{-1}$ . Such high values for the wind shear can be an indicator for supercells

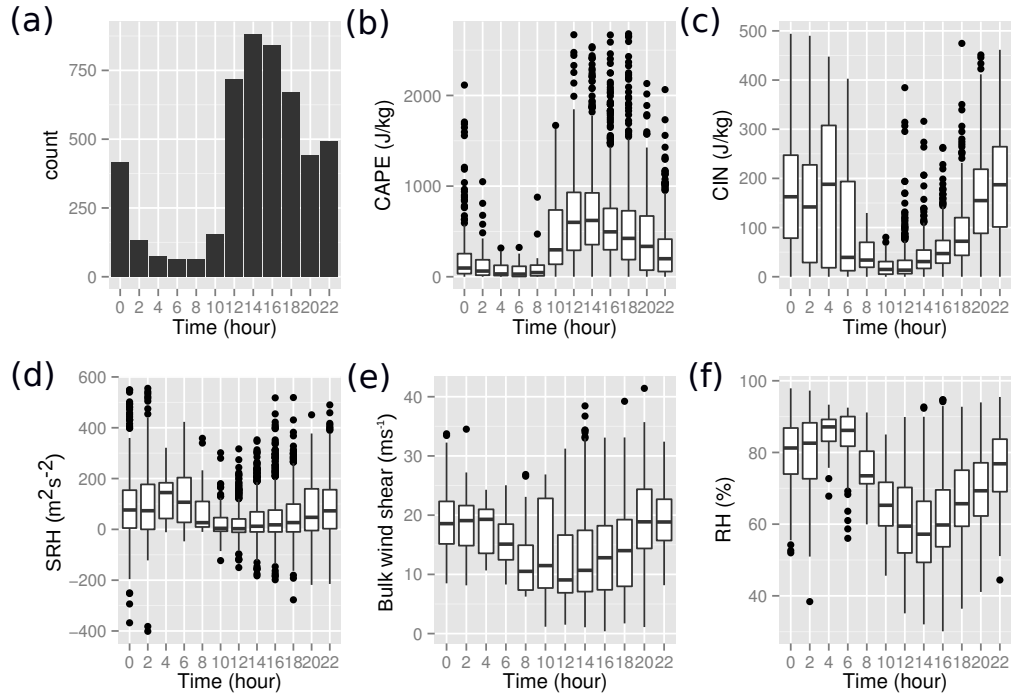


Figure 6.3: Temporal evolution of the environmental characteristics of convective cells over all 9 cases during the day. All cells are divided into bins of two hours (time in UTC). (a) The number of cells, (b) CAPE (in J/kg), (c) CIN (in J/kg), (d) SRH (integrated over 0 to 3 km from the surface, in  $\text{m}^2\text{s}^{-2}$ ), (e) 0-6 km bulk wind shear (in  $\text{ms}^{-1}$ ) and (f) RH (in %). All parameters are calculated in a  $31 \times 31$  grid point environment of the updraft.

[e.g. Thompson et al., 2003]. As for the other parameters, the spread for the bulk wind shear is also large, with extremes up to  $35 \text{ ms}^{-1}$ .

Other convective variables, like the stability indices Showalter Index (SI) and Lifted Index (LI), show similar spread for the different cases (not shown). In conclusion, there is enough variation in the synoptic- and mesoscale background of the storm cells to create representative composites.

### 6.3.1 Spatial and temporal dependence of cell characteristics

In Fig. 6.3 the daily evolution of environmental characteristics is shown. As for the 5 June and 22 June cases, generally most cells are found between 14 and 16 UTC (Fig. 6.3a). There is a second maxima just before midnight (UTC). During the night and the early morning, only a few cells are initiated. CAPE (Fig. 6.3b) values show a similar daily variation as the number of cells, although the maximum CAPE is earlier during the day, with about  $650 \text{ J/kg}$  at 14h UTC. CIN (Fig. 6.3c) values have an inverse daily cycle, with almost zero values from 10 to 16 UTC and quite large magnitudes at midnight of almost  $200 \text{ J/kg}$ . During the night the atmospheric boundary layer stabilises, which creates a stable boundary layer (i.e. large values of CIN), and this prohibits the initiation of Deep Moist Convection (DMC).

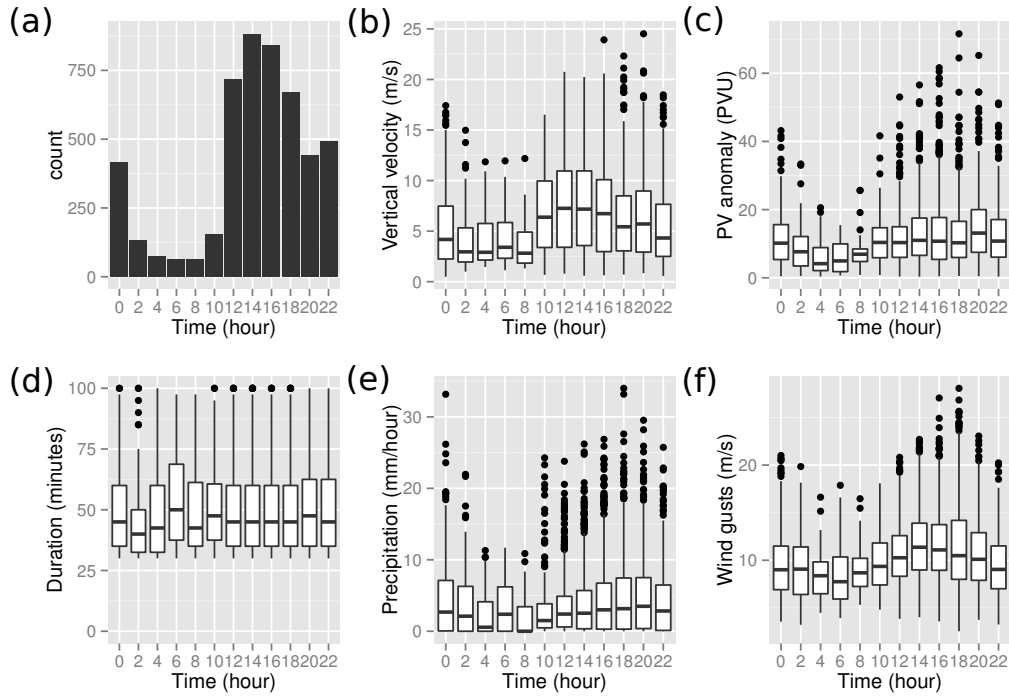


Figure 6.4: Temporal evolution of the cell characteristics over all 9 cases during the day. All cells are divided into bins of two hours (time in UTC). (a) the number of cells, (b) vertical velocity (in  $\text{ms}^{-1}$ ), (c) The PV maximum (in a  $5 \times 5$  grid point environment of the updraft), (d) duration (in minutes), (e) precipitation rates (in  $\text{mm}/\text{hour}$ ), and (f) the wind gust, as measured by  $V_{\text{gust}}$ .

SRH (Fig. 6.3d) is mostly positive, median values increase from approximately 0 at 12 h UTC to about  $80 \text{ m}^2\text{s}^{-2}$  at midnight. The average positive SRH is consistent with the on average clockwise hodograph of the atmospheric wind in the planetary boundary layer in the Northern hemisphere [Doswell III, 1991]. The bulk wind shear (Fig. 6.3e) maximises in the late evening, and in the early night. Median values maximise at about  $20 \text{ ms}^{-1}$  at 22h UTC, although extremes up to  $25 \text{ ms}^{-1}$  are found during most of the day, except for the early morning.

The RH (Fig. 6.3f), has minimum values in the late evening and early night, with median values of about 90%. During the day, median values of RH drop to about 60%. The Vertically integrated divergence of specific humidity  $q_v$  (HDIV) (not shown) has a similar daily cycle, but is generally negative (i.e., as expected, since one expects always moisture convergence during convection).

The storm properties, like maximum vertical velocity and maximum PV show a less clear daily variation (Fig. 6.4). Vertical velocity (Fig. 6.4b) has an almost similar daily variation as for CAPE, indicating that those two variables are highly correlated. Median vertical velocity is about  $7.5 \text{ ms}^{-1}$  at 14 UTC, with outliers up to  $20 \text{ ms}^{-1}$ . A similar daily cycle is seen for the PV anomalies (Fig. 6.4c). Median PV maxima are about 10 Potential Vorticity Unit (PVU), which is an order of magnitude larger than ambient PV values (i.e. synoptic scale PV anomalies in the mid-troposphere). Largest values of PV are observed during 16-18 UTC, with extremes up to 60 PVU. There is almost no daily variation in the duration of a convective cell (Fig. 6.4d), for most times the median duration slightly under

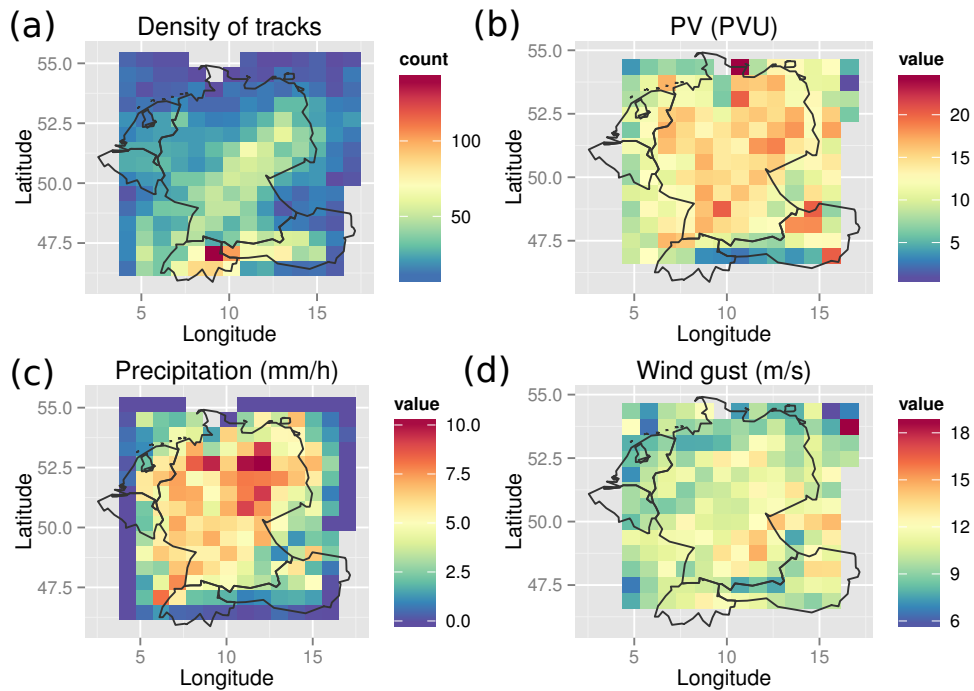


Figure 6.5: Spatial variation of the cell characteristics over all 9 cases during the day. All convective cells are distributed into bins. (a) The number of convective cells in a respective bin. Binned average of (b) The PV maximum (in a  $5 \times 5$  grid point environment of the updraft, in PVU), (c) precipitation rates associated with an updraft (in mm/hour), and (d) the wind gust associated with an updraft, as measured by  $V_{gust}$  (in  $\text{ms}^{-1}$ ).

50 minutes. There is, however a large variation in the duration of a convective cell, about 25% of the storm cells last longer than a hour. The median precipitation rates (Fig. 6.4e) associated with a convective cell maximises around 18-20 UTC. Median values are of about 4 mm/hour, and outliers can reach up to 30 mm/hour. Wind gusts (Fig. 6.4f) maximise around 18h UTC, which is roughly in between the time of maximum CAPE and the time when the maximum bulk wind shear is reached.

One should note that these differences found in convective parameters and storm properties are not necessary due to a daily cycle. These differences might be caused by the small sample size of severe weather cases, and are therefore not necessary representative for all cases. The findings in Fig. 6.3 are, however, physically consistent. For example, the RH is higher during the night because colder air can hold less moisture. Moreover, the daily cycle of PV and precipitation rates is consistent with the daily cycle of precipitation rates found in the high-resolution COSMO-REA2<sup>6</sup> reanalysis [Bollmeyer, 2015]. This confirms that a physically representative set of weather cases was selected.

<sup>6</sup> The COSMO-REA2 reanalysis uses the COSMO-model on a similar resolution (2 km), and on a slightly larger model domain as for COSMO-DE.

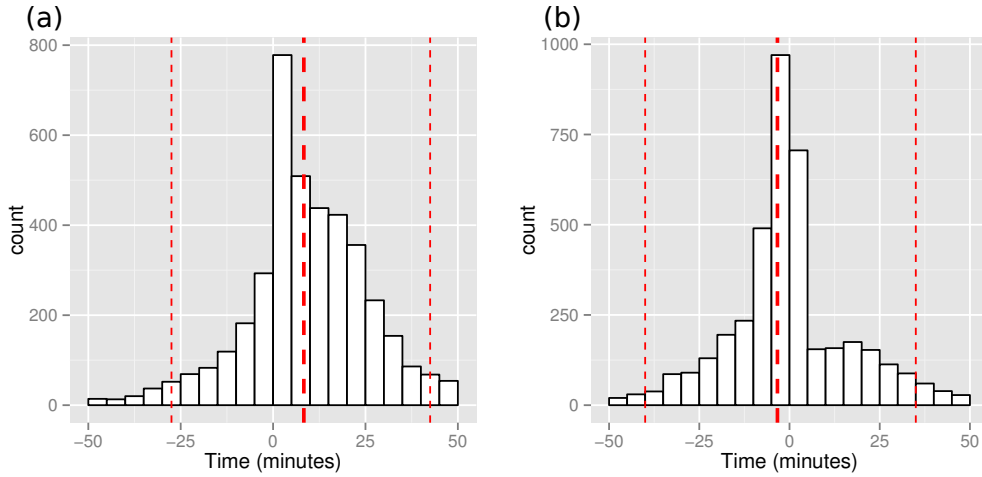


Figure 6.6: Difference in minutes between time of maximum Gaussian filtered  $w$  and (a) time of maximum PV in the  $5 \times 5$  grid point neighbourhood of the updraft and (b) time of maximum  $\theta$ . The thick dashed lines indicate the median value and the thin dashed lines indicate the 5% and 95% quantiles.

The spatial distribution of the tracks (Fig. 6.5a) shows that convective cells are found mainly within a band from North Eastern France to North Eastern Germany. A further (small) maximum can be found at the North-West of Germany, at the border with the Netherlands. Moreover, there are a lot of cells in Switzerland, which probably are generated orographically. This is confirmed by average values of CAPE, which are relatively low for this region (not shown). PV (Fig. 6.5b) and precipitation rates (Fig. 6.5c) also maximise in the same band over Germany, with maxima over North-East Germany. Over this band, PV maxima range from 15 to 20 PVU, while average precipitation rates are up to 10 mm/hour. Wind gusts (Fig. 6.5d) show less clear variations, maximum averages are found of more than  $15 \text{ ms}^{-1}$  over South-East Germany.

One might expect that the maximum PV is reached after the maximum Gaussian filtered vertical velocity. The physical argument for this is that the Gaussian filtered vertical velocity is proportional to the diabatic heating rate  $\dot{\theta}$ . Since the PV dipole is a consequence of the diabatic heating rate, one would expect that the PV maximum occurs generally later than the maximum of Gaussian filtered vertical velocity. This is analysed further in Fig. 6.6a, which shows the time difference in minutes between those two maxima. Although the maximum PV is reached later on average, about 7.5 minutes, there is still a significant amount of cases in which the PV maximum is reached earlier than the maximum in vertical velocity. We saw in Chapter 4 that the updraft is associated with a positive  $\theta$  maximum. The time at which this maximum is reached coincides with the time at which the maximum (Gaussian filtered) vertical velocity is reached (Fig. 6.6b). Again the spread is large, therefore one has to be careful in taking conclusions.

### 6.3.2 EOF analysis

Before clustering on different synoptic characteristics and storm properties we first want to select a subset of these parameters. This section discusses an Empirical Orthogonal Function (EOF) analysis on both the storm environment variables and the storm properties. EOF, often also called principle component analysis, is one of the most used multivariate statistical techniques [Wilks, 2011]. The essential goal of EOF analysis is to reduce the degrees of freedom of a high-dimensional data set, while retaining a maximum of variance.

EOF analysis is an orthogonal linear transformation, which uses the eigenvectors of the covariance matrix to transform a set of variables into a new basis of variables. The eigenvectors of the covariance matrix are called Empirical Orthogonal Functions (EOFs).

Suppose one has a set of  $N$  storm cells and  $M$  convective variables<sup>7</sup>. For each convective variable, a set of  $N$  observations (i.e. storm cells)  $\psi_m$  is available. Since most of the meteorological parameters have different units and physical interpretation, one has to normalise the parameters before performing the EOF analysis [e.g. Venegas, 2001]:

$$F_m = \frac{\psi_m - \bar{\mu}_m}{\sigma_m} \quad (6.1)$$

for each parameter  $\psi_m$ , with  $\sigma_m$  the standard deviation of  $\psi_m$  and  $\mu_m$  its mean. The  $(M \times N)$  data matrix  $F$  used in the EOF analysis is the matrix with on the rows the normalised parameters  $F_m$ .

The covariance matrix  $\mathbf{R}_{FF}$  (or the correlation matrix, since the parameters are normalised by the variance) is then given by,

$$\mathbf{R}_{FF} = F \times F^T. \quad (6.2)$$

Here  $F^T$  is the transpose of  $F$ . The EOFs are then found by solving the eigenvalue problem,

$$\mathbf{R}_{FF} \times \mathbf{E} = \mathbf{E} \times \Delta, \quad (6.3)$$

with  $\mathbf{E}$  the matrix with the eigenvectors of  $\mathbf{R}_{FF}$  as column vectors  $E_k$ , corresponding to the eigenvalues  $\lambda_k$  ( $k = 1, \dots, K$ , with  $K$  the minimum of  $N$  and  $M$ ).  $\Delta$  is a  $M \times M$  diagonal matrix with on the diagonals the eigenvalues  $\lambda_k$ . Although the dimension of  $\Delta$  is  $M \times M$ , only  $K$  eigenvalues are zero, with  $K$  the minimum of  $M$  and  $N$  [Venegas, 2001].

Multiplying the transpose of  $\mathbf{E}$  with the original data matrix  $F$  gives,

$$\mathbf{A} = \mathbf{E}^T \times F \quad (6.4)$$

Rows of  $\mathbf{A}$  are of length  $N$ , the number of storm cells. These rows are referred to as Principle Components.

<sup>7</sup> In the more traditional spatial-temporal EOF analysis is  $N$  the number of time steps and  $M$  the number of locations.

The variance explained by each mode  $k$ , is proportional to the eigenvalue  $\lambda_k$ :

$$\% \text{ Variance Mode } k = \frac{\lambda_k}{\sum_{k=1}^K \lambda_k} \times 100 \quad (6.5)$$

The first mode explains most of the variance and is the most easily to interpret. All other eigenvectors are designed to be orthogonal on this first eigenvector. This implies that the new orthogonal basis is not physical relevant per se, see Venegas [2001] for further details.

#### 6.3.2.1 EOF analysis: variability of environment

For our EOF analysis, we select the following storm environmental parameters, see Table 5.1 for an overview:

- Stability and buoyancy related parameters: CAPE, CAPE<sub>3km</sub>, CIN, the LI, the SI, the Level of Free Convection (LFC) and the Lifted Condensation Level (LCL).
- Shear parameters: Bulk wind shear (The magnitude of the 0-6 km wind velocity difference), the low wind shear (The magnitude of the 0-0.7 km wind velocity difference), and SRH in respectively the lowest 1 and lowest 3 km of the troposphere.
- Moisture parameters: RH and HDIV.

For each convective cell all of these environmental characteristics are calculated, which gives a data matrix of 3135 (convective cells)  $\times$  13 (convection parameters). Since for some cells CAPE and CIN are not available, only a subset of 3036 convective cells is used.

In Fig. 6.7 the EOFs (i.e. the eigenvectors) and the correlation matrix  $\mathbf{R}_{FF}$  is shown. Although the explained variance of the first two components amounts to more than 50%, the EOF analysis does not give a clear answer which environmental characteristics we have to cluster on. The first eigenvector has components of similar magnitude for each convective parameter. This is also the case for the second and third eigenvectors. Therefore it is difficult to estimate which convective variables explain most of the variance. The principle components (not shown) are easier to interpret. The first principle component is negatively correlated with CAPE (correlation coefficient of -0.77), and moderately positively correlated with the (0 to 6 km) bulk wind shear (correlation coefficient of -0.57). This indicates that these variables vary together, the strong shear and weak CAPE cells can be seen as typical found for a case like 22 June 2011. Since the cold front provides some lifting, not much CAPE is needed to initiate DMC. The strong CAPE and weak shear cells are more typical for a local convection case like 5 June 2011. The second (fourth) principle component is (negatively) positively correlated with the SRH parameters. Other principal components only show weak correlations with the variables chosen.

We conclude therefore, that besides the discussed relation between CAPE and bulk wind shear, that the EOF is not consistent enough for the selection of a subset of parameters (see Fig. 6.7b). The correlation matrix shows, however,

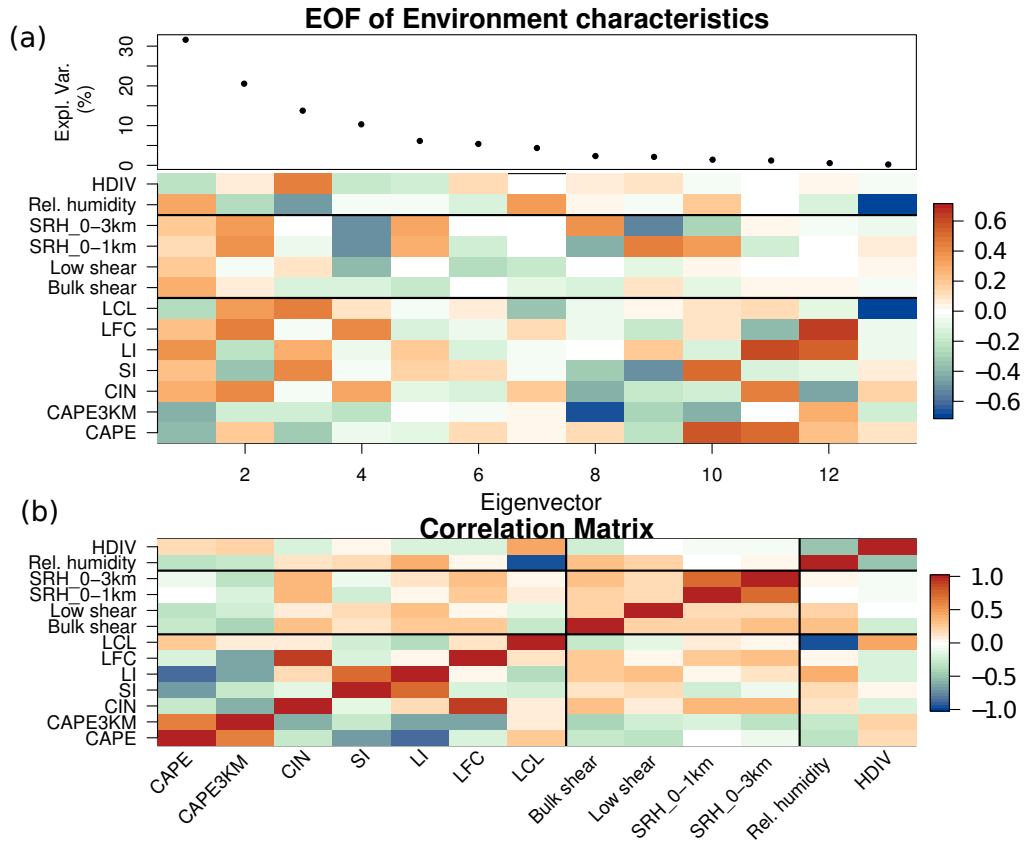


Figure 6.7: (a) Explained variance of each of the eigenvectors (top) and Eigenvectors as function of convective parameter (bottom). (b) Correlation matrix for the convective parameters. In (a) and (b) from top to bottom and from right to left the following variables are used: HDIV, the RH, SRH in respectively the lowest 1 and lowest 3 km of the troposphere, the low wind shear and the bulk wind shear, LCL, LFC, LI, SI, CIN, CAPE<sub>3km</sub>, and CAPE. All these parameters are calculated in a 31x31 grid point environment of the updraft, prior to start of tracking.

that as expected there are large correlations between the different buoyancy parameters. CAPE for example is moderately correlated with  $CAPE_{3km}$  (0.63) and negatively correlated with the SI (-0.64) and LI (-0.87). The height of the LFC is strongly correlated with CIN. Similar correlations are found between the shear parameters and moisture parameters. The two SRH parameters (0.72) are highly correlated. There is only a small correlation (coefficient of 0.29) between the bulk wind shear and the wind shear as measured by the wind velocity difference in the lowest 10 model levels.

### 6.3.2.2 EOF analysis: variability of storm properties

For the EOF analysis of the storm cell properties we use the following variables, see Table 5.2 for more details:

- Intensity measures, like the maximum vertical velocity  $w$ , the maximum Gaussian filtered vertical velocity (which is used in tracking), and the maximum and minimum PV anomaly associated with the convective cell.
- Extremes associated with the storm cell; precipitation, as measured in one hour around the maximum Gaussian filtered velocity, and wind gust, as measured by  $V_{gust}$ .
- The longitudinal and latitudinal location of the storm cell
- The (horizontal) speed at which the cell moves, the correlation coefficient  $r$  between PV and  $w$  and the lifetime of the convective cell.

The eigenvectors and corresponding explained variances are shown in Fig. 6.8a. The explained variance of the first eigenvector amounts to more than 35%, moreover it is clearly separated from the other eigenvectors, which have a much lower explained variance. This eigenvector seems to select especially the intensity measures (maximum  $w$ , maximum Gaussian filtered  $w$ , maximum and minimum PV). Moreover, there is also a significant contribution of the precipitation rates and wind gusts to this first eigenvectors. For the second EOF the correlation coefficient  $r$  dominates the EOF, and the cell speed contributes most to the third eigenvector. Similar findings are found for the principle components. The first principle component is strongly negatively correlated (-0.92) with the Gaussian filtered vertical velocity, and with the maximum PV (-0.88). This principle component is also significantly negatively correlated (-0.70) with precipitation rates associated with convective cells. This shows that most of the variation in storm properties can be associated with the intensity measures. The second principle component is strongly negative correlated (-0.81) with the correlation coefficient  $r$ . Note, however, that this mode only explains 12.2% of the variance. The third principle component is, as was the case for the third EOF, associated with the cell movement speed. There is a negative correlation of approximately -0.82 for this principle component with the cell speed.

The correlation matrix also indicates that the different intensity measures are correlated with each other (Fig. 6.8b). The correlation coefficient of 0.74 (-0.68) implies that intense updrafts (with strong Gaussian filtered vertical velocity

w) generally also have strong PV maxima (minima). There is also a moderate correlation with the precipitation rates and the maximum PV anomalies (0.58). Only weak correlations are found between the PV anomalies and wind gusts (0.23). The other storm properties, like cell movement speed and the lifetime (duration) of a storm cell, are not significantly correlated with each other.

### 6.3.3 *Choice of convective variables*

The EOF analysis for the storm environmental parameters did not give a satisfying answer on which parameters we should rely the clustering of the composites. We therefore select the parameters on a more dynamical basis. Since the shear parameters are expected to have a huge influence on the storm cell morphology, we select both of the SRH parameters and the bulk wind shear. From the instability/buoyancy parameters we select only CAPE and CIN, since these are the most used parameters and the other stability are highly correlated with these two variables. Lastly we select the HDIV as a measure for atmospheric moisture. From the storm properties, the EOF analysis indicated that intensity measures like the PV maximum explain most of the variance. Moreover, in previous chapters it was shown that these intense convective cells have significant different characteristics. Therefore, the focus will be on these intensity measures, i.e. the cells with intense Gaussian filtered vertical velocity, strong PV anomalies and cells associated with severe precipitation.

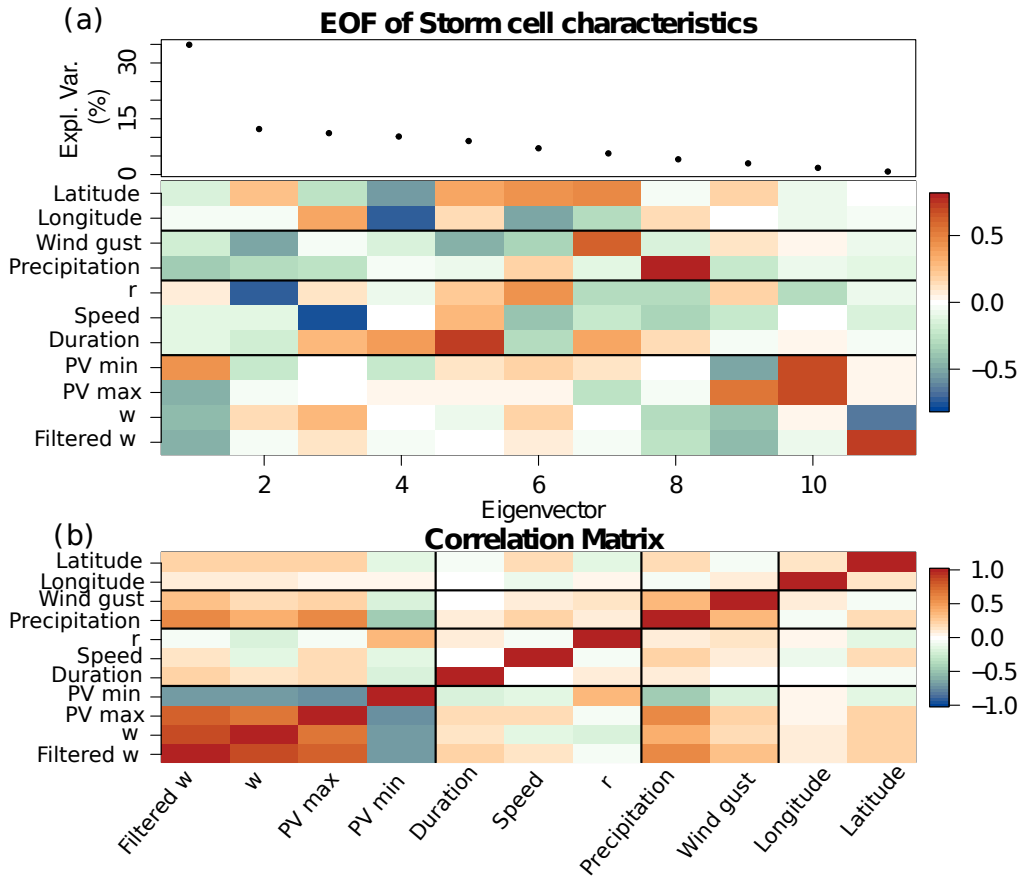


Figure 6.8: (a) Explained variance (in %) of each of the eigenvectors (top), Eigenvectors as function of parameter (bottom). (b) Correlation matrix for the storm properties variables. In (a) and (b) from top to bottom and from right to left the following variables are used: The latitude and longitude of the convective cell, the wind gust associated with the convective cell, the precipitation rate associated with the convective cell, the average (over storm duration) correlation coefficient  $r$ , the horizontal movement speed of the storm cell, the duration in minutes, the minimum and maximum PV (in a  $5 \times 5$  grid point environment around the updraft), the maximum vertical velocity during the lifetime, and the maximum Gaussian filtered vertical velocity.

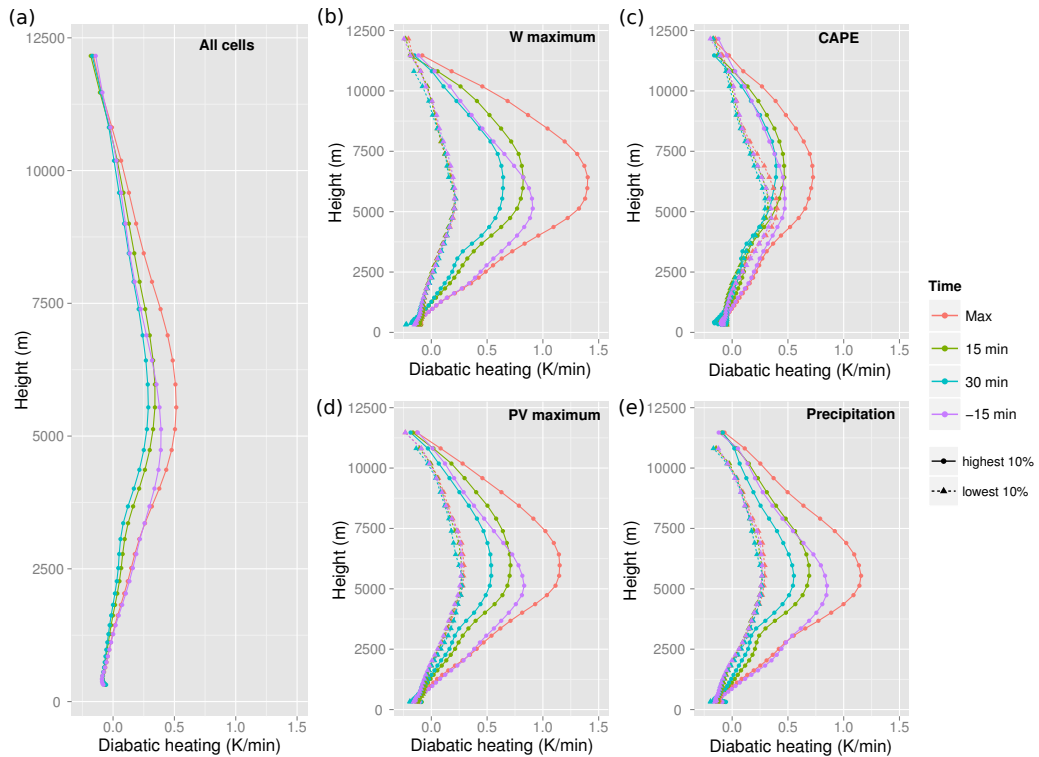


Figure 6.9: Composite of the vertical diabatic heating (in K/min) profile for 4 different time steps, (a) for all cells, and (b-e) for the convective cells with the lowest 10% and highest 10% (b) Gaussian filtered vertical velocity  $w$ , (c) CAPE, (d) PV maximum and (e) precipitation rates.

## 6.4 COMPOSITES

### 6.4.1 Diabatic forcing

Before we look at the composites of PV and corresponding flow anomalies, we first look at composites of the vertical profile of the diabatic heating  $\dot{\theta}$ . The diabatic heating can be seen as a forcing for the PV anomalies, since it is the tilting of horizontal vorticity against a gradient of  $\dot{\theta}$  which generates the PV anomalies (see Section 2.4.3 and Section 4.2).

Diabatic heating rates  $\dot{\theta}$  (Fig. 6.9a) maximise in the middle troposphere at the maximum of the Gaussian filtered  $w$ . This is at about 5.5 km height, with average maximum diabatic heating rates of about 0.55 K/min. The height of maximum  $\dot{\theta}$ , changes from about 5 km height 15 minutes before the maximum in Gaussian filtered  $w$ , to about 5.5 to 6 km height 15 to 30 minutes after the maximum in  $w$ .

A similar pattern is seen when selecting the 10% most intense cells or the 10% weakest cells of the vertical velocity  $w$  (Fig. 6.9b). Main difference is that the heating rates are much larger, up to 1.5 K/min for the 10% cells with largest vertical velocity. This maximum is also located slightly higher up in the troposphere (at a height of about 6.25 km). Not much temporal differences are visible

for the 10% weakest vertical velocity cells. For all times the diabatic heating rate maximum is about 0.2 to 0.25 K/min.

CAPE is an indicator of instability and moderately correlated with the vertical velocity, therefore one might expect similar large differences. However, not much differences in the magnitude of the vertical diabatic heating profile for strong CAPE cells is visible (Fig. 6.9c), compared to weak CAPE cells. There are however, clear differences in the height of the maximum. The diabatic heating maxima is higher in the troposphere for the intense CAPE cells (6.5 km) compared with weak CAPE cells (5.0 km). This is an indicator for deeper updrafts for these strong CAPE cells.

For intense PV (Fig. 6.9d) and intense precipitation cells (Fig. 6.9e) the maximum  $\dot{\theta}$  is slightly smaller than for the strong vertical velocity cells, about 1.2 K/min at the 0 time step. The general structure and the temporal evolution are, however, very similar as those intense  $w$  cells.

#### 6.4.2 General evolution

Figure 6.10 shows the composite over all 3135 tracked cells from the 9 selected cases. It is remarkable that even with this large amount of cells a clear PV dipole is visible, which is orientated as expected along the West to East axis (remember that we rotated the cells in such way that the wind shear is eastwards). The orientation is exactly as expected from the hypothesis in Fig. 4.1, with a positive PV anomaly in the South and a negative PV anomaly in the North. The updraft is almost perfectly in the centre between the positive and negative PV anomaly for up to the 0 time step (Fig. 6.10a-c). 30 minutes before the maximum Gaussian filtered vertical velocity (Fig. 6.10a), the correlation coefficient  $r$ , defined in Eq. 4.4 is about 0.25. Slightly later, at the -15 and the 0 time step, the updraft stays approximately centred (Fig. 6.10b). No large differences are found up to the time of maximum Gaussian filtered vertical velocity (Fig. 6.10c). The wind velocity anomalies are relatively small compared to the average environment wind, which is on the order of about 13 to 14  $\text{ms}^{-1}$ . The maximum wind velocity anomalies, however, are 2.45, 2.31 and 3.73  $\text{ms}^{-1}$  at respectively -30, -15 and at the 0 time step. This maximum wind velocity anomaly is located at the updraft in between the positive and negative PV pole.

Of the 3135 storm cells at the time of maximum Gaussian filtered vertical velocity (Fig. 6.10c), 2605 (83.1%) cases survive for at least 15 minutes (Fig. 6.10d), but only 1124 (35.9%) cells survive for 30 minutes (Fig. 6.10e) and 353 (11.26%) cells for 45 minutes (Fig. 6.10f). Note that the intensification phase of the storm cell is much shorter than the decay phase. Whereas at the -30 minute time step only 580 storm cells contribute to the composite, about double that number (1124) contribute in the composite of 30 minutes after the maximum Gaussian filtered vertical velocity.

The magnitude of the PV maximum stays approximately equal, the maximum PV decreases from 4.85 PVU (at maximum Gaussian filtered velocity) to 4.21 PVU (45 minutes after maximum Gaussian filtered  $w$ ). In previous chapters we found that especially long lasting cells show a more monopole structure, in which the

positive PV pole is dominant compared to the negative pole. We also see this for the composite for the longer lasting convective cells. The updraft is moved slightly northwards in Fig. 6.10d and f. As for the composites for the 22 June 2011 case, the positive PV anomaly clearly dominates, especially after the maximum  $w$  intensity: at the 30 minutes time step (Fig. 6.10e) the positive PV anomaly (4.03 PVU) is almost twice as large as the negative PV anomaly (2.18 PVU). This asymmetry is even stronger 45 minutes after the Gaussian filtered vertical velocity (Fig. 6.10f). For the 30 minutes and 45 minutes time steps there are only significant cyclonic flow anomalies, which are associated with the positive PV pole.

The main question asked in Chapter 1 was if significant and consistent PV anomalies exist. This chapter showed that there are significant PV anomalies during the whole convective lifetime. Average anomalies are on average one order of magnitude larger than synoptic scale values (in the middle troposphere), which are of about 0.5 PVU. The main goal was to analyse whether there are statistically balanced dipoles, with associated flow anomalies. The composites in Fig. 6.10 show that even when averaging over a lot of convective storms in different environments we get a clear PV dipole with associated cyclonic and anticyclonic flow anomalies. However, one has to note that the variability in the PV anomalies is quite large. This is confirmed by the recurrence analysis, p-recurrence values are comparable to that of the composites in Chapter 5. The PV maxima (minima) are about 61-63.5% (54.5-59.5%) p-recurrent.

#### 6.4.3 Evolution of extreme cells

For the 5 and 22 June cases, particularly the intense cells showed a “supercell structure” (Chapter 4 and Chapter 5). The diabatic heating rates for intense  $w$  cells, intense PV cells and convective storms with strong precipitation rates are very similar (Fig. 6.9). Moreover, these different kind of intensity measures are highly correlated (Fig. 6.8b). One would therefore expect also similar PV composites. This is indeed the case as shown in Fig. 6.11.

For all three intensity measures, the positive PV pole is colocated with the updraft, even at the 0 time step. For the 10% strongest vertical velocity cells (i.e. the cells with a vertical velocity above  $7.71 \text{ ms}^{-1}$ , see Fig. 6.11a), the PV maximum (11.6 PVU) is clearly larger than the PV minimum (-5 PVU). Because the 10% strongest cells are selected, there are 314 storm cells included in these composites. A half an hour later (Fig. 6.11b), the positive PV anomaly is only slightly lower (9.1 PVU), while the negative PV anomaly is almost half (-2.7 PVU) the value at the Gaussian filtered vertical velocity. About 139 (approximately 44%) convective cells survive for 30 minutes, this survival rate is larger compared to all cells (which is about 35%, see Section 6.4.2).

Strong PV cells (Fig. 6.11c-d) show a similar morphology. Maximum PV values are even larger for the intense PV composite, with a maximum of more than 14 PVU at the 0 time step (Fig. 6.11c). The number of cells at the 30 minute time step is also larger compared to the intense vertical velocity cells, about 149 (47.5%) of the convective cells survives for 30 minutes after the Gaussian filtered vertical

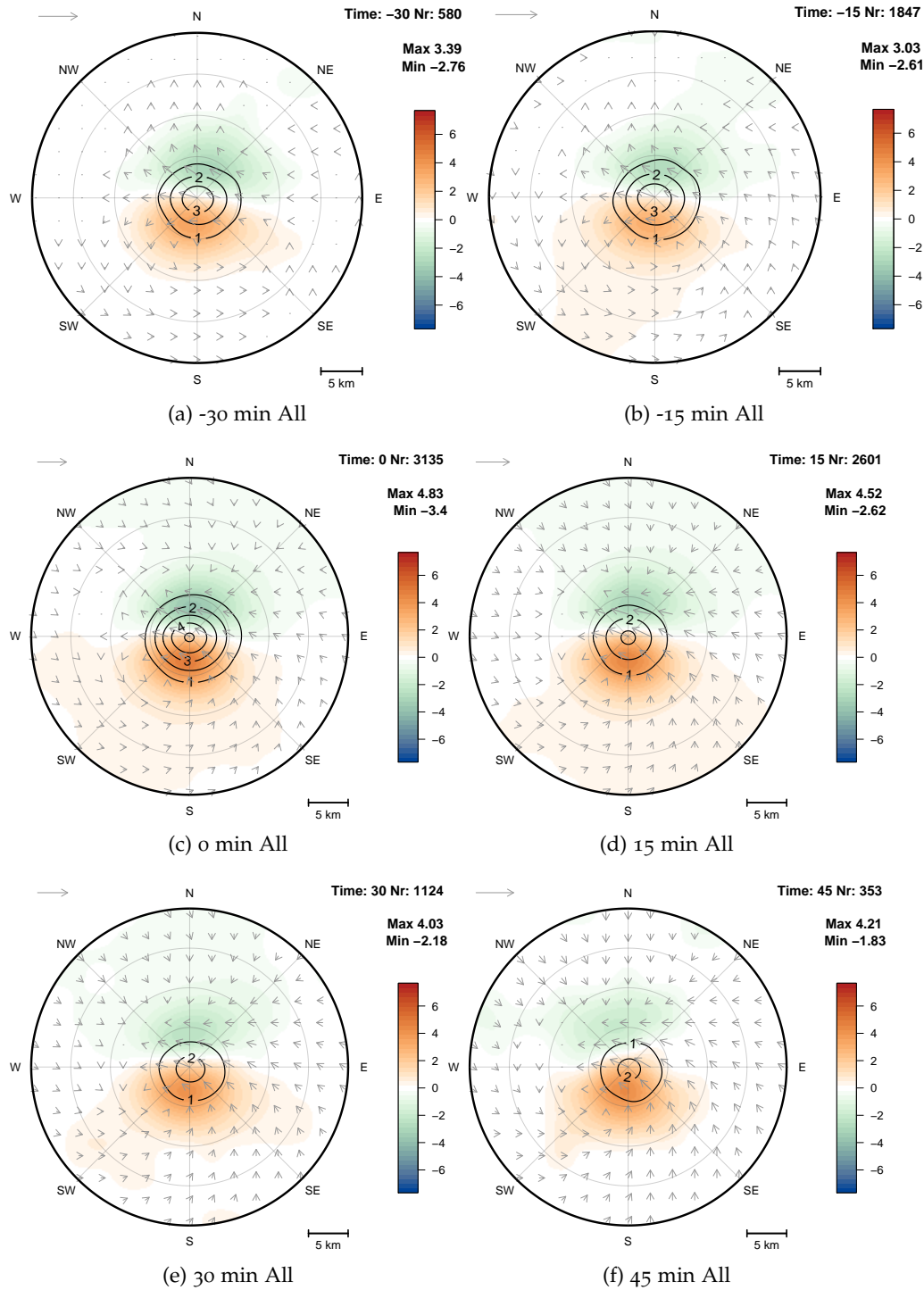


Figure 6.10: General evolution of storm cells for different time steps, where the 0 time step indicates the time step with maximum (Gaussian filtered) vertical velocity. Filled contours denote PV anomalies (in PVU), contour lines indicate vertical velocity (non-filtered, in m/s) and arrows denote horizontal wind velocity anomalies. A reference vector of 5 m/s is added at the top-left. Indicated at the top-right: the time (in minutes after the maximum Gaussian filtered vertical velocity), the number of cells in the composite, and the spatial maximum and minimum PV of the composite.

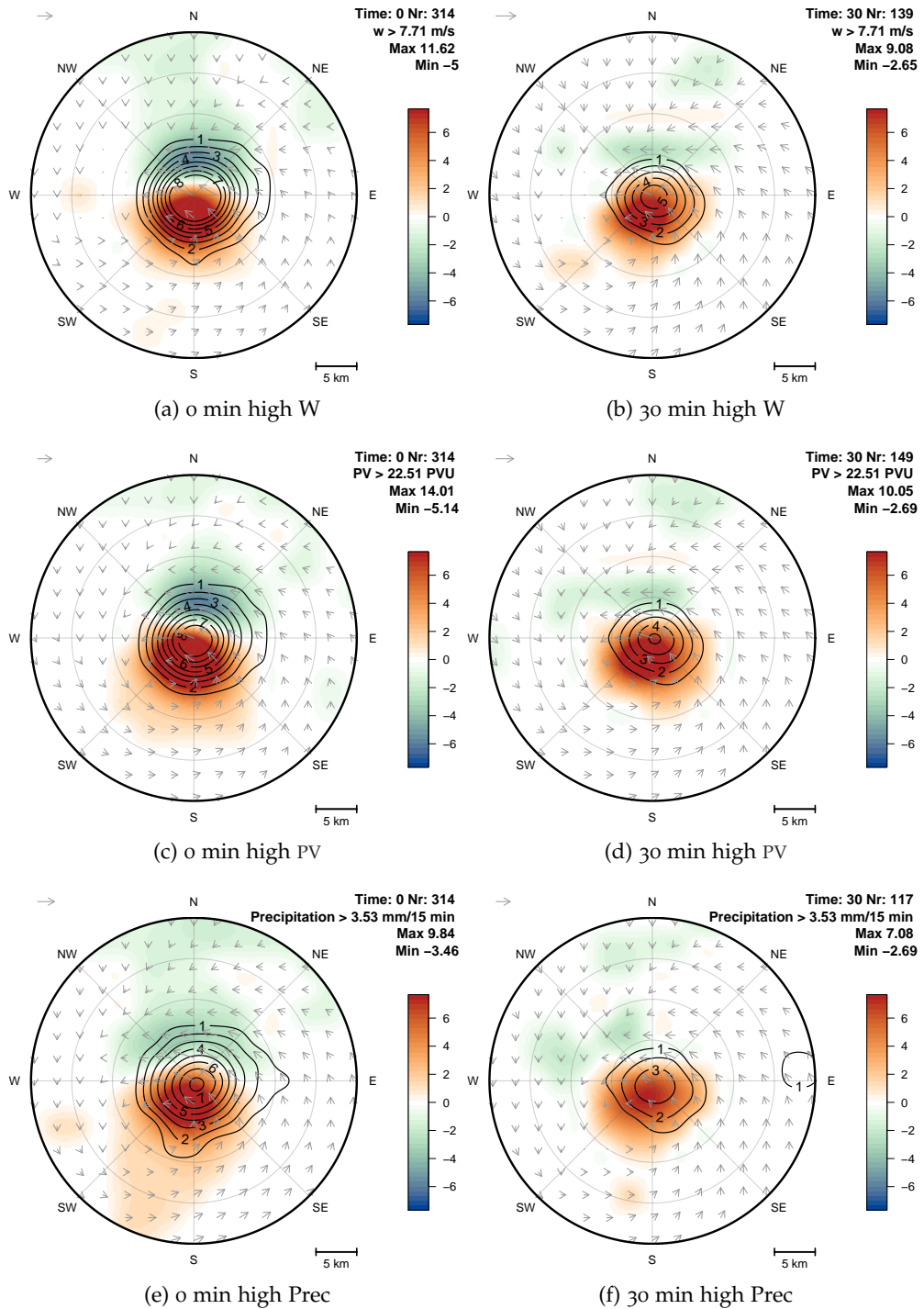


Figure 6.11: Evolution of storm cells for the cells with the 10% strongest values of Gaussian filtered vertical velocity, PV and precipitation, for different time steps. Here the 0 time step indicates the time step with maximum (Gaussian filtered) vertical velocity. Filled contours denote PV anomalies (in PVU), contour lines indicate vertical velocity (non-filtered) anomalies (in m/s) and arrows denote horizontal wind velocity. A reference vector of 5 m/s is added at the top-left. Indicated at the top-right: the time (in minutes after the maximum Gaussian filtered vertical velocity), the number of cells in the composite, the threshold of the respective variable used in the composite, and the spatial maximum and minimum PV of the composite.

velocity. As for the intense vertical velocity cells, there is a strong asymmetry in the PV dipole, the positive PV anomaly is almost four times as strong as the negative PV anomaly at the 30 minutes time step (Fig. 6.11d). Moreover, the maximum wind velocity anomaly also increases, it is about  $7.7 \text{ ms}^{-1}$  in Fig. 6.11c and  $5.5 \text{ ms}^{-1}$  in Fig. 6.11d. Consistent with the strong asymmetry in the PV dipole, only a clear cyclonic flow around the positive PV anomaly is observed.

Strong precipitation cells (Fig. 6.11e-f) also are strongly asymmetric. This asymmetry and the corresponding PV anomalies are less strong compared to the strong vertical velocity and intense PV cells. However, the PV anomalies are still two to three times as strong compared to the composites over all cells. In conclusion, we see that the morphology of intense cells shows a clear dominant “supercell” structure: an intense long-lasting rotating updraft. Although this is trivial for the intense PV composite, since we selected the 10% cells with the largest PV maxima, it indicates again that the different intensity measures are correlated.

Selecting other thresholds for making the composites, namely the 95% and 97.5% quantiles, gives even stronger PV composites and a clearer monopole structure (Fig. 6.12). In this figure, only the composites for strong PV cells (Fig. 6.12a-b) and strong precipitation cells (Fig. 6.12c-d) are plotted, for the 30 minutes time step. Even 30 minutes after the Gaussian filtered vertical velocity, the intense PV convective cells have an average maximum PV anomaly of 12 PVU for the 5% most intense PV storms (Fig. 6.12a) and almost 14 PVU for the 97.5% quantile storms (Fig. 6.12b). Although there is still a small negative PV anomaly visible in the composite of Fig. 6.12a, only the cyclonic flow is significant. Flow anomalies are also larger, with maxima of over  $7 \text{ ms}^{-1}$ , even after 30 minutes. At the time of maximum Gaussian filtered vertical velocity (not shown), the PV maximum is even larger (almost 20 PVU for the 2.5% strongest PV cells, with flow anomalies of more than  $9 \text{ ms}^{-1}$ ). The monopole morphology, however is less clear.

The composites of convective cells with large precipitation rates (Fig. 6.12c-d) are again very similar, although maximum PV anomalies are slightly smaller; 8.6 PVU and 10.0 PVU for the composite with the 5% and 2.5% strongest cells respectively. For these severe precipitation cells, there is a significant vertical velocity anomaly about 20 km downshear, indicating the generation of a new updraft downshear of the existing updraft.

#### 6.4.4 *Influence environment on storm cell morphology*

One of the hypotheses in this study is that strong shear and/or strong SRH is a good predictor for supercell like storms. Moreover, the wind shear might influence the morphology of the PV anomaly, too, by advecting the dipoles downshear. We therefore look at the composite for the convective cells with the 10% largest values for the buoyancy parameters CAPE and CIN, the shear parameters bulk wind shear and SRH (integrated over both the lowest 1 and the lowest 3 km of the atmosphere). For the moisture variable, HDIV, the composites are made for the 10% lowest values, because for DMC convergence is more

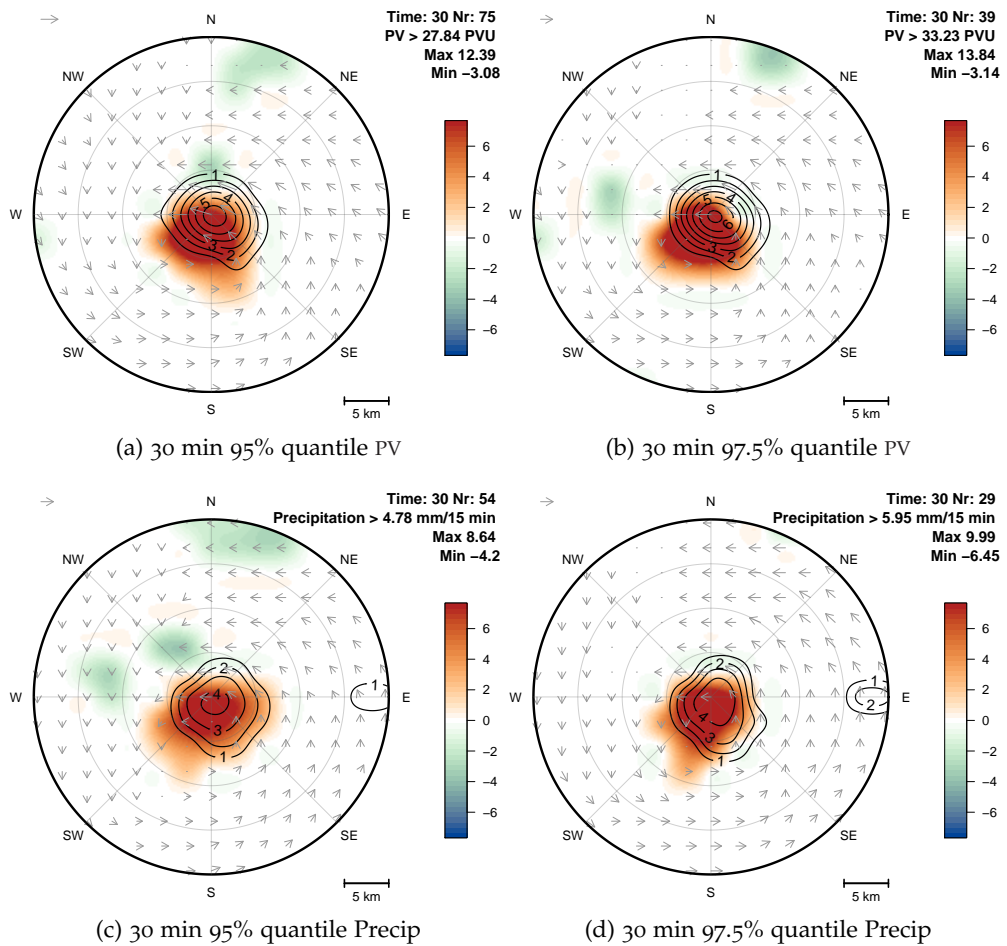


Figure 6.12: Composites of storm cells for the 95% and 97.5% quantiles thresholds of PV (a-b) and precipitation (c-d), 30 minutes after the maximum (Gaussian filtered) vertical velocity. Filled contours denote PV anomalies (in PVU), contour lines indicate vertical velocity (non-filtered) anomalies (in m/s) and arrows denote horizontal wind velocity. A reference vector of 5 m/s is added at the top-left.

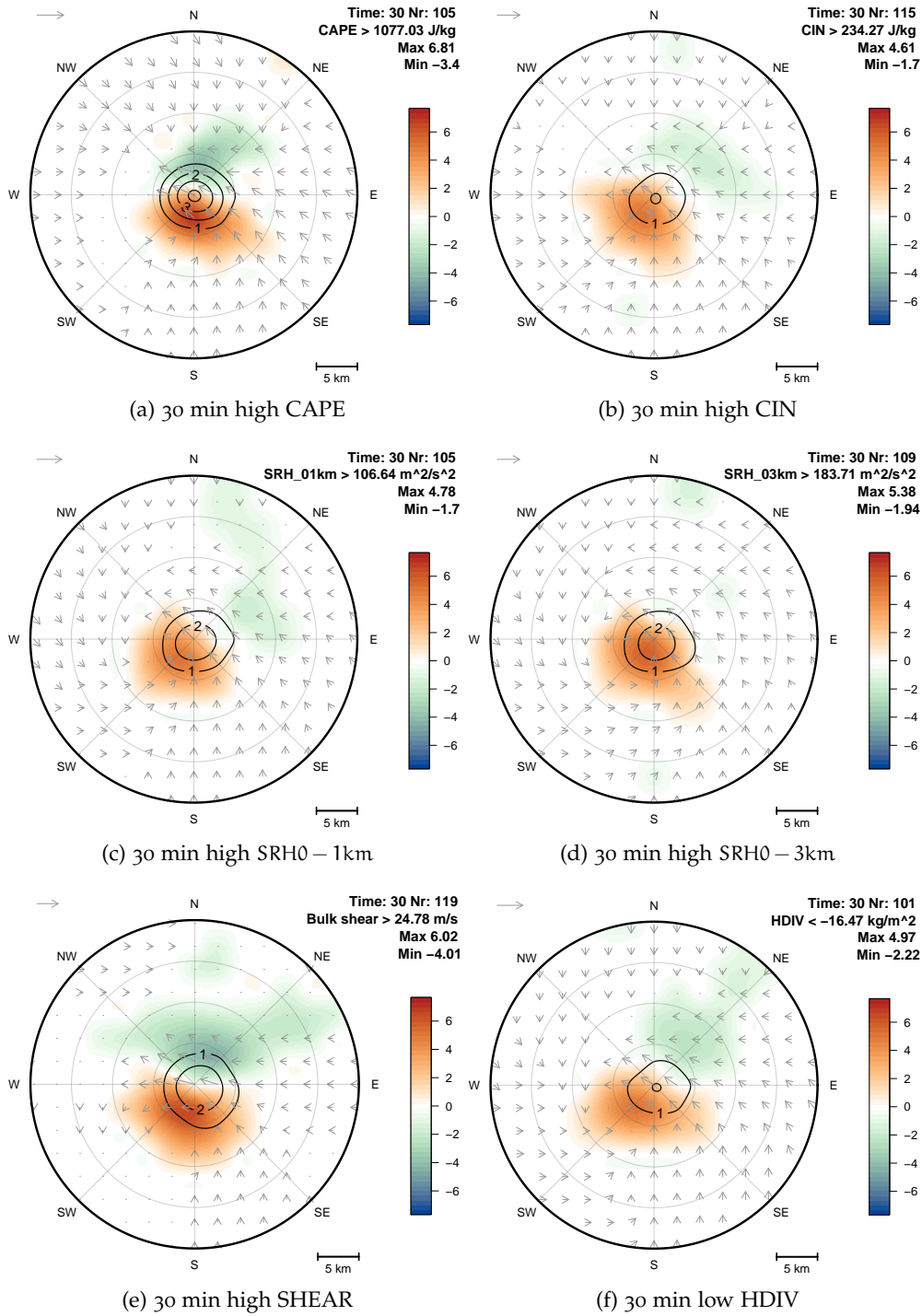


Figure 6.13: As in Fig. 6.11, but now for the evolution of storm cells for the 90% quantile thresholds of (a) CIN, (b) CAPE, (c) the 0 to 1 km SRH, (d) the 0 to 3 km SRH, (e) the bulk wind shear and (f) the 10% quantile of HDIV.

interesting as indicator for convection than divergence. For these composites, only the 30 minute time step is plotted in Fig. 6.13.

Although there is a moderate correlation between  $w$  and CAPE (correlation coefficient of about 0.49), the composite for strong CAPE cells (Fig. 6.13a) does not resemble that of the strong (Gaussian filtered)  $w$  storm cells. PV anomalies are less strong compared to the intense  $w$  composite, and although the positive PV pole is stronger than the negative PV pole (respectively 6.8 and -3.4 PVU), the updraft is almost centred in between the dipole. The updraft is of similar strength at the 30 min time step compared with the intense PV and intense precipitation composites, namely of about  $5 \text{ ms}^{-1}$ . For the composite using the convective cells with strong CIN (Fig. 6.13b) the asymmetry is clearer, although the PV anomalies are smaller. Remember that CIN is defined as the negative buoyancy up to the LFC (see Eq. 2.13). These large values indicate that the planetary boundary layer is very stable, significant lifting is necessary to initiate convection.

The composites of strong SRH cells (Fig. 6.13c-d), show a dominant positive PV anomaly, but not nearly as clear as for the intense PV and strong precipitation cells. Both the 0 to 1 km and 0 to 3 km integrated SRH composite, have a very similar morphology, with the main difference that for the former there is still a significant negative PV anomaly. The PV maximum is not much stronger as for the general composite in Fig. 6.10 (4.8 and 5.4 PVU for the 0-1 km and 0-3 km SRH respectively). For both composites, the PV dipole is slightly rotated in clockwise direction. We rotated every convective cell with the bulk wind shear difference between 0 and 6 km. Strong (positive) SRH indicates a clockwise hodograph, which explains the different orientation of the dipole.

For the convective cells with strong bulk wind shear (Fig. 6.13e), the PV dipole is more stretched out compared to the other composites we have seen so far. This is another confirmation that advection effects associated with the wind shear play a role in the formation of bands seen for e.g. for the 22 June case. The composite for the cells with the 10% lowest wind shear values are more local and the dipole is rotated counter-clockwise (not shown).

For the moisture variables like the HDIV there are little differences with the general composite in terms of magnitude of the PV anomalies. But, as for the strong SRH composites, the PV dipole is rotated clockwise. We did not find an explanation of this different orientation, HDIV is not correlated with the SRH variables (Fig. 6.7b), so that cannot be an explanation.

In conclusion, differences exist between convective cells in COSMO-DE initiated in different convective environments, but these differences are less clear as one might expect from the differences between strong and weak convective cells. Strong CAPE cells have stronger PV anomalies compared to general cells, but the PV anomalies are less strong than for intense cells. Moreover, the dipole asymmetry is also not that strong. Although there are hints of a more morphology structure in the composite of strong SRH, it is not as clear as compared to the intense cells discussed in Section 6.4.3. Studies of [Thompson et al., 2003] already indicated that besides strong SRH, also significant CAPE and bulk wind shear might be needed for formations of supercells. Moreover, they and others like Groenemeijer and van Delden [2007] found that the variability of environ-

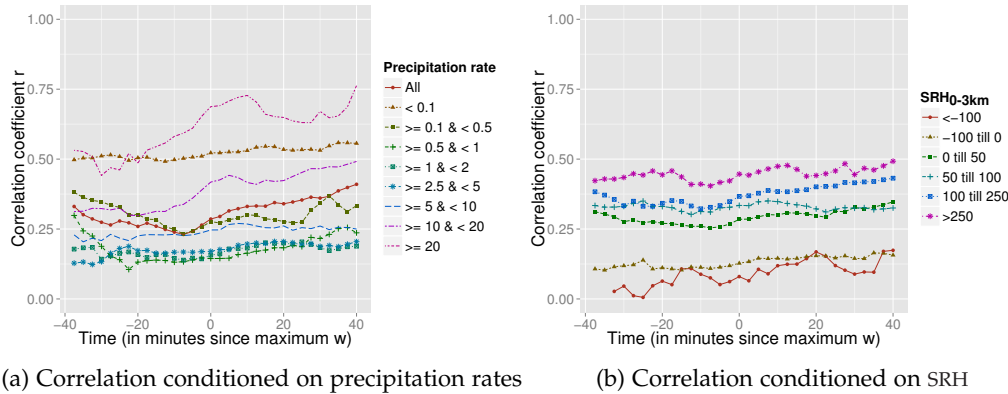


Figure 6.14: Correlation coefficient  $r$ , as defined in Eq. 4.4, between  $w$  and PV, as function of time (from the maximum Gaussian filtered vertical velocity). (a) For different thresholds for the precipitation rates (in mm/hour) and (b) for different threshold of the SRH (0 to 3 km height integrated, in  $\text{m}^2\text{s}^{-2}$ ). In (a) and (b) the different thresholds are indicated at the top right.

ments in which supercells are formed is large. Therefore a clustering using a combination of thresholds for different variables might be necessary to get a more “monopole” morphology found for intense cells.

#### 6.4.5 Properties extreme cells

We now go back to the intense cells. We have seen that in the intense cell composites the vertical velocity and the positive PV anomaly are colocated. Chapter 4 introduced the correlation coefficient  $r$  (see Eq. 4.4) as a measure of how much the updraft and the positive PV pole are colocated.

The average correlation coefficient as function of time since maximum Gaussian vertical velocity is plotted for different threshold of the precipitation rates in Fig. 6.14a. Especially for precipitation rates higher than 10 and 20 mm/hour there is a very strong correlation between the two variables. For convective cells with precipitation rates of at least 20 mm/hour, the average correlation coefficient  $r$  rises up to 0.75 after the maximum Gaussian filtered vertical velocity. This confirms the conclusion drawn in Section 6.4.3, that particularly intense cells have a more monopole structure. One has to note, however, that convective cells with small precipitation rates (<0.1 mm/hour and 0.1-0.5 mm/hour) have a high correlation coefficient, too. For these cells one has to be careful in interpreting  $r$ , since the vertical velocity and PV anomalies are generally small.

In Fig. 6.14b the correlation coefficient is plotted as function of time, but now for different SRH thresholds. We also see that the (0 to 3 km height integrated) SRH is generally not a very good predictor for the correlation coefficient. Values for  $r$  are on average only 0.3/0.4, and there is only a strong increase of  $r$  with increasing threshold of SRH. Largest correlation coefficients are found for the cells with significant negative SRH (larger than  $250 \text{ m}^2\text{s}^{-2}$ , light blue line in Fig. 6.14b). Another difference is that the increase in  $r$  over time is not that sudden as for the strong precipitation cells in Fig. 6.14a.

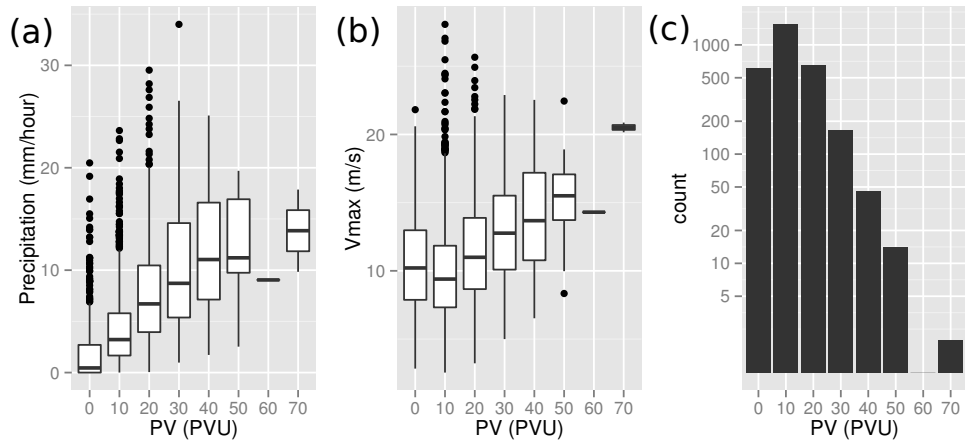


Figure 6.15: PV as predictor for severe convective weather. Binned PV for all convective cells is plotted against (a) model precipitation rates, (b)  $V_{gust}$  (measure of model wind gusts) and (c) the number of convective cells in each bin (note that the y-axis is on a logarithmic scale).

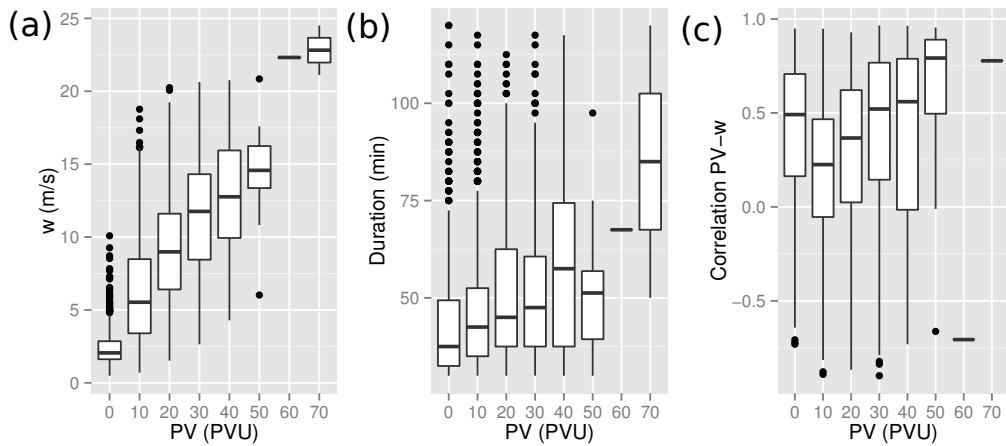


Figure 6.16: PV as predictor for supercells. Binned PV for all convective cells is plotted against (a) maximum  $w$ , (b) duration of the updraft (c) the correlation coefficient  $r$ . The bins are the same as in Fig. 6.15.

#### 6.4.6 PV as possible predictor for severe convective cells

This chapter showed that on average convective cells with strong PV anomalies have a supercell structure and that these cells have on average higher precipitation rates. Moreover, they are associated with stronger (horizontal) wind velocity anomalies. This could indicate that PV might be a good predictor for severe rain and/or wind gusts. To test this, the PV maxima (in bins of 10 PVU sizes) are plotted against the precipitation rate (as measured by the hourly precipitation rate around the maximum Gaussian filtered  $w$ ) and the wind gust (using  $V_{gust}$  around updraft). There is a clear correlation between the maximum PV anomaly associated with a storm cell and the precipitation rates (Fig. 6.15a). While convective cells associated with PV maxima of up to 10 PVU have on average only

precipitation rates of 2.5 mm/h, convective storms with PV anomalies of at least 30 PVU are associated with median precipitation anomalies of 10 mm/h. The correlation between  $V_{\text{gust}}$  and maximum PV anomalies is much less strong (Fig. 6.15b). The median wind gust associated with cells with PV values of 0-10 PVU is the same as the median wind gust associated with 20-30 PVU cells.

Besides as predictor for severe precipitation, the composites of intense cells suggested that PV might also be a predictor for supercells: a severe, persistent, and rotating updraft. Particularly intense PV cells are characterised by a monopole morphology. Although the maximum PV is correlated strongly with the maximum vertical velocity (Fig. 6.16a), correlation with the storm duration (Fig. 6.16b) is less strong.

## 6.5 SUMMARY AND DISCUSSION

This chapter discussed composites of PV anomalies associated with convective updrafts from nine severe weather events with different convective environments. The nine selected cases show a considerable spread in storm cell convective parameters like CAPE and SRH. The storm cells generated during these cases can be regarded as a representative sample of cells for COSMO-DE. An EOF analysis indicated that for storm cell properties most of the variance can be explained due to differences in storm intensity.

Even though there is a strong variation in synoptic background in these 9 cases, a clear PV dipole is still visible in the composites. As for the composites in Chapter 5 mainly long-lasting and intense convective cells show a “supercell” structure. This is independent whether the intensity is measured by the vertical velocity  $w$ , the maximum PV or by precipitation rates associated with the updraft. This “supercell” morphology increases consistently with increasing thresholds of the different intensity measures.

The storm cell morphology is less sensitive to ambient parameters. Strong SRH cells do show a more monopole “supercell” composite, but the asymmetry in the PV dipole is less clear than when clustering on intensity directly. Strong CAPE cells are associated with a stronger PV dipole but the morphology is not very different than from the composites over all cells. Clustering on the bulk wind shear, however, does give a more elongated dipole, as expected from the discussion of previous chapters.

Intense PV cells are associated with stronger precipitation rates, and slightly larger wind gusts. Moreover, PV is the one of the only parameters which shows some correlation with storm duration, although this correlation is not that strong. To conclude, PV might be a good predictor particularly for precipitation extremes. This will be investigated briefly in the next chapter.



## PV AS PREDICTOR FOR SEVERE WEATHER

---

*In this chapter we will explore the question of the practical use of Potential Vorticity (PV) as a predictor for severe weather on the convective weather scale. In the previous chapters the focus was on the coherent PV structure associated with storm cells. We hypothesise that the spectrum of potential enstrophy on the mesoscale can be used as a predictor for severe mesoscale weather extremes. The consistency of PV anomalies associated with Deep Moist Convection (DMC) during the summer months of 2011 till 2013 is investigated with help of the potential enstrophy spectrum. An anisotropic spectrum is calculated to analyse the general orientation of the PV anomalies.*

### 7.1 AIMS AND MOTIVATIONS

In previous chapters, it was shown that there are coherent PV anomalies associated with DMC. These PV anomalies are generated due to diabatic heating anomalies associated with convective cells. The amplitude of the PV anomalies increases for severe convection, moreover there is a “supercell” structure associated with intense storm cells. These results indicate that PV might be a predictor for extreme convective weather, especially for severe precipitation.

Bierdel [2012] showed that there is an increase in spectral energy for the horizontal kinetic energy spectrum on the mesoscale in the COSMO-DE weather model during DMC. Therefore it is interesting to investigate how a spectral quantity related to PV behaves during severe convection. One possible candidate is the potential enstrophy  $Q$ , a measure of the nonuniformity of the PV distribution. It is defined as the integral of the squared PV (e.g. Salmon [1998]):

$$Q \equiv \iint dx \Pi^2, \quad (7.1)$$

with  $x$  a 3d position vector and  $\Pi$  the PV. Note that sometimes the definition of  $Q$  contains an extra factor  $1/2$ .

Likewise, a moist potential enstrophy can be defined. The equivalent potential enstrophy  $Q_e$  is defined using the Equivalent Potential Vorticity (EPV)  $\Pi_e$ ,

$$Q_e \equiv \iint dx \Pi_e^2. \quad (7.2)$$

Spectra of the potential enstrophy might show a similar increase on the mesoscale as the kinetic energy spectrum. PV is only redistributed in the free atmosphere [Haynes and McIntyre, 1987, 1990], even under diabatic conditions. The PV dipoles associated with DMC are a manifestation of the redistribution. This global conservation property is not valid for the potential enstrophy, since it is the squared version of PV. Therefore, one would expect large anomalies on the convective weather scale.

We propose to use the spectral variance of the potential enstrophy on the mesoscale as a predictor for severe mesoscale weather extremes. The spectral variance is a good estimation of the PV anomalies over the whole model domain. A local estimator using PV might be more valuable, but because of the highly variable nature of PV on the convective weather scale (see Chapter 4), some averaging over a larger area is necessary. Moreover, the PV anomalies are associated with diabatic perturbations produced by the weather model. A Numerical Weather Prediction (NWP) model is not able to perfectly reproduce the amplitude and location of the diabatic perturbations (and associated precipitation). This gives another motivation to use a large scale predictor.

A further goal of this chapter is to investigate the consistency of PV anomalies on a larger scale. In Chapter 4 we showed that during the 22 June case, which has a relatively large ambient speed wind shear, bands of PV form along the direction of the wind shear. Similar bands are found for other cases with a large magnitude of the bulk wind shear, e.g. for 30 June 2012. An anisotropic measure of the potential enstrophy spectrum might be useful to quantify the anisotropy in the PV.

Main questions addressed in this chapter are:

- Q1 Can we quantify how consistent the orientation of the PV dipoles and bands is?
- Q2 Could PV be used as a predictor for severe convective weather like precipitation and wind gust extremes?

## 7.2 METHODOLOGY

To determine the one-dimensional spectrum of potential enstrophy and kinetic energy, we follow Errico [1985]. First, a two dimensional Fast Fourier Transform (FFT)  $C_{\kappa_x, \kappa_y}$  is calculated, with  $\kappa_x$  and  $\kappa_y$  the discrete wavenumbers for the  $x$  and  $y$  direction. This FFT is calculated on model level 24 ( $\approx 6$  km height) to minimise the effect of the orography on the spectrum. This is slightly lower than Bierdel et al. [2012], and about the height of maximum PV anomalies. Since the dynamics near the lateral boundaries are largely determined by the boundary forcing, we remove 50 grid points at each lateral boundary (i.e. we use the indicated area in Fig. 3.1a). For the calculation of the one-dimensional variance spectrum we average the wave coefficients  $C_{\kappa_x, \kappa_y}$  over an annulus  $A_\kappa$  in the wavenumber space

$$S(\kappa) \equiv \sum_{\kappa_x, \kappa_y \in A_\kappa} C_{\kappa_x, \kappa_y} C_{\kappa_x, \kappa_y}^* \quad (7.3)$$

Here,  $*$  denotes a complex conjugate,  $\kappa = \kappa_x^2 + \kappa_y^2$  is the one-dimensional wave number, and  $S(\kappa)$  is the spectral variance at wavenumber  $\kappa$ . The summation is performed over the annulus  $A_\kappa$  given by  $\kappa - \delta\kappa/2 < (\kappa_x^2 + \kappa_y^2)^{0.5} < \kappa + \delta\kappa/2$ .  $\delta\kappa$  is determined as the minimum value of  $\kappa_x$  and  $\kappa_y$ , which in our case is

$$\delta\kappa = \frac{2\pi}{\delta y} \frac{1}{N_y - 1} \quad (7.4)$$

with  $\delta y$  the grid distance (in the  $y$  direction) and  $N_y$  the number of grid points used in the FFT in the  $y$  direction (i.e. 361). This defines  $\delta\kappa$  and values of  $\kappa$  are given by,

$$\kappa = l\delta\kappa, \quad (7.5)$$

where  $l$  is an integer is an integer from  $0, 1, \dots, \frac{N_y}{2}$ . As in Errico [1985] we truncate the values of  $\kappa$  at  $\delta\kappa(N_y/2)$ , since otherwise some combinations of  $\kappa_x$  and  $\kappa_y$  would be missing, which could distort the one-dimensional spectrum. As in Errico [1985] and Bierdel et al. [2012], we define the one-dimensional spectrum  $E(\kappa)$  of the horizontal kinetic energy as half of the sum of the spectra of the variance  $u$  and  $v$  fields

$$E(\kappa) \equiv \frac{1}{2}[S_u(\kappa) + S_v(\kappa)]. \quad (7.6)$$

Equivalently, the one-dimensional (equivalent) potential enstrophy spectrum is defined as the spectrum of the variance of the PV (EPV) field.

Since the Fourier transform requires the data to have periodic boundary conditions, which is in generally not valid for PV on a limited area domain, the data should be detrended. We tested different methods. The detrending method used in Errico [1985] has large unrealistic values for the  $\kappa_x = 0$  and  $\kappa_y = 0$  wavenumbers, which might largely influence the calculation of the anisotropic spectrum. The method described in Salvador et al. [1999] is found more reliable. We detrend the raw data first by removing a plane regression. Since this does not guarantee that the data at one boundary is everywhere the same as the other boundary, a cosine filter function at the boundaries is applied which gradually forces the PV towards the mean value. Although this method will still affect the spectrum and might not always be physically realistic, high values at zero wavenumbers in the Fourier spectrum are most effectively removed. Low wavenumbers might strongly influence the anisotropy analysis, therefore a latitudinal mean (at each longitude) and a longitudinal mean (at each latitude) are subtracted before calculating the Fourier transform. There are no large differences in the 1D spectrum for the different detrending methods tested. The chosen method of detrending will give the best estimate of the anisotropy in the spectrum.

The composites provide a localised view on storm organisation. To determine the orientation of the PV dipoles and/or bands more quantitatively, an anisotropic Fourier spectrum is calculated. The goal is to find the direction of largest spectral variance. The Fourier spectrum of PV is then integrated for a specific direction, specified by the angle  $\beta$  with respect to the longitudinal axes, and over a specific wavelength (16 to 44 km),

$$S(\beta) = \int_{\kappa=2\pi/(16\text{km})}^{\kappa=2\pi/(44\text{km})} \hat{\Pi}(\kappa, \beta) d\kappa \quad (7.7)$$

where  $\hat{\Pi}(K, \beta)$  is the 2D Fourier spectrum of the potential enstrophy at the wavenumber  $\kappa \equiv (\kappa_x^2 + \kappa_y^2)^{0.5}$ , where  $\kappa_x$  and  $\kappa_y$  are the longitudinal and meridional wave numbers, respectively. A schematic overview of the calculation of the anisotropic spectrum  $S$  can be found in Fig. 7.1. The choice of the wavelength

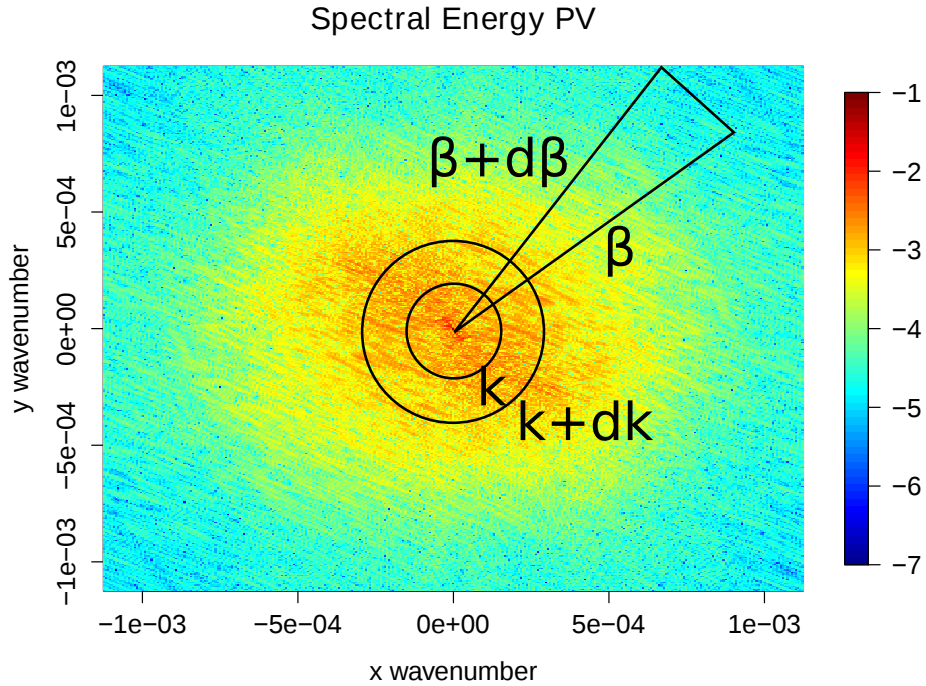


Figure 7.1: Schematic depiction of calculation of spectral energy  $S$  for a specific angle  $\beta$ , in a specific wavelength range  $\kappa$  till  $\kappa + d\kappa$ .

band is such that the lower limit is larger than the effective resolution of the model. The effective resolution of a weather model is about 5-7 times the grid spacing, or 10-15 km for the COSMO-DE model [Bierdel et al., 2012]. Moreover, the wavelength should be characteristic for the size of the dipoles, and therefore it should not be too large. The upper limit of 44 km should be large enough to capture the size of convective storms.

### 7.2.1 Spectral severe weather predictors

We calculate the one-dimensional kinetic energy, potential enstrophy and equivalent potential enstrophy spectra from COSMO-DE-EPS data on model level 24. We do this for each ensemble member and for each forecast hour of the forecasts initiated at 0 h and 12 h UTC, during the summer months (June, July and August) of 2011, 2012 and 2013. In order to estimate how far the (equivalent) potential enstrophy spectrum and the kinetic energy spectrum are away from typical spectra we use:

- The estimation of the spectral slope on the mesoscale. As in Bierdel et al. [2012] we calculate the one-dimensional spectrum for each ensemble member of COSMO-DE EPS. We fit a linear trend on a log-log scale between 20 and 200 km to the ensemble mean spectrum. The slope of this fit is used as a predictor. For the kinetic energy spectrum, the slope is  $-5/3$  on the

mesoscale. Subsequently in this chapter, the term ‘spectral slope’ is used to describe the slope of linear fit to the spectral variance.

- The ensemble and spatial mean of the spectral variance  $S(\kappa)$  between 16 and 44 km is:

$$\bar{S}_{\text{convective}} \equiv \frac{\sum_{e=1}^N \int_{\kappa=2\pi/(16\text{km})}^{\kappa=2\pi/(44\text{km})} S_e(\kappa) d\kappa}{N \int_{\kappa=2\pi/(16\text{km})}^{\kappa=2\pi/(44\text{km})} d\kappa}.$$

Here  $S_e(\kappa)$  denotes the spectrum of ensemble member  $e$  at wavelength  $\kappa$ , and  $N$  is the number of ensemble members.  $\bar{S}_{\text{convective}}$  is an estimate how large the spectral variance is on the convective weather scale. Since this can vary a lot, the  $\log_{10}$  is taken as a predictor, not directly the value itself.

### 7.3 SPECTRA FOR THE SEVERE WEATHER CASES

We will now discuss typical spectra associated with DMC, using the two weather cases discussed in Chapter 4 and Chapter 5. The horizontal kinetic energy spectrum can roughly be divided into two parts: On large scales the spectral slope consistently approaches -3, while on smaller scales (about 2 till 300-400 km) observations show that the spectral slope is about -5/3 [Nastrom and Gage, 1985]. Research of Bierdel et al. [2012] showed that the COSMO-DE NWP is capable of reproducing the -5/3 power law commonly observed on the mesoscale. During severe convection, however, the spectrum in COSMO-DE flattens. We have reproduced the spectrum of the horizontal kinetic energy in Fig. 7.2 for the 5 and 22 June 2011 weather cases. While at 10 UTC the mesoscale spectral slope between 20 and 200 km is about -5/3, the spectrum is much flatter at 17 UTC, especially for the 5 June 2011 case. Bierdel [2012] found that the minimum spectral slopes during the day are -1.1 and -1.3 for the 5 and 22 June case respectively.

One might expect a similar flattening of the spectrum for the Potential Enstrophy Spectrum (PES). In Fig. 7.3 the PES is plotted for the two weather cases. There is no theoretical argument and/or observational evidence that there must be a constant slope for the potential enstrophy spectrum. In the late morning, at 10 UTC, the spectrum for both cases is almost flat. For the 5 June case, there is a slight maximum in spectral variance at about 20km. At 17 UTC this maximum has displaced to smaller scales at about 15 km and has become much stronger. This maximum implies that there is more spectral variation at smaller scales than at the larger synoptic scale. Seen from the case study in Chapter 4 and from the composites, this might not come as a surprise because of the large variations ( $\mathcal{O}(10)$  times larger than synoptic anomalies) of PV on the convective weather scale. For the 22 June case a similar trend is seen, although the maximum is not that strong as on 5 June, and the maximum is located at a larger wavenumber ( $\approx 20$  km). Furthermore, the maximum is broader compared to the potential enstrophy spectrum of the 5 June 2011 case. These findings are consistent with the formation of the larger scale mesoscale PV bands on this day (Fig. 4.4a).

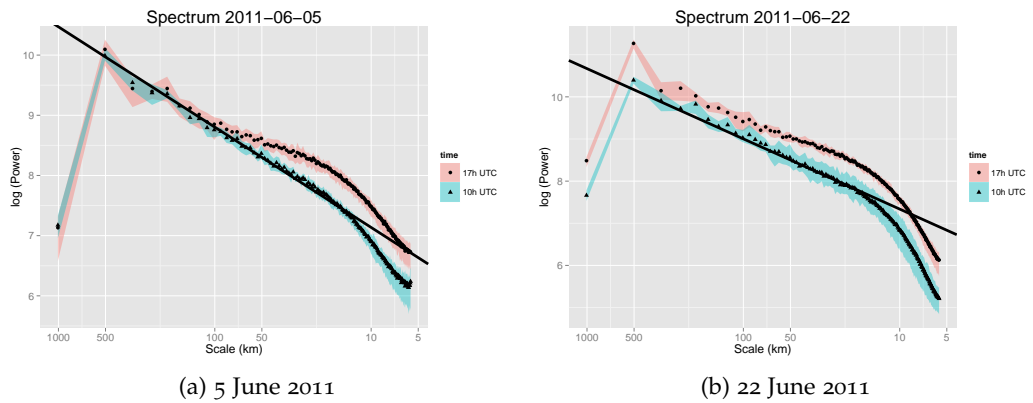


Figure 7.2: Horizontal kinetic energy spectra for the 5 June and 22 June 2011 cases discussed in Chapter 4 at 10 and 17 UTC. Data of COSMO-DE-EPS are used, the black triangles (dots) indicate the mean value over the ensemble for 10 UTC (17 UTC) and the coloured area indicates the 5% to 95% confidence interval. The thick solid black line indicates a reference line with a spectral slope of  $-5/3$ .

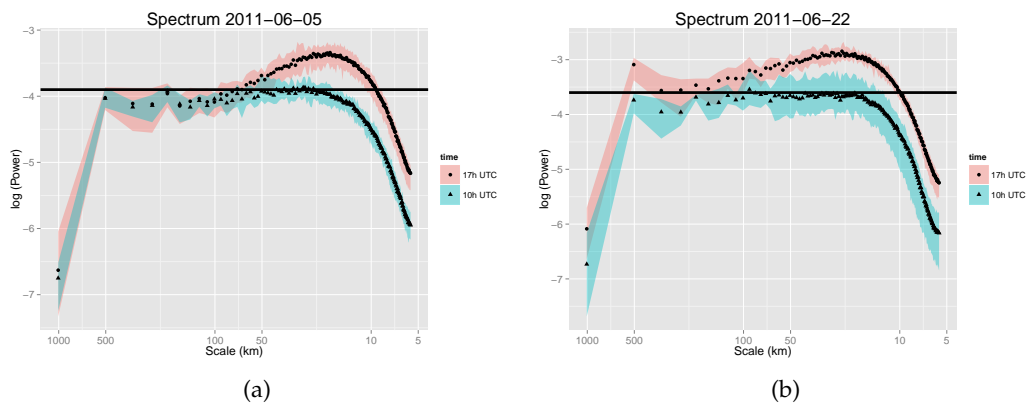


Figure 7.3: Potential enstrophy spectra for the 5 June and 22 June 2011 cases discussed in Chapter 4 at 10 and 17 UTC. Data of COSMO-DE-EPS are used, the black triangles (dots) indicate the mean value over the ensemble for 10 UTC (17 UTC) and the coloured area indicates the 5% to 95% confidence interval. The thick solid black line indicates a reference line with zero spectral slope.

7.3.1 Anisotropy in spectrum

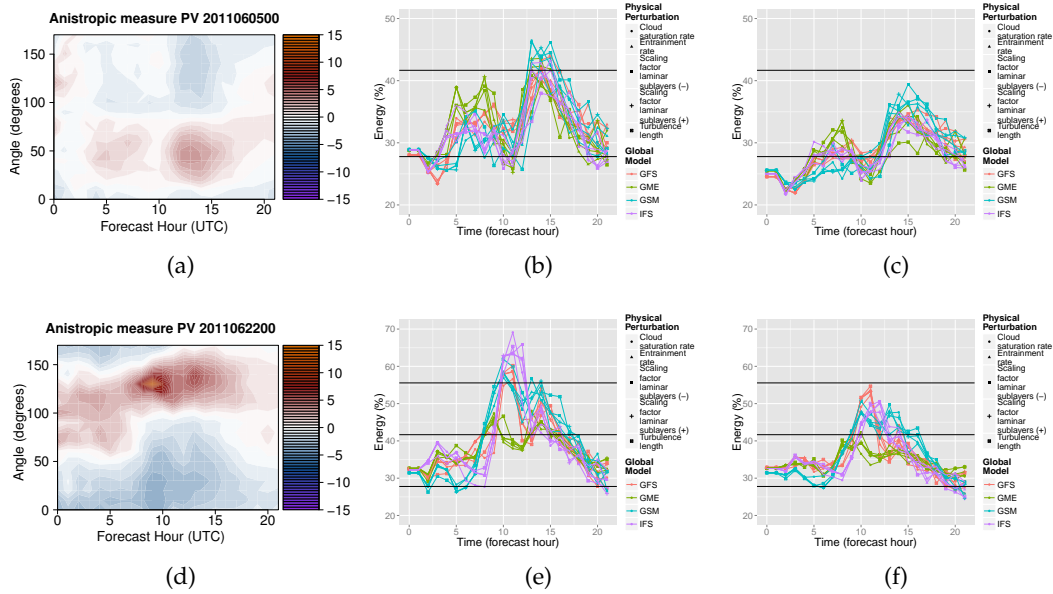


Figure 7.4: Difference (in %) from isotropy from PV spectrum on convective weather scale (16-44 km) as function of angle, defined from the longitudinal axes for (a) 5 June and (d) 22 June. For details of computation and explanation of the abbreviations, see text. Fraction of spectral energy of PV on the convective weather scale (16-44 km) in the (b) 30-70° direction for 5 June and (e) in the 110-150° direction for 22 June. Lines indicate different ensemble members, initialised with different global models (colours) and physical perturbations (shapes of points). Lowest black line indicates spectral energy for complete isotropic case, upper two lines indicate an 1.5 and 2 times increase of energy respectively compared to the isotropic case. (c) and (f): As (b) and (e) but for the kinetic energy instead of PV.

The composites show that the PV dipoles are consistent in strength and direction. However, the composites give mainly a local view on the bands (i.e. around a single storm updraft). To get the exact orientation of the bands,  $S(\beta)$  is calculated for the two weather cases. In Fig. 7.4a and d.,  $S(\beta)$  is normalised and the deviation from isotropy (in %) is plotted

For the 5 June weather case, there is on average a 5-10% deviation in spectral variance from isotropy in the 50° direction (Fig. 7.4a), which is roughly the direction of the large scale wind and wind shear. Note that the Fourier spectrum measures gradients of PV, an angle of 0° (90°) indicates PV gradients in the longitudinal (latitudinal) direction. Therefore, the angle of 50° is consistent with the south-easterly wind on 5 June. For 22 June the anisotropy is even higher, with a 15% increase of spectral variance at approximately 130°(Fig. 7.4d). At 10 UTC the frontal system was lying at the western side of the model domain. There is some change in wind direction across the front (see Fig. 4.4a), therefore it is expected that the anisotropy is highest at 10 UTC as background conditions are most uniform. The angle of 130° is again in the direction of large scale wind shear. For later times, the anisotropy is weaker and after about 15h the most

anisotropic angle changes to about  $120\text{-}125^\circ$ , consistent with the clockwise turn of the dipole orientation in the composites (Fig. 4.10).

To check the consistency of the results and compare the ensemble members, the spectral variance of the potential enstrophy is integrated in a  $50^\circ$  bin around the maximum spectral variance (Section 4.5). The results are quite consistent among the different ensemble members. For all ensemble members there is an increase of almost 50% deviation from isotropy for both days (Fig. 7.4b and e). There are clear differences between the ensemble members driven by boundary conditions from different global models, indicating that the large-scale conditions play a dominant role in the organisation of convection on smaller scales. This is consistent with the hypothesis that the organisation of PV is mainly determined by the wind shear. The runs that are initialised with the GME model show significant differences, especially for the 22 June case. For the GME model run on 22 June the vertical wind shear is weaker, which could explain the differences. These results suggest that forecasting organisation of storms should mainly focus on the uncertainty of the large scale flow. The dominance of boundary conditions in determining the uncertainty is a general problem of COSMO-DE-EPS [see e.g. Wahl, 2015]. This might be generally the case, Durran and Weyn [2015] found that minimising the errors on scales of about 100 km is more likely to improve a forecast than minimising errors at much smaller scales.

As discussed in Section 4.5, there are flow perturbations closely linked to the PV anomalies. Kinetic energy spectra, calculated using the average of the meridional and zonal wind spectra, show that the main variations of the flow are in the same direction as for the PV (Fig. 7.4c and f). Since the PV anomalies create velocity perturbations in every direction, the deviation from isotropy is less strong than for the PV. Still, for the for 22 June case, the spectral variance in the  $120\text{-}170^\circ$  direction is 1.5 times larger than one would expect if isotropy is assumed. Again the main differences between ensemble members in the spectral variance come from the boundary conditions, initial conditions and the physical perturbations are relatively unimportant.

## 7.4 RELATION OF SPECTRA TO EXTREMES

For the 5 and 22 June 2011 cases, the PES showed a consistent increase of spectral variation at the convective weather scale. As a first check for PV as a predictor for precipitation and/or wind gust extremes, we compare the slope of the PES between 200 and 20 km during the three summer months in 2011 with precipitation rates and wind gusts from the COSMO-DE NWP model. For each forecast hour, the mean and the 5% and 95% quantile of the potential enstrophy spectral slope between 200 and 20 km are calculated. Both the 0 UTC and 12 UTC runs are used, and they are treated as one ensemble (i.e. at time steps when there is a forecast for both runs, we take the mean over 40 ensemble members). The spectral slope of the PES is compared with the 99% quantile of the hourly precipitation rates in the model, over the same 321 times 361 grid points as used in the calculation of the PV power law (see Fig. 3.1a). As a model wind gust estimation we use the 99.9% quantile of  $V_{gust}$ . These 99.9% quantiles serve as a model estimate for the precipitation and wind gust extremes.

The slope of the PES is strongly correlated with the hourly precipitation rates (Fig. 7.5). The hourly spectral slope (Fig. 7.5b) and the 99% quantile of the model precipitation rates (Fig. 7.5b) show maxima for the same time periods, e.g. for 4-7 June and 22 June. These are all periods during which significant DMC took place. There seems to be a daily trend for both variables, with maxima at the end of the afternoon, especially during days of convection. This is consistent with the findings of Bierdel et al. [2012]. For wind gusts the correlation is much less clear. Although there are wind gusts for e.g. 22 June, there are also days (e.g. end of August) at which the spectral slope of the PES is negative, although there are relatively strong wind gusts modelled. One could have expected this result, as precipitation itself is associated with diabatic processes and therefore with PV anomalies. Although wind gusts are associated with DMC, there are other factors which contribute to the location and strength of these wind gusts.

If we compare the spectral slope of potential enstrophy directly with the 99%, 99.5% and the 99.9% quantiles of the model precipitation, we see the correlation even more clearly (Fig. 7.5d). The correlation coefficients are 0.54, 0.60 and 0.63 respectively for the 99%, 99.5% and the 99.9% model precipitation quantile. This implies that the spectral slope is especially correlated with severe precipitation, because the correlation coefficients for the lower quantiles are smaller. Correlations between the wind gust quantiles and the spectral slope of potential enstrophy are approximately 0, indicating that the power law of potential enstrophy is not informative as predictor for severe wind gusts.

As another check if PV can be used as predictor, we use the hourly precipitation rates of 1060 weather stations over Germany, and compared it to the spectral slope, and spectral variance  $\bar{S}_{convective}$ . We do this for all 6624 hourly time steps for the summer months of 2011, 2012 and 2013. As in Fig. 7.5, the ensemble members of the 0 UTC and 12 UTC runs are treated as one ensemble. Again the 99% quantile of the precipitation rates is calculated, but now over the observed precipitation rates of all weather stations over Germany at a specific time. These quantiles provide an estimate of the observed precipitation extremes. The idea is that, although the PV anomalies in the model might be located at a

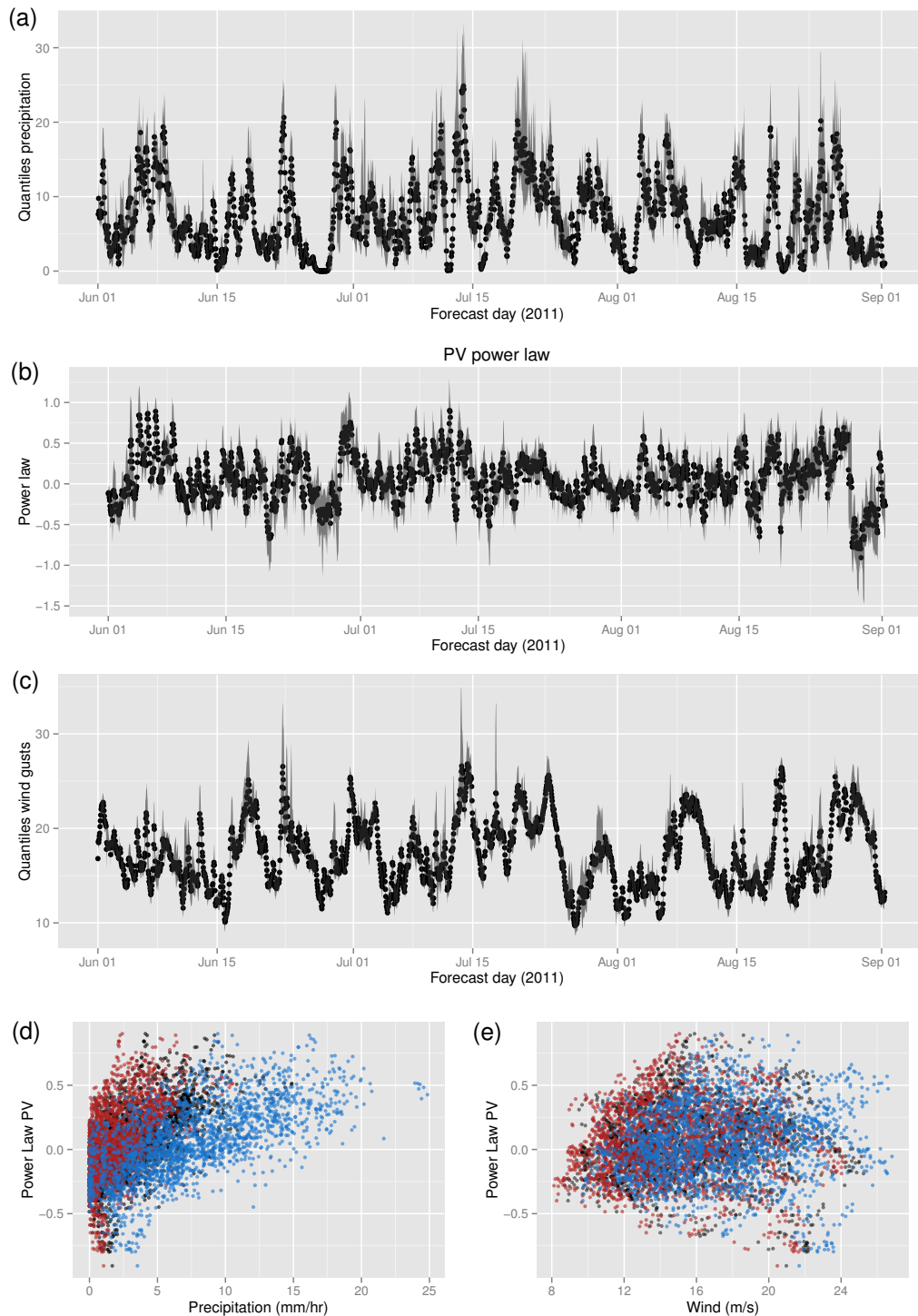


Figure 7.5: (a) The 99.9% quantile of the COSMO-DE model domain precipitation rates for the 2011 summer months. The mean (over the ensemble) at a specific time step is indicated by the black dots, the grey area indicates a 5% and 95% confidence interval over the ensemble. (b) As in (a), but for the spectral slope of the PES. (c) as in (a), but for the wind gusts. (d) Hourly ensemble mean spectral slope of the PES against the 99% (red dots), 99.5% (black dots) and the 99.9% (blue dots) quantiles of the hourly COSMO-DE-EPS model precipitation rates. (e) as (d), but against the model wind gusts (i.e.  $V_{gust}$ )

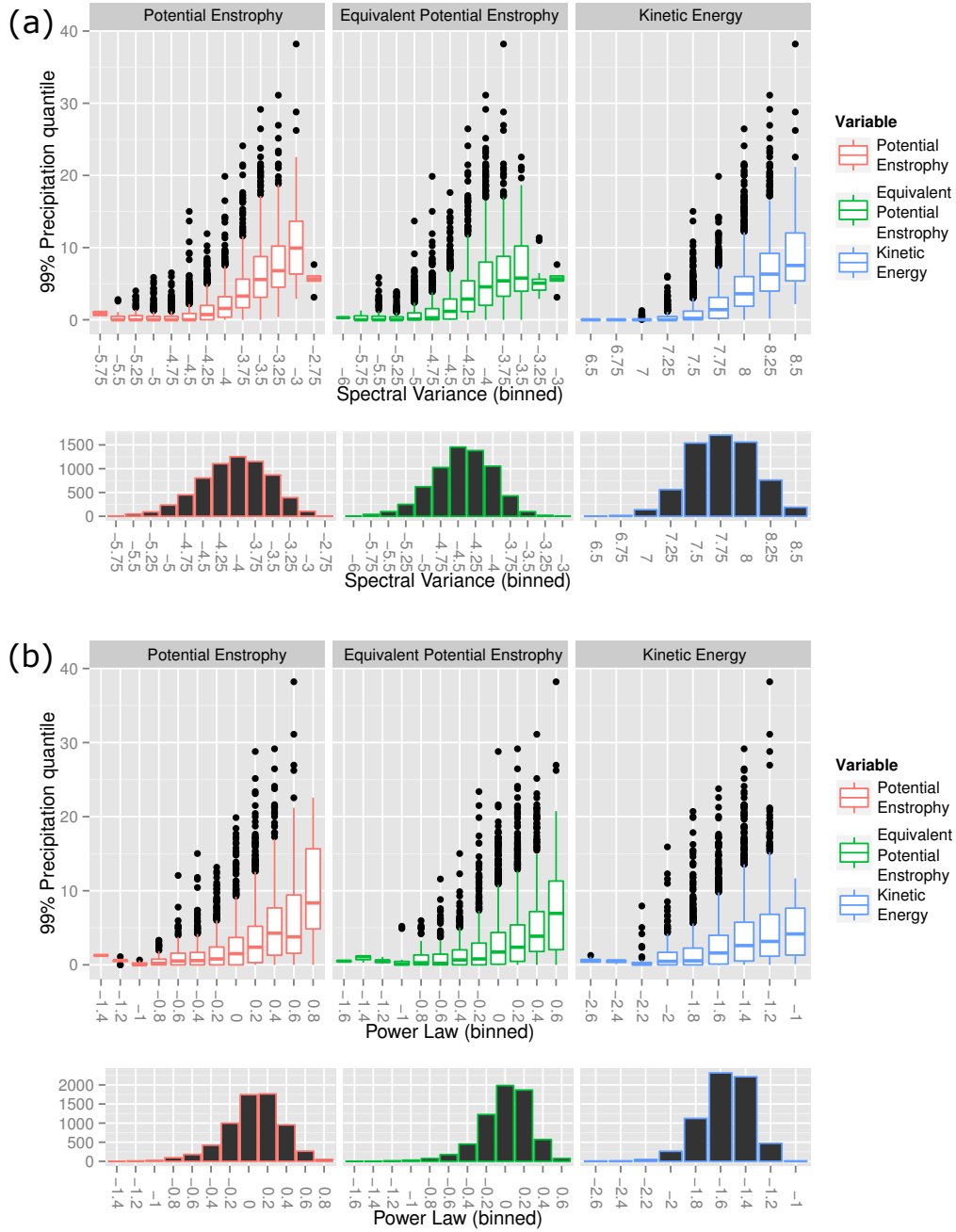


Figure 7.6: (a) Observed extreme precipitation rates (99% quantile over 1060 weather stations in Germany) as function of the spectral variance at the convective weather scale  $\bar{S}_{convective}$  of the potential enstrophy (red), equivalent potential enstrophy (green) and kinetic energy (blue).  $\bar{S}_{convective}$  is divided into bins, the boxplot indicates the variance over all time steps included in a specific bin. The bottom picture in (a) shows the number of time steps included in a specific bin. As indicated in the text, the  $\log_{10}$  is taken of  $\bar{S}_{convective}$ , because of its highly variable nature. (b) As in (a) but now the spectral slope between 200 and 20 km of the spectrum of potential enstrophy, equivalent potential enstrophy and kinetic energy is used as a predictor.

wrong location, the PES gives a good estimate of the average diabatic processes (and therefore of precipitation) for the model domain. Besides the PES, we use the same parameters for the equivalent potential enstrophy spectrum and the horizontal kinetic energy spectrum. The comparison with modelled wind gusts already indicated that the PES is not an informative predictor for wind gusts, therefore we only compare with precipitation observations.

We see that for both the spectral variance  $\bar{S}_{convective}$  and the spectral slope estimate all three variables are positively correlated with the observed severe precipitation rates (Fig. 7.6). The spectral variance  $\bar{S}_{convective}$  of the potential enstrophy  $Q$  seems to be the best estimator for severe precipitation rates above 10 mm/h. For the PES, the spectral variance  $\bar{S}_{convective}$  is normally distributed (see bottom panel of Fig. 7.6a, note that the  $\log_{10}$  of  $\bar{S}_{convective}$  is taken), and there are hardly severe precipitation rates above 10 mm/hour for the left side of the distribution. The median value of the  $\bar{S}_{convective}$  bin of the PES centred at -3 lies at about 10 mm/hour, indicating that about 50% of the cases in this had precipitation rates above 10 mm/hour. For the other two variables, the equivalent potential enstrophy  $Q_e$  and the kinetic energy, there is still a clear correlation between observed precipitation and  $\bar{S}_{convective}$ . This correlation is less clear, however, as compared to that for the PES.

The spectral slopes of the three variables used show similar correlations with observed precipitation rates (Fig. 7.6b). For all three variables, the distribution of the spectral slope seems to be skewed towards lower values, indicating that a flat spectrum is less common than a steep spectrum. The median of the spectral slope of the (equivalent) potential enstrophy above 0.8 (0.6) approaches 10 (8) mm/h. There exist, however, many extreme outliers at smaller values of the spectral slope. It might be logical that there is a correlation between PV and EPV anomalies and precipitation rates, since PV is a good indicator of diabatic effects [e.g. Grams et al., 2011]. It is not that trivial, however, that this correlation is especially high for extremes. One potential problem in using PV as predictor for severe rain is that it only produces PV anomalies when the model produces diabatic perturbations (i.e. convection). When the model fails to initiate convection, no PV anomalies are generated. Moreover, scores have to be calculated to quantify the performance of the spectral predictors compared to e.g. model precipitation rates. The results do show, however, that the PV has potential as a predictor for severe precipitation.

## 7.5 SUMMARY AND DISCUSSION

In this chapter the use of PV as predictor for weather extremes on the convective weather scale was briefly investigated. Moreover, this chapter investigated if the PV bands found in strong shear environments (see Chapter 4), could be quantified. As a predictor for severe weather, the spectrum of potential enstrophy (PES) was used. The spectral variance on the convective weather scale was used to calculate an anisotropic measure of the PES.

For the two weather cases discussed in Chapter 4, 5 and 22 June 2011, there is a significant increase in spectral variance on the convective weather scale during

DMC. Moreover, the PES is anisotropic on the mesoscale, there is more spectral variance in the direction of the large scale wind shear. This is particularly visible for the strong shear (22 June) case. This anisotropy is also visible in the kinetic energy spectrum, although it is less clear than for the PES.

The spectral slope (between 200 and 20 km) of the PES is correlated with the 99% quantile of the hourly model precipitation rates. There is a weaker correlation with the modelled wind gusts. The comparison of the spectral estimates and the 99% quantile of the hourly observed precipitation rates over Germany shows that PV might be useful as predictor for severe precipitation.



## CONCLUSION AND DISCUSSION

---

The main purpose of this thesis was to analyse the consistency of Potential Vorticity (PV) anomalies on the convective weather scale using “real” weather cases in a nonhydrostatic Numerical Weather Prediction (NWP) model. Chagnon and Gray [2009] argued that on the convective weather scale PV dipoles are generated centred around a convective updraft. They used a linearised Boussinesq model to theoretically describe the generation of mesoscale PV dipoles. In their derivation, they used quite strong assumptions, e.g. they relied on hydrostatic and geostrophic balance. This study hypothesised that those dipoles might be quasi-balanced. Arguments for these quasi-balanced dipoles is that they have a relatively long lifetime, furthermore Chagnon and Gray [2009] estimated that the time-scale to adjustment is only half an hour.

If the PV dipoles are quasi-balanced, PV inversion is desirable. Inversion of PV is impossible, however, because of the unstable convection and the unknown balance condition. Therefore, this work proposed to look at composites of PV anomalies associated with storm cells. Although PV inversion is impossible, one would expect coherent PV dipoles with associated flow anomalies. We first looked in Chapter 4 at two severe weather cases, one which consisted out of local convection and an other case which was characterised by convection along a cold front. In Chapter 4 composites were made using Ensemble Prediction System (EPS) data of the nonhydrostatic NWP model COSMO-DE ). Differences between the typical PV anomalies with a strong and weak bulk wind shear case were discussed.

In Chapter 5 the composites of the evolution of the 5 and 22 June cases were analysed, using tracks of the vertical velocity. The tracking algorithm was described. Besides composites of PV and flow anomalies, precipitation composites were determined, for all cells and for strong PV cells. A vorticity budget of the vertical component of the vorticity was carried out, focusing on the stretching and tilting terms.

The composite analysis was extended to seven other severe weather cases in Chapter 6. The general variability of the convective environment of the different cases was discussed. The composites were clustered on severe rain rates, on strong  $w$  and strong PV cells to investigate the difference in morphology of normal and intense cells. Moreover, the influence of different environmental variables like Convective Available Potential Energy (CAPE) and Storm Relative Helicity (SRH) on storm cell morphology was discussed.

Lastly, in Chapter 7 the use of the potential enstrophy spectrum as a predictor for severe convective weather was investigated. Moreover, the anisotropic spectrum of potential enstrophy was used to quantify the direction of PV dipoles and bands for the 5 and 22 June weather cases.

### 8.1 SUMMARY OF MAIN RESULTS

A short summary has been given at the end of each (result) chapter, we now return to the questions asked in Section 1.2<sup>8</sup>.

*Q1 - What are the general characteristics of PV anomalies associated with severe convective weather?*

Chapter 4 discussed a case study of two cases, 5 and 22 June 2011. Many of the dipole characteristics discussed theoretically in Chagnon and Gray [2009] are found in the much more complex case of the COSMO-DE model. Composites around convective cells confirm that the strength and direction of the PV dipoles mainly depends on the wind shear. Flow anomalies are also consistent, with cyclonic (anticyclonic) flow around the positive (negative) PV anomaly. As suggested by Chagnon and Gray [2009], the largest flow anomalies are found in between the positive and negative PV anomaly. For the case with a positive background helicity, 22 June, the positive PV anomaly is advected towards the updraft. This is consistent with the hypothesis in Davies-Jones [1984]. Furthermore, a consistent helicity dipole exists of equal sign as the PV dipole. This helicity dipole is much more pronounced for the 22 June case.

*Q2 - Are there (convective scale) PV anomalies that organise themselves on a larger scale than the convective weather scale?*

The case study in Chapter 4 showed that PV anomalies can organise themselves in elongated bands of positive and negative PV, with a direction that depends on the large scale wind shear of the horizontal wind. These bands are particularly visible in the more organised 22 June case. These PV bands are stronger in magnitude compared to the orographically generated bands described by Aebischer and Schär [1998]. A similarity is, however, that advection plays a role in the creation of the PV bands. These PV bands are also visible in the spectrum of potential enstrophy discussed in Chapter 7, which is anisotropic in the direction of the PV bands. Moreover, the kinetic energy spectrum is also anisotropic on the convective weather scale.

*Q3 - How consistent is the evolution of the PV dipole described by Chagnon and Gray [2009] and how does this depend on the environment characteristics?*

For the 5 and 22 June weather cases, there is a consistent evolution, with significant PV anomalies (see Chapter 5). Not all flow anomalies are significant, however, at all times. A possible explanation therefore is the number of cells in the composites is not high enough, or that the variability in flow anomalies is too high. General differences in morphology are consistent, however, with the differences in synoptic background of these cases. On average, the bulk wind shear of the storm cell environment is much higher for the 22 June case. The

---

<sup>8</sup> Parts of the conclusion are reproduced from Weijenborg et al. [2015]

dipoles are much more stretched out for this case. Moreover, especially the composite for intense and long-lasting cells looks like a “supercell”: a long-lasting persistent updraft. This is consistent with the higher environmental SRH for the 22 June case.

Most of the results are confirmed by the evolution composites taken over all nine severe weather cases (Chapter 6). Even when averaging over 3135 storm cells with a different synoptic background a clear PV dipole is visible. The magnitude of these dipoles are about  $\mathcal{O}(10)$  larger compared to ambient values. These dipoles are associated with significant cyclonic and anticyclonic wind velocity anomalies, with average maxima up to  $3.7 \text{ ms}^{-1}$ . Moreover, these significant PV anomalies last over the whole lifetime of the convective updraft. Especially the longer lasting convective updrafts show a more monopole structure, in which the positive PV anomaly dominates over the negative PV anomaly.

Although the magnitude of the PV is larger for strong CAPE cells, the differences in morphology of strong CAPE and normal cells are small. Strong wind shear cells show on average a more stretched PV dipole, consistent with the hypothesis that moderate to strong wind shear environment will advect the PV dipole downshear. Cells associated with large values of SRH show a monopole “supercell” structure. This “supercell” morphology is, however, less clear as for intense cells.

*Q4 - Do extreme storm cells have significant different characteristics?*

Strong PV cells, cells with strong vertical velocity, as well cells associated with severe (model) precipitation show the before mentioned “supercell” structure. Maximum PV anomalies, and dipole asymmetry increase consistently with increasing thresholds of PV, precipitation rates, and vertical velocity. Moreover, associated flow anomalies show a similar consistent increase. The flow anomalies are dominated by the cyclonic flow around the positive PV anomaly. Vertical diabatic heating profiles, which can be seen as the forcing for the dipoles, are also similar for all intensity measures. On average, the intense PV cells last longer, although the direct correlation between the PV maximum and storm cell duration is weak. A vorticity budget for the 5 and 22 June 2011 weather cases showed that, that particularly for intense PV cells stretching plays a crucial role in intensifying these intense cells after the maximum vertical velocity has been reached.

*Q5 - Could PV be used as predictor for severe convective weather like precipitation and/or wind gust extremes?*

The spectral slope on the mesoscale of the Potential Enstrophy Spectrum (PES) is correlated with severe precipitation rates in the COSMO-DE model (see Chapter 7). Only a weak correlation with the modelled wind gusts exists, therefore it is unlikely that PV is a good predictor for severe wind gusts. The strong correlations between the spectral variance and spectral slope on the mesoscale for

the (equivalent) PES indicate that (equivalent) PV might be a good predictor for severe precipitation.

### 8.1.1 *Main implication of results*

The structure and magnitude of the PV anomalies on the convective weather scale give valuable information which is not exploited yet currently. This study hypothesised that the PV might be “quasi”-balanced. It deliberately did not address the question of what kind of balance is to be expected for the PV dipoles. The main aim in calculating the composites was to determine the general structure and evolution of PV anomalies around storm cells modelled in a nonhydrostatic model. Chagnon and Gray [2009] already suggested that the PV dipoles might be balanced to some degree. This study confirmed this on a statistical basis, since the strength of the PV and associated flow anomalies consistently increase with increasing updraft strength. It is remarkable that even when averaging over storm cells associated with 9 highly variable cases, a coherent PV dipole (evolution) exists. The results in study confirm that ‘PV-thinking’ [Hoskins et al., 1985] is also relevant on convective weather scales. Although there are qualitative differences, the flow anomalies associated are remarkably similar to the anomalies on synoptic and sub-synoptic scales. This might imply that PV can be used in the data-reduction problem. Moreover, the correlation of PV and precipitation observations suggests that PV might be a good predictor for severe precipitation. These and other suggestions for future research will be discussed in the following section.

## 8.2 REMAINING QUESTIONS AND FURTHER ANALYSIS

We did not explicitly state what kind of balance is to be expected, and how much of the flow is unbalanced. Since both components play probably a significant role, also the unbalanced flow has to be treated. Although a PV inversion is by no means trivial, a possible pathway is using the methodology described in Viúdez and Dritschel [2004], who explicitly take the unbalanced flow into account.

Since the PV dipoles can only be quasi-stationary (there is always a diabatic perturbation at the storm updraft), there will be an adjustment to full balance. Possible candidates how balance is restored are by exciting gravity waves and/or sound waves. Gravity waves are generated by convection, but the exact process(es) is still a matter of debate [Fritts and Alexander, 2003]. Sound waves are generated in the process of hydrostatic adjustment [Bannon, 1995]. Vertical velocity spectra might give an answer whether gravity waves play a role in our cases.

Our results and the theoretical analysis of Chagnon and Gray [2009] indicate that the PV dipoles have a longer lifetime than the convection which initiated them. The dipoles might influence the flow and/or initiate new convection even after the original updraft has died out. A more sophisticated tracking method (e.g. an object based one) might be necessary, since the PV dipoles are gener-

ally larger in size than the associated updrafts. Moreover splitting/merging of anomalies should be treated in a more sophisticated way.

Since the PV dipoles orientate themselves in a structured way in PV bands, one might argue that they exert a momentum on larger scales. This idea has already been suggested by Chagnon and Gray [2009]. Moreover, Montgomery et al. [2006] found that Vortical Hot Towers (VHTs) play an essential role in building a larger scaled mesoscale convective vortex. Although the individual PV anomalies themselves might be too small to influence the flow on larger scales, their integrated behaviour could still be of influence, if they are organised coherently.

The focus in this study was on deep moist convection, therefore the results are not necessary valid for shallow convection. Shallow convection is characterised by a different diabatic profile [Houze Jr, 2004]. This explains why the PV anomalies in the mid troposphere are mainly generated at the cold front on 22 June, where the precipitation is more convective. The COSMO-DE model makes no distinction between shallow and deep convection in the precipitation output, the PV anomalies at the middle troposphere might give an indication to a forecaster how much of the precipitation is convective. The convective PV dipoles extent over a large part of the troposphere, from the boundary layer up to the tropopause, with maximum anomalies somewhere at 5 till 6 km.

It is interesting to examine how the general morphology of convective cells changes with model resolution. One could apply the tracking and compositing algorithm to models with a higher resolution. The size of the convective cells is generally too large in a model with a grid space of a few km [e.g. Stein et al., 2015]. Decreasing the grid spacing below 1 km can improve this. The convective cells initiated in a model with a higher resolution are therefore expected to be more physically realistic. Moreover, in forecasting supercells, often parameters as the SRH are used [Lilly, 1986b]. Strong SRH cells did have such a strong monopole structure, although this might be due to the incapability of the COSMO-DE model of capturing the full supercell dynamics. Modelling at higher resolution might answer this question. Difficulties can arise however, when increasing the model grid spacing to the order of 1km. The so called "Terra incognita" does not necessary improve the forecast, since parameterisations do not scale with resolution [Wyngaard, 2004]. Ching et al. [2014] found that poorly resolved convective induced secondary circulations, and violations in the boundary parameterisation schemes are examples of problems in modelling the "Terra incognita".

In this study, an Empirical Orthogonal Function (EOF) was performed on both the storm cell properties as well storm environment characteristics. Clustering on environment parameters individually did not give a definite answer to which parameters are associated with the supercell structure found for intense cells. It might therefore be useful to extend the EOF analysis to a canonical-correlation analysis [Wilks, 2011], to analyse which storm cell properties are associated with which environment variables. Moreover, it might be useful to cluster the storm cells to strong forcing and weak forcing, using the convective time scale defined in Zimmer et al. [2011].

One could further investigate if PV could be used in the data reduction problem. Prior research has shown that the inclusion of physical correlations in post-processing methods improves the exploitation of the available forecast information [e.g. Röpnack et al., 2013; Keune et al., 2014]. Most physically based post-processing are only two dimensional, e.g. for wind speed [Schuhen et al., 2012], or wind speed and temperature [Baran and Möller, 2015]. PV holds a lot of dynamic and thermodynamic information in one variable. Furthermore, it is related to other variables like pressure, temperature and the wind field by the invertibility principle. The coherent PV anomalies suggest, together with the linear model used by Chagnon and Gray [2009], that a significant data reduction might be possible. One approach might use Vertical Normal Modes (VNM), as in Renkl [2013]. One could compare this with Ensemble Copula Coupling (ECC), which also preserves physical and spatial correlations between variables [Scheffzik et al., 2013], and is relatively easy to apply on a large data set.

## EVOLUTION CONSERVED QUANTITIES

---

### A.1 PV EVOLUTION EQUATION

The evolution of PV substance  $\rho\Pi$  can be put in a flux conservation form (see Haynes and McIntyre [1987]):

$$\frac{\partial \rho\Pi}{\partial t} + \nabla \cdot \mathbf{J} = 0 \quad (\text{A.1})$$

Where  $\mathbf{J}$  should be interpreted as a 3d potential vorticity substance flux. To derive this, we start from the momentum equation:

$$\frac{\partial \mathbf{u}}{\partial t} + \mathbf{u} \cdot \nabla \mathbf{u} + 2\boldsymbol{\Omega} \times \mathbf{u} = -\rho^{-1} \nabla p - \nabla \Phi + \mathbf{F} \quad (\text{A.2})$$

Here  $\mathbf{u}$  is the 3d velocity vector,  $p$  is the pressure field,  $\boldsymbol{\Omega}$  is the planetary rate of rotation,  $\rho$  is the density of the fluid and  $\mathbf{F}$  is a general body force applied to the fluid (e.g. friction).

By taking the curl of eq. Eq. A.2 and using the definition of absolute vorticity  $\zeta_a \equiv 2\boldsymbol{\Omega} + \boldsymbol{\zeta}$ , one gets:

$$\begin{aligned} \frac{\partial \nabla \times \mathbf{u}}{\partial t} + \nabla \times (\mathbf{u} \cdot \nabla \mathbf{u}) + \nabla \times (2\boldsymbol{\Omega} \times \mathbf{u}) = \\ \nabla \times \left( \frac{-1}{\rho} \nabla p \right) - \nabla \times \nabla \Phi + \nabla \times \mathbf{F} \end{aligned} \quad (\text{A.3})$$

Using the vector identities,

$$\mathbf{u} \cdot \nabla \mathbf{u} = -\mathbf{u} \times \nabla \times \mathbf{u} + \frac{1}{2} \nabla (\mathbf{u} \cdot \mathbf{u}) = \boldsymbol{\zeta} \times \mathbf{u} + \frac{1}{2} \nabla (\mathbf{u} \cdot \mathbf{u}) \quad (\text{A.4})$$

$$\nabla \times \nabla \Phi = 0 \quad (\text{A.5})$$

$$\nabla \times \frac{1}{2} \nabla (\mathbf{u} \cdot \mathbf{u}) = 0 \quad (\text{A.6})$$

$$\nabla \times \left( \frac{-1}{\rho} \nabla p \right) = \frac{1}{\rho^2} \nabla \rho \times \nabla p \quad (\text{A.7})$$

We end up with the vorticity evolution equation:

$$\frac{\partial \zeta_a}{\partial t} + \nabla \times (\zeta_a \times \mathbf{u}) = \frac{1}{\rho^2} \nabla \rho \times \nabla p + \nabla \times \mathbf{F} \quad (\text{A.8})$$

To get the evolution equation for potential vorticity we take the inner product of Eq. A.8 with  $\nabla \theta$ , since the Ertel potential vorticity is generally defined as  $\Pi = \frac{\zeta_a \cdot \nabla \theta}{\rho}$ . Moreover, it is useful to define a quantity called PV substance  $\rho\Pi \equiv \zeta_a \cdot \nabla \theta$ . Multiplying Eq. A.8 with  $\cdot \nabla \theta$  we get:

$$\frac{\partial \zeta_a}{\partial t} \cdot \nabla \theta + \nabla \times \zeta_a \times \mathbf{u} \cdot \nabla \theta = \frac{1}{\rho^2} (\nabla \rho \times \nabla p) \cdot \nabla \theta + \nabla \times \mathbf{F} \cdot \nabla \theta \quad (\text{A.9})$$

Using

$$\frac{\partial \zeta_{\alpha}}{\partial t} \cdot \nabla \theta = \frac{\partial \rho \Pi}{\partial t} - \zeta_{\alpha} \cdot \nabla \dot{\theta} \quad (\text{A.10})$$

$$\nabla \times \mathbf{F} \cdot \nabla \theta = \nabla \cdot (\mathbf{F} \times \nabla \theta) + \mathbf{F} \cdot (\nabla \times \nabla \theta) = \nabla \cdot (\mathbf{F} \times \nabla \theta) \quad (\text{A.11})$$

$$(\nabla \rho \times \nabla p) \cdot \nabla \theta = 0 \quad (\text{A.12})$$

Were in the last equation it is used that  $\theta$  is a function of  $p$  and  $\rho$  only. Moreover, the last term on the left side of Eq. A.9 can be written as:

$$\begin{aligned} (\nabla \times \zeta_{\alpha} \times \mathbf{u}) \cdot \nabla \theta &= \left[ -\mathbf{u}(\nabla \cdot \zeta_{\alpha}) + \zeta_{\alpha}(\nabla \cdot \mathbf{u}) \right. \\ &\quad \left. + (\mathbf{u} \cdot \nabla) \zeta_{\alpha} - (\zeta_{\alpha} \cdot \nabla) \mathbf{u} \right] \cdot (\nabla \theta). \end{aligned} \quad (\text{A.13})$$

But,

$$\begin{aligned} \nabla \cdot ((\zeta_{\alpha} \cdot \nabla \theta) \mathbf{u}) - \left( \frac{\partial \theta}{\partial t} + \mathbf{u} \cdot \nabla \theta \right) \zeta_{\alpha} &= \mathbf{u} \cdot \nabla (\zeta_{\alpha} \cdot \nabla \theta) + (\zeta_{\alpha} \cdot \nabla \theta) \mathbf{u} \\ - \zeta_{\alpha} \nabla \frac{\partial \theta}{\partial t} - \frac{\partial \theta}{\partial t} \nabla \cdot \zeta_{\alpha} - \zeta_{\alpha} \cdot \nabla (\mathbf{u} \cdot \nabla \theta) - (\mathbf{u} \cdot \nabla \theta) \nabla \zeta_{\alpha} \end{aligned} \quad (\text{A.14})$$

Therefore,

$$\begin{aligned} (\nabla \times \zeta_{\alpha} \times \mathbf{u}) \cdot \nabla \theta &= \nabla \cdot ((\zeta_{\alpha} \cdot \nabla \theta) \mathbf{u}) - \left( \frac{\partial \theta}{\partial t} + \mathbf{u} \cdot \nabla \theta \right) \zeta_{\alpha} \\ &\quad + \zeta_{\alpha} \nabla \frac{\partial \theta}{\partial t} + \frac{\partial \theta}{\partial t} \nabla \cdot \zeta_{\alpha}. \end{aligned} \quad (\text{A.15})$$

The last term in Eq. A.15 is zero because  $\zeta_{\alpha}$  is divergence free. So one finally end up with,

$$\frac{\partial \rho \Pi}{\partial t} = -\nabla \cdot (\rho \Pi \mathbf{u} - \zeta_{\alpha} \dot{\theta} - \mathbf{F} \times \nabla \theta). \quad (\text{A.16})$$

Which states that PV substance locally change due to advection, diabatic effects or by applying a body force on the fluid perpendicular to the gradient of  $\theta$ .

## PERFORMANCE OF ROTATION ALGORITHM

---

The composites in Chapter 6 are rotated with the bulk wind shear between 0 and 6 km height. Because the rotation is performed after calculating the 3 till 7.3 km height integrated fields, one cannot calculate the bulk wind shear after rotation. Therefore, it is difficult to determine the performance of the rotation algorithm. To test the performance of the rotation algorithm, all the results are rotated (towards the east) with the 3 till 7.3 km height integrated winds. The results are shown in Fig. B.1. Before rotation (Fig. B.1a) there is a significant variation in the orientation of the mean height integrated winds. After rotation (Fig. B.1), the height integrated wind is towards the east, and the meridional component is almost zero for all convective cells.

### B.1 SENSITIVITY OF COMPOSITE ON ROTATION

There are only minor qualitative differences between the direction of the bulk wind shear (Fig. 6.1) and the mean height integrated wind (Fig. B.1a). Therefore, one might use the height integrated wind instead of the bulk wind shear for the rotation. To check the sensitivity of the composite on the rotation method used, different rotation methods are tested using the 5 and 22 June cases. As discussed in Chapter 4 and Chapter 5, these two cases have a significant mean background wind. Composites over those two cases are made using the following rotation methods:

- Rotation with the direction of 0 to 6 km bulk wind shear, as in Chapter 6 (Fig. B.2).
- Rotation with the mean wind on the model level 23, the model level used in tracking the Gaussian filtered vertical velocity (Fig. B.3a-b).
- Rotation with the 3 till 7.3 km height integrated wind (Fig. B.3c-d).
- No rotation at all (Fig. B.3e-f).

The composites over the two cases are shown in Fig. B.2 (for the rotation using the bulk wind shear), and Fig. B.3. Note that the number of storm cells in these composites (803) is slightly higher than the sum of the cells included in the cases of Chapter 5. This is because for these sensitivity tests, data is saved only in a 19x19 grid point environment (instead of the 31x31 grid point used before). Therefore there are less “boundary” cases, which were excluded in making the composites of Chapter 5.

The general morphology and evolution is similar for all rotation algorithms tested. Strongest Potential Vorticity (PV) anomalies are found when rotating with the bulk wind shear (Fig. B.2a), of about 4.74 (3.53) Potential Vorticity Unit (PVU) for the maximum (minimum) PV anomaly. The PV is slightly weaker after 30

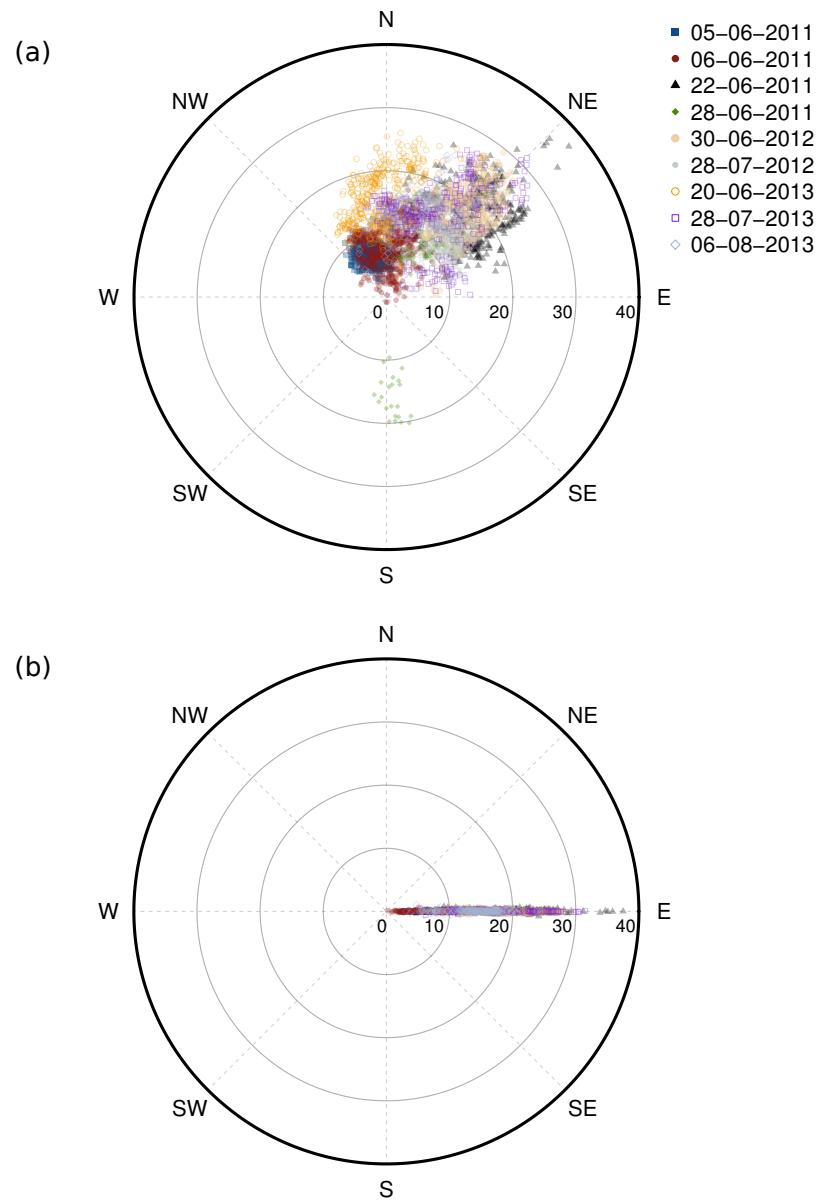


Figure B.1: Rotation with 3 to 7.3 km height integrated mean wind (in a  $31 \times 31$  grid point environment). (a) Mean wind before rotation, (b) mean wind after rotation.

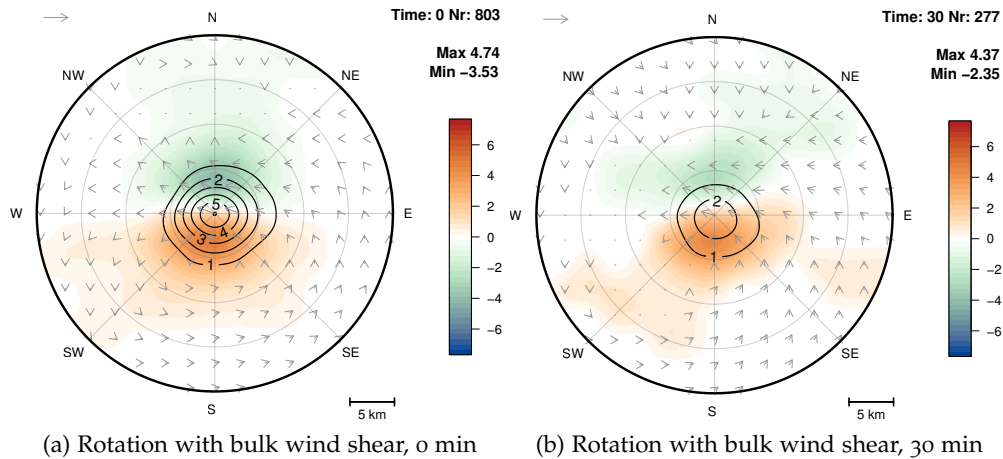


Figure B.2: As in Fig. 6.10, but using only the 5 and 22 June 2011 cases at (a) Gaussian filtered vertical velocity, and (b) 30 minutes. In this composites the rotation of the storm cells is done using the bulk wind shear.

minutes (Fig. B.2b). The other two rotation methods show slightly weaker PV anomalies, the maximum PV is 4.60 (4.36) PVU for the composites rotated with the mean (height integrated) wind (Fig. B.3a-d). When no rotation is applied before determining the composites, a PV dipole still exists (Fig. B.3e-f). These composites are, however, orientated more northwards. This is consistent with the average direction of the wind shear over the two cases (see Chapter 4 and Chapter 5). Wind flow anomalies are much weaker for the no-rotation composites.

In conclusion, there are no large qualitative differences between the different rotation methods. The composites do show, however, that a rotation is necessary, while otherwise the composites might be falsely interpreted.

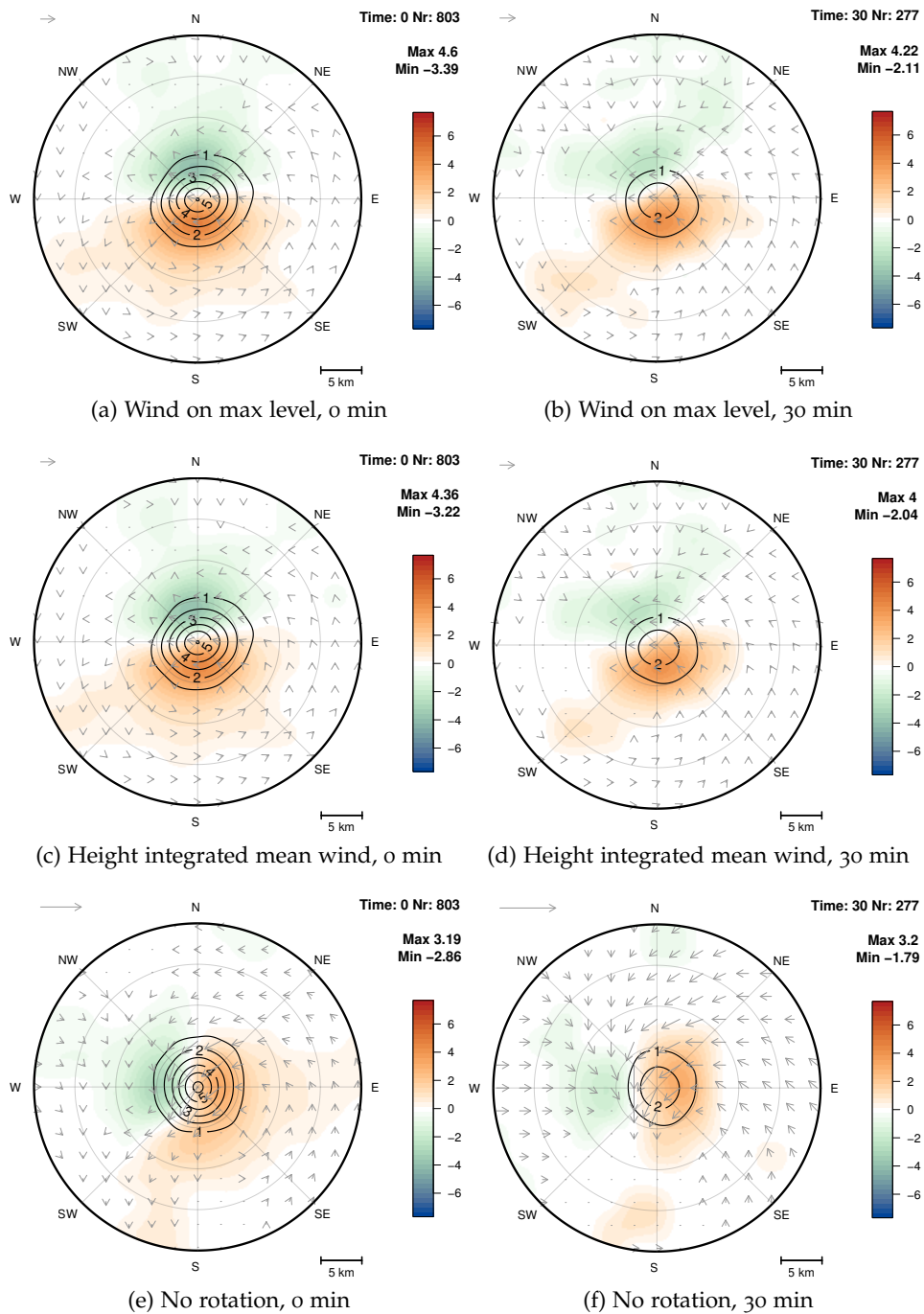


Figure B.3: Composites of storm cells, for different rotation methods. (a-b) As Fig. 6.10, but rotating using the mean wind on model level 23, (c-d) As Fig. 6.10, but rotation with the mean 3 till 7.3 km height integrated wind, (e-f) Fig. 6.10, but here the composites are made without rotating the fields beforehand.

## BIBLIOGRAPHY

---

- Aebischer, U. and Schär, C. (1998). Low-level potential vorticity and cyclogenesis to the lee of the Alps. *J. Atmos. Sci.*, 55(2):186–207.
- Appenzeller, C. and Davies, H. C. (1996). PV morphology of a frontal-wave development. *Meteor. Atmos. Phys.*, 58(1-4):21–40.
- Arnaud, Y., Desbois, M., and Maizi, J. (1992). Automatic Tracking and Characterization of African Convective Systems on Meteosat Pictures. *J. Appl. Meteorol.*, 31(5):443–453.
- Baldauf, M., Seifert, A., Förstner, J., Majewski, D., Raschendorfer, M., and Reinhardt, T. (2011). Operational convective-scale numerical weather prediction with the COSMO model: description and sensitivities. *Mon. Weather Rev.*, 139(12):3887–3905.
- Bannon, P. R. (1995). Hydrostatic adjustment: Lamb’s problem. *J. Atmos. Sci.*, 52(10):1743–1752.
- Baran, S. and Möller, A. (2015). Joint probabilistic forecasting of wind speed and temperature using Bayesian model averaging. *Environmetrics*, 26(2):120–132.
- Bartels, H., Weigl, E., Reich, T., Lang, P., Wagner, A., Kohler, O., and Gerlach, N. (2004). Projekt RADOLAN, Routineverfahren zur Online-Aneicherung der Radarniederschlagsdaten mit Hilfe von automatischen Bodenniederschlagsstationen (Ombrometer) - Deutscher Wetterdienst (in German).
- Betchov, R. (1961). Semi-isentropic turbulence and helicoidal flows. *Phys. Fluids*, 4:925–926.
- Bierdel, L. (2012). Mesoskalige Turbulenz in dem Konvektionaufloesenden Wettervorhersagemodell COSMO-DE. Master’s thesis, University of Bonn.
- Bierdel, L., Friederichs, P., and Bentzien, S. (2012). Spatial kinetic energy spectra in the convection-permitting limited-area NWP model COSMO-DE. *Meteorol. Z.*, 21:245–258.
- Bollmeyer, C. (2015). *A high-resolution regional reanalysis for Europe and Germany - Creation and verification with a special focus on the moisture budget*. Bonner meteorologische abhandlungen, Heft 69.
- Bolton, D. (1980). The Computation of Equivalent Potential Temperature. *Mon. Weather Rev.*, 108(7):1046–1053.
- Born, K., Ludwig, P., and Pinto, J. G. (2012). Wind gust estimation for Mid-European winter storms: towards a probabilistic view. *Tellus A*, 64(0):1–17.

- Browning, K. A. (1964). Airflow and Precipitation Trajectories Within Severe Local Storms Which Travel to the Right of the Winds. *J. Atmos. Sci.*, 21(6):634–639.
- Byers, H. and Braham, R. (1949). The thunderstorm. Technical report, U.S Government Printing Office.
- Byers, H. and Braham, Jr, R. (1948). Thunderstorm structure and circulation. *J. Meteorol.*, 5:71–86.
- Caine, S., Lane, T. P., May, P. T., Jakob, C., Siems, S. T., Manton, M. J., and Pinto, J. (2013). Statistical assessment of tropical convection-permitting model simulations using a cell-tracking algorithm. *Mon. Weather Rev.*, 141(2):557–580.
- Chagnon, J. M. and Gray, S. L. (2009). Horizontal potential vorticity dipoles on the convective storm scale. *Quart. J. Roy. Meteor. Soc.*, 135:1392–1408.
- Chagnon, J. M., Gray, S. L., and Methven, J. (2012). Diabatic processes modifying potential vorticity in a North Atlantic cyclone. *Quart. J. Roy. Meteor. Soc.*, 139(674):1270–1282.
- Changnon, S. A., Changnon, D., Fosse, E. R., Hoganson, D. C., Sr, R. J. R., and Totsch, J. M. (1997). Effects of Recent Weather Extremes on the Insurance Industry : Major Implications for the Atmospheric Sciences. *Bull. Am. Meteorol. Soc.*, 78(3):425–435.
- Chen, Q., Chen, S., and Eyink, G. L. (2003). The joint cascade of energy and helicity in three-dimensional turbulence. *Phys. Fluids*, 15:361–374.
- Ching, J., Rotunno, R., and LeMone, M. (2014). Convectively induced secondary circulations in fine-grid mesoscale numerical weather prediction models. *Mon. Weather Rev.*, 142:3284–3302.
- Clark, A. and Bullock, R. (2014). Application of object-based time-domain diagnostics for tracking precipitation systems in convection-allowing models. *Weather Forecast.*, 29:517–542.
- Claußnitzer, A. and Névir, P. (2009). Analysis of quantitative precipitation forecasts using the Dynamical State Index. *Atmos. Res.*, 94:694–703.
- Coniglio, M. C., Corfidi, S. F., and Kain, J. S. (2012). Views on Applying RKW Theory: An Illustration Using the 8 May 2009 Derecho-Producing Convective System. *Mon. Weather Rev.*, 140(3):1023–1043.
- Conzemius, R. J. and Montgomery, M. T. (2009). Clarification on the generation of absolute and potential vorticity in mesoscale convective vortices. *Atmos. Chem. Phys.*, 9:7591–7605.
- Cram, T. A. and Montgomery, M. T. (2002). Early evolution of vertical vorticity in a numerically simulated idealized convective line. *J. Atmos. Sci.*, 59:2113–2127.
- Dacre, H. F. and Gray, S. L. (2009). The Spatial Distribution and Evolution Characteristics of North Atlantic Cyclones. *Mon. Weather Rev.*, 137(1):99–115.

- Davies-Jones, R. (1984). Streamwise vorticity: The origin of updraft rotation in supercell storms. *J. Atmos. Sci.*, 41(20):2991–3006.
- Davis, C. A. and Weisman, M. L. (1994). Balanced dynamics of mesoscale vortices produced in simulated convective systems. *J. Atmos. Sci.*, 51:2005–2030.
- Dixon, M. and Wiener, G. (1993). TITAN: Thunderstorm Identification, Tracking, Analysis, and Nowcasting—A Radar-based Methodology. *J. Atmos. Ocean. Technol.*, 10(6):785–797.
- Doms, G., Förstner, Heise, E., J., Herzog, H., Mironov, D., Raschendorfer, M., Reinhardt, T., Ritter, B., Schrodin, R., Schultz, J.-P., and Vogel, G. (2014). A Description of the Nonhydrostatic Regional COSMO-Model, part II: Physical Parameterization.
- Doswell III, C. A. (1985). The Operational Meteorology of Convective Weather. Volume 2. Storm Scale Analysis.
- Doswell III, C. A. (1987). The distinction between large-scale and mesoscale contribution to severe convection: A case study example. *Wea. Forecast.*, 2(1):3–16.
- Doswell III, C. A. (1991). A review for forecasters on the application of hodographs to forecasting severe thunderstorms. *Natl. Wea. Dig.*, 16(1):2–16.
- Doswell III, C. A. and Burgess, D. (1993). Tornadoes and toradic storms: A review of conceptual models. In Church, C., Burgess, D., Doswell, C., and Davies-Jones, R., editors, *Tornado Its Struct. Dyn. Predict. Hazards*. American Geophysical Union.
- Droegemeier, K. K., Lazarus, S. M., and Davies-Jones, R. (1993). The influence of helicity on numerically simulated convective storms. *Mon. Weather Rev.*, 121(7):2005–2029.
- Durrán, D. R. and Weyn, J. A. (2015). Thunderstorms Don't Get Butterflies. *Bull. Am. Meteorol. Soc.*, page in Press.
- Errico (1985). Spectra computed from a limited area grid. *Mon. Weather Rev.*, 113:1554–1562.
- Ertel, H. (1942). Ein neuer hydrodynamischer Wirbelsatz. *Meteor. Z.*, 59:277–281.
- Fortak, H. (1982). *Meteorologie*. Dietrich Reimer Verlag, Berlin, 2nd edition.
- Fritts, D. C. and Alexander, M. J. (2003). Gravity wave dynamics and effects in the middle atmosphere. *Rev. Geophys.*, 41(1):3.
- Fujita, T. (1986). Mesoscale classifications: their history and their application to forecasting. In *Mesoscale Meteorol. Forecast.*, pages 18–35.
- Galway, J. (1956). The lifted index as a predictor of latent instability. *Bull. Amer. Meteor. Soc.*, 37:528–529.

- Gebhardt, C., Theis, S., Krahe, P., and Renner, V. (2008). Experimental ensemble forecasts of precipitation based on a convection-resolving model. *Atmos. Sci. Lett.*, 9(2):67–72.
- Ghil, M., Yiou, P., Hallegatte, S., Malamud, B. D., Naveau, P., Soloviev, A., Friederichs, P., Keilis-Borok, V., Kondrashov, D., Kossobokov, V., and Others (2011). Extreme events: dynamics, statistics and prediction. *Nonlinear Process. Geophys.*, 18(3):295–350.
- Grams, C. M., Wernli, H., Böttcher, M., Čampa, J., Corsmeier, U., Jones, S. C., Keller, J. H., Lenz, C.-J. J., and Wiegand, L. (2011). The key role of diabatic processes in modifying the upper-tropospheric wave guide: A North Atlantic case-study. *Q. J. R. Meteorol. Soc.*, 137(661):2174–2193.
- Groenemeijer, P. H. and van Delden, A. (2007). Sounding-derived parameters associated with large hail and tornadoes in the Netherlands. *Atmos. Res.*, 83(2-4 SPEC. ISS.):473–487.
- Haklander, A. and van Delden, A. (2003). Thunderstorm predictors and their forecast skill for the Netherlands. *Atmos. Res.*, 67:273–299.
- Han, L., Fu, S., Zhao, L., Zheng, Y., Wang, H., and Lin, Y. (2009). 3D convective storm identification, tracking, and forecasting - An enhanced TITAN algorithm. *J. Atmos. Ocean. Technol.*, 26(4):719–732.
- Haynes, P. H. and McIntyre, M. E. (1987). On the Evolution of Vorticity and Potential Vorticity in the Presence of Diabatic Heating or Other Forces. *J. Atmos. Sci.*, 44:828–841.
- Haynes, P. H. and McIntyre, M. E. (1990). On the Conservation and Impermeability Theorems for Potential Vorticity. *J. Atmos. Sci.*, 47(16):2021–2031.
- Hense, A. (2012). Skript zur Vorlesung Theoretische Meteorologie 2 Wintersemester 2012/13.
- Holton, J. R. (2004). *An introduction to dynamic meteorology*. Elsevier Academic Press, fourth edition.
- Hoskins, B. J. (1997). A potential vorticity view of synoptic development. *Meteorol. Appl.*, 4:325–334.
- Hoskins, B. J., McIntyre, M. E., and Robertson, A. W. (1985). On the use and significance of isentropic potential vorticity maps. *Q. J. R. Meteorol. Soc.*, 111:877–946.
- Houze Jr, R. A. (2004). Mesoscale convective systems. *Rev. Geophys.*, 42(4):RG4003.
- Huntrieser, H. and Schiesser, H. (1997). Comparison of traditional and newly developed thunderstorm indices for Switzerland. *Weather Forecast.*, 12:108–124.

- Johnson, J. T., MacKeen, P. L., Witt, A., Mitchell, E. D. W., Stumpf, G. J., Eilts, M. D., and Thomas, K. W. (1998). The Storm Cell Identification and Tracking Algorithm: An Enhanced WSR-88D Algorithm. *Weather Forecast.*, 13(2):263–276.
- Kaltenböck, R., Diendorfer, G., and Dotzek, N. (2009). Evaluation of thunderstorm indices from ECMWF analyses, lightning data and severe storm reports. *Atmos. Res.*, 93:381–396.
- Keune, J., Ohlwein, C., and Hense, A. (2014). Multivariate probabilistic analysis and predictability of medium-range ensemble weather forecasts. *Mon. Weather Rev.*, 142:4074–4090.
- Klemp, J. (1987). Dynamics of tornadic thunderstorms. *Annu. Rev. Fluid Mech.*, 19:369–402.
- Kyznarová, H. and Novák, P. (2009). CELLTRACK - Convective cell tracking algorithm and its use for deriving life cycle characteristics. *Atmos. Res.*, 93(1-3):317–327.
- Lewis, J. M. (2005). Roots of ensemble forecasting. *Mon. Weather Rev.*, 133(7):1865–1885.
- Ligda, M. (1951). Radar storm observation. *Compend. Meteorol.*, pages 1265–1282.
- Lilly, D. K. (1986a). The structure, energetics and propagation of rotating convective storms. Part I: Energy exchange with the mean flow. *J. Atmos. Sci.*, 43(2):113–125.
- Lilly, D. K. (1986b). The structure, energetics and propagation of rotating convective Storms. Part II: Helicity and storm stabilization. *J. Atmos. Sci.*, 43(2):126140.
- Limbach, S., Schömer, E., and Wernli, H. (2012). Detection, tracking and event localization of jet stream features in 4-D atmospheric data. *Geosci. Model Dev.*, 5(2):457–470.
- Malardel, S., Joly, A., Courbet, F., and Courtier, P. (1993). Nonlinear evolution of ordinary frontal waves induced by low-level potential vorticity anomalies. *Quart. J. Roy. Meteor. Soc.*, 119:681–713.
- Markowski, P. and Richardson, Y. (2010). *Mesoscale Meteorology in Midlatitudes*. Advancing Weather and Climate Science. Wiley.
- Marquet, P. (2014). On the definition of a moist-air potential vorticity. *Q. J. R. Meteorol. Soc.*, 140(680):917–929.
- McCann, D. (1995). Three-dimensional computations of equivalent potential vorticity. *Weather Forecast.*, 10:798–802.
- McCaul Jr, E. W. and Weisman, M. L. (2001). The sensitivity of simulated supercell structure and intensity to variations in the shapes of environmental buoyancy and shear profiles. *Mon. Weather Rev.*, 129(4):664–687.

- McIntyre, M. E. (2015). Potential vorticity. *Encycl. Atmos. Sci. 2nd Ed.*, 2:375–383.
- Mellor, G. L. and Yamada, T. (1982). Development of a turbulence closure model for geophysical fluid problems. *Rev. Geophys.*, 20(4):851–875.
- Mills, E. (2005). Insurance in a climate of change. *Science (80-. )*, 309:1040–1044.
- Montgomery, M. T., Nicholls, M. E., Cram, T. A., and Saunders, A. B. (2006). A Vortical Hot Tower Route to Tropical Cyclogenesis. *J. Atmos. Sci.*, 63(1):355–386.
- Moseley, C., Berg, P., and Haerter, J. (2013). Probing the precipitation life cycle by iterative rain cell tracking. *J. Geophys. Res. Atmos.*, 118(24):13–361.
- Moseley, C. and Hohenegger, C. (2015). Intensification of convective extremes driven by cloud-cloud interaction. *arXiv Prepr. arXiv*, page 1510.03831.
- Murray, R. J. and Simmonds, I. (1991). A numerical scheme for tracking cyclone centres from digital data. Part I: Development and operation of the scheme. *Aust. Meteorol. Mag.*, 39(3):155–166.
- Nastrom, G. and Gage, K. (1985). A Climatology of Atmospheric Wavenumber Spectra of Wind and Temperature Observed by Commercial Aircraft. *J. Atmos. Sci.*, 42(9):950–960.
- Névir, P. (2004). Ertel's vorticity theorems, the particle relabelling symmetry and the energy-vorticity theory of fluid mechanics. *Meteorol. Zeitschrift*, 13(6):485–498.
- Orlanski, I. (1975). A rational subdivision of scales for atmospheric processes. *Bull. Am. Meteorol. Soc.*, 56:527–530.
- Pelly, J. L. and Hoskins, B. J. (2003). A new perspective on blocking. *J. Atmos. Sci.*, 60(5):743–755.
- Peralta, C., Ben Bouallègue, Z., Theis, S. E., Gebhardt, C., and Buchhold, M. (2012). Accounting for initial condition uncertainties in COSMO-DE-EPS. *J. Geophys. Res.*, 117.
- Petrik, R., Baldauf, M., Schlünzen, H., and Gassmann, A. (2011). Validation of a mesoscale weather prediction model using subdomain budgets. *Tellus A*, 63(4):707–726.
- Pinto, J. G., Spanghel, T., Ulbrich, U., and Speth, P. (2005). Sensitivities of a cyclone detection and tracking algorithm: Individual tracks and climatology. *Meteorol. Zeitschrift*, 14(6):823–838.
- Plant, R. S. (2008). Statistical properties of cloud lifecycles in cloud-resolving models. *Atmos. Chem. Phys. Discuss.*, 8(6):20537–20564.
- Raymond, D. J. and Jiang, H. (1990). A theory of long-lived mesoscale convective systems. *J. Atmos. Sci.*, 47:3067–3077.

- Renkl, C. (2013). *The Vertical Structure of the Atmosphere in COSMO-DE-EPS: Multivariate Ensemble Postprocessing in the Space of Vertical Normal Modes*. Master thesis, University of Bonn.
- Ritter, B. and Geleyn, J.-F. (1992). A comprehensive radiation scheme for numerical weather prediction models with potential applications in climate simulations. *Mon. Weather Rev.*, 120(2):303–325.
- Röpnack, A., Hense, A., Gebhardt, C., and Majewski, D. (2013). Bayesian Model Verification of NWP Ensemble Forecasts. 141(1):375–387.
- Rossby, C.-G. (1939). Relation between variations in the intensity of the zonal circulation of the atmosphere and the displacements of the semi-permanent centers of action. *J. Mar. Res.*, 2(1):38–55.
- Rossby, C. G. (1940). Planetary flow patterns in the atmosphere. *Quart. J. Roy. Meteor. Soc.*, 66:68–87.
- Rotunno, R., Klemp, J., and Weisman, M. L. (1988). A theory for strong, long-lived squall lines. *J. Atmos. Sci.*, 45(3):463–485.
- Rudeva, I. and Gulev, S. K. (2007). Climatology of Cyclone Size Characteristics and Their Changes during the Cyclone Life Cycle. *Mon. Weather Rev.*, 135(7):2568–2587.
- Rutherford, B. (2012). Lagrangian coherent structures in tropical cyclone intensification. *Atmos. Chem. Phys.*, 12(12):5483–5507.
- Salmon, R. (1998). *Lectures on Geophysical Fluid Dynamics*. Oxford University Press.
- Salvador, R., Calbó, J., and Millán, M. M. (1999). Horizontal grid size selection and its influence on mesoscale model simulations. *J. Appl. Meteorol.*, 38(9):1311–1329.
- Schär, C. (1993). A generalization of Bernoulli's theorem. *J. Atmos. Sci.*, 50(10):1437–1443.
- Schär, C., Sprenger, M., Lüthi, D., Jiang, Q., Smith, R. B., and Benoit, R. (2003). Structure and dynamics of an Alpine potential-vorticity banner. *Quart. J. Roy. Meteor. Soc.*, 129(588):825–855.
- Schättler, U., Doms, G., and Schraff, C. (2014). A Description of the Nonhydrostatic Regional COSMO-Model, part VII: User's Guide.
- Schefzik, R., Thorarinsdottir, T. L., and Gneiting, T. (2013). Uncertainty Quantification in Complex Simulation Models Using Ensemble Copula Coupling. *Stat. Sci.*, 28(4):616–640.
- Schubert, W., Ruprecht, E., Hertenstein, R., Ferreira, R. N., Taft, R., Rozoff, C., Ciesielski, P., and Kuo, H. (2004). English translations of twenty-one of Ertel's papers on geophysical fluid dynamics. *Meteorol. Z.*, 13:527–576.

- Schubert, W. H., Hausman, S. A., Garcia, M., Ooyama, K. V., and Kuo, H.-C. (2001). Potential Vorticity in a Moist Atmosphere. *J. Atmos. Sci.*, 58(21):3148–3157.
- Schuhen, N., Thorarinsdottir, T. L., and Gneiting, T. (2012). Ensemble Model Output Statistics for Wind Vectors. *Mon. Weather Rev.*, 140(10):3204–3219.
- Schultz, D. M. and Schumacher, P. N. (1999). The use and misuse of conditional symmetric instability. *Mon. Weather Rev.*, 127(12):2709–2732.
- Serway, R. and Jewett, J. (2013). *Physics for scientists and engineers with modern physics*. Cengage learning, Boston, MA, 9th edition.
- Shapiro, M. A. and Thorpe, A. J. (2004). THORPEX international science plan. *WMO/TD*, 1246.
- Showalter, A. (1953). A stability index for thunderstorm forecasting. *Bull. Amer. Meteor. Soc.*, 34(6):250–252.
- Stein, T. H. M., Hogan, R. J., Clark, P. A., Halliwell, C. E., Hanley, K. E., Lean, H. W., Nicol, J. C., and Plant, R. S. (2015). The DYM ECS Project: A Statistical Approach for the Evaluation of Convective Storms in High-Resolution NWP Models. *Bull. Am. Meteorol. Soc.*, 96(6):939–951.
- Stensrud, D. J., Coniglio, M. C., Davies-Jones, R. P., and Evans, J. S. (2005). Comments on “A Theory for Strong Long-Lived Squall Lines’ Revisited”. *J. Atmos. Sci.*, 62:2989.
- Stephan, K., Klink, S., and Schraff, C. (2008). Assimilation of radar-derived rain rates into the convective-scale model COSMO-DE at DWD. *Quart. J. Roy. Meteor. Soc.*, 134(634):1315–1326.
- Stevens, B. (2005). Atmospheric moist convection. *Annu. Rev. Earth Planet. Sci.*, 33(1):605–643.
- Thompson, R. L., Edwards, R., Hart, J. a., Elmore, K. L., and Markowski, P. (2003). Close Proximity Soundings within Supercell Environments Obtained from the Rapid Update Cycle. *Weather Forecast.*, 18(6):1243–1261.
- Thompson, R. L., Mead, C. M., and Edwards, R. (2007). Effective Storm-Relative Helicity and Bulk Shear in Supercell Thunderstorm Environments. *Weather Forecast.*, 22(1):102–115.
- Tiedtke, M. (1989). A comprehensive mass flux scheme for cumulus parameterization in large-scale models. *Mon. Weather Rev.*, 117(8):1779–1800.
- Tory, K., Kepert, J., Sippel, J., and Nguyen, C. (2011). On the Use of Potential Vorticity Tendency Equations for Diagnosing Atmospheric Dynamics in Numerical Models. *J. Atmos. Sci.*, 69:942–960.
- Venegas, S. (2001). Statistical methods for signal detection in climate. Technical report, Danish Center for Earth System Science (DCESS).

- Viúdez, Á. and Dritschel, D. G. (2004). Optimal potential vorticity balance of geophysical flows. *J. Fluid Mech.*, 521:343–352.
- von Storch, H. and Zwiers, F. W. (1988). Recurrence analysis of climate sensitivity experiments. *J. Clim.*, 1(2):157–171.
- von Storch, H. and Zwiers, F. W. (2001). *Statistical analysis in climate research*. Cambridge University Press.
- Wahl, S. (2015). *Uncertainty in mesoscale numerical weather prediction: probabilistic forecasting of precipitation*. Bonner meteorologische abhandlungen, Heft 71.
- Weckwerth, T. M. and Parsons, D. B. (2006). A Review of Convection Initiation and Motivation for IHOP\_2002. *Mon. Weather Rev.*, 134(1):5–22.
- Weijenborg, C., Friederichs, P., and Hense, A. (2015). Organisation of potential vorticity on the mesoscale during deep moist convection. *Tellus A*, 67.
- Weisman, M. and Klemp, J. (1982). The dependence of numerically simulated convective storms on vertical wind shear and buoyancy. *Mon. Weather Rev.*, 110:504–520.
- Weisman, M. L. and Klemp, J. B. (1984). The Structure and Classification of Numerically Simulated Convective Storms in Directionally Varying Wind Shears. *Mon. Weather Rev.*, 112(12):2479–2498.
- Weisman, M. L. and Rotunno, R. (2004). 'A Theory for Strong Long-Lived Squall Lines' Revisited. *J. Atmos. Sci.*, 61(4):361–382.
- Wilks, D. S. (2011). *Statistical Methods in the Atmospheric Sciences*. Academic Press. Academic Press, third edition.
- Wilson, J. W. and Roberts, R. D. (2006). Summary of Convective Storm Initiation and Evolution during IHOP: Observational and Modeling Perspective. *Mon. Weather Rev.*, 134(1):23–47.
- Wyngaard, J. C. (2004). Toward Numerical Modeling in the 'Terra Incognita'. *J. Atmos. Sci.*, 61(14):1816–1826.
- Xie, S., Zhang, Y., Giangrande, S. E., Jensen, M. P., McCoy, R., and Zhang, M. (2014). Interactions between cumulus convection and its environment as revealed by the {MC3E} sounding array. *J. Geophys. Res. Atmos.*, 119:11–784.
- Zhang, X., Walsh, J. E., Zhang, J., Bhatt, U. S., and Ikeda, M. (2004). Climatology and interannual variability of Arctic cyclone activity: 1948–2002. *J. Clim.*, 17(12):2300–2317.
- Zimmer, M., Craig, G. C., Keil, C., and Wernli, H. (2011). Classification of precipitation events with a convective response timescale and their forecasting characteristics. *Geophys. Res. Lett.*, 38(5):L05802.



## BONNER METEOROLOGISCHE ABHANDLUNGEN

Herausgegeben vom Meteorologischen Institut der Universität Bonn durch Prof. Dr. H. FLOHN (Hefte 1-25), Prof. Dr. M. HANTEL (Hefte 26-35), Prof. Dr. H.-D. SCHILLING (Hefte 36-39), Prof. Dr. H. KRAUS (Hefte 40-49), ab Heft 50 durch Prof. Dr. A. HENSE.

Heft 1-49: siehe <http://www.meteo.uni-bonn.de/bibliothek/bma>

- Heft 50: **Petra Friederichs**: Interannuelle und dekadische Variabilität der atmosphärischen Zirkulation in gekoppelten und SST-getriebenen GCM-Experimenten. 2000, 133 S. + VIII. € 25
- Heft 51: **Heiko Paeth**: Anthropogene Klimaänderungen auf der Nordhemisphäre und die Rolle der Nordatlantik-Oszillation. 2000, 168 S. + XVIII. € 28
- Heft 52: **Hildegard Steinhorst**: Statistisch-dynamische Verbundsanalyse von zeitlich und räumlich hoch aufgelösten Niederschlagsmustern: eine Untersuchung am Beispiel der Gebiete von Köln und Bonn. 2000, 146 S. + XIV. € 25
- Heft 53: **Thomas Klein**: Katabatic winds over Greenland and Antarctica and their interaction with mesoscale and synoptic-scale weather systems: three-dimensional numerical models. 2000, 146 S. + XIV. € 25
- Heft 54: **Clemens Drüe**: Experimentelle Untersuchung arktischer Grenzschichtfronten an der Meereisgrenze in der Davis-Straße. 2001, 165 S. + VIII. € 28
- Heft 55: **Gisela Seuffert**: Two approaches to improve the simulation of near surface processes in numerical weather prediction models. 2001, 128 S. + VI. € 25
- Heft 56: **Jochen Stuck**: Die simulierte axiale atmosphärische Drehimpulsbilanz des ECHAM3-T21 GCM. 2002, 202 S. + VII. € 30
- Heft 57: **Günther Haase**: A physical initialization algorithm for non-hydrostatic weather prediction models using radar derived rain rates. 2002, 106S. + IV. € 25
- Heft 58: **Judith Berner**: Detection and Stochastic Modeling of Nonlinear Signatures in the Geopotential Height Field of an Atmospheric General Circulation Model. 2003, 157 S. + VIII. € 28
- Heft 59: **Bernd Maurer**: Messungen in der atmosphärischen Grenzschicht und Validation eines mesoskaligen Atmosphärenmodells über heterogenen Landoberflächen. 2003, 182 S. + IX. € 30
- Heft 60: **Christoph Gebhardt**: Variational reconstruction of Quaternary temperature fields using mixture models as botanical – climatological transfer functions. 2003, 204 S. + VIII. € 30
- Heft 61: **Heiko Paeth**: The climate of tropical and northern Africa – A statistical-dynamical analysis of the key factors in climate variability and the role of human activity in future climate change. 2005, 316 S. + XVI. € 15
- Heft 62: **Christian Schölzel**: Palaeoenvironmental transfer functions in a Bayesian framework with application to Holocene climate variability in the Near East. 2006, 104 S. + VI. € 15
- Heft 63: **Susanne Bachner**: Daily precipitation characteristics simulated by a regional climate model, including their sensitivity to model physics, 2008, 161 S. € 15

- Heft 64: **Michael Weniger**: Stochastic parameterization: a rigorous approach to stochastic three-dimensional primitive equations, 2014, 148 S. + XV. open access<sup>1</sup>
- Heft 65: **Andreas Röpnick**: Bayesian model verification: predictability of convective conditions based on EPS forecasts and observations, 2014, 152 S. + VI. open access<sup>1</sup>
- Heft 66: **Thorsten Simon**: Statistical and Dynamical Downscaling of Numerical Climate Simulations: Enhancement and Evaluation for East Asia, 2014, 48 S. + VII. + Anhänge open access<sup>1</sup>
- Heft 67: **Elham Rahmani**: The Effect of Climate Change on Wheat in Iran, 2014, [erschienen] 2015, 96 S. + XIII. open access<sup>1</sup>
- Heft 68: **Pablo A. Saavedra Garfias**: Retrieval of Cloud and Rainwater from Ground-Based Passive Microwave Observations with the Multi-frequency Dual-polarized Radiometer ADMIRARI, 2014, [erschienen] 2015, 168 S. + XIII. open access<sup>1</sup>
- Heft 69: **Christoph Bollmeyer**: A high-resolution regional reanalysis for Europe and Germany - Creation and Verification with a special focus on the moisture budget, 2015, 103 S. + IX. open access<sup>1</sup>
- Heft 70: **A S M Mostaquimur Rahman**: Influence of subsurface hydrodynamics on the lower atmosphere at the catchment scale, 2015, 98 S. + XVI. open access<sup>1</sup>
- Heft 71: **Sabrina Wahl**: Uncertainty in mesoscale numerical weather prediction: probabilistic forecasting of precipitation, 2015, 108 S. open access<sup>1</sup>
- Heft 72: **Markus Übel**: Simulation of mesoscale patterns and diurnal variations of atmospheric CO<sub>2</sub> mixing ratios with the model system TerrSysMP-CO<sub>2</sub>, 2015, [erschienen] 2016, II, 158 S. open access<sup>1</sup>
- Heft 73: **Christian Bernardus Maria Weijenborg**: Characteristics of Potential Vorticity anomalies associated with mesoscale extremes in the extratropical troposphere, 2015, [erschienen] 2016, XI, 151 S. open access<sup>1</sup>

---

<sup>1</sup>Available at <http://hss.ulb.uni-bonn.de/fakultaet/math-nat/>





METEOROLOGISCHES INSTITUT  
MATHEMATISCH NATURWISSENSCHAFTLICHE FAKULTÄT  
UNIVERSITÄT BONN

